



Continuous-variable quantum codes for fault-tolerant quantum information processing

Jacob Hastrup

PhD Thesis

Supervisors:
Professor Ulrik Lund Andersen
Senior Researcher Jonas Schou Neergaard-Nielsen

Technical University of Denmark
Department of Physics
August 2021

Title: Continuous-variable quantum codes for fault-tolerant quantum information processing

Author: Jacob Hastrup

Supervisors: Professor Ulrik Lund Andersen
Senior Researcher Jonas Schou Neergaard-Nielsen

Period: September 2018 - August 2021

University: Technical University of Denmark

Department: DTU Physics, Department of Physics
Section of Quantum Physics and Information Technology, QPIT
bigQ - Center for Macroscopic Quantum States

Abstract

Quantum computers can potentially revolutionize computational science and technology, but their full-scale realization has proven to be an enormous challenge. A central issue is that noise severely limits the performance of quantum computers. To make quantum computers fault tolerant, quantum error-correction protocols are needed. A promising type of quantum error correction is bosonic error correction in which each qubit is encoded into the continuous variables of a bosonic mode. Experimental progress over the past two decades has enabled a high degree of control over several continuous-variable quantum systems, making bosonic codes a promising direction towards fault tolerance.

In this thesis, I investigate two prominent groups of continuous-variable quantum systems and propose novel schemes for quantum state generation and manipulation in these systems, with a primary focus on bosonic error correction.

The first group is optics, in which Gaussian operations across a large number of modes can be easily implemented. Optical platforms thus have many favorable features in terms of scalability and control, but losses constitute a central challenge. While losses can in principle be mitigated with bosonic quantum error-correcting codes, implementing these codes with available techniques is non-trivial. Here, I present schemes to optically generate and perform error correction on cat codes through linear optics and photon counting. Furthermore, I propose a method to generate Gottesman-Kitaev-Preskill (GKP) states using a cavity quantum electrodynamics system as a non-Gaussian resource. Finally, I show that, contrary to common belief, the cubic phase gate is not a suitable resource for non-Clifford operations of GKP states.

The second group consists of systems in which strong boson-qubit couplings allow for the efficient implementation of conditional displacement gates. With current technology, this includes trapped ions and microwave cavity modes coupled to superconducting circuits. Here, I present and analyze improved protocols to generate and measure GKP states encoded in such systems. Additionally, I present two more general-purpose quantum continuous-variable algorithms. The first algorithm is a method to generate squeezed states in the absence of a squeezing Hamiltonian, by instead superimposing multiple coherent states in phase space. The second algorithm is a method to transfer arbitrary continuous-variable states into a discrete-variable qubit register.

In summary, the protocols presented herein aim to facilitate and expand the possibilities for control of continuous-variable quantum systems with existing and near-future technology.

Resumé (Danish)

Kvantecomputere kan potentielt revolutionere computervidenskab og -teknologi, men deres realisering har vist sig at være en yderst vanskelig udfordring. Et centralt problem er, at støj i høj grad begrænser ydeevnen af kvantecomputere. For at gøre kvantecomputere fejltolerante er kvante-fejlkorrektion derfor nødvendig. En lovende type af kvante-fejlkorrektion er bosoniske koder, hvor hver qubit er indkodet i de kontinuerte variable af en bosonisk tilstand. Eksperimentelle fremskridt over de sidste to årtier har muliggjort en høj grad af kontrol over de kvantemekaniske egenskaber af systemer med kontinuerte variable, hvilket har gjort bosoniske koder til en lovende tilgang til fejltolerance.

I denne afhandling undersøges to typer af kvantesystemer med kontinuerte variable, og nye protokoller til at generere og manipulere kvantetilstande i disse systemer fremlægges med et primært fokus på bosonisk fejlkorrektion.

Det første system er optik, hvori Gaussiske operationer over mange tilstande nemt kan implementeres. Optik har således mange fordele i forhold til skalering og kontrol, men tab udgør en central udfordring. Selvom tab i princippet kan mitigeres med bosoniske fejlkorrigerende koder, er det uvist, hvordan disse koder kan implementeres med nuværende teknikker. I denne afhandling præsenteres metoder til at generere og udføre fejlkorrektion på optiske katkoder ved hjælp af lineær optik og fotontælling. Derudover præsenteres en metode til at generere Gottesman-Kitaev-Preskill (GKP) tilstande ved hjælp af kavitetskvanteelektrodynamik som en ikke-Gaussisk ressource. Endeligt viser jeg, at den kubiske fasegate ikke er en egnet ressource til at udføre ikke-Clifford operationer på GKP tilstande.

Det andet system består af platforme, hvori en stærk boson-qubit kobling muliggør en effektiv implementering af betingede forskydningsgates. Med nuværende teknologi inkluderer dette fangede ioner og mikrobølgekavitets tilstande koblet til superledende kredsløb. Jeg præsenterer og analyserer forbedrede protokoller til at generere og måle GKP tilstande i disse systemer. Derudover præsenteres to kontinuertvariable kvantealgoritmer med mere generelle formål. Den ene algoritme er en metode til at generere klemte tilstande i fraværet af et klemme-Hamilton ved at lave en superposition af kohærente tilstande. Den anden algoritme er en metode til at flytte vilkårlige kontinuertvariable tilstande til et diskretvariabelt qubit register.

Samlet set har resultaterne, der er præsenteret i denne afhandling, til formål at facilitere og udvide mulighederne for at kontrollere kontinuertvariable kvantesystemer gennem teknologi, der er tilgængeligt i dag eller i den nærmeste fremtid.

Acknowledgments

First of all, I want to acknowledge you, Ulrik, for giving me the unique opportunity to spend the past three years expanding my knowledge and stimulating my curiosity for quantum information and physics. As a young and inexperienced scientist, I think it is common to look with envy towards the successes of ones peers and perhaps second guess ones choice of PhD project. However, I have repeatedly concluded that I would prefer my own project most of all. This is all due to the continuous encouragement you have provided as well as the freedom you have trusted in me to explore whatever direction I found interesting at the time, and for this I am very grateful.

Thanks to my co-supervisor Jonas as well as Jonatan and Alex. Your inputs, feedback and helpfulness have been much appreciated and have improved the quality of much of the work in this thesis.

Thanks to Radim for many stimulating discussions as well as endless amounts of high-quality feedback and encouragement. I am very grateful that you would spend so much of your time aiding my projects. Your enthusiasm has always been highly motivating and much appreciated.

Thanks to Kimin, your insights and our discussions have provided a spark for many of the ideas within this thesis. I have always enjoyed your company and your ever calm and humble spirit. I wish you and your family the best of luck on your future journeys.

Thanks to my Australian colleagues Tim, Austin and Matt. I am still saddened that my visit was cut short. Still, I highly appreciate all the time I spent with you. Thanks to Austin for our discussions on boson sampling and thanks to Matt for being my friend away from home.

And not least, I send my deepest thanks and love to Laura. Your everlasting support and encouragement has made my PhD, and indeed all aspects of my life, a truly meaningful and fulfilling journey.

Contents

Abstract	i
Resumé (Danish)	ii
Acknowledgments	iii
1 Introduction	1
1.1 Quantum computing	1
1.2 Quantum error correction	3
1.3 Thesis structure	5
2 Quantum continuous variables	7
2.1 Fundamentals of quantum continuous variables	7
2.1.1 Density matrices	8
2.1.2 Position and momentum	9
2.1.3 Electromagnetic field quadratures	11
2.1.4 The Wigner function	11
2.1.5 Fock representation	12
2.2 States	14
2.3 Gates	17
2.4 Noise channels	21
2.5 Bosonic quantum error correction	24
2.5.1 The cat code	25
2.5.2 The GKP code	28
3 Deterministic generation of a four-component optical cat state	32
3.1 Abstract	32
3.2 Introduction	32
3.3 Protocol	33
3.4 Conclusion	38
4 All-optical cat-code quantum error correction	39
4.1 Abstract	39
4.2 Introduction	39
4.3 Protocol	40
4.4 Conclusion	45
4.5 Appendix A: Teleportation without losses	46

4.6	Appendix B: Teleportation with losses	47
4.7	Appendix C: generation of logical Bell states with cavity QED	49
5	Generation of optical Gottesman-Kitaev-Preskill states with cavity QED	51
5.1	Abstract	51
5.2	Introduction	51
5.3	Preliminaries	52
5.4	Results	55
5.5	Conclusion	58
5.6	S1: Realistic reflection channel	58
5.7	S2: Squeezing in the limit $\eta \rightarrow 1$ and $C \rightarrow \infty$	61
5.8	S3: Input squeezing	63
5.9	S4: Displacement amplitudes	63
5.10	S5: Required cooperativity and escape efficiency	64
5.11	S6: Calculation of effective squeezing parameters	64
5.12	S7: Generation of squeezed vacuum states	66
6	Unsuitability of cubic phase gates for non-Clifford operations on Gottesman-Kitaev-Preskill states	68
6.1	Abstract	68
6.2	Introduction	68
6.3	Preliminaries	69
6.4	Error-corrected fidelity	71
6.5	Modular bosonic subsystem fidelity	72
6.6	Conclusion	74
6.7	Supplementary Material	74
7	Measurement-free preparation of grid states	77
7.1	Abstract	77
7.2	Introduction	77
7.3	Results	79
7.4	Discussion	89
7.5	S1: Effective shift error	89
7.6	S2: Preparation gate interaction strengths	90
7.7	S3: No initial squeezing	92
7.8	S4: Realistic noise parameters	92
8	Improved readout of qubit-coupled Gottesman-Kitaev-Preskill states	95
8.1	Abstract	95
8.2	Introduction	95
8.3	Preliminaries	96
8.4	Protocol	99
8.5	Conclusion	101
8.6	Appendix A: Improved measurement error probability	102
8.7	Appendix B: Post-measurement state	104
9	Unconditional preparation of squeezed vacuum from Rabi interactions	106
9.1	Abstract	106
9.2	Introduction	106
9.3	Protocol	107

9.4	Conclusion	113
9.5	S1: Discrete coherent state representation of squeezed vacuum	113
9.6	S2: Optimizing excess anti-squeezing	114
9.7	S3: Fisher information	115
10	Universal unitary transfer of continuous-variable quantum states into a few qubits	117
10.1	Abstract	117
10.2	Introduction	117
10.3	Protocol	118
10.4	Conclusion	123
10.5	S1: Fidelity of recovered states	124
10.6	S2: Analytical analysis of the protocol	124
10.7	S3: Overlap between $ \tilde{0}\rangle_{CV}$ and squeezed vacuum	127
10.8	S4: Random states	127
11	Conclusion and outlook	129
A	Notes on numerical implementations	132
	Bibliography	138

Chapter 1

Introduction

1.1 Quantum computing

Before diving into the details of continuous-variable quantum information processing, we warm up by going through a brief introduction to quantum computing in order to motivate the field and clear up a few common misconceptions. The concept of a *quantum computer* was first suggested by Richard Feynman in the early 1980's [1]. His motivation was based on the observation that quantum mechanics seemingly cannot be simulated efficiently by conventional classical (non-quantum) computers. That is, classical computers cannot always efficiently predict the behavior of quantum systems. An important concept here is the notion of efficiency, which means that the number of components, or bits, in the computer should not increase exponentially with the number of elements, e.g. particles or photons, that the computer is trying to simulate. Similarly, the time required for the computer to carry out the simulation should not increase exponentially with the size of the physical system. Thus, the fact that quantum systems in general require an exponentially large classical computer to simulate, means that it quickly becomes impractical, and even impossible, to predict the behavior of modest sized quantum systems. As an example, the spin state of a system consisting of 60 electrons is in general described by $2^{60} \approx 10^{18}$ complex numbers. For comparison, Summit, one of the worlds largest supercomputers, has a memory capacity of 2.5×10^{17} bytes [2], making it insufficient to even store the state of 60 electrons. And while that example might be conquerable by the next generation of supercomputers, going to 300 electrons requires $2^{300} \approx 10^{90}$ complex numbers, which exceeds the number of atoms in the universe. So not only are such quantum systems impractical to simulate exactly with classical computers, it even becomes strictly impossible given the finite amount of resources in the universe, and even more so given the finite amount of resources we can allocate to computers on Earth.

Quantum computers overcome this problem by storing and manipulating information using quantum bits, *qubits*, instead of conventional bits. Similarly to a conventional bit, which can store either a 0 or a 1, a qubit is described by two distinguishable states, $|0\rangle$ and $|1\rangle$. Here, the bracket notation, $|\cdot\rangle$, signifies that these are quantum states, meaning that a qubit can take on any superposition state of the form

$$c_0|0\rangle + c_1|1\rangle, \tag{1.1}$$

where the coefficients c_0 and c_1 are complex numbers satisfying $|c_0|^2 + |c_1|^2 = 1$. The classical bit is then a special case of the qubit, for which one of the coefficients is zero. At first glance, it

might appear that a quantum bit can store infinitely more information than a classical bit, since the coefficients can take on infinitely many values. For example, one might be tempted to state that a single bit can encode the four-bit string '1010' by setting $c_0 = 0.0101$. However, while the qubit can indeed be set to this state, we run into a problem when we want to retrieve the input bit string. This is because a measurement of the qubit always returns either a 0 with probability $|c_0|^2$, or a 1 with probability $|c_1|^2$. Furthermore, the state of the qubit after the measurement is reduced to a classical bit corresponding to the measurement outcome, such that the exact values of the coefficients before the measurement are erased. So unless we want to run a casino, it is not the fact that the qubit coefficients can take on infinitely many values that gives quantum computers an edge.

Instead, the difference between the computational power of a bit and a qubit is much more subtle, and arises from the fact that the complex-valued qubit coefficients can interfere in ways that classical bits cannot. For example, an important operation of a quantum computer is the Hadamard gate, H , which is defined by applying the transformations

$$|0\rangle \xrightarrow{H} \frac{1}{\sqrt{2}}|0\rangle + \frac{1}{\sqrt{2}}|1\rangle \quad \text{and} \quad |1\rangle \xrightarrow{H} \frac{1}{\sqrt{2}}|0\rangle - \frac{1}{\sqrt{2}}|1\rangle. \quad (1.2)$$

Thus either of the states $|0\rangle$ and $|1\rangle$ are transformed into superpositions of $|0\rangle$ and $|1\rangle$ by the Hadamard gate. A weak classical analogue to this would be to randomly set the state of the input bit to either 0 or 1. However, applying the Hadamard gate to a qubit in a superposition state with $c_0 = c_1 = 1/\sqrt{2}$ we get:

$$\begin{aligned} \frac{1}{\sqrt{2}}|0\rangle + \frac{1}{\sqrt{2}}|1\rangle &\xrightarrow{H} \frac{1}{\sqrt{2}} \left(\frac{1}{\sqrt{2}}|0\rangle + \frac{1}{\sqrt{2}}|1\rangle \right) + \frac{1}{\sqrt{2}} \left(\frac{1}{\sqrt{2}}|0\rangle - \frac{1}{\sqrt{2}}|1\rangle \right) \\ &= \left(\frac{1}{2} + \frac{1}{2} \right) |0\rangle + \left(\frac{1}{2} - \frac{1}{2} \right) |1\rangle \\ &= |0\rangle. \end{aligned} \quad (1.3)$$

Thus, the superposition state is transformed into the state $|0\rangle$ with certainty due to the negative interference of the $|1\rangle$ term. Such interference behavior cannot be simulated with a single classical bit, and opens up new types of algorithms using quantum computers.

Of course, since a single qubit is completely described by just 2 numbers, c_0 and c_1 , we can easily simulate it with a few bits in a classical computer. However, when we go to many-qubit systems this is no longer the case. This is because we need to store a complex number for each possible configuration of bits, i.e. 4 numbers for 2 qubits (combinations $\{00, 01, 10, 11\}$), 8 numbers for 3 qubits (combinations $\{000, 001, 010, 011, 100, 101, 110, 111\}$), and in general 2^n numbers for n qubits.

Furthermore, these multi-qubit superposition states give rise to correlations between the qubits, denoted entanglement, which are beyond what can be explained with classical physics. For example, consider the two-qubit state $\frac{1}{\sqrt{2}}|0\rangle|0\rangle + \frac{1}{\sqrt{2}}|1\rangle|1\rangle$. Measuring one qubit gives either 0 or 1 with probability 50:50, and measuring the second qubit will always give the same result as the first. Thus the two states are perfectly correlated. This correlation by itself is not particularly impressive as one could spoof those results with classical bits by choosing the number 0 or 1 randomly and then preparing two classical bits in the chosen state. However, an interesting behavior appears when applying the Hadamard gate to each of the qubits individually, in which

case we get

$$\begin{aligned}
\frac{1}{\sqrt{2}}|0\rangle|0\rangle + \frac{1}{\sqrt{2}}|1\rangle|1\rangle &\xrightarrow{\text{H on both qubits}} \frac{1}{2\sqrt{2}}(|0\rangle + |1\rangle)(|0\rangle + |1\rangle) + \frac{1}{2\sqrt{2}}(|0\rangle - |1\rangle)(|0\rangle - |1\rangle) \\
&= \frac{1}{2\sqrt{2}}\left((1+1)|0\rangle|0\rangle + (1+1)|1\rangle|1\rangle + (1-1)|0\rangle|1\rangle + (1-1)|1\rangle|0\rangle\right) \\
&= \frac{1}{\sqrt{2}}|0\rangle|0\rangle + \frac{1}{\sqrt{2}}|1\rangle|1\rangle. \tag{1.4}
\end{aligned}$$

That is, the anti-correlation terms $|0\rangle|1\rangle$ and $|1\rangle|0\rangle$ are cancelled out due to quantum interference, such that the state of the qubits is completely unchanged and they remain perfectly correlated! But if the Hadamard gate is applied to either $|0\rangle|0\rangle$ or $|1\rangle|1\rangle$, which represent our non-quantum spoof, the anti-correlation terms would not cancel out and measurement outputs would instead be completely random and uncorrelated between the two bits. Classical bits are therefore insufficient to reproduce the level of correlation present in entangled particles [3].

The effects of superposition, interference and entanglement thus allows for behaviours which are impossible to replicate efficiently without qubits. Yet, due to the complex dynamics of quantum systems, the probabilistic nature of qubits, and the high efficiency of modern classical computers, harnessing these quantum phenomena into useful quantum algorithms is no trivial task. A breakthrough occurred in 1994 when Peter Shor famously showed that quantum computers can be used to factor large integers with an exponential speed-up over classical computers [4]. This was a shocking result, partly due to the fact that the difficulty of factorization underlies the so-called RSA encryption scheme which is widely used in modern cryptography. An efficient factorization algorithm would therefore enable the decryption of RSA encoded messages, which has huge, negative, implications to the general public. Furthermore, the fact that quantum computers can be used for factorization—a problem which is seemingly completely unrelated to quantum mechanics—begs the question of what other algorithms can be sped up by quantum computers. Another seminal quantum algorithm is Grover’s search algorithm from 1996 [5], which provides a quadratic speed up for searching unstructured data, and has a much wider application potential compared to Shor’s algorithm.

Since the 90’s, many new quantum algorithms have been devised [6], which has driven an increasing amount research and interest in quantum computers across a wide range of fields. A notable example is quantum machine learning [7, 8] which aims to leverage quantum algorithms to enhance machine learning tasks. Meanwhile, the original motivation of Feynman to simulate physical systems has merged the fields of computational chemistry and quantum computing [9, 10], which could lead to discoveries of novel medicinal drugs and new materials. Other application potentials include problems in climate change [11], finance [12] and energy optimization [13].

1.2 Quantum error correction

The past two decades have seen an accelerating worldwide effort to realise functional quantum computers, and notably there is now experimental evidence that quantum computers can indeed exponentially outperform classical computers in certain tasks [14–16]. Yet, quantum computers have so far solved exactly zero real-world problems. This is because building quantum computers with multiple controllable and interacting qubits has proven to be an enormously challenging task. A key challenge is to prevent undesired errors from accumulating during the execution of an algorithm. In particular, any interaction between a qubit and its environment can cause

the quantum information stored in the qubit to leak out into the environment. This means, that in practice superposition states are typically stable only on timescales much smaller than a second, and entanglement can be observed between only a handful of qubits. To move beyond this regime, we need to design qubits which can be isolated from their environment, but at the same time be controlled and interact with each other. The good news is that we don't need perfect qubits to build a useful large-scale quantum computer. Instead, we can program the quantum computer itself to detect and correct small errors, preventing them from accumulating. This is known as *quantum error correction*.

The key principle of quantum error correction is to redundantly spread each qubit of information across multiple physical systems, such that even if one or more physical qubits fail, the logical information can still be retrieved. A simple classical example is to copy a single bit onto three bits, i.e. 0 becomes 000 and 1 becomes 111. If one of the bits flips due to noise, we can still guess what the original state was by taking a majority vote. This means that the effective error rate of the logical information can be reduced, provided the probability of two simultaneous errors is low. Essentially, multiple faulty bits are used to simulate a single good bit.

The field of classical error-correcting codes has been well developed for a long time, and more advanced techniques than the example above exist which require much lower resource overheads [17, 18]. Such techniques are routinely used in conventional information processing to the point where we would never expect a conventional computer to make a computational error.

Implementing error correction of quantum computers, on the other hand, is much more difficult for three main reasons: First, while the only type of error for a classical bit is a bit flip, i.e. an undesired change from a 0 to a 1 or vice versa, qubits can also experience phase errors. That is, a qubit in the state $\frac{1}{\sqrt{2}}|0\rangle + \frac{1}{\sqrt{2}}|1\rangle$ might change to the state $\frac{1}{\sqrt{2}}|0\rangle - \frac{1}{\sqrt{2}}|1\rangle$. Since the phase is a key element to quantum computers, such an error can drastically change the outcome of a quantum algorithm. Thus, a quantum error-correcting code needs to detect not only bit flips, but also phase flips. Second, the act of measurement changes the quantum state, as described earlier. While a classical error-correcting code can measure each bit directly, we cannot directly observe the qubits individually as this would destroy any superposition state. Third, due to the complexity of controlling physical systems at the quantum level, the error rate of qubits are in practice much, much higher than that of classical bits.

The first two reasons above mean that conventional error correction cannot be directly transferred to quantum computers. Instead, completely new quantum error-correcting codes have to be developed. The first such code was proposed by Peter Shor in 1995 [19], in which 9 physical qubits are used to implement a single logical qubit. Another encoding was subsequently independently proposed by Andrew Steane in 1996 [20] using only 7 physical qubits. Since then, the field of quantum error correction has rapidly matured and many different quantum error-correcting codes have been discovered.

So what makes a good quantum error-correcting code? Essentially, we would like to be able to perform arbitrarily long computations, yet if the single-qubit error rates are non-zero, they will eventually add up and ruin the calculation. To prevent this, we need to be able to suppress the effective error rates of the logical qubits to arbitrarily low levels. Fortunately, this is achievable, for example by concatenating multiple layers of a code. Using Shor's code, one can use 9 logical qubits, each comprising 9 physical qubits to realize an even better logical qubit consisting of a total of 81 physical qubits. This can be iterated to reduce the logical error rate to arbitrarily low levels, at the cost of a larger and larger resource overhead. Of course, the more qubits, the larger the chance that a single physical qubit experiences an error. For quantum error correction to

work, the code should fix more errors than it introduces, which is only possible if the physical error rate is lower than a certain threshold. Different codes have different thresholds, and preferably we would want to use a code with a high threshold to relax the requirements on the physical qubits. Additionally, we would prefer an efficient reduction of the logical error rate when we increase the number of qubits, in order to minimize the total number of required physical qubits. Finally, the code should only require local interactions between physical qubits, as it can be very challenging, if not impossible, to implement direct interactions between an arbitrary pair of qubits in a quantum computer.

Arguably, the most promising quantum error-correcting code is the surface code [21–23] as it can be implemented with qubits in a square lattice architecture, and it has a fault-tolerance threshold of about 1%, which is rather high. Still, with the surface code it is expected that more than 1000 physical qubits will be needed for each logical qubit in order to reach sufficiently low logical error rates to implement e.g. Shor’s factorization algorithm [24, 25]. This is a huge resource overhead and so efforts to reduce this overhead are needed to make quantum computers practical.

Designing qubits of a high quality at the physical level is essential to get below the fault-tolerance threshold, and extremely good qubits will eventually be required in order to reduce the resource overhead of quantum error correction to manageable levels. One approach towards designing such high-quality qubits is to encode each qubit into a bosonic system and use bosonic error correction to add an additional layer of protection against noise. Contrary to the qubit-based error correction described above which uses multiple physical systems to simulate a single logical qubit, bosonic error correction uses multiple states of a single bosonic mode to encode a logical qubit. A such bosonic mode could for example be an optical field or the motion of a trapped ion. These systems have infinitely many energy levels which can provide a suitable redundancy for error correction. A classical analogue is found in optical communication systems where laser pulses are used to transmit classical bits. In such systems, a bit value of 1 can be represented by a high energy pulse, such that even when photons are inevitably lost throughout the optical fiber, the pulses still have enough energy to be correctly identified at the receiver. Unfortunately, we cannot directly use this simple classical strategy to make robust qubits, due to the possibility of phase errors. Instead, more advanced encodings, specifically tailored to protect quantum states, have been developed. These codes, and in particular the cat code [26, 27] and the Gottesman-Kitaev-Preskill (GKP) code [28], are the primary focus of this thesis. While the mathematical frameworks of these codes have been well described, their implementation in real-world systems remains challenging, limiting their usefulness in practice. This thesis presents novel techniques and strategies to implement and control these bosonic codes, tailored for state-of-the-art experimental settings. Hopefully, the results presented herein can thus guide future experimental efforts towards implementing bosonic codes and, ultimately, the realization of useful quantum computers.

1.3 Thesis structure

The remainder of this thesis is structured as follows:

In chapter 2 we introduce the mathematical framework of continuous-variable quantum systems as well the cat code and the GKP code.

Chapters 3 to 10 contain the research papers of Refs. [29–36] which were produced as a result of this PhD project. The content of these papers is exactly as their most recent/published versions.

Chapter 3 presents a method for generating four-component cat states from two-component cat

states using photon counting. With loss being the dominant source of noise in optical systems, the cat code might be a suitable encoding for optical systems. However, few proposals exist on how to optically generate the required four-component cat states. Here, we show that two two-component cat states can be “merged” to create a single four-component cat state using optical components.

Chapter 4 presents a method for performing error correction on optical cat-code qubits. While the cat code is a promising encoding to protect against losses, its implementation in optics has so far remained unclear. Here, we show that error correction can be performed in a teleportation-based setup using photon counters and logical Bell-encoded cat states.

Chapter 5 presents a method for generating optical GKP states using a cavity QED system. While multiple protocols have been proposed to generate GKP states, none of them have so far been successfully implemented in optics. However, it has recently been experimentally demonstrated that a cavity QED system can be used to generate optical Schrödinger’s cat states. Here, we show how such a system can also be used to generate GKP states and analyze the performance for systems of finite cooperativity and escape efficiency.

Chapter 6 analyzes the performance of cubic phase gates when used to implement non-Clifford gates on GKP qubits. We show that the cubic phase gate is not a suitable resource for the GKP code, and that non-Clifford gates should instead be implemented through gate teleportation of encoded magic states.

Chapter 7 presents a method to deterministically generate GKP states through conditional displacement gates. The proposal builds upon previously implemented protocols, but eliminates the need for qubit measurements. This allows for faster generation of GKP states which we show should ultimately result in higher quality states.

Chapter 8 presents a method to perform logical GKP state measurements in the absence of homodyne detectors. Homodyne detectors are usually the preferred method to measure GKP states, but these are not readily available in the systems for which GKP states have so far been experimentally generated. Here, we show that it is still possible to perform high-fidelity measurements in these systems by utilizing qubit interactions through conditional displacements.

Chapter 9 presents a method to deterministically generate squeezed vacuum states through conditional displacements. Squeezed vacuum states are a central resource for many continuous-variable quantum tasks. Here, we show how they can be generated from vacuum without the need to engineer a squeezing Hamiltonian.

Chapter 10 presents a protocol to transfer arbitrary continuous-variable states to a discrete-variable qubit register using conditional displacements. This allows for qubits to store continuous-variable states and could open up new types of control in qubit-coupled continuous-variable systems.

Finally, chapter 11 concludes the work, and outlines relevant near-term challenges and directions for continuous-variable quantum platforms.

Chapter 2

Quantum continuous variables

In this section we introduce the quantum mechanical mathematical background and formalism used throughout the thesis. As one can easily fill a textbook on this subject [37–41], not every aspect will be explained in full mathematical rigor. Instead, we will simply introduce the most relevant aspects of quantum continuous-variables, before introducing the cat and GKP quantum error-correcting codes.

2.1 Fundamentals of quantum continuous variables

The fundamental mathematical objects of quantum mechanics are *states* and *operators*. In the Schrödinger picture, a state represents a physical system, and thus contains all the information there is to know about that particular physical system. Mathematically, the states are vectors with a dimensionality depending on the type of physical system. For continuous-variable systems the dimensionality is infinite. Meanwhile, the operators are used to probe and change the states, and can be categorised into two groups: observables and unitary transformations. For now, we focus our attention to observables, returning to unitary transformations in Section 2.3. Observables, as the name suggests, represent physical quantities, or properties, that we are able to observe for a given system. Some common examples are the position and momentum of a particle along a specific axis. For each observable we associate a Hermitian operator, \hat{A} , from which we can furthermore identify its eigenstates, $|a\rangle$, and corresponding eigenvalues, a . These quantities thus satisfy

$$\hat{A}|a\rangle = a|a\rangle. \quad (2.1)$$

Physically, the eigenvalues are the possible measurement outcomes of the corresponding physical quantity. Here, we focus our attention to observables for which the possible measurement outcomes span a continuous interval, as is the case for position and momentum.

A central principle in quantum mechanics is the *superposition principle*. Let a \hat{A} denote any observable with continuous eigenvalues and corresponding eigenstates $|a\rangle$. The superposition principle states that any state $|\psi\rangle$ can be represented as a superposition (weighted sum) of these eigenstates:

$$|\psi\rangle = \int da \psi(a)|a\rangle, \quad (2.2)$$

where the complex-valued function

$$\psi(a) = \langle a|\psi\rangle, \quad (2.3)$$

is called the wavefunction of the state with respect to the observable \hat{A} . Applying $\langle a'|$ to Eq. (2.2) we get

$$\langle a'|\psi\rangle = \psi(a') = \int da \psi(a) \langle a'|a\rangle, \quad (2.4)$$

from which we conclude that the observable eigenstates should satisfy

$$\langle a'|a\rangle = \delta(a' - a), \quad (2.5)$$

where δ is the Dirac delta function. Additionally, applying $\int da |a\rangle\langle a|$ to Eq. (2.2) get

$$\left(\int da |a\rangle\langle a| \right) |\psi\rangle = \int da \int da' \psi(a') |a\rangle\langle a|a'\rangle = \int da \psi(a) |a\rangle = |\psi\rangle, \quad (2.6)$$

from which we obtain the identity relation

$$\int da |a\rangle\langle a| = \hat{I}, \quad (2.7)$$

where \hat{I} is the identity operator.

According to quantum mechanics all measurements are fundamentally probabilistic, and the wavefunction therefore only allows us to calculate the probability density of a particular measurement outcome through the Born rule,

$$P(a) = |\langle a|\psi\rangle|^2 = |\psi(a)|^2. \quad (2.8)$$

Since a measurement of the observable \hat{A} should always return some outcome, the probability density should integrate to 1:

$$\int P(a) da = \int |\psi(a)|^2 da = 1. \quad (2.9)$$

Thus the wavefunction of any physical state should be normalized to $\int |\psi(a)|^2 = \langle \psi|\psi\rangle = 1$. Note that the eigenstates of continuous-variable observables are not normalizable since $\langle a|a\rangle = \delta(0) \neq 1$. Thus, for continuous variables, the observable eigenstates do not represent physical states, but are rather a mathematical tool from which we build actual physical states, according to the superposition principle of Eq. (2.2).

2.1.1 Density matrices

For each pure state, $|\psi\rangle$, we can construct a corresponding object $\rho = |\psi\rangle\langle\psi|$ called the density matrix. Just like the state vector $|\psi\rangle$, the density matrix contains a complete description of the state. Moreover, we can use the density matrix formalism to construct more general states, such as a classical probabilistic ensemble of pure states

$$\rho = \sum_k p_k |\psi_k\rangle\langle\psi_k|, \quad (2.10)$$

where all the p_k 's are positive and sum to 1, just like a classical probability distribution. However, the decomposition of (2.10) is not unique, and so the interpretation of the state as a distribution

of pure states is not unique either. If there are no representations for which the density matrix can be described by a single pure state, we say that the state is mixed.

Similarly to state vectors, density matrices can be expanded in terms of the eigenstates of an observable

$$\rho = \int da' da'' \Psi(a', a'') |a'\rangle \langle a''|, \quad (2.11)$$

with a corresponding wavefunction

$$\Psi(a', a'') = \langle a' | \rho | a'' \rangle. \quad (2.12)$$

Additionally, the probability density of observing measurement outcome a is given by

$$P(a) = \langle a | \rho | a \rangle = \Psi(a, a). \quad (2.13)$$

Density matrices are particularly useful when a system of interest becomes entangled with its environment. Generally, when two systems interact they become entangled and can be described by the combined two-mode state vector

$$|\psi_{1,2}\rangle = \int da_1 da_2 \psi_{1,2}(a_1, a_2) |a_1\rangle \otimes |a_2\rangle. \quad (2.14)$$

This two-mode state vector has a corresponding density matrix

$$\rho_{1,2} = |\psi_{1,2}\rangle \langle \psi_{1,2}| = \int da'_1 da''_1 da'_2 da''_2 \psi_{1,2}(a'_1, a'_2) \psi_{1,2}^*(a''_1, a''_2) |a'_1\rangle \langle a''_1| \otimes |a'_2\rangle \langle a''_2| \quad (2.15)$$

In the real world it is extremely difficult to perfectly isolate a quantum system from its environment, and so most quantum systems will rapidly become entangled with a larger and larger environment. However, if the initial quantum system is a logical state in our quantum computer, we are not so interested in the state of the environment around it, and furthermore we typically cannot control or measure the environment at the quantum level anyway. Conveniently, the density matrix formalism allows us to write a density matrix that describes only the mode of interest, by tracing out the environment mode, i.e.

$$\rho_1 = \text{Tr}_2(\rho_{1,2}). \quad (2.16)$$

The single-mode density matrix wavefunction is then given by

$$\Psi_1(a', a'') = \int da \psi_{1,2}(a', a) \psi_{1,2}^*(a'', a). \quad (2.17)$$

If modes 1 and 2 were initially entangled ρ_1 will not correspond to a pure state, i.e. it cannot be written as $|\psi\rangle \langle \psi|$, and it is therefore equivalent to a statistical mixture of pure states. Thus interactions with an environment introduce classical uncertainties, or noise, to the logical quantum state, which will eventually drown out vital quantum features if not properly dealt with.

2.1.2 Position and momentum

We now introduce the position and momentum operators, which are the central continuous-variable observables of this thesis. We denote the one-dimensional position operator by \hat{q} ¹. This

¹Often x or X are used to represent position, but for quantum information this symbol is already reserved for the Pauli x operator and thus q is chosen as the convention in this chapter. Still, we will later deviate from this logic and use x or X to denote the position quadrature in the papers of chapters 3, 5, 6, 7 and 9. I apologize for this inconvenience.

operator represents exactly what it sounds like, namely the position coordinate of a given particle along some predefined axis. Thus, for a particle with wavefunction $\psi(q)$, the probability density of seeing it at position q is equal to $|\psi(q)|^2$.

The momentum operator should allow us to find the momentum wavefunction of a particle. It turns out that a sensible, although perhaps non-trivial, definition of the momentum operator in terms of the position wavefunction is

$$\hat{p} = -i\hbar \frac{\partial}{\partial q}. \quad (2.18)$$

The eigenstates of the momentum operator are the states satisfying

$$\hat{p}|p\rangle = p|p\rangle \leftrightarrow -i\hbar \frac{\partial \psi_p(q)}{\partial q} = p\psi_p(q). \quad (2.19)$$

This is solved by the position wavefunction given by

$$\psi_p(q) = N e^{\frac{i}{\hbar} p q}, \quad (2.20)$$

where N is a constant which is found by constraining the wavefunction to satisfy the normalization relation of Eq. (2.5):

$$\langle p'|p'\rangle = \int dq N^* e^{-ip'q} N e^{ipq} = |N|^2 \int dq e^{\frac{i}{\hbar}(p-p')q} = \delta(p-p'). \quad (2.21)$$

From the relation $1/2\pi \int dz e^{i(x-x')z} = \delta(x-x')$ we conclude that $N = 1/\sqrt{2\pi\hbar}$, i.e. the momentum-eigenstates in the position basis are:

$$|p\rangle = \frac{1}{\sqrt{2\pi\hbar}} \int dq e^{ipq}|q\rangle, \quad \psi_p(q) = \frac{1}{\sqrt{2\pi\hbar}} e^{ipq}. \quad (2.22)$$

Importantly, $|\psi_p(q)|^2$ is uniform and non-zero for all q , meaning that a state with perfectly well-defined momentum has a completely random position. Conversely, the momentum wavefunction of the position eigenstates are

$$\psi_q(p) = \langle q|p\rangle = \frac{1}{\sqrt{2\pi\hbar}} \int dq' e^{ipq'} \langle q|q'\rangle = \frac{1}{\sqrt{2\pi\hbar}} e^{-iqp}, \quad (2.23)$$

which have completely random momentum. This feature is captured more generally by the Heisenberg uncertainty principle which relates the uncertainties of two observables, \hat{A} and \hat{B} , by

$$\Delta_A \Delta_B \geq \frac{1}{2} |\langle [\hat{A}, \hat{B}] \rangle|, \quad (2.24)$$

where $\Delta_O = \sqrt{\langle \hat{O}^2 \rangle - \langle \hat{O} \rangle^2}$ is the standard deviation of the observable \hat{O} , $\langle \hat{O} \rangle = \langle \psi | \hat{O} | \psi \rangle$ is the expectation value of \hat{O} and $[\hat{A}, \hat{B}] = \hat{A}\hat{B} - \hat{B}\hat{A}$ is the commutator. For position and momentum, we can find the commutator by applying it on an arbitrary position wavefunction:

$$[\hat{q}, \hat{p}]\psi(q) = -i\hbar \left(q \frac{\partial \psi(q)}{\partial q} - \frac{\partial (q\psi(q))}{\partial q} \right) = -i\hbar \left(q \frac{\partial \psi(q)}{\partial q} - q \frac{\partial \psi(q)}{\partial q} - \frac{\partial \psi(q)}{\partial q} \right) = i\hbar \psi(q). \quad (2.25)$$

Thus

$$[\hat{q}, \hat{p}] = i\hbar, \quad (2.26)$$

and therefore

$$\Delta_q \Delta_p \geq \frac{\hbar}{2}. \quad (2.27)$$

As a consequence, there exists no state for which measurements of both the position and momentum will always return a well-defined value.

An important feature of the momentum is, that the momentum wavefunction is completely determined by the position wavefunction since

$$\psi(p) = \langle p | \psi \rangle = \langle p | \int dq \psi(q) | q \rangle = \int dq \psi(q) \langle p | q \rangle = \frac{1}{\sqrt{2\pi\hbar}} \int dq \psi(q) e^{-iqp}. \quad (2.28)$$

That is, the momentum wavefunction is the Fourier transform of the position wavefunction. Conceptually, the momentum is thus encoded in the phase of the position wavefunction and vice-versa.

2.1.3 Electromagnetic field quadratures

Another relevant continuous-variable system is the electromagnetic field. The value of the electric field at a particular point in space is a physical observable quantity and can thus be associated with a quantum mechanical Hermitian operator. Furthermore, from optics we know that it is often convenient to break down the electromagnetic field into frequency components. With a slight foresight and abuse of notation, we denote the electric field of a specific frequency with the operator \hat{q} , which is also called the amplitude quadrature. According to Maxwell's equations, the electric field evolves over time, and from this evolution it makes sense to define a "momentum" operator for the electric field, denoted \hat{p} , which we call the phase quadrature operator. The phase quadrature thus describes the rate of change of the electric field. For a standing electromagnetic field wave in a cavity, \hat{p} is proportional to the magnetic field. The amplitude and phase quadratures turn out to obey the commutation relation $[\hat{q}, \hat{p}] \propto i$, just like the position and momentum of a particle. From this it follows that the quadrature operators \hat{q} and \hat{p} defined here have all the same quantum mechanical relations and properties as the position and momentum described in the previous section. This conveniently allows us to use a single mathematical formulation to describe two physically very different systems. In the following we will refer to \hat{q} and \hat{p} as position and momentum, keeping in mind that they could as well represent electromagnetic quadratures.

2.1.4 The Wigner function

While both the position and momentum of a state are completely described by the position wavefunction, it is nonetheless useful to have a representation that more directly includes both position and momentum. For example, the position and momentum of a classical particle along a specific axis can be represented by a point in a two-dimensional phase space with coordinates of position and momentum. Furthermore, if the precise position and momentum are unknown, we can instead consider a probability distribution over this phase space.

Due to the intrinsic relationship between the position and momentum wavefunctions, a similar phase-space distribution function for quantum states is bit more tricky to define. In fact, it turns out that there are multiple different meaningful ways to define such a function. One of these is the Wigner function which was defined by E. Wigner and L. Szilard [42], and is given in terms of the density matrix by

$$W(q, p) = \frac{1}{\pi\hbar} \int_{-\infty}^{\infty} dy \langle q + y | \rho | q - y \rangle e^{2ipy/\hbar}. \quad (2.29)$$

Although the definition might appear a bit obscure at first glance, it turns out that the Wigner function has many useful properties. First, just like the wavefunction, the Wigner function gives a complete description of the state with respect to the position and momentum observables. Moreover, unlike the wavefunction, the Wigner function is real-valued for all physical states. This means that the Wigner function can be easily visualized. Additionally, the marginal distributions of the position and momentum behave just like that of a classical probability distribution, i.e.:

$$P(q) = \int dp W(q, p), \quad P(p) = \int dq W(q, p). \quad (2.30)$$

Consequently, the Wigner function is normalized according to:

$$\int dq \int dp W(q, p) = 1. \quad (2.31)$$

But unlike a classical probability distribution, the Wigner function can take on negative values.

Another pleasant feature of the Wigner function is that different quantum states are visually distinguishable by their Wigner functions. This follows from the fact that the overlap between two states can be calculated from the overlap of their Wigner functions:

$$|\langle \psi_1 | \psi_2 \rangle|^2 = \int dq \int dp W_1(q, p) W_2(q, p). \quad (2.32)$$

So if the states are orthogonal, $|\langle \psi_1 | \psi_2 \rangle|^2 = 0$, their Wigner functions must be different enough to make the above integral 0. While the Wigner function can be used as useful a mathematical tool, it will primarily be used as a visualisation tool in this thesis, allowing us to gain some intuition on the behavior continuous-variable quantum states. In section 2.2 we will see some examples of Wigner functions of different states.

2.1.5 Fock representation

Besides the position and momentum operators, a central observable in continuous-variable quantum mechanics, and indeed in all of quantum mechanics, is the Hamiltonian, \hat{H} , which describes the energy of a particular system. The Hamiltonian is important, as it allows us to calculate how a state changes over time according to the Schrödinger equation,

$$\frac{d}{dt} |\psi(t)\rangle = -\frac{i}{\hbar} \hat{H} |\psi(t)\rangle. \quad (2.33)$$

The exact form of the Hamiltonian depends on the physical system, but a particularly important case for this thesis is that of the harmonic oscillator,

$$\hat{H} = \frac{1}{2} \hbar \omega (\hat{p}^2 + \hat{q}^2). \quad (2.34)$$

For \hat{q} and \hat{p} representing position and momentum, the \hat{p}^2 term corresponds to the kinetic energy while the \hat{q}^2 term corresponds to potential energy in a quadratic potential. Thus Eq. (2.34) is the Hamiltonian for a particle trapped in a quadratic potential, where ω is the angular frequency of oscillation and \hat{q} and \hat{p} have been non-dimensionalized such that the position is in units of $\sqrt{\hbar/m\omega}$ and the momentum is in units of $\sqrt{m\omega\hbar}$ where m is the mass of the particle. As an example, the length scale for the motion of the trapped calcium ion used in the experiment of Ref. [43] is on the order of 10 nm. Note that in these units, the commutation relation of \hat{q} and \hat{p} is $[\hat{q}, \hat{p}] = i$, which is the convention used throughout this thesis.

For \hat{q} and \hat{p} representing electric field quadratures, Eq. (2.34) is exactly energy of the electromagnetic field in vacuum at the frequency ω , obtained from quantizing Maxwell's equations with a suitable non-dimensionalization.

It turns out that although \hat{q} and \hat{p} represent continuous observables, the Hamiltonian of the harmonic oscillator has discrete eigenvalues corresponding to possible energy levels,

$$E_n = \hbar\omega \left(n + \frac{1}{2} \right), \quad (2.35)$$

with corresponding eigenstates $|n\rangle$ for all non-negative integer n . These states are called Fock states and form an orthonormal basis, so any wavefunction can be described in the Fock basis as

$$|\psi\rangle = \sum_{n=0}^{\infty} c_n |n\rangle, \quad (2.36)$$

where $c_n = \langle \psi | n \rangle$, and $|c_n|^2$ is the probability of measuring the energy of the state to be E_n . Thus $\sum_n |c_n|^2 = 1$. Physically, we interpret the state $|n\rangle$ as containing n bosonic excitations, which we call phonons in the case of trapped particle, or photons if we are considering the electromagnetic field.

The Fock states are related to the position states through [37]

$$\langle q | n \rangle = \sqrt{\frac{1}{\sqrt{\pi} 2^n n!}} e^{-\frac{q^2}{2}} H_n(q), \quad (2.37)$$

where H_n is the n 'th Hermite polynomial.

Some very useful operators for the Fock representation are the annihilation operator \hat{a} , its conjugate the creation operator \hat{a}^\dagger , and their product the number operator $\hat{n} = \hat{a}^\dagger \hat{a}$. These are defined by the relations

$$\hat{a} = \frac{1}{\sqrt{2}}(\hat{q} + i\hat{p}), \quad \hat{a}^\dagger = \frac{1}{\sqrt{2}}(\hat{q} - i\hat{p}), \quad (2.38)$$

or conversely,

$$\hat{q} = \frac{1}{\sqrt{2}}(\hat{a} + \hat{a}^\dagger), \quad \hat{p} = \frac{1}{i\sqrt{2}}(\hat{a} - \hat{a}^\dagger). \quad (2.39)$$

The harmonic oscillator Hamiltonian can therefore be rewritten as

$$\hat{H} = \hbar\omega \left(\hat{a}^\dagger \hat{a} + \frac{1}{2} \right). \quad (2.40)$$

These operators have particularly simple relations to the Fock states:

$$\hat{a}|n\rangle = \sqrt{n}|n-1\rangle, \quad \hat{a}^\dagger|n\rangle = \sqrt{n+1}|n+1\rangle, \quad \hat{n}|n\rangle = n|n\rangle. \quad (2.41)$$

Thus the annihilation operator subtracts an excitation while the creation operator adds an excitation. Since the annihilation and creation operator are neither Hermitian nor unitary they do not by themselves correspond to any physical observable or deterministic process. However, other operators can be expanded in terms of the annihilation and creation operators, allowing us to interpret physical processes in terms of exchange of energy quanta.

2.2 States

We now go through some typically encountered states, all of which are visualized by their Wigner functions, position and momentum marginal distributions, and Fock basis distributions in Fig. 2.1.

The vacuum state. The vacuum state is shown in Fig. 2.1a and is the lowest possible energy state of the harmonic oscillator, i.e. the state $|0\rangle$ in the Fock basis. The position wavefunction can be obtained from Eq. (2.37) and is given by the Gaussian function

$$\psi_{\text{vac}}(q) = \frac{1}{\pi^{1/4}} e^{-\frac{q^2}{2}}. \quad (2.42)$$

Furthermore, the momentum wavefunction is equal to the position wavefunction and the standard deviation of the position and momentum is $\Delta_q = \Delta_p = \frac{1}{\sqrt{2}}$, meaning the vacuum state saturates the Heisenberg uncertainty principle. Still, the vacuum state has a non-zero probability for measurements of $q \neq 0$ and $p \neq 0$, i.e. the vacuum exhibit small fluctuations in both the position and momentum.

Thermal states. Many real-world systems exchange energy with their surrounding, which eventually brings the state into thermal equilibrium with its environment. A state in such thermal equilibrium is characterised by its temperature, T , and can be described by a density matrix in the Fock basis as

$$\rho_{\text{thermal}} = \frac{1}{\bar{n} + 1} \sum_{n=0}^{\infty} \left(\frac{\bar{n}}{\bar{n} + 1} \right)^n |n\rangle\langle n| \quad (2.43)$$

where $\bar{n} = \langle \hat{n} \rangle = [\exp(\hbar\omega/k_B T) - 1]^{-1}$, where k_B is the Boltzmann constant. A thermal state with $\bar{n} = 2$ is shown in Fig. 2.1b.

Coherent states. The coherent state is the closest we get to a classical oscillation of a trapped particle, or the electromagnetic field of a laser. These states can thus have high energy and highly defined position and momentum. Coherent states can be considered as displaced versions of the vacuum state, as exemplified in Fig. 2.1c. They are parametrized by the expectation value of their position and momentum, which for coherent states are written compactly by the complex number $\alpha = \frac{1}{\sqrt{2}}\langle q \rangle + i\frac{1}{\sqrt{2}}\langle p \rangle$. Note here the factor $1/\sqrt{2}$, which is a consequence of our unit choice. The position wavefunction is

$$\psi_{\text{coh}}(q) = \frac{1}{\pi^{1/4}} e^{-(q - \sqrt{2}\text{Re}(\alpha))^2/2} e^{i\sqrt{2}\text{Im}(\alpha)q}, \quad (2.44)$$

and the Fock basis representation is

$$|\alpha\rangle = e^{-|\alpha|^2/2} \sum_{n=0}^{\infty} \frac{\alpha^n}{\sqrt{n!}} |n\rangle. \quad (2.45)$$

An interesting property of coherent states is that they are eigenstates of the annihilation operator with eigenvalue α ,

$$\hat{a}|\alpha\rangle = \alpha|\alpha\rangle, \quad (2.46)$$

as can be verified from Eqs. (2.41) and (2.45). However, since \hat{a} is not Hermitian, α is not an observable quantity, i.e. it cannot be determined in a single-shot experiment.

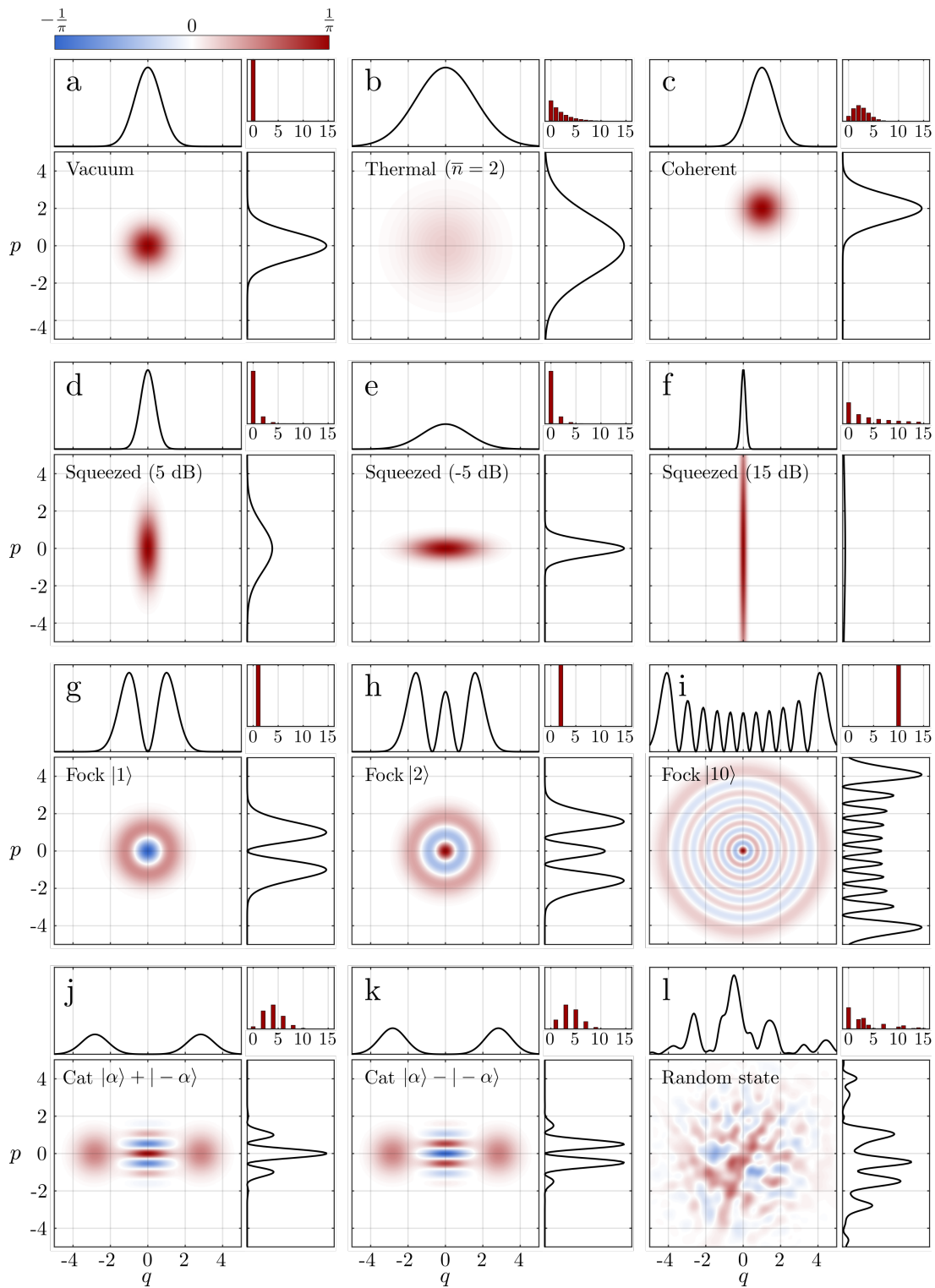


Figure 2.1: A zoo of quantum continuous-variable states. The colormaps show the Wigner functions, $W(q, p)$, the line plots show the position and momentum probability distributions, $|\psi(q)|^2$ and $|\psi(p)|^2$, and the bar plots show the Fock basis distributions, $|c_n|^2$. The scale of the position and momentum probability distributions vary from state to state.

Squeezed vacuum. The squeezed vacuum states have an asymmetric phase space distribution, such that the uncertainty in the position is reduced at the cost of an increased uncertainty in momentum or vice versa. Squeezed vacuum states thus have an uncertainty in one quadrature which is below that of the vacuum state. The magnitude of the uncertainty reduction, or "squeezing", is quantified by the squeezing parameter r . Positive r correspond to a reduced position uncertainty while negative r correspond to a reduced momentum uncertainty. Like the vacuum and coherent states, the position wavefunction of the squeezed vacuum is also a Gaussian:

$$\psi_{\text{sqs}}(q) = e^{r/2} \frac{1}{\pi^{1/4}} e^{-\frac{q^2}{2e^{-2r}}}. \quad (2.47)$$

and the Fock basis coefficients are given by

$$c_n = \begin{cases} \frac{1}{\sqrt{\cosh(r)}} (-\tanh(r))^{n/2} \frac{\sqrt{n!}}{(n/2)!} & \text{for even } n, \\ 0 & \text{for odd } n. \end{cases} \quad (2.48)$$

Note that despite the name, squeezed vacuum states also have support on states other than the vacuum state, and therefore have a higher average energy than the vacuum.

The standard deviation of the position of a squeezed vacuum state is given by $\Delta_q = e^{-r}/\sqrt{2}$, and often the squeezing parameter is expressed in units of dB, denoting the reduction in the variance with respect to the vacuum, i.e.

$$r[\text{dB}] = -10 \log_{10}(e^{-2r}) = \frac{20}{\ln(10)} r \approx 8.7r \quad (2.49)$$

Figs. 2.1(d-f) show different squeezed vacuum states with 5 dB squeezing, -5 dB squeezing, and 15 dB squeezing, which corresponds to the largest experimentally achieved level of squeezing [44]

Fock states. Wigner functions of the Fock states, i.e. the energy eigenstates, with excitation numbers 1, 2 and 10 are shown in Fig. 2.1(g-h). These have the characteristic feature of being rotationally symmetric, with large uncertainties in both the position and momentum. Despite their deceptively simple formulation as states with well-defined energy, high energy Fock states are very challenging to generate experimentally, especially in optics. Fock states are thus highly non-classical states, which is also evident by the negative values of their Wigner functions.

Cat states. Another non-classical state is the Schrödinger's cat state, which is a superposition of two coherent states, typically at opposite points in phase space, i.e. $|\alpha\rangle + e^{i\phi} |-\alpha\rangle$. Here, ϕ is the quantum phase between the coherent states. The Wigner functions for $\alpha = 2$ and $\phi = 0$ and $\phi = \pi$ are shown in Fig. 2.1j and k. There are three notable parts of these Wigner functions, namely the two positive Gaussian peaks at $\pm\alpha$ and an oscillating contribution between them. Importantly, the central oscillating term is a signature of the quantum phase ϕ , and the value of ϕ determines the phase of this oscillation. Physically, this is revealed in the momentum marginal distribution, which exhibits fluctuations on a scale smaller than the vacuum quantum uncertainty.

Other states. The states considered so far represent some of the historically most interesting continuous-variables states, which all have certain structures giving rise to Wigner functions with different symmetries or dissectible elements. However, we should keep in mind that infinitely many different states are allowed by the laws of quantum mechanics, e.g. by choosing whatever normalizable Fock basis coefficients we like. An example of a state with randomly chosen complex coefficients under a suitable energy constraint is shown in Fig. 2.1l. For this state, the

positive and negative parts of the Wigner function have no clear separation or structure, and thus it becomes difficult to associate a physical interpretation to any specific point of the Wigner function. One might question how such a state can be produced experimentally or whether it has any applications. We will not attempt to address those questions here, but instead we simply show it as a remainder of the richness and diversity continuous-variable quantum states.

2.3 Gates

In order to use quantum states as computational resources in a quantum computer, we need to be able to control and manipulate them. As mentioned, quantum states evolve according to the Schrödinger equation, Eq. (2.33). Solving the Schrödinger equation, we find that a mode in the initial state $|\psi(0)\rangle$ evolves to the state $|\psi(t)\rangle = \exp(-it\hat{H}/\hbar)|\psi(0)\rangle$ after time t , assuming a time-independent Hamiltonian. The evolution is thus described by the unitary operator $\hat{U} = \exp(-it\hat{H}/\hbar)$. By controlling the Hamiltonian, we can therefore change one quantum state into another. Exactly how the Hamiltonian is controlled in experiment depends greatly on what kind of physical system we are considering and which unitary we wish to implement. In the perspective of the quantum states representing carriers of logical information in quantum computer, we refer to such a discrete unitary evolution as a quantum gate. Some common continuous-variable gates are:

Rotation gate. The rotation gate is the one generated by the harmonic oscillator and can be written as,

$$\hat{R}(\theta) = \exp(-i\theta\hat{n}) = e^{i\theta/2} \exp\left(-i\frac{\theta}{2}(\hat{q}^2 + \hat{p}^2)\right). \quad (2.50)$$

For the harmonic oscillator, this gate is implemented simply by waiting for a time $t = \theta/\omega$. The effect of the rotation gate is to rotate the state by an angle θ in phase space. Thus the rotation gate corresponds to a transformation of the Wigner function according to

$$W(q, p) \rightarrow W(\cos(\theta)q + \sin(\theta)p, -\sin(\theta)q + \cos(\theta)p). \quad (2.51)$$

Displacement gate. The displacement gate is defined as

$$\hat{D}(\beta) = \exp(\alpha\hat{a}^\dagger - \alpha^*\hat{a}) = \exp(i\sqrt{2}(\text{Im}[\alpha]\hat{q} - \text{Re}[\alpha]\hat{p})). \quad (2.52)$$

The effect of the displacement gate is to displace the state in phase space and corresponds to the Wigner function transformation

$$W(q, p) \rightarrow W(q - \sqrt{2}\text{Re}[\alpha], p - \sqrt{2}\text{Im}[\alpha]) \quad (2.53)$$

Thus the displacement operator can be used to generate any coherent state from the vacuum state through $|\alpha\rangle = \hat{D}(\alpha)|\text{vac}\rangle$.

Squeezing gate. The squeezing gate is defined as

$$\hat{S}(\xi) = \exp\left(\frac{1}{2}(\xi^*\hat{a}^2 - \xi\hat{a}^{\dagger 2})\right) = \exp\left(i\frac{r}{2}[\cos(\phi)(\hat{q}\hat{p} + \hat{p}\hat{q}) - \sin(\phi)(\hat{q}^2 - \hat{p}^2)]\right) \quad (2.54)$$

with $\xi = re^{i\phi}$. The squeezing operator "squeezes" the state in phase space by contracting it in one direction while expanding it in the orthogonal direction. This corresponds to the Wigner function transformation

$$\begin{aligned} W(q, p) \rightarrow & W((e^r \cos^2(\phi) + e^{-r} \sin^2(\phi))q + \cos(\phi) \sin(\phi)(e^r - e^{-r})p, \\ & \cos(\phi) \sin(\phi)(e^r - e^{-r})q + (e^r \sin^2(\phi) + e^{-r} \cos^2(\phi))p), \end{aligned} \quad (2.55)$$

which for $\phi = 0$ this simplifies to

$$W(q, p) \rightarrow W(e^r q, e^{-r} p). \quad (2.56)$$

Conditional displacement gate. Although not as common as the previously mentioned gates, the conditional displacement gate is a central element of chapters 7-10 and is therefore given an introduction here. It is a two-mode gate acting on a system consisting of a continuous-variable mode and a 2-dimensional qubit mode,

$$\begin{aligned} CD_k(\beta) &= \exp(i\hat{\sigma}_k \otimes [-\operatorname{Re}(\beta)\hat{p} + \operatorname{Im}(\beta)\hat{q}]) \\ &= |+_k\rangle\langle+_k| \otimes \hat{D}\left(\frac{\beta}{\sqrt{2}}\right) + |-_k\rangle\langle-_k| \otimes \hat{D}\left(-\frac{\beta}{\sqrt{2}}\right), \end{aligned} \quad (2.57)$$

where $\hat{\sigma}_k$ with $k \in \{x, z, y\}$ denotes a qubit Pauli matrix with eigenstates $|+_k\rangle$ and $|-_k\rangle$. The conditional displacement thus performs a displacement of the continuous-variable mode in a direction depending on the state of the qubit. This will in general entangle the qubit and the continuous-variable mode. Alternatively, the conditional displacement can also be interpreted as a rotation of the qubit with a magnitude depending on the state of the continuous-variable mode. For example, for purely imaginary β we can write:

$$CD_k(i|\beta|) = \int dq \exp(iq|\beta|\hat{\sigma}_k) \otimes |q\rangle\langle q| \quad (2.58)$$

Thus the qubit is rotated around the k axis with a direction and magnitude proportional to the position of the continuous-variable mode.

There are different methods to implement a conditional displacement, depending on the physical platform. Here, we present a method suitable for a trapped ion as well a method suitable for a microwave field coupled to a superconducting circuit.

To implement a conditional displacement in a trapped ion platform, we can utilize the coupling between a phononic mode of the ion (the continuous-variable mode) and its internal electronic energy levels [45, 46]. Trapped ions typically have a rich energy structure, with multiple viable qubit subspaces [47]. Here, we restrict our attention to a qubit subspace comprising two long-lived electronic energy levels, $|g\rangle$ and $|e\rangle$, separated by an energy gap in the optical frequency domain, such that a resonant laser can drive transitions between the two states. The motional modes are typically in the MHz range and can be addressed by tuning lasers to the so-called motional sidebands, as shown in Fig. 2.2a. Physically, if a laser is blue-detuned from the qubit resonance such that the photon energy equals the qubit transition energy plus that of a phonon, both the qubit and a phonon can be simultaneously excited. This is described by the operator $\hat{\sigma}_+ \hat{a}^\dagger$ with $\hat{\sigma}_+ = |e\rangle\langle g|$. Meanwhile, such laser can also stimulate a simultaneous decay of the qubit and a phonon, represented by the operator $\hat{\sigma}_- \hat{a}$ with $\hat{\sigma}_- = |g\rangle\langle e|$. In total, the Hamiltonian of the system in this blue motional sideband, in a rotating frame, is

$$\frac{1}{\hbar} \hat{H}_{\text{blue}} = \Omega_{\text{blue}} \hat{\sigma}_+ \hat{a}^\dagger + \Omega_{\text{blue}}^* \hat{\sigma}_- \hat{a}, \quad (2.59)$$

where Ω_{blue} depends on the coupling strength and phase of the laser. Similarly, if the laser is red detuned, a photon can be absorbed to excite the qubit while annihilating a phonon, or the qubit can deexcite while exiting a phonon. The Hamiltonian in this case is thus

$$\frac{1}{\hbar} \hat{H}_{\text{red}} = \Omega_{\text{red}} \hat{\sigma}_- \hat{a}^\dagger + \Omega_{\text{red}}^* \hat{\sigma}_+ \hat{a}. \quad (2.60)$$

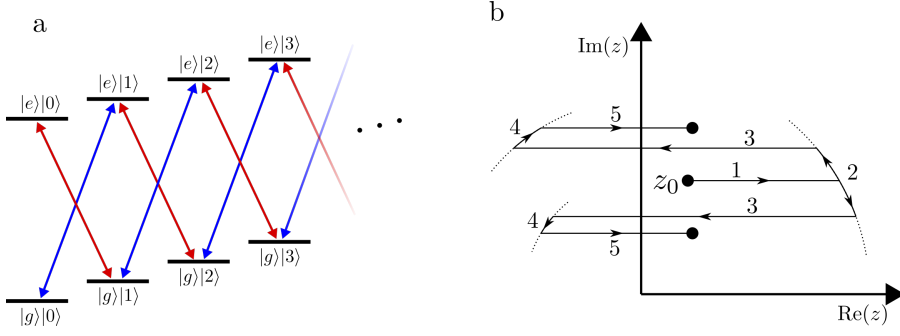


Figure 2.2: (a): Energy structure of a trapped ion with two electronic states $\{|g\rangle, |e\rangle\}$ plus a ladder of motional states, $\{|0\rangle, |1\rangle, \dots\}$. The arrows indicate the blue and red motional sideband transitions. (b): Evolution of a point represented by a complex number, z_0 , of the Wigner function under the transformations used to implement a conditional displacement gate from a dispersive Hamiltonian, e.g. in a superconducting platform. The two different directions at step 2 correspond to the evolution associated with the qubit states $|g\rangle$ and $|e\rangle$ respectively. The dotted curves indicate circles centered at the origin, along which the state rotates due to the dispersive coupling.

Driving both transitions simultaneously with a bichromatic laser with real $\Omega_{\text{blue}} = \Omega_{\text{red}} \equiv \Omega$ we get:

$$\frac{1}{\hbar} \hat{H} = \Omega (\hat{\sigma}_+ + \hat{\sigma}_-) (\hat{a} + \hat{a}^\dagger) = \sqrt{2} \Omega \hat{\sigma}_x \hat{q}, \quad (2.61)$$

which is exactly the generator of a conditional displacement. Additionally, by tuning the phases of $\Omega_{\text{red}} = |\Omega| e^{i\phi_{\text{red}}}$ and $\Omega_{\text{blue}} = |\Omega| e^{i\phi_{\text{blue}}}$ we can achieve the more general expression

$$\frac{1}{\hbar} \hat{H} = \sqrt{2} |\Omega| (e^{i\phi_-} \hat{\sigma}_+ + e^{-i\phi_-} \hat{\sigma}_-) \frac{e^{i\phi_+} \hat{a}^\dagger + e^{-i\phi_+} \hat{a}}{\sqrt{2}}, \quad (2.62)$$

with $\phi_+ = (\phi_{\text{blue}} + \phi_{\text{red}})/2$ and $\phi_- = (\phi_{\text{blue}} - \phi_{\text{red}})/2$, which corresponds to a displacement in an arbitrary quadrature direction conditioned on an arbitrary qubit direction in the x - y plane of the Bloch sphere.

The conditional displacement gate can also be implemented in superconducting circuits, as was done in [48], through a driven dispersive coupling between a microwave cavity field (the continuous-variable mode) and a superconducting qubit. The dispersive Hamiltonian in a rotating reference frame is

$$\frac{1}{\hbar} \hat{H} = -\frac{\chi}{2} \hat{n} \hat{\sigma}_z + iE(t) \hat{a}^\dagger - iE^*(t) \hat{a}, \quad (2.63)$$

where $\hat{\sigma}_z$ is the Pauli- z operator of the transmon and $E(t)$ is a microwave drive resonant with the cavity frequency. The conditional displacement is achieved by implementing a sequence of fast displacements through the microwave drive along with waiting periods of free Hamiltonian evolution [49], which we describe below. To show mathematically that the sequence implements a conditional displacement, we can use the fact that the involved continuous-variable operations are Gaussian and thus simply corresponds to a coordinate transformation of the Wigner function. We find this transformation by keeping track of a point in the Wigner function, denoted by the complex number $z_0 = q_0 + ip_0$. The sequence is depicted in Fig. 2.2b and is as follows:

1. A short intense pulse causes a large displacement of magnitude α of the cavity mode,

$$z_0 \rightarrow z_0 + \alpha. \quad (2.64)$$

2. The cavity evolves for time $T/2$ under the dispersive Hamiltonian, rotating it in a direction depending on the state of the transmon,

$$z_0 + \alpha \rightarrow (z_0 + \alpha)e^{\pm iT\chi/4}, \quad (2.65)$$

with '+' corresponding to the qubit in the state $|0\rangle$ and '-' corresponding to the qubit in the state $|1\rangle$.

3. The cavity is displaced in the opposite direction by magnitude -2α and simultaneously the transmon is flipped by a $\hat{\sigma}_x$ gate using another microwave drive resonant with the transmon,

$$(z_0 + \alpha)e^{\pm iT\chi/4} \rightarrow (z_0 + \alpha)e^{\pm iT\chi/4} - 2\alpha. \quad (2.66)$$

4. The cavity evolves again for time $T/2$ under the dispersive Hamiltonian, but in the direction opposite to the first rotation due to the flip of the transmon,

$$(z_0 + \alpha)e^{\pm iT\chi/4} - 2\alpha \rightarrow \left[(z_0 + \alpha)e^{\pm iT\chi/4} - 2\alpha \right] e^{\mp iT\chi/4}. \quad (2.67)$$

5. The cavity is displaced back again with magnitude α ,

$$\begin{aligned} \left[(z_0 + \alpha)e^{\pm iT\chi/4} - 2\alpha \right] e^{\mp iT\chi/4} &\rightarrow \left[(z_0 + \alpha)e^{\pm iT\chi/4} - 2\alpha \right] e^{\mp iT\chi/4} + \alpha \\ &= z_0 + 2\alpha \left(1 - e^{\mp iT\chi/4} \right) \\ &= z_0 + 2\alpha(1 - \cos(T\chi/4)) \pm i2\alpha \sin(T\chi/4) \end{aligned} \quad (2.68)$$

We thus end up with an unconditional displacement along the α direction, and a conditional displacement in the orthogonal direction. The strength of the unconditional part compared to the conditional part vanishes for $T \ll \chi/4$, but the unconditional part can also be removed simply by slightly adjusting the final displacement pulse. Importantly, a large conditional displacement can be implemented on a time scale smaller than $1/\chi$ by choosing a sufficiently large α , i.e. using an intense microwave drive.

Even if the microwave displacement pulses are not instantaneous, we can still model the system as a transformation of the Wigner function coordinates. In particular, the Hamiltonian can be transformed into a differential equation for the coordinates, with the \hat{n} term corresponding to a rotation and the drive term corresponding to a velocity:

$$\frac{dz(t)}{dt} = \pm i \frac{\chi}{2} z(t) + \sqrt{2}E(t). \quad (2.69)$$

For $E(t + T/2) = -E(t)$ and a flip of the sign of the rotation term at $t = T/2$, the solution is

$$\begin{aligned} z(T) &= z(0) + \int_0^{T/2} dt' \sqrt{2}E(t') \left(e^{\pm it'\chi/2} - e^{\pm i(T/2-t')\chi/2} \right) \\ &= z(0) + \int_0^{T/2} dt' \sqrt{2}E(t') (\cos(t'\chi/2) - \cos((T/2-t')\chi/2)) \\ &\quad \pm i \int_0^{T/2} dt' \sqrt{2}E(t') (-\sin(t'\chi/2) + \sin((T/2-t')\chi/2)). \end{aligned} \quad (2.70)$$

Thus we still obtain an unconditional displacement and a conditional displacement.

2.4 Noise channels

While we typically think of gates as operations which we can control and apply in any sequence, e.g. in order to implement a quantum algorithm, quantum states also interact with their environment in uncontrollable ways. This causes decoherence of the quantum states which can be detrimental if not properly dealt with. Noise can be modelled using the Master equation, which generalizes the Schrödinger equation in terms of density matrices and accounts for interactions with an environment which is subsequently traced out. The Master equation is

$$\frac{d}{dt}\rho = -\frac{i}{\hbar}[\hat{H}, \rho] + \sum_j \kappa_j \left(\hat{L}_j \rho \hat{L}_j^\dagger - \frac{1}{2} \left(\hat{L}_j^\dagger \hat{L}_j \rho + \rho \hat{L}_j^\dagger \hat{L}_j \right) \right) \quad (2.71)$$

where \hat{L}_j are called the Lindblad operators which depend on the type of the noise and κ_j denotes the strength of each noise type, which depends on how strongly the system couples to its environment. For $\hat{H} = 0$, e.g. by considering a rotating reference frame, the Master equation can be solved to find the density matrix at time t , which can be written in the Kraus representation as [50]

$$\rho(t) = \sum_k \hat{K}_k(t) \rho(0) \hat{K}_k^\dagger(t), \quad (2.72)$$

where $\hat{K}_k(t)$ are called the Kraus operators. From Eq. (2.72) we can interpret the noisy evolution as a discrete channel which applies one of the operators $\hat{K}_k(t)$ to the state according to the probability distribution given by $\text{Tr}(\hat{K}_k(t) \rho \hat{K}_k^\dagger(t))$. Since we do not know exactly which operator was applied, the state becomes mixed. In essence, quantum error correction can be thought of as the process of estimating which \hat{K}_k was applied and, if possible, apply a corrective gate to undo the effect of that particular Kraus operator. The estimation is done by probing the state $\rho(t)$ using carefully designed measurements that do not collapse the encoded quantum information. In section 2.5 we will see a couple of examples of this.

Here, we go through some of the most common continuous-variable noise channels. The effects of each of these channels are exemplified in Fig. 2.3, which shows the evolution of a probe state given by a superposition of two displaced squeezed vacuum states. This probe state exhibits both squeezing and Wigner function negativities and therefore serves to highlight some important effects of the different channels.

Loss. Loss represents a loss of excitations and is typically the dominant noise channel in optics. It is given by the Lindblad operator

$$\hat{L}^{(\text{loss})} = \hat{a}, \quad (2.73)$$

or equivalently the Kraus operators

$$\hat{K}_k^{(\text{loss})} = \sqrt{\frac{1}{k!} \left(\frac{l}{1-l} \right)^k} \hat{a}^k (1-l)^{\hat{n}/2}. \quad (2.74)$$

where $l = 1 - e^{-\kappa t}$ is the fraction of the total energy lost. Each Kraus operator corresponds to the event of losing k excitations. From Fig. 2.3 we see that loss impacts the probe state in multiple ways. First, the position peaks are shifted towards the center of phase space, which is intuitively expected for a loss of energy. Second, the squeezed peaks are broadened along the squeezing direction, such that their widths closer match that of the vacuum state. Finally, the central oscillating region gets washed out. This can be understood as a simultaneous broadening of the negative and positive parts of the oscillation, causing the entire region to be destructively

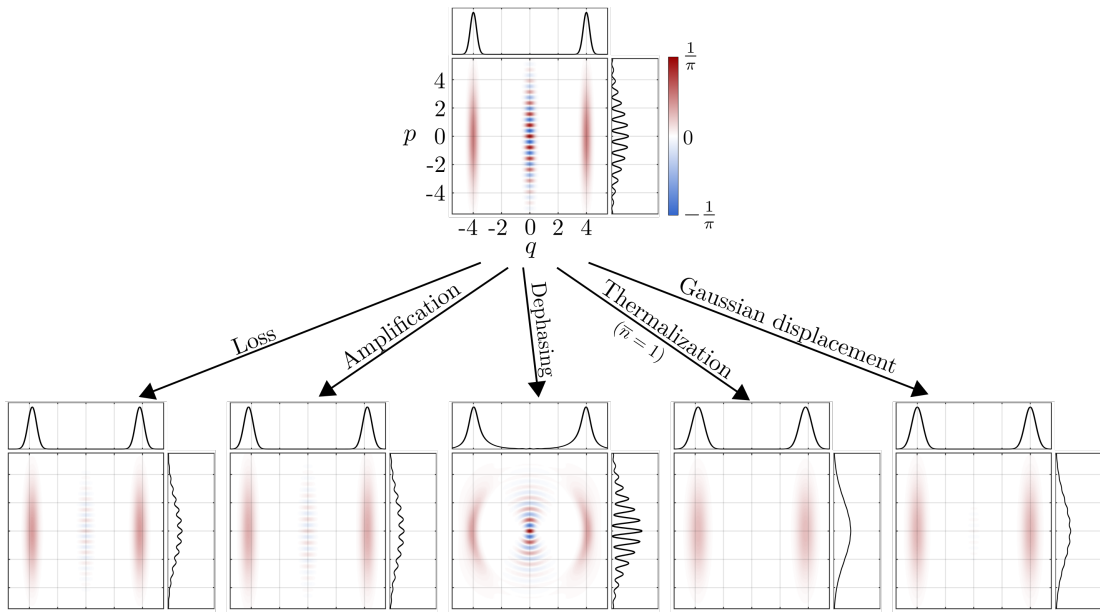


Figure 2.3: Effect of some common noise channels on a probe state given by a superposition of two displaced squeezed vacuum states. The strengths for all five channel are set to $\kappa t = 0.1$.

cancelled out. The impact of a reduced oscillation amplitude is also seen in the momentum marginal distribution, which shows a much less pronounced oscillation.

Amplification. Amplification is in some sense the opposite of loss, and represents a gain of energy. It is described by the Lindblad operator

$$\hat{L}^{(\text{amp})} = \hat{a}^\dagger, \quad (2.75)$$

or the Kraus operators

$$\hat{K}_k^{(\text{amp})} = \sqrt{\frac{1}{k!} \frac{1}{G} \left(\frac{G-1}{G} \right)^k} \hat{a}^{\dagger k} G^{-\hat{n}/2}, \quad (2.76)$$

where $G = e^{\kappa t}$ is the gain. Amplification is typically not a relevant adversarial noise channel in physical systems. However, it is sometimes applied on purpose in a controlled fashion to counteract the peak-shifting effects of loss. Unlike the classical description of an amplification channel which simply multiplies the power with the gain, the quantum amplification channel unavoidably also adds a bit of noise, and as a consequence also adds energy to the vacuum state. As seen in Fig. 2.3, amplification pushes the position peaks out, while also broadening them. As with the loss channel, this broadening causes a significant damping of the central oscillations of the Wigner function.

Dephasing. Dephasing causes a random rotation of the state according to a Gaussian distribution with standard deviation σ_ϕ , i.e.:

$$\rho \rightarrow \frac{1}{\sqrt{2\pi}\sigma_\phi} \int d\phi e^{-\frac{1}{2} \frac{\phi^2}{\sigma_\phi^2}} \hat{R}(\phi) \rho \hat{R}^\dagger(\phi). \quad (2.77)$$

This evolution is also described by the Master equation with the Lindblad operator

$$\hat{L}^{(\text{deph})} = \hat{n}, \quad (2.78)$$

with $\sigma_\phi^2 = \kappa t$. Additionally, the channel can be described by the Kraus operators [51, 52]

$$\hat{K}_k^{(\text{deph})} = \frac{\sigma_\phi^k}{\sqrt{k!}} e^{-\frac{1}{2}\sigma_\phi^2 \hat{n}^2} \hat{n}^k. \quad (2.79)$$

As seen in Fig. 2.3, dephasing causes a rotational smearing of the state in phase space. As a consequence, parts of the Wigner function further from the origin experience a larger distortion. Since the Kraus operators are functions of only \hat{n} and thus diagonal in the Fock basis, the dephasing channel does not add or remove excitations from the state.

Thermalization. Thermalization occurs when a system exchanges energy with an environment of temperature T , and can mathematically be described by a combination of loss and amplification with Lindblad operators

$$\hat{L}_1^{(\text{therm})} = \sqrt{\bar{n} + 1} \hat{a} \quad \text{and} \quad \hat{L}_2^{(\text{therm})} = \sqrt{\bar{n}} \hat{a}^\dagger, \quad (2.80)$$

with $\bar{n} = [\exp(\hbar\omega/k_B T) - 1]^{-1}$. Loss is thus a special case of thermalization in the limit of $T \rightarrow 0$. The thermal channel is equivalent to loss preceded by amplification [53] and can therefore be described by the Kraus operators

$$\hat{K}_{k_1, k_2}^{(\text{therm})} = \hat{K}_{k_2}^{(\text{amp})}(G') \hat{K}_{k_1}^{(\text{loss})}(l'), \quad (2.81)$$

with

$$G' = (1 - e^{-\kappa t}) \bar{n} + 1, \quad l' = \frac{(1 - e^{-\kappa t})(\bar{n} + 1)}{(1 - e^{-\kappa t}) \bar{n} + 1}. \quad (2.82)$$

Alternatively, if $e^{-\kappa t} > \bar{n}/(\bar{n} + 1)$, the thermal channel is equivalent to pre-amplification followed by loss, giving the Kraus operators

$$\hat{K}_{k_1, k_2}^{(\text{therm})} = \hat{K}_{k_2}^{(\text{loss})}(l'') \hat{K}_{k_1}^{(\text{amp})}(G''), \quad (2.83)$$

with

$$G'' = \frac{e^{-\kappa t}}{e^{-\kappa t} - (1 - e^{-\kappa t}) \bar{n}}, \quad l'' = (1 - e^{-\kappa t})(1 + \bar{n}) \quad (2.84)$$

As seen in Fig. 2.3, the effect of thermalization is qualitatively the same as that of loss, i.e. a shift towards the phase space origin and a peak broadening. Comparing to the loss channel, we note that the peak broadening effect is more severe, which makes sense as the thermal channel combines peak broadening of both loss and amplification.

Gaussian displacement. The Gaussian displacement channel is a normally distributed random displacement of the state in phase space

$$\rho \rightarrow \frac{1}{2\pi\sigma_\alpha^2} \int d^2\alpha e^{-\frac{1}{2}\frac{|\alpha|^2}{\sigma_\alpha^2}} \hat{D}(\alpha) \rho \hat{D}^\dagger(\alpha). \quad (2.85)$$

This channel can be described by the Master equation with the Lindblad operators

$$\hat{L}_1^{(\text{Gauss})} = \hat{a} \quad \text{and} \quad \hat{L}_2^{(\text{Gauss})} = \hat{a}^\dagger. \quad (2.86)$$

with $2\sigma_\alpha^2 = \kappa t$. Comparing to the thermalization channel, the Gaussian displacement channel corresponds to the limit of $\bar{n} \rightarrow \infty$ and $\kappa \rightarrow 0$ with constant $\bar{n}\kappa = 2\sigma_\alpha^2/t$. Gaussian displacement can thus be thought of as heating. Therefore, similarly to the thermalization channel, the Gaussian displacement channel is equivalent to loss followed by amplification, giving Kraus operators

$$\hat{K}_{k_1, k_2}^{(\text{Gauss})} = \hat{K}_{k_2}^{(\text{amp})}(G') \hat{K}_{k_1}^{(\text{loss})}(l'), \quad (2.87)$$

with

$$G' = 1 + 2\sigma_\alpha^2, \quad l' = \frac{2\sigma_\alpha^2}{2\sigma_\alpha^2 + 1}. \quad (2.88)$$

If $2\sigma_\alpha^2 < 1$, the Gaussian displacement channel is also equivalent to amplification followed by loss, giving Kraus operators

$$\hat{K}_{k_1, k_2}^{(\text{Gauss})} = \hat{K}_{k_2}^{(\text{loss})}(l'') \hat{K}_{k_1}^{(\text{amp})}(G''), \quad (2.89)$$

with

$$G'' = \frac{1}{1 - 2\sigma_\alpha^2}, \quad l'' = 2\sigma_\alpha^2. \quad (2.90)$$

As seen in Fig. 2.3, the Gaussian displacement channel causes a broadening of the peaks, with no change in their position. Again, such peak broadening causes a rapid washout of oscillating parts of the Wigner functions.

2.5 Bosonic quantum error correction

As we have seen, bosonic modes are represented by infinite-dimensional vectors, and therefore a single bosonic mode can in principle encode infinitely many qubits. However, in section 2.4 we saw that small amounts of noise can quickly erase quantum features, such as squeezing and Wigner function negativity. Therefore, in practice we would not be able to distinguish between many different quantum states if they were encoded in a single bosonic mode. Instead, the goal of bosonic quantum error correction is to encode a single qubit into a single bosonic mode, in such a way that logical states remain distinguishable in the presence of small errors. This means that physical errors should not directly translate into logical errors, e.g., 1% loss should not result in 1% qubit errors.

Recall from the previous section that noisy channels can be thought of as an adversarial entity applying an unknown Kraus operator to the state. The goal of the error-correcting code is to guess which Kraus operator was applied and undo its effect, without disturbing the logical information. The act of guessing the Kraus operator is typically referred to as a syndrome measurement. A helpful guiding principle to find useful error-correcting codes that allows for successful error correction are the Knill-Laflamme conditions [54]:

$$\langle 0_L | \hat{K}_a^\dagger \hat{K}_b | 1_L \rangle = 0 \quad (2.91)$$

$$\langle 0_L | \hat{K}_a^\dagger \hat{K}_b | 0_L \rangle = \langle 1_L | \hat{K}_a^\dagger \hat{K}_b | 1_L \rangle, \quad (2.92)$$

where \hat{K}_a and \hat{K}_b are arbitrary Kraus operators from the set of possible Kraus operators given by the channel, and $|0_L\rangle$ and $|1_L\rangle$ are the encoded logical states. The first condition states that logical states remain orthogonal under the possible errors. This is a necessary condition for us to be able to recover the logical state after the syndrome has been identified. The second condition implies that the norm of the logical states are identical under each possible syndrome.

This is required for us to be able to perform the syndrome measurement without disturbing the logical information. If the Knill-Laflamme conditions are satisfied, we can in principle correct any error described by the set of Kraus operators. Unfortunately, for many physically relevant noise channels it is impossible to find a set of logical states which satisfy the Knill-Laflamme conditions. For example, under the loss channel there is a possibility for any state to be mapped to the vacuum state, meaning we can never satisfy Eq. (2.91). What we can do instead, is to find codes for which the Knill-Laflamme conditions are satisfied, or approximately satisfied, for the most likely syndrome outcomes.

In this thesis we consider two different codes, namely the cat code [26] and the Gottesman-Kitaev-Preskill (GKP) code [28]. Throughout the thesis, relevant aspects of these codes will be introduced as they are needed, and therefore we will not give an exhaustive introduction here. Instead, we will simply highlight key features of the codes in order to develop our intuition and motivate the remaining chapters.

2.5.1 The cat code

The cat code was proposed in 2012 by Leghtas et al. [26] and is designed to protect against losses. The computational basis states are two-component Schrödinger's cat states:

$$|0_{\text{cat}}\rangle = \frac{|\alpha\rangle + |-\alpha\rangle}{\sqrt{2(1 + e^{-2|\alpha|^2})}} = \frac{1}{\cosh(\alpha^2)} \sum_{n=0}^{\infty} \frac{(\alpha^2)^n}{\sqrt{(2n)!}} |2n\rangle, \quad (2.93a)$$

$$|1_{\text{cat}}\rangle = \frac{|i\alpha\rangle + |-i\alpha\rangle}{\sqrt{2(1 + e^{-2|\alpha|^2})}} = \frac{1}{\cosh(\alpha^2)} \sum_{n=0}^{\infty} \frac{(-\alpha^2)^n}{\sqrt{(2n)!}} |2n\rangle. \quad (2.93b)$$

Some different logical qubit states of the cat code are visualized in Fig. 2.4a. Importantly, the states have support only on even Fock states. Thus, if we measure the state in the Fock basis and find an odd number of photons, we can infer that a photon has been lost. Of course, measuring the state in the Fock basis will collapse the state to a Fock state and so is not a good idea. Instead, the ideal syndrome measurement is a Fock basis parity measurement, which tells us whether a photon has been lost without collapsing the state to a single Fock state.

There are a few important things to note about the cat code. First, the cat code satisfies $\hat{a}^2(|0_{\text{cat}}\rangle + |1_{\text{cat}}\rangle) \propto (|0_{\text{cat}}\rangle - |1_{\text{cat}}\rangle)$. Thus the operator \hat{a}^2 implements a logical Z gate. However, \hat{a}^2 is involved in the $k = 2$ Kraus operator for loss, Eq. (2.74), and so this event results in an undetectable error. Therefore, the cat code is only suitable in cases where single-photon loss events are the dominant noise source, i.e. when the loss, l , is small.

Second, the basis states are generally not orthogonal, i.e., $\langle 0_{\text{cat}} | 1_{\text{cat}} \rangle = \cos(\alpha^2) / \cosh(\alpha^2)$. Thus the first Knill-Laflamme criteria, Eq. (2.91), is not even satisfied for the identity channel. This means that the cat code has intrinsic errors, which must be suppressed by choosing sufficiently large α .

Third, even single-photon losses can cause decoherence for the cat code when α is small. This is most easily seen by considering the limit of $\alpha \rightarrow 0$, in which case the logical Pauli X states take the form $|+_{\text{cat}}\rangle = |0_{\text{cat}}\rangle + |1_{\text{cat}}\rangle \rightarrow |0\rangle$ and $|-_{\text{cat}}\rangle = |0_{\text{cat}}\rangle - |1_{\text{cat}}\rangle \rightarrow |2\rangle$. In this case, if a syndrome measurement tells us that the state contains an odd number of photons, i.e., a photon has been lost, we know that the initial state cannot have been $|+_{\text{cat}}\rangle$ as this state had no photons to lose to begin with. Thus the syndrome measurement collapses the state in the Pauli X basis. To avoid this, we again need to choose α sufficiently large.

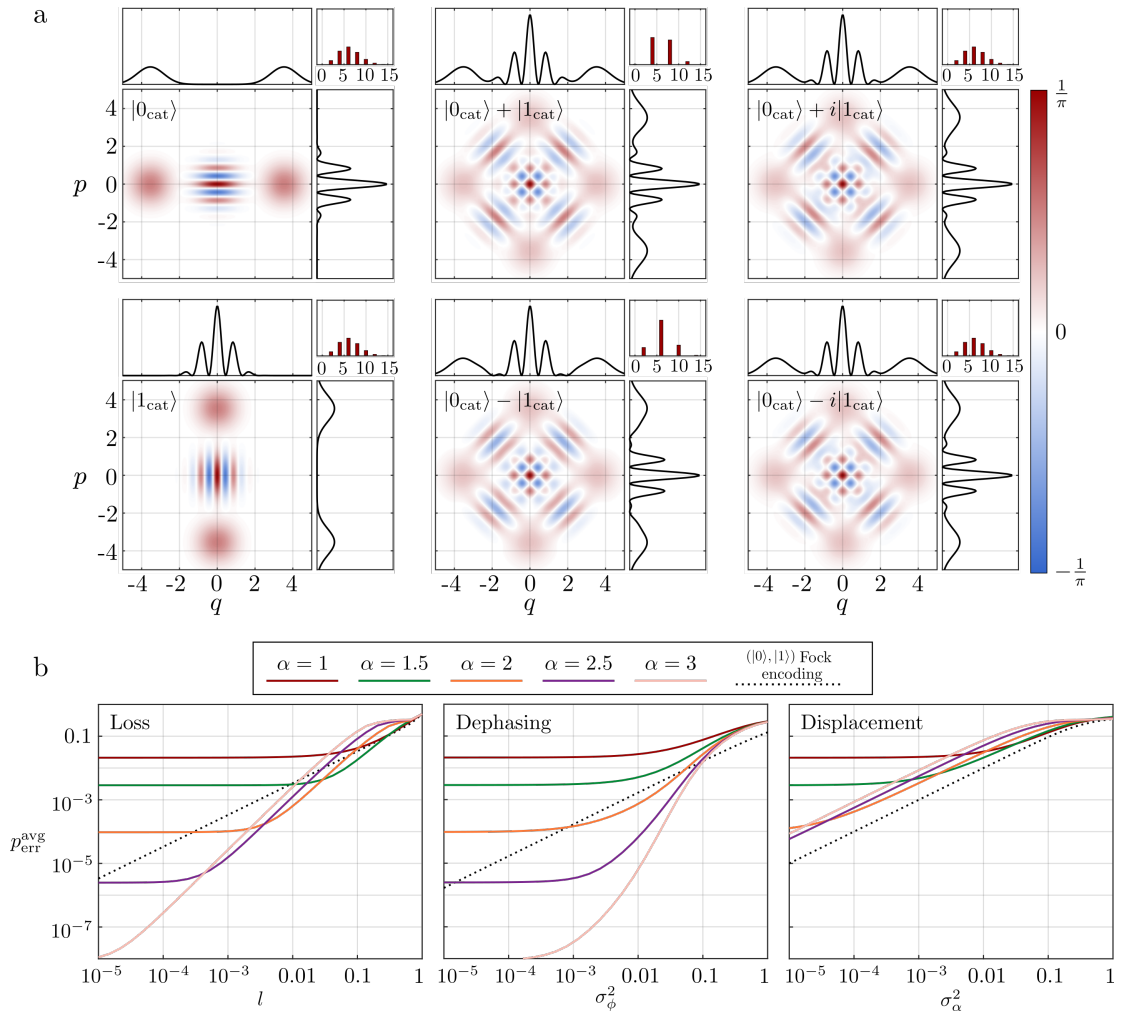


Figure 2.4: (a): Wigner functions, quadrature distributions and Fock basis distributions of the logical Pauli eigenstates for the cat code with $\alpha = 2.5$. (b): Average error rate (see text around Eq. (2.94)) of the cat code under different noise channels.

In conclusion, α cannot be too small for the cat code to work well. However, as we increase α we also increase the chance of two-photon losses. Thus α should be optimized depending on the amount of loss in the system.

Let us now attempt to quantify the error-correction capabilities of the cat code. Previous studies have quantified the cat code in terms of channel fidelity [55], Hashing bound [55] and syndrome measurement fidelity [27]. Here, we complement those figures of merit with one that is based on the requirement that logically different states should remain distinguishable under the noise channel. In particular, we consider how well we can discriminate between two initially logically orthogonal states after they have been subjected to noise. The probability to correctly distinguish between two states ρ_0 and ρ_1 is bounded by the Helstrom bound [56]:

$$p_{\text{cor}} = \frac{1}{2} + \frac{1}{4}(\|\rho_0 - \rho_1\|_1), \quad (2.94)$$

with $\|\cdot\|_1$ denoting the trace norm. The chance of misidentification is then $p_{\text{err}} = 1 - p_{\text{cor}}$. For our figure of merit we consider pairs of states in each of the three logical Pauli directions. For each direction we calculate a corresponding error rate, p_{err}^X , p_{err}^Y and p_{err}^Z . For example, $1 - p_{\text{err}}^Z$ is the probability correctly to distinguish the states $|0_L\rangle$ and $|1_L\rangle$ after each of them have undergone the same noise channel. Finally we compute the average $p_{\text{err}}^{\text{avg}} = (p_{\text{err}}^X + p_{\text{err}}^Y + p_{\text{err}}^Z)/3$. Unlike the entanglement fidelity and Hashing bound studied in [55], $p_{\text{err}}^{\text{avg}}$ depends on our choice of logical basis states and not just the space spanned by these states. This means that the non-zero overlap of the basis states are explicitly included in $p_{\text{err}}^{\text{avg}}$, yielding imperfect performance in the absence of noise.

The result for the cat code undergoing loss, dephasing and Gaussian displacement is shown in Fig. 2.4b. The results are compared to a simple Fock state encoding for which the logical basis states are the $|0\rangle$ and $|1\rangle$ Fock states. As the Fock encoding has no intrinsic error-correction capabilities, its logical error rate, $p_{\text{err}}^{\text{avg}}$, is approximately proportional to the physical error rate for all three noise channels. We see that the cat code beats the simple encoding in terms of losses, as expected, provided α is suitably chosen. Additionally, as the magnitude of losses decreases, the optimum value of α increases in order to reduce the overlap of the cat states.

The cat code is also seen to perform well in the presence of dephasing. Indeed, recalling that the dephasing channel does not change the Fock basis probability distribution, the Pauli X states, $|0_{\text{cat}}\rangle + |1_{\text{cat}}\rangle$ and $|0_{\text{cat}}\rangle - |1_{\text{cat}}\rangle$, remain perfectly orthogonal for any degree of dephasing. Moreover, since the Pauli Z states, $|0_{\text{cat}}\rangle$ and $|1_{\text{cat}}\rangle$, can be distinguished by the position of their constituent coherent states which are relatively far from each other in phase space, these can still be distinguished well after small amounts of dephasing. In total, this makes the cat code rather robust against dephasing.

For the Gaussian displacement channel, however, the cat code has no error correcting capabilities. This is because the parity syndrome measurement of the cat code cannot tell the difference between a loss event and an amplification event. Since both of these are possible for the Gaussian displacement channel, we can no longer identify the correct syndrome, and are thus unable to correct this type of noise.

The cat code has been generalized by Bergmann and van Loock in 2016 [27], as well as by Li et al. [57], to superpositions of $S + 1$ coherent states :

$$|0_{\text{cat},S}\rangle \propto \sum_{k=0}^S \hat{R} \left(\frac{2k\pi}{S+1} \right) |\alpha\rangle \quad (2.95a)$$

$$|1_{\text{cat},S}\rangle \propto \sum_{k=0}^S \hat{R} \left(\frac{(2k+1)\pi}{S+1} \right) |\alpha\rangle \quad (2.95b)$$

This generalization also includes the simpler coherent state encoding [58–60], corresponding to the case of $S = 0$. These general cat codes can correct S excitation losses. However, higher S values also require larger values of α in order to keep the overlap between the logical states negligible. A further generalization was put forward in 2019 by Grimsmo et al. [61], which considers arbitrary states instead of coherent states to produce an even broader class of rotation-symmetric bosonic codes, which also includes the so-called binomial codes [62]. Such a generalization makes sense because discrete phase-space rotation symmetry is equivalent to a spacing of the support of the state in the Fock basis. For example, any state with 2-fold rotation symmetry has support only on every 2nd Fock state, and states with 3-fold symmetry have support on every 3rd Fock state, etc. Such gaps in the Fock basis can in turn enable the detection of a number of lost photons

equal to the size of the gaps. However, while some of these generalizations perform better than the original cat-codes in some aspects [55], their experimental realization and manipulation is also correspondingly increasingly complex, especially in optics. Meanwhile, since the original cat-code is based on only a few coherent states, one can construct specialized preparation protocols that more efficiently utilize experimentally available interactions [29, 63, 64] to generate and manipulate these “simpler” states. As a consequence, the original cat code [26] is so far the only quantum error-correcting code, bosonic or otherwise, which has managed to successfully increase the lifetime of a qubit beyond what is possible without error correction [65].

2.5.2 The GKP code

The GKP code is named after its inventors Gottesman, Kitaev and Preskill who proposed it in 2000 [28]. The code was originally designed to protect against the Gaussian displacement channel, but has turned out to be suitable against loss as well [53, 55]. The ideal GKP states are superpositions of equidistantly spaced position eigenstates:

$$|0_{\text{GKP}}\rangle = \sum_{s \in \mathbb{Z}} |q = 2s\sqrt{\pi}\rangle \quad (2.96a)$$

$$|1_{\text{GKP}}\rangle = \sum_{s \in \mathbb{Z}} |q = (2s + 1)\sqrt{\pi}\rangle \quad (2.96b)$$

If a GKP state experiences an unknown shift in the q direction, this can be revealed by measuring the value of q modulus $\sqrt{\pi}$. We can then actively displace the state back by the measured value, and if the true displacement was less than $\sqrt{\pi}/2$, we will have correctly reset the GKP qubit to its original state. Importantly, the GKP states in the p basis can be written as:

$$|0_{\text{GKP}}\rangle = \sum_{s \in \mathbb{Z}} |p = s\sqrt{\pi}\rangle \quad (2.97a)$$

$$|1_{\text{GKP}}\rangle = \sum_{s \in \mathbb{Z}} (-1)^s |p = s\sqrt{\pi}\rangle, \quad (2.97b)$$

i.e., they have the same structure in the p basis and thus displacements in the p direction can also be corrected. Since any displacement can be decomposed into a displacement in the q direction plus a displacement in the p direction, the GKP code can correct small displacements in all directions. Of course, the GKP states as defined in Eqs. (2.96b) are nonphysical as they are not normalizable and have infinite energy under the harmonic oscillator Hamiltonian. Therefore, we can only hope to realise them approximately. There are a few different ways to define approximate GKP states [66]. One definition, which is quite physically intuitive, is to replace the position eigenstates with displaced squeezed vacuum states, and enforce a Gaussian envelope over the sum, such that peaks far away from the origin are dampened:

$$|\tilde{0}_{\text{GKP}}\rangle \propto \sum_{s \in \mathbb{Z}} e^{-\frac{(2\sqrt{\pi}s)^2}{2\Delta^2}} \hat{D}(s\sqrt{2\pi}) \hat{S}(r)|\text{vac}\rangle \quad (2.98a)$$

$$|\tilde{1}_{\text{GKP}}\rangle \propto \sum_{s \in \mathbb{Z}} e^{-\frac{(2\sqrt{\pi}(s+\frac{1}{2}))^2}{2\Delta^2}} \hat{D}\left(\left(s + \frac{1}{2}\right)\sqrt{2\pi}\right) \hat{S}(r)|\text{vac}\rangle, \quad (2.98b)$$

where r is the squeezing parameter of each peak and Δ is the width of the envelope. In the limit of $r \rightarrow \infty$ and $\Delta \rightarrow \infty$, i.e., for infinitely squeezed states with an infinitely broad envelope, these approximate states converge to the ideal GKP states. Fig. 2.5a shows some of the logical states

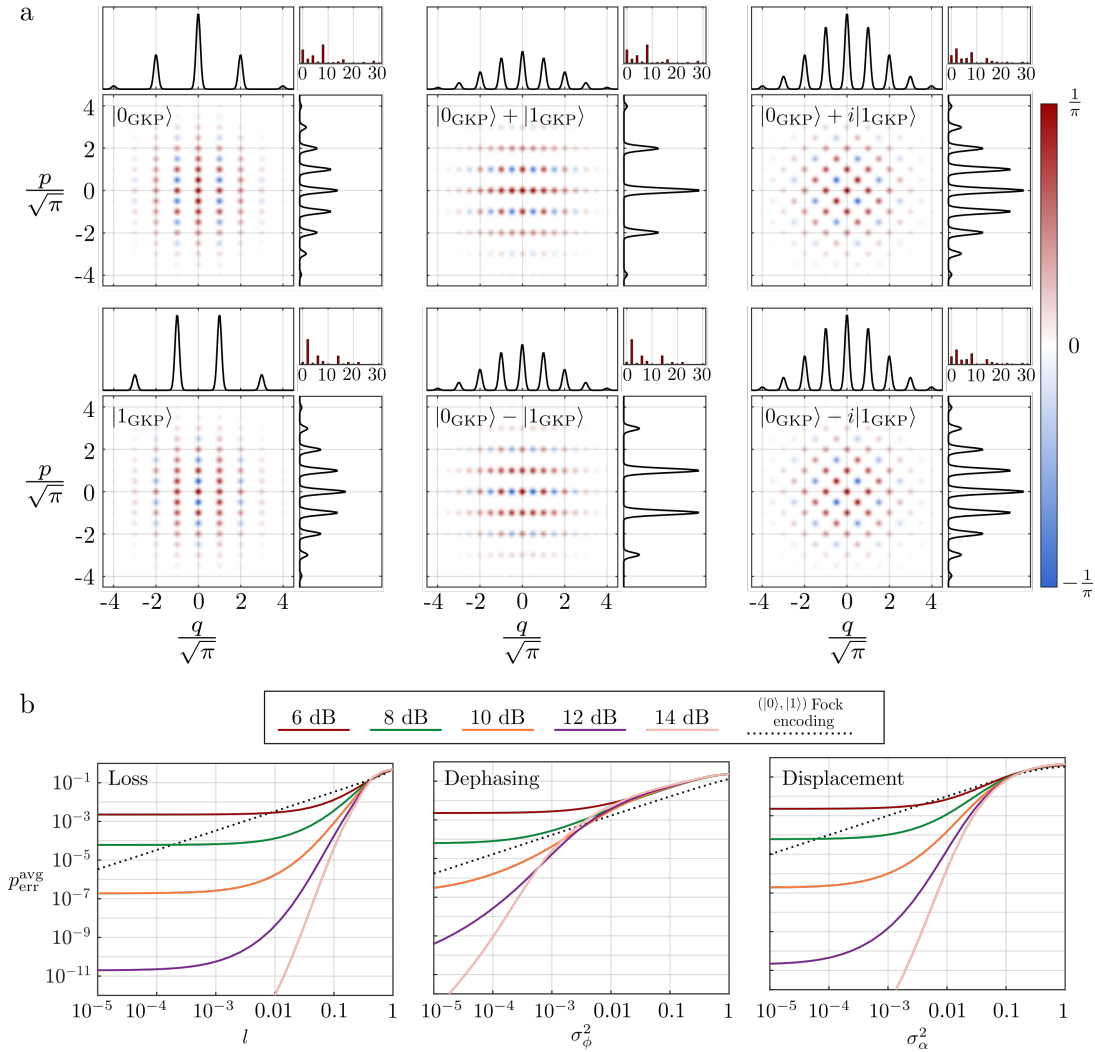


Figure 2.5: (a): Wigner functions, quadrature distributions and Fock basis distributions of the logical Pauli eigenstates for the GKP code with 12 dB squeezing. (b): Average error rate (see text around Eq. (2.94)) of the GKP code under different noise channels.

of the GKP code with $r = 1.38$ (corresponding to 12 dB squeezing) and $\Delta = e^r$ which results in equal squeezing of q and p peaks.

In Fig. 2.5b we examine how robust the GKP code is against noise, using the same figure of merit as for the cat code above. As expected, approximate GKP states with larger squeezing generally perform better. Additionally, we see that the GKP code is robust against both loss, dephasing and displacement errors. We can understand this by examining the Wigner functions of the GKP state. These consist of peaks, which for high amounts of squeezing are well-defined and separated from each other. Therefore, any type of broadening, e.g. from loss or Gaussian displacements, does not cause an immediate ‘‘collision’’ of positive and negative regions, as is the case for e.g. cat states or Fock states. As a result, small local perturbations of the Wigner

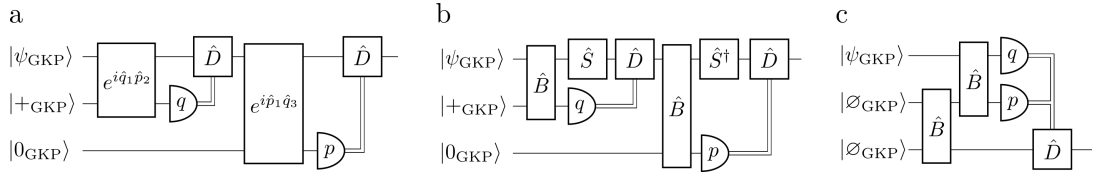


Figure 2.6: Different error-correction circuits for the GKP code. (a): The circuit originally proposed in [28], also known as Steane-type error correction. (b): Error-correcting circuit proposed by Glancy and Knill [67]. \hat{B} denotes 50/50 beamsplitters and the strengths of the squeezing operations are $r = \log(\sqrt{2}) \approx 3$ dB. (c): Teleportation-based error correction as proposed in [68]. The state $|\emptyset_{\text{GKP}}\rangle$ is called a GKP quanaught state [68], and is similar to a regular GKP state but with an adjusted lattice spacing.

function do not disturb the encoded quantum information.

Another important feature of the GKP code is, that both error correction and logical operations can be performed using Gaussian operations. The original GKP paper [28] proposed the circuit shown in Fig. 2.6a to perform error correction. This consists of a relatively simple two-mode $\hat{q}\hat{p}$ -type interaction, which is known as a sum gate, in addition to two ancilla GKP states and two homodyne detectors. The homodyne detections of the ancilla modes effectively carry out the required stabilizer measurement of q and p modulus $\sqrt{\pi}$, which is then fed forward to a corrective displacement operation. A modified error-correction circuit, shown in Fig. 2.6b, was proposed in [67] which uses a 50/50 beamsplitter interaction, \hat{B} , instead of the experimentally challenging sum gate. However, this approach requires an inline squeezing operation which is also challenging. It was later shown [69] that this inline squeezing can be removed by slightly changing the ancilla states. A third type of GKP error correction was proposed in [68] and is shown in Fig. 2.6c. This method is based on using a GKP-encoded Bell state to perform teleportation-based error correction. Apart from not requiring inline squeezing, this third method has been shown to perform better than the previous methods when considering ancilla states with finite amounts of squeezing [70]. The main challenge of GKP-based error correction is thus centered on the task of generating high-quality states, particularly in optics where beamsplitters and homodyne detectors are easily implemented.

In the years following their proposal, not much interest was given to the GKP code, likely because the required logical states are highly non-classical and non-trivial to produce experimentally. However, beginning in the mid 2010's the interest in GKP states surged. In fact, GKP-based research has seen a split into two different directions. In one direction, the GKP code has turned out to be particularly suitable in conjunction with measurement-based continuous-variable quantum computing [71, 72]. This is particularly relevant in the field of optics, where large cluster states capable of performing arbitrary Gaussian transformations can be produced using only a few optical components [73–76]. Using GKP states, such cluster states can perform universal fault-tolerant quantum computing [77, 78]. However, producing GKP states in optics remains a central unsolved challenge.

In another direction, GKP states have been generated experimentally in a trapped-ion platform [43] and in a microwave cavity coupled to a superconducting circuit [48]. The common trait of these systems is, that they allow for efficient boson-qubit couplings which provide a suitable non-Gaussian element required for the generation of GKP states [79]. However, in these systems beamsplitters and homodyne detectors are not as readily implemented as in optics. Thus, there is an open question on how to most efficiently utilize the GKP states in these systems.

Finally, it was recently proposed to encode GKP states in the current of a superconducting circuit [80], opening up a possible third branch of GKP-based quantum computing.

In summary, GKP states might be able to significantly reduce the effects of noise, but no single platform have yet demonstrated all the required elements to realise their full potential.

Chapter 3

Deterministic generation of a four-component optical cat state

In this chapter we present the paper “Deterministic generation of a four-component optical cat state” [29], authored by Jacob Hastrup, Jonas S. Neergaard-Nielsen and Ulrik L. Andersen. This work is published in *Optics Letters*.

3.1 Abstract

The four-component cat state represents a particularly useful quantum state for realizing fault-tolerant continuous variable quantum computing. While such encoding has been experimentally generated and employed in the microwave regime, the states have not yet been produced in the optical regime. Here we propose a simple linear optical circuit combined with photon counters for the generation of such optical four-component cat states. This work might pave the way for the first experimental generation of fault-tolerant optical continuous variable quantum codes.

3.2 Introduction

Quantum continuous variables (CV) have recently emerged as a promising platform for scalable quantum computing and communication. The main challenge, as for any other quantum information platform, is the ability to manipulate, store and communicate CV quantum information in a fault-tolerant manner in the presence of noise. In order to cope with noise, different bosonic error correction codes have been proposed, including the Gottesman-Kitaev-Preskill (GKP) codes, the cat codes and the binomial codes [26, 28, 55, 57, 61, 62, 81]. These codes have recently been experimentally generated in microwave cavity fields coupled to superconducting circuits [48, 65, 82] and in the vibrational mode of a single trapped ion [43, 83], and have been used to demonstrate quantum error correction and universal gate set operations.

While the superconducting circuit and ion platforms are highly suitable for the storage and manipulation of quantum information, they are less suitable for communication over larger distances. Bosonic error-correcting codes for long-distance communication will eventually require the usage of a low-loss optical platform where the codes will be embedded in the CV optical

quadratures of light [84,85]. Moreover, optical encoding is not only relevant for communication: There is an increasing interest in CV optical quantum computing partly fuelled by the recent advances in producing one-dimensional [86,87] and two-dimensional [74,75] CV cluster states

There have been several theoretical proposals on the generation of optical GKP codes using either deterministic or probabilistic schemes. The most feasible approach is based on linear optics and photon counting detectors in which the required, and notoriously difficult, optical non-linear transformation is enabled by the non-Gaussian photon counter [88,89]. Another interesting approach requires an initial resource of cat states from which GKP states can be grown with a linear optical beam splitter network and homodyne detection [90,91].

On the other hand, there are very few proposals for the direct generation of cat codes in the optical regime and the hope is that this might be significantly simpler than the generation of GKP states. Cat codes [26,57] consist of four-component cat states comprising superpositions of four coherent states, in contrast to the more common optical cat state which is a superposition of two coherent states. These latter states have undergone numerous experimental studies and have been produced in the optical regime using probabilistic approaches based on linear optics and photon counting [92–96], and very recently, using a deterministic approach based on the Jaynes-Cumming interaction between light and a single atom in a high-finesse cavity [64].

One approach for generating four-component cat states was very recently proposed by Thekkadath et al. [97]. Their method uses photon number resolving detectors and coherent state ancillas to project one mode of a two-mode squeezed vacuum state into an approximate two- or four-component cat state. However, their method is probabilistic, with low success probability for larger cat states, and furthermore it requires high two-mode squeezing to obtain four-component cat states with high fidelity.

In this article, we propose a simple circuit for the deterministic generation of an optical four-component cat state based on linear optics and photon counting using an initial resource of either two-component cat states or single-photon-subtracted squeezed states. While using two-component cat states will produce exact four-component cat states, the usage of single-photon-subtracted squeezed states is able to produce approximate four-component cat states with reasonable amplitudes.

3.3 Protocol

One can define four mutually orthogonal four-component cat states as

$$|\Phi_k\rangle = \frac{1}{N_k} (|\beta\rangle + (-1)^k|-\beta\rangle + (-i)^k|i\beta\rangle + i^k|-i\beta\rangle) \propto \sum_{n=0}^{\infty} \frac{\beta^n}{\sqrt{n!}} \delta_{n(\bmod 4),k}|n\rangle \quad (3.1)$$

for $k = 0, 1, 2, 3$, where N_k is a normalization factor and β is the coherent state amplitude. $\delta_{a,b}$ is the Kronecker delta, i.e. the 4-component cat states have support on every 4th photon number state. The main result of this article is that these states can be readily produced by interfering two two-component cat states on a balanced beam splitter followed by a projective measurement as illustrated in Fig. 3.1. If the two input cat states are given by $(|\alpha\rangle + |-\alpha\rangle)/N_\alpha$ and $(|i\alpha\rangle + |-i\alpha\rangle)/N_\alpha$ respectively, where α is the cat state amplitude and $N_\alpha = (2(1+e^{-2|\alpha|^2}))^{1/2}$ is the two-component normalization factor, the beam splitter $\hat{U}_{\text{BS}} = e^{\pi/4(\hat{a}_1^\dagger\hat{a}_2 - \hat{a}_1\hat{a}_2^\dagger)}$ transforms

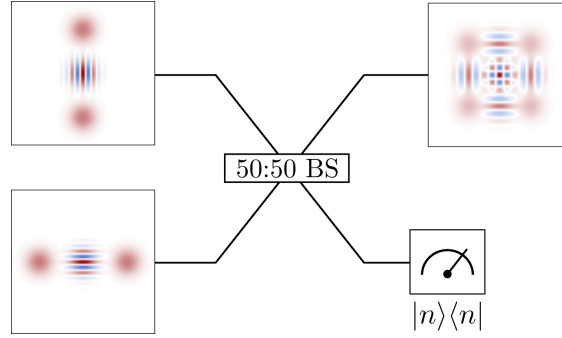


Figure 3.1: Schematic of proposed idea for generating four-component cat states using a balanced beam splitter and a projecting measurement. The state is generated probabilistically by projecting onto vacuum with an on-off photon counter (or a heterodyne detector) or is generated deterministically by projecting onto any photon number state using a photon number resolving detector.

the input state as

$$(|\alpha\rangle_1 + |-\alpha\rangle_1)(|i\alpha\rangle_2 + |-i\alpha\rangle_2) \xrightarrow{50:50 \text{ BS}} |\beta\rangle_1|i\beta\rangle_2 + |-i\beta\rangle_1|-\beta\rangle_2 + |i\beta\rangle_1|\beta\rangle_2 + |-\beta\rangle_1|-i\beta\rangle_2$$

where $\beta = \alpha e^{i\pi/4}$. By transforming mode 2 into the Fock basis, the output state, $|\Psi\rangle$, can be written as

$$|\Psi\rangle = \frac{e^{-|\beta|^2/2}}{N_\alpha^2} \sum_{n=0}^{\infty} \frac{(i\beta)^n}{\sqrt{n!}} (|\beta\rangle_1 + (-1)^n|-\beta\rangle_1 + (-i)^n|i\beta\rangle_1 + i^n|-i\beta\rangle_1)|n\rangle_2, \quad (3.2)$$

It is clear that by projecting mode 2 onto a photon number state $|n\rangle_2$, using a photon number resolving detector (PNRD), the resulting state in mode 1 is the exact four-component cat state given in Eq. (3.1) with $k \equiv n \pmod{4}$. As all outcomes of the PNRD will herald a four-component cat state, the circuit is deterministic.

We next examine the impact on the fidelity of a non-unity quantum efficiency of the PNRD. The PNRD with quantum efficiency η is modelled by a perfect PNRD following a lossy channel with transmission η . For this detector we compute the fidelity, $F = \langle \Phi_n | \rho | \Phi_n \rangle$, where ρ is the generated state and $|\Phi_n\rangle$ is the target depending on the measurement result of the photon number $n \equiv 0, 1, 2, 3 \pmod{4}$. The resulting expected fidelities over all measurement outcomes (a numerical cut-off at $n = 20$ was used for simulation) for four different input two-component cat states are shown in Fig. 3.2a. It is clear that a non-unity detector efficiency largely impacts the quality of the detected states, and it is therefore important to use a PNRD with very high efficiency. We note that there has been significant progress in developing high-efficiency PNRDs reaching nearly 100% quantum efficiency [98, 99]. Fig. 3.2b shows the Wigner functions of the output states when measuring $n \equiv 0 \pmod{4}$ photons with $\eta = 0.9$ for $|\beta| = 1.5$ (i) and $|\beta| = 2.5$ (ii), as well as the corresponding pure states obtained when $\eta = 1$ (iii, iv). For $|\beta| = 1.5$, the phase-space features of the state are still clearly visible with imperfect detection. For $|\beta| = 2.5$ the interference patterns are significantly dampened, particularly in the center of the state, but some negativity is still present. Thus, even though the fidelity is low (54%), the characteristic phase-space features of the four-component cat state are still present.

Since larger photon number states are more sensitive to loss than smaller number photon states, one should expect the fidelity to depend on the measurement outcome. However, for $|\beta| \geq 2$

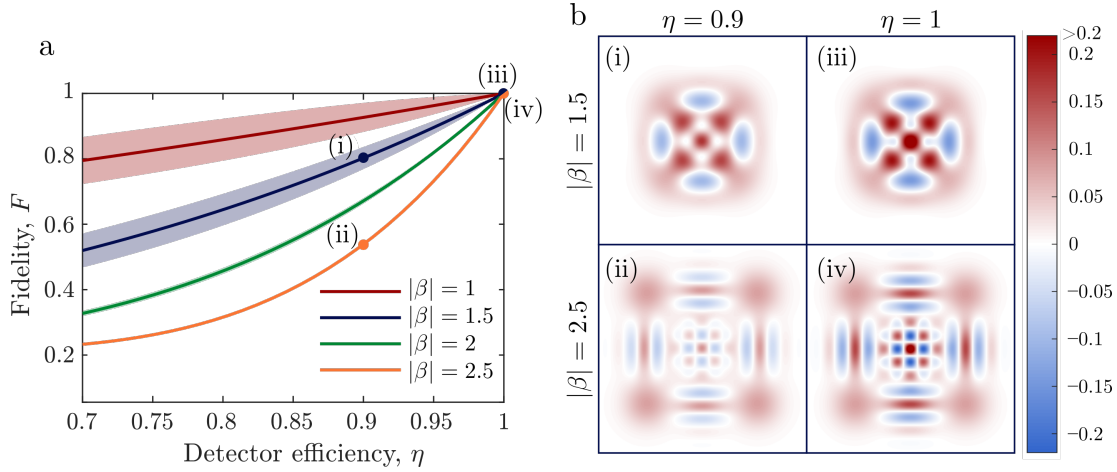


Figure 3.2: (a) Fidelities between the actual and target four-component cat states for different input cat states as a function of the PNRD quantum efficiency. The fidelity is the mean fidelity for all measurement results, weighted according to the probability of obtaining each result, and the shaded areas show the standard deviation. (b) Wigner functions for four different realizations as marked by (i–iv) in the upper figures.

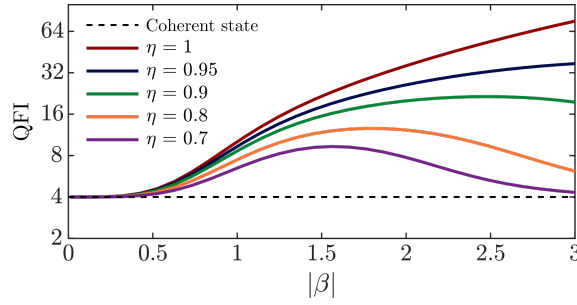


Figure 3.3: Quantum Fisher information with respect to phase space displacements defined as $\text{QFI}_\phi = 8 \lim_{\varepsilon \rightarrow 0} \left(1 - \sqrt{F(\rho_0, \rho_{\varepsilon, \phi})}\right) / \varepsilon^2$ with the displaced state $\rho_{\varepsilon, \phi} = \hat{D}(e^{i\phi}\varepsilon)\rho_0\hat{D}^\dagger(e^{i\phi}\varepsilon)$. For four-component cat states the QFI is independent of ϕ .

the fidelity is practically independent of the measurement outcome, as seen in Fig. 3.2a. This is because the increasing difficulty of detecting many photons with an imperfect detector, which would cause a lower fidelity for large n , is counteracted by the fact that the initial photon distribution decays exponentially for large n . For completeness, we also plot in Fig. 3.3 the state's quantum Fisher information (QFI) with respect to phase space displacements [100, 101] (irrespective of the direction) as the sensitivity scales as the QFI inverse. We note that for states generated with a non-unity efficiency PNRD, the sensitivity is optimized for a finite value of $|\beta|$. For comparison, the QFI of a coherent state is 4, independent of the amplitude.

We have now seen that four-component cat states can be produced deterministically using a PNRD. Using an on-off photon detector, which is typically more experimentally feasible, one can still produce an exact four-component cat state by projecting onto the vacuum state, $|n = 0\rangle_2$.

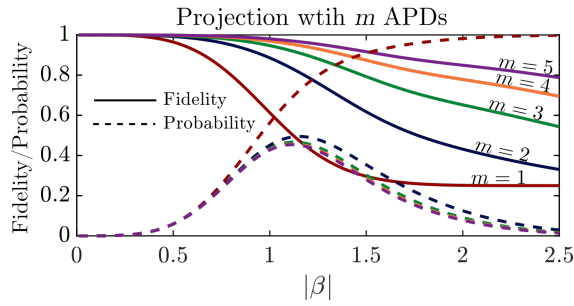


Figure 3.4: Fidelity and probability of the resulting state, post-selecting on a single 'on' event using m on-off detectors (e.g. avalanche photodiodes (APDs)) as a function of the amplitude of the input cat states

The state is produced with a success rate of $P = e^{-|\beta|^2} \left(1 + e^{-2|\beta|^2} + 2e^{-|\beta|^2} \cos(|\beta|^2) \right) / (1 + e^{-2|\beta|^2})^2$ employing an ideal on-off photon counter. One could also project onto vacuum using a heterodyne detector and post selecting on results near $(x, p) = (0, 0)$.

Since the probability of successfully projecting mode 2 onto the vacuum state decreases exponentially with $|\beta|$, it is also interesting to investigate the quality of the cat state when projecting onto the other outcome of the on-off photon detector as this will often be more probable. It is described by the projector $\Omega_{n>0} = I - |0\rangle\langle 0|$ and corresponds to a projection onto all Fock states except vacuum. Using such a measurement, the heralded output will contain a mixture of four different four-component cat states rendering the state mixed with the degree of mixedness determined by the amplitude of the input cat states. As a result, the fidelity drops rapidly as shown by the $m = 1$ curve in Fig. 3.4. For very low amplitudes, the output is fairly pure (and the fidelity high) while for amplitudes larger than ~ 0.5 , the fidelity experiences a rapid decrease. This is explained by the increased occurrence of higher-order Fock states which the detector cannot discriminate.

One can improve the fidelity by equally splitting mode 2 into m modes and subsequently measuring each mode with an on-off photon detector [102]. The POVM element corresponding to observing exactly 1 'on' click is $\sum_{n=1}^{\infty} m^{-(n-1)} |n\rangle\langle n|$. As seen in Fig. 3.4, having multiple detectors allows for larger high fidelity cat states. The probability of observing exactly 1 'on' click is shown by the dashed lines, showing reasonable success probabilities for $|\beta| \in [0.5, 2]$. Post-selecting on a higher number of clicks would similarly allow for even larger cat states with reasonable success probability given a sufficient number of detectors.

We have now shown that exact four-component cat states can be produced using a simple circuit if we have at our disposal a pair of two-component cat states. The two-component cat states can be produced deterministically using the strong interaction between a single atom and light as recently demonstrated [64]. However, knowing that single photon-subtracted squeezed states resemble two-component cat states [92], it is interesting to investigate the possibility of using such states as inputs to the circuit for the generation of approximate four-component cat states. Using two single photon-subtracted squeezed vacuum states, $\hat{a}_1 \hat{S}_1^\dagger |0\rangle$ and $\hat{a}_2 \hat{S}_2^\dagger |0\rangle$, where \hat{a}_i is the annihilation operator for mode $i = 1, 2$ and $\hat{S}_i = e^{r/2(\hat{a}_i^2 - \hat{a}_i^{\dagger 2})}$ is the squeezing operator with

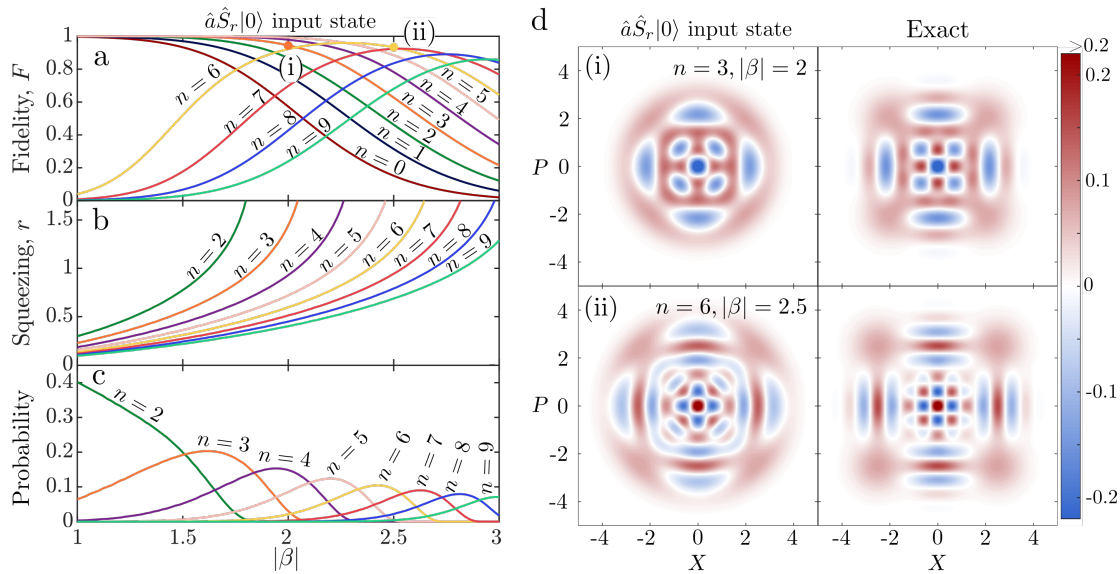


Figure 3.5: (a) Fidelity of output states relative to the ideal target state as a function of the amplitude of the target state where the input states to the circuit are photon-subtracted squeezed states. (b) The squeezing parameters r of the input states are chosen for each β to optimize the fidelity. (c) The probability of measuring n photons for the corresponding optimum squeezing parameter, r . (d) Left: Wigner functions of the output states marked by (i) and (ii) in (a) and (b). Right: corresponding Wigner functions of the exact 4-component cat state target.

r being the squeezing parameter, as the input cat states, the state after the beam splitter reads

$$\begin{aligned} & \hat{U}_{\text{BS}} \left(\hat{a}_1 \hat{S}_1 \hat{a}_2 \hat{S}_2^\dagger |0\rangle_1 |0\rangle_2 \right) \\ &= \frac{1}{2} \frac{1}{\cosh(r)} \sum_n \tanh^n(r) \left(\sqrt{n(n-1)} |n-2\rangle_1 - \sqrt{(n+2)(n+1)} \tanh^2(r) |n+2\rangle_1 \right) |n\rangle_2 \quad (3.3) \end{aligned}$$

where we have used the equality $\hat{U}_{\text{BS}} \hat{a}_1 \hat{a}_2 = \frac{1}{2} (\hat{a}_1^2 - \hat{a}_2^2) \hat{U}_{\text{BS}}$. It is clear that the scheme will herald a two-photon Fock state, $|2\rangle_1$, when projecting on $|0\rangle_2$ and a three-photon Fock state, $|3\rangle_1$, when projecting on $|1\rangle_2$. It is, however, more interesting to project onto even higher Fock states as this will herald Fock state superpositions, e.g. the (unnormalized) states $\sqrt{2}|0\rangle_1 - \sqrt{6} \tanh^2(r) |4\rangle_1$ and $\sqrt{6}|1\rangle_1 - \sqrt{20} \tanh^2(r) |5\rangle_1$ are produced when the PNRD counts 2 and 3 photons, respectively. In Fig. 3.5a we present the fidelity of these states with respect to the ideal four component cat states for different photon counting measurement outcomes from 0 to 9 photons. In these plots we have optimized the squeezing parameter for each realization to maximize the fidelity, with the optimized values shown in Fig. 3.5b and corresponding probability of measuring n photons shown in Fig. 3.5c. Note, that all measurement results of more than 1 photon yield a state which approximates a four-component cat state to some degree, according to (3.3), even if the squeezing parameter is chosen to optimize the fidelity for a specific outcome. In experiment, one might therefore post-select on several measurement outcomes. The abrupt drop in fidelity at small $|\beta|$ for $n \geq 6$ is due to the lowest Fock term missing from the output state, compared to the exact four-component cat state, as seen in (3.3). Fig. 3.5d shows the Wigner functions of the generated approximate states marked by (i) and (ii) in Fig. 3.5a, in comparison to the exact target states.

As shown in [92], better two-component cat states can be produced by subtracting multiple photons from squeezed states. From numerical analysis we have found that using such states as input will also result in even higher fidelity output states. However, it is an open question whether arbitrarily large high-fidelity 4-component cat states can be produced with this approach.

3.4 Conclusion

In conclusion, we have proposed a simple circuit for the generation of four-component cat states which eventually could be used for fault-tolerant quantum computing and communication. The scheme is deterministic and exact if two-component cat states and photon-number-resolving detectors are available.

Chapter 4

All-optical cat-code quantum error correction

In this chapter we present the paper “All-optical cat-code quantum error correction” [30], authored by Jacob Hastrup and Ulrik L. Andersen. This work is available at [arxiv.org](https://arxiv.org/abs/2108.12225) (arXiv:2108.12225).

4.1 Abstract

The cat code is a promising encoding scheme for bosonic quantum error correction as it allows for correction against losses—the dominant error mechanism in most bosonic systems. However, for losses to be detected efficiently without disturbing the encoded logical information, one needs to implement a parity measurement of the excitation number. While such a measurement has been demonstrated in the microwave regime using a superconducting transmon ancilla, it has remained unclear how it can be implemented in the optical regime. Here, we introduce a teleportation-based error-correction scheme for the cat code, using elements suitable for an optical setting. The scheme detects and corrects single-photon losses while restoring the amplitude of the cat states, thereby greatly suppressing the accumulation of errors in lossy channels.

4.2 Introduction

Quantum states are notoriously vulnerable to external noise sources, posing a central challenge towards making useful quantum technologies. To overcome the effects of noise, numerous quantum error-correction protocols have been developed over the past 25 years. The main idea behind quantum error correction is to redundantly encode each logical qubit into a larger Hilbert space, such that noise can be detected before it accumulates into logical errors. The most common approach is to use multiple physical modes to encode each qubit. Alternatively, one can encode a qubit into multiple energy levels of a single bosonic mode [27, 28, 55, 59, 61, 62, 65, 81]. Such bosonic encoding can provide an advantage in terms of hardware efficiency, reducing the number of physical modes per logical qubit. Furthermore, bosonic error correction—and in particular the cat code—has been experimentally used to extend the lifetime of a qubit beyond what is achievable in the same system without error correction [65]; a feat which remains to be demonstrated in conventional qubit systems.

A prominent bosonic system is the electromagnetic field, which has seen much development towards quantum technologies in recent years in both the optical regime [64, 74–76, 78, 103] as well as the microwave regime [48, 65, 82, 104]. In this work, we are concerned with the optical regime, which provides several advantages. For example, optical field modes are naturally in the vacuum state at room temperature, limiting the requirement for cryogenics. Additionally, optical modes are easily entangled using beamsplitters, enabling large-scale entanglement [73–75]. Furthermore, travelling optical modes constitute an uncontested platform for quantum communication.

However, optical losses can rapidly wash out vital quantum signatures. Therefore, the quantum states should be encoded such that small losses can be detected and corrected before they accumulate. The two most promising bosonic encodings against losses [55] in the optical regime are the Gottesman-Kitaev-Preskill (GKP) code [28, 77, 105, 106] and the cat code [26, 27, 57]. The GKP code, in particular, has in recent years gained renewed interest and numerous new developments for optical systems have been witnessed. This interest has largely been fueled by the potential ease of implementing gates and error correction, given a supply of high-quality encoded states. However, GKP-encoded states have yet to be produced in the optical regime, and theoretical analyses indicate that GKP states of useful quality will be challenging to produce using practical noisy components [31, 105].

Meanwhile, optical two-component Schrödinger’s cat states—which are the encoded states of the cat code—have already been produced experimentally [64, 94]. And while their superpositions, corresponding to four-components Schrödinger’s cat states remain to be produced optically, several schemes have been proposed for this task [29, 97, 107]. But unlike the GKP codes, there has been no proposal on how to implement gates or perform error correction on cat codes using tools available in the optical regime, thereby limiting their use in practice. In this work, we address part of this issue by proposing an all-optical teleportation setup which allows for single-photon losses to be detected and corrected without disturbing the encoded logical information.

4.3 Protocol

The logical basis states of the cat code are two-component Schrödinger’s cat states given by:

$$|0_L\rangle = \frac{|\alpha\rangle + |-\alpha\rangle}{\sqrt{2(1 + e^{-2|\alpha|^2})}}, \quad (4.1)$$

$$|1_L\rangle = \frac{|i\alpha\rangle + |-i\alpha\rangle}{\sqrt{2(1 + e^{-2|\alpha|^2})}}, \quad (4.2)$$

where $|\alpha\rangle$ is a coherent state. The amplitude, α , which we assume to be real, should be chosen to optimize the performance of the code, as we will discuss later. Note that due to the finite overlap between coherent states, $\langle\beta_1|\beta_2\rangle = e^{i\text{Im}(\beta_1^*\beta_2)}e^{-|\beta_1-\beta_2|^2/2}$, the logical basis states are generally not orthogonal, i.e. $\langle 0_L|1_L\rangle = \cos(\alpha^2)/\cosh(\alpha^2)$. However, the exponential increase of the hyperbolic cosine causes the overlap to quickly vanish for $\alpha \gtrsim 2$.

The encoded states in the Fock basis are given by:

$$|0_L\rangle = \frac{1}{\cosh(\alpha^2)} \sum_{n=0}^{\infty} \frac{(\alpha^2)^n}{\sqrt{(2n)!}} |2n\rangle, \quad (4.3)$$

$$|1_L\rangle = \frac{1}{\cosh(\alpha^2)} \sum_{n=0}^{\infty} \frac{(-\alpha^2)^n}{\sqrt{(2n)!}} |2n\rangle. \quad (4.4)$$

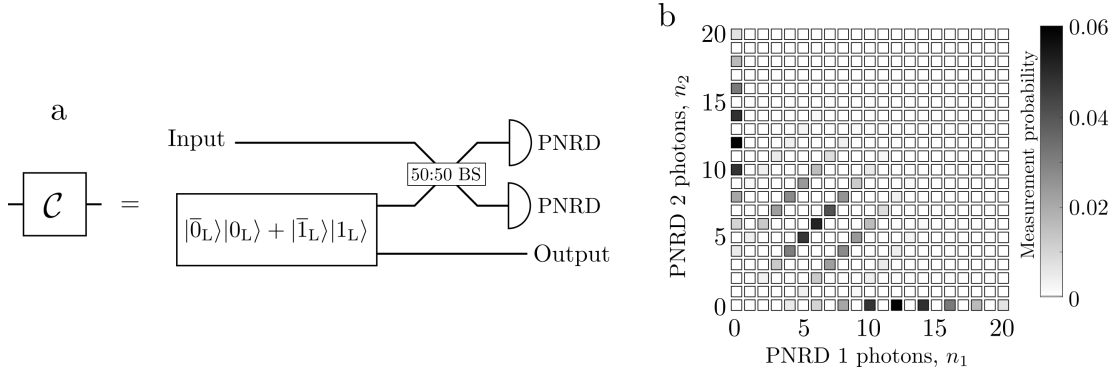


Figure 4.1: (a): Proposed error-correction circuit for performing all-optical error correction of the cat codes. The input state to be corrected is mixed on a 50:50 BS with one half of a logical Bell state and the output modes are subsequently measured with PNRDs. This teleports the input state to the other half of the Bell state while correcting single-photon losses. (b): Probability of obtaining measurement result (n_1, n_2) for an input logical state with amplitude $\alpha = 2.5$, without losses. The results are either distributed with both modes around α^2 , or with one mode containing 0 photons and the other mode containing about $2\alpha^2$ photons, in accordance with Eq. (4.6).

Notably, the states have support only on every second photon-number state, which is a common property of states with a 2-fold phase-space symmetry [61]. Therefore, we can detect if a single photon (or an odd number of photons) has been lost by measuring the photon-number parity of the state. Furthermore, the logical Pauli-X eigenstates $|\pm_L\rangle \propto |0_L\rangle \pm |1_L\rangle$ have support only on every fourth photon number, with $|+_L\rangle$ having support on $n \equiv 0 \pmod{4}$ and $|-_L\rangle$ having support on $n \equiv 2 \pmod{4}$. Thus a direct photon-number measurement realises a measurement in the logical X-basis. To detect photon loss without collapsing the logical state, we therefore need to extract information only on the parity without getting any information on the exact photon number.

This can be done using the error-correction circuit illustrated in Fig. 4.1a. It consists of a 50:50 beamsplitter (BS), two photon-number-resolving detectors (PNRDs), and an ancilla resource state in the form of a logical Bell state, $|\bar{0}_L\rangle|0_L\rangle + |\bar{1}_L\rangle|1_L\rangle$, where the bar denotes cat states with a reduced amplitude that matches that of the input state after loss. In the Appendix we present a proposal on how this logical Bell state could be produced optically. The input state interferes with one half of the logical Bell state on the BS, the outputs of which are measured with the PNRDs. As a result of this measurement, the input state is teleported to the other half of the Bell state, while correcting for single-photon losses, i.e. Knill-type error correction is performed [108]. Conceptually, since each mode of the Bell state contains an even number of photons the parity of the total number of photons measured by the PNRDs is determined by the parity of the input state, enabling the detection of losses. Meanwhile, since the state is mixed with the one half of the Bell state, we do not reveal information on the exact number of photons in the input state. Additionally, as the logical state is teleported onto a fresh cat-state ancilla, the cat-state amplitudes are restored to their initial values.

Before further discussions on the error-corrective properties of the circuit we interrogate the functionality of the qubit teleportation circuit in the absence of losses. Consider an arbitrary logical input state, $\mu|0_L\rangle + \nu|1_L\rangle$, written in the coherent state basis (neglecting normalization

and with subscripts denoting the different modes):

$$\left[\mu(|\alpha\rangle_1 + |-\alpha\rangle_1) + \nu(i|\alpha\rangle_1 + |-i\alpha\rangle_1) \right] \left[(|\alpha\rangle_2 + |-\alpha\rangle_2)(|\alpha\rangle_3 + |-\alpha\rangle_3) + (i|\alpha\rangle_2 + |-i\alpha\rangle_2)(i|\alpha\rangle_3 + |-i\alpha\rangle_3) \right]. \quad (4.5)$$

As the BS transforms coherent states according to $|\beta_1\rangle_1|\beta_2\rangle_2 \rightarrow |(\beta_1+\beta_2)/\sqrt{2}\rangle_1|(-\beta_1+\beta_2)/\sqrt{2}\rangle_2$, the transformed state can be written in the form

$$\begin{aligned} & \rightarrow \mu \left[|\sqrt{2}\alpha\rangle_1|0\rangle_2 + |0\rangle_1|-\sqrt{2}\alpha\rangle_2 + |0\rangle_1|\sqrt{2}\alpha\rangle_2 + |-\sqrt{2}\alpha\rangle_1|0\rangle_2 \right] |0_L\rangle_3 \\ & + \nu \left[|i\sqrt{2}\alpha\rangle_1|0\rangle_2 + |0\rangle_1|-i\sqrt{2}\alpha\rangle_2 + |0\rangle_1|i\sqrt{2}\alpha\rangle_2 + |-i\sqrt{2}\alpha\rangle_1|0\rangle_2 \right] |1_L\rangle_3 \\ & + \mu \left[|\tilde{\alpha}\rangle_1|-\tilde{\alpha}^*\rangle_2 + |\tilde{\alpha}^*\rangle_1|-\tilde{\alpha}\rangle_2 + |-\tilde{\alpha}^*\rangle_1|\tilde{\alpha}\rangle_2 + |-\tilde{\alpha}\rangle_1|\tilde{\alpha}^*\rangle_2 \right] |1_L\rangle_3 \\ & + \nu \left[|\tilde{\alpha}\rangle_1|\tilde{\alpha}^*\rangle_2 + |-\tilde{\alpha}^*\rangle_1|-\tilde{\alpha}\rangle_2 + |\tilde{\alpha}^*\rangle_1|\tilde{\alpha}\rangle_2 + |-\tilde{\alpha}\rangle_1|-\tilde{\alpha}^*\rangle_2 \right] |0_L\rangle_3, \quad (4.6) \end{aligned}$$

where $\tilde{\alpha} = (\alpha + i\alpha)/\sqrt{2}$ and * denotes complex conjugation. Two distinct cases appear: Either, one of the modes 1 and 2 is in the vacuum state with the other in a coherent state of magnitude $\sqrt{2}\alpha$, or both modes are in coherent states of magnitude $|\tilde{\alpha}| = \alpha$. In the regime where α is not too small, these two cases are distinguished by the PNRD results, as illustrated in Fig. 4.1b. In the first case, the coefficients μ and ν get mapped to the correct corresponding logical state in mode 3. In the second case, the coefficients get swapped, in which case a corrective logical X gate should be applied. Further analysis (see Appendix) shows that measurement results with a total photon number of 2 (mod 4) add a -1 phase to the ν term, thus requiring a logical Z gate correction. In summary, the circuit performs a teleportation of mode 1 onto mode 3, with the measurement result signaling which Pauli correction should be applied to mode 3 to retrieve the input state, just like standard qubit teleportation.

An important caveat should be noted: Knowing whether a logical X correction should be applied relies on the fact that we can distinguish the first two lines of Eq. (4.6) from the last two with the PNRDs. If α is too small, the probability of measuring e.g. $(n_1, n_2) = (0, 4)$ has contributions from both cases. That is, the central contributions in Fig. 4.1b overlap with the edge cases. It turns out that the total probability in this case depends on the input state, and in particular, such measurement results become a weak unwanted logical X measurement (See Appendix for details). To intuitively understand this, consider the extreme case of measuring $(n_1, n_2) = (0, 0)$. This can only occur if both arms before the BS have support on the vacuum state. But the state $| -_L \rangle$ does not have support on the vacuum, and so this measurement projects the input state onto $| +_L \rangle$. This can thus effectively cause logical depolarization of e.g. logical Z or Y states. To avoid this, we should choose large enough α , such that this measurement result becomes unlikely.

To characterize the performance of the circuit, we consider how well input logical Pauli-eigenstates remain distinguishable. That is, we consider three sets of input states, $\{|0_L\rangle, |1_L\rangle\}$, $\{|+_L\rangle, |-_L\rangle\}$ and $\{|+i_L\rangle, |-i_L\rangle\}$, where $|\pm i_L\rangle \propto |0_L\rangle \pm i|1_L\rangle$ denotes the logical Pauli-Y eigenstates. Denoting the channel realized by the error-correction circuit by \mathcal{C} , averaging over the PNRD measurement results weighted according to their probability distribution and keeping track of any induced Pauli-rotations, we calculate the resulting, generally mixed, output states, e.g. $\rho_0^Z = \mathcal{C}(|0_L\rangle)$ and $\rho_1^Z = \mathcal{C}(|1_L\rangle)$. We then calculate the probability of misidentifying the input 0 state as a 1 or vice

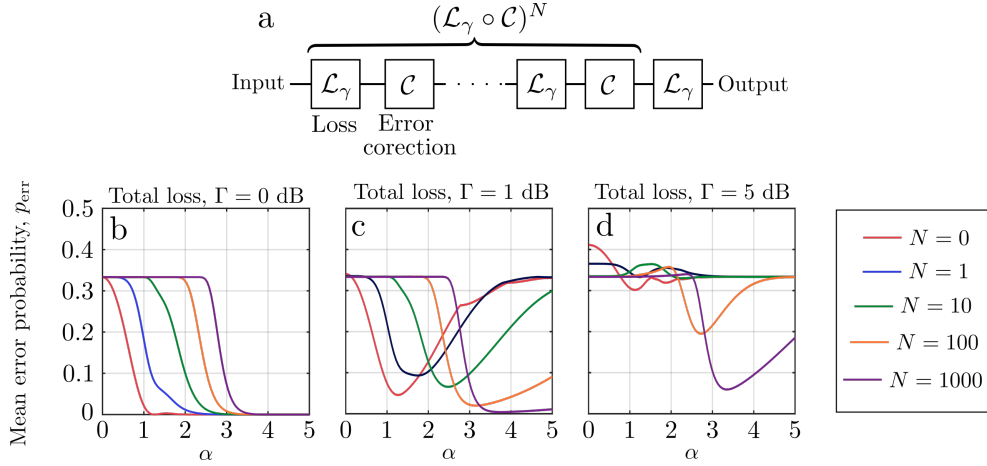


Figure 4.2: (a): The lossy channel \mathcal{L}_Γ is divided into smaller segments, \mathcal{L}_γ with N error correction steps. (b): Minimum measurement error probability of input logical Pauli states after N applications of the correction circuit of Fig. 4.1a, averaging over all possible PNRD measurement outcomes. $N = 0$ corresponds to the identity channel. (c,d): Minimum error probability after a lossy channel divided into $N + 1$ smaller segments with N correction circuits distributed between the lossy segments.

versa, which is bounded by the Helstrom bound [56]:

$$p_{\text{err}}^Z = \frac{1}{2} - \frac{1}{4}(\|\rho_0^Z - \rho_1^Z\|_1), \quad (4.7)$$

where $\|\cdot\|_1$ denotes the trace norm. We consider the Helstrom bound to focus our attention to the intrinsic properties of the circuit.

Similarly, we denote the error probabilities of the Pauli X and Y states as p_{err}^X and p_{err}^Y . We then define the average of these error rates as our figure of merit,

$$p_{\text{err}} \equiv (p_{\text{err}}^X + p_{\text{err}}^Y + p_{\text{err}}^Z)/3. \quad (4.8)$$

A value of $p_{\text{err}} = 0.5$ thus corresponds to a complete loss of the logical information, while $p_{\text{err}} = 0$ is a perfect preservation of the information.

Fig. 4.2b shows the performance of the error-correction circuit in the absence of any losses, repeatedly applying the circuit N times to the same state. The red $N = 0$ curve thus simply corresponds to the identity channel. For this curve, we note that p_{err} goes to $1/3$ for small α . This is due to the indistinguishability of the logical Z and Y states, which all converge to the vacuum state in the limit of small α . The logical X states, however, remain perfectly distinguishable for all non-zero α , resulting in a total average error rate of $2/3 \times 0.5 = 1/3$.

When applying the teleportation circuit, p_{err} increases at small α due to the weak Pauli X measurement discussed earlier. This effect accumulates when applying the circuit multiple times. However, if α is sufficiently large, e.g. at $\alpha = 4$, this effect becomes negligible even when the circuit is applied many times.

We now consider the case of lossy input states. Losses of magnitude Γ are described by the

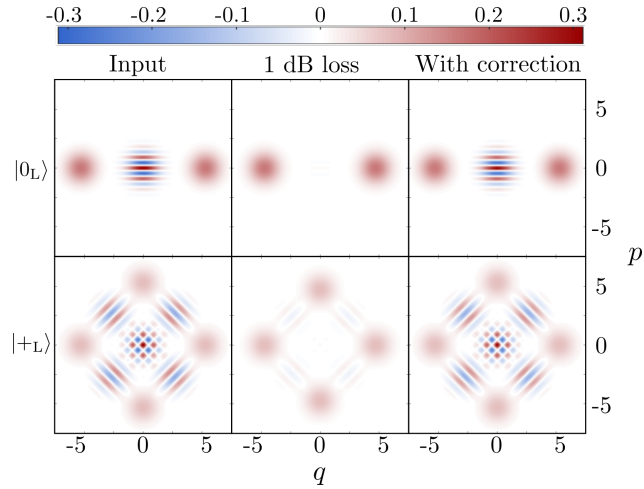


Figure 4.3: Wigner functions for cat states with $\alpha = 3$ before loss (input), after $\Gamma = 1$ dB loss without error correction, and $\Gamma = 1$ dB loss divided by $N = 100$ error correction steps. Top row: input logical Z state, $|0_L\rangle$. Bottom row: input logical X state, $|+_L\rangle$. The shown error-corrected states are averaged over PNRD measurement results, and post-selected such that the required corrective Pauli rotation adds up to the identity.

channel

$$\mathcal{L}_\Gamma(\rho) = \sum_{l=0}^{\infty} \hat{K}_\Gamma^{(l)} \rho (\hat{K}_\Gamma^{(l)})^\dagger, \quad (4.9)$$

with Kraus operators:

$$\hat{K}_\Gamma^{(l)} = \sqrt{\frac{\Gamma}{1-\Gamma}} \frac{\hat{a}^l}{\sqrt{l!}} \sqrt{1-\Gamma}^{\hat{n}}. \quad (4.10)$$

For a fixed total loss, Γ , we break the channel into $N + 1$ equal segments using N correction circuits, yielding the total channel $(\mathcal{L}_\gamma \circ \mathcal{C})^N \circ \mathcal{L}_\gamma$ with segment loss $\gamma = 1 - \sqrt[N+1]{1-\Gamma}$, as shown in Fig. 4.2a.

Fig. 4.2c and d show the performance for $\Gamma = 1$ dB and $\Gamma = 5$ dB respectively, with units in dB defined as $-10 \log_{10}(1 - \Gamma)$. For non-zero losses we now observe an optimum value of α , depending on N . This is because states with large α contain more photons on average, and are thus more sensitive to losses. The error-correction circuit can correct single-photon losses, but not two-photon losses, and so α should be small enough to make two-photon losses improbable. Importantly, we see that repeated application of the correction circuit throughout the channel can significantly suppress the effects of loss.

As seen in Fig. 4.2c and d, more frequent error correction, i.e. larger N , allows for fewer errors by suitably optimizing α . However, in practice we are limited in how frequently we can perform error correction. This limitation can be due to finite amounts of hardware but also due to finite losses introduced by the imperfect components of the error correction circuit itself.

Fig. 4.3 compares the Wigner functions of the input states $|0_L\rangle$ and $|+_L\rangle$, with and without error correction for $\Gamma = 1$ dB total loss and $N = 100$ error-correction steps. We see that the states, and in particular the negativities, are well-preserved by the error-correction protocol.

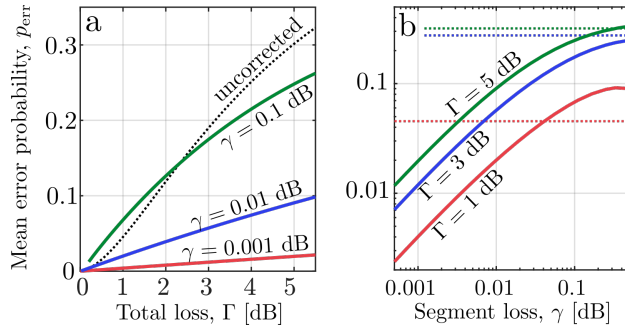


Figure 4.4: (a): Minimum error probability as a function of total channel loss, when performing error correction after every 0.1 dB (green), 0.01 dB (blue) or 0.001 dB (red) loss. The dotted line corresponds to direct transmission of a logical cat state through the channel. For all curves, α is chosen to minimize p_{err} . (b): Minimum error probability as a function of the loss between error-correction steps for a total amount of loss of 5 dB (green), 3 dB (blue) and 1 dB (red). The dotted lines show the corresponding uncorrected cases.

Fig. 4.4a shows how well the error-correction circuit protects against loss when optimizing over α , with an amount of loss between error-correction steps of 0.1 dB (2.3%), 0.01 dB (0.23%) and 0.001 dB (0.023%). Comparing to the uncorrected case (dotted line), we see that error correction needs to be applied quite frequent to gain an advantage.

In addition to loss correction in quantum communication, the circuit can also be relevant for loss correction in optical quantum computing. In particular, we can imagine a temporal measurement-based computation scheme similar to what has been demonstrated in continuous-variable optics [73, 76], where a single set of detectors can be used to perform arbitrarily many subsequent teleportations to repeatedly error-correct an encoded bosonic qubit. Of course, for such a scheme to be useful, we also need to be able to implement gates on the encoded state, which is outside the scope of this work.

The more frequently we apply error correction, the faster we might accumulate errors due to the intrinsic weak Pauli X measurement of the circuit, as was shown in Fig. 4.2b. To suppress this effect we require larger α , which in turn results in more losses. It is therefore relevant to ask whether this trade-off is favourable, i.e. how low can the total error rate be. This is examined in Fig. 4.4b, showing p_{err} as a function of the segment loss, γ , for different total loss channels, optimizing α for all curves. On the log-log plot we observe a linear relationship between p_{err} and γ , indicating that the error can indeed in principle be made arbitrarily low given frequent enough error correction and a suitable choice of α . In practice this relationship will be limited by hardware constraints, such as detector inefficiencies and Bell state preparation inefficiencies, which need to be negligible compared to γ for Fig. 4.4 to hold.

4.4 Conclusion

We have presented an all-optical scheme for performing quantum error correction on bosonic cat-code qubits, allowing single-photon loss events to be detected and corrected. The scheme relies on photon counting and logical Bell state resources and works like a conventional teleportation scheme in the absence of loss. For small cat-state amplitudes, some measurement results of the protocol act as a weak unwanted logical Pauli X measurement, thereby effectively inducing

depolarization around the X -axis. To minimize this effect, α should be optimized accordingly.

While frequent error correction is needed to effectively suppress errors using the proposed scheme, the errors can in principle be made arbitrarily low, greatly surpassing the uncorrected state. This work thus constitutes a step towards optical cat-based fault-tolerant quantum computation. Important future work will be to find methods of optically implementing gates on the encoded states, and improving the quality of experimentally generated cat-states.

4.5 Appendix A: Teleportation without losses

As stated in the main text, the state after BS interaction is given by:

$$\begin{aligned}
& \hat{U}_{BS} (\mu|0_L\rangle_1 + \nu|1_L\rangle_1) (|0_L\rangle_2|0_L\rangle_3 + |1_L\rangle_2|1_L\rangle_3) \\
&= \mu \left[|\sqrt{2}\alpha\rangle_1|0\rangle_2 + |0\rangle_1|-\sqrt{2}\alpha\rangle_2 + |0\rangle_1|\sqrt{2}\alpha\rangle_2 + |-\sqrt{2}\alpha\rangle_1|0\rangle_2 \right] |0_L\rangle_3 \\
&\quad + \nu \left[|i\sqrt{2}\alpha\rangle_1|0\rangle_2 + |0\rangle_1|-i\sqrt{2}\alpha\rangle_2 + |0\rangle_1|i\sqrt{2}\alpha\rangle_2 + |-i\sqrt{2}\alpha\rangle_1|0\rangle_2 \right] |1_L\rangle_3 \\
&\quad + \mu \left[|\tilde{\alpha}\rangle_1|-\tilde{\alpha}^*\rangle_2 + |\tilde{\alpha}^*\rangle_1|-\tilde{\alpha}\rangle_2 + |-\tilde{\alpha}^*\rangle_1|\tilde{\alpha}\rangle_2 + |-\tilde{\alpha}\rangle_1|\tilde{\alpha}^*\rangle_2 \right] |1_L\rangle_3 \\
&\quad + \nu \left[|\tilde{\alpha}\rangle_1|\tilde{\alpha}^*\rangle_2 + |-\tilde{\alpha}^*\rangle_1|-\tilde{\alpha}\rangle_2 + |\tilde{\alpha}^*\rangle_1|\tilde{\alpha}\rangle_2 + |-\tilde{\alpha}\rangle_1|-\tilde{\alpha}^*\rangle_2 \right] |0_L\rangle_3, \tag{4.11}
\end{aligned}$$

We now consider how mode 3 is projected when we measure n_1 and n_2 photons in modes 1 and 2 respectively. For this we make use of the relation

$$\langle n|\beta\rangle = e^{-|\beta|^2/2} \frac{\beta^n}{\sqrt{n!}}. \tag{4.12}$$

First, we consider the case when $n_1 \neq 0$ and $n_2 \neq 0$, in which case only the last two lines contribute. Recalling that $\tilde{\alpha}^* = -i\tilde{\alpha}$ we get:

$$\begin{aligned}
& \langle n_1|_1 \langle n_2|_2 \hat{U}_{BS} (\mu|0_L\rangle_1 + \nu|1_L\rangle_1) (|0_L\rangle_2|0_L\rangle_3 + |1_L\rangle_2|1_L\rangle_3) \\
&= \frac{e^{-|\alpha|^2}}{\sqrt{n_1!n_2!}} \tilde{\alpha}^{n_1+n_2} (i^{n_1} + i^{n_2}) (1 + (-1)^{n_1+n_2}) \left(\mu|1_L\rangle_3 + \frac{(-1)^{n_1} + (-1)^{n_2}}{2} \nu|0_L\rangle_3 \right). \tag{4.13}
\end{aligned}$$

There are a few things to note in this expression: First, the prefactor $1 + (-1)^{n_1+n_2}$ yields 0 whenever n_1 and n_2 are of different parity, i.e. when the total photon number is odd. Thus we are guaranteed to measure an even total photon number, as expected since the input states contains only even photon numbers. Second, the prefactor $i^{n_1} + i^{n_2}$ yields 0 whenever n_1 and n_2 are different modulus 4, assuming equal parity of n_1 and n_2 . This is less trivial, and a result of quantum interference on the BS. This can also be seen in Fig. 4.1b. Third, the coefficients get swapped, i.e. μ is mapped onto $|1_L\rangle$ and ν to $|0_L\rangle$, requiring a corrective logical X gate, as stated in the main text. Finally, the $[(−1)^{n_1} + (−1)^{n_2}]/2$ term contributes a $(−1)$ phase factor whenever n_1 and n_2 are odd, requiring a corrective logical Z gate. Since $n_1 \equiv n_2 \pmod{4}$ this corresponds to the cases when $n_1 + n_2 \equiv 2 \pmod{4}$.

Next, we consider the case when $n_2 = 0$ and $n_1 \neq 0$:

$$\begin{aligned}
& \langle n_1|_1 \langle 0|_2 \hat{U}_{BS} (\mu|0_L\rangle_1 + \nu|1_L\rangle_1) (|0_L\rangle_2|0_L\rangle_3 + |1_L\rangle_2|1_L\rangle_3) \\
&= \frac{e^{-|\alpha|^2}}{\sqrt{n_1!}} (\sqrt{2}\alpha)^{n_1} (1 + (-1)^{n_1}) (\mu|0_L\rangle_3 + i^{n_1}\nu|1_L\rangle_3) \\
&\quad + \frac{e^{-|\alpha|^2}}{\sqrt{n_1!}} \tilde{\alpha}^{n_1} (i^{n_1} + 1)(1 + (-1)^{n_1}) \left(\mu|1_L\rangle_3 + \frac{(-1)^{n_1} + 1}{2} \nu|0_L\rangle_3 \right) \\
&= \frac{e^{-|\alpha|^2}}{\sqrt{n_1!}} \sqrt{2}^{n_1} \alpha^{n_1} (1 + (-1)^{n_1}) \\
&\quad \times \left[\left(\mu + \frac{e^{in_1\pi/4}}{\sqrt{2}^{n_1}} (i^{n_1} + 1) \frac{(-1)^{n_1} + 1}{2} \nu \right) |0_L\rangle_3 + \left(i^{n_1}\nu + (i^{n_1} + 1) \frac{e^{in_1\pi/4}}{\sqrt{2}^{n_1}} \mu \right) |1_L\rangle_3 \right]. \quad (4.14)
\end{aligned}$$

When $n_1 \equiv 2 \pmod{4}$ this reduces to:

$$\propto [\mu|0_L\rangle_3 - \nu|1_L\rangle_3]. \quad (4.15)$$

That is, we recover the state with a corrective logical Z gate. When $n_2 \equiv 0 \pmod{4}$ we get:

$$\propto \left[\left(\mu + \frac{(-1)^{n_1/4}}{\sqrt{2}^{n_1-2}} \nu \right) |0_L\rangle_3 + \left(\nu + \frac{(-1)^{n_1/4}}{\sqrt{2}^{n_1-2}} \mu \right) |1_L\rangle_3 \right]. \quad (4.16)$$

In this case we induce a non-correctable error on the output state. However, when n_1 is large, the expression reduces to $\mu|0_L\rangle_3 + \nu|1_L\rangle_3$, i.e. we recover the state without error. On the other hand, when $n_1 = 4$, for example, we get $(\mu - 0.5\nu)|0_L\rangle_3 + (\nu - 0.5\mu)|1_L\rangle_3$. In this case, the amplitudes are reduced when μ and ν are of the same sign, and increased when their signs differ. Thus this measurement outcome is more likely for $| -_L \rangle$ states compared to $|+_L\rangle$ states, i.e. the measurement becomes a weak logical Pauli X measurement. To avoid this, α should be chosen sufficiently large to reduce the probability of this measurement outcome for all logical input states.

Finally, we consider the case when $n_1 = n_2 = 0$:

$$\begin{aligned}
& \langle 0|_1 \langle 0|_2 \hat{U}_{BS} (\mu|0_L\rangle_1 + \nu|1_L\rangle_1) (|0_L\rangle_2|0_L\rangle_3 + |1_L\rangle_2|1_L\rangle_3) \\
&= 4e^{-|\alpha|^2} (\mu + \nu) [|0_L\rangle_3 + |1_L\rangle_3]. \quad (4.17)
\end{aligned}$$

In this case, the output is completely independent of the input. Furthermore, this outcome does not occur when $\mu = -\nu$, and thus the result projects the output onto the $|+_L\rangle$ state. Again, to avoid this scenario α should be chosen sufficiently large.

4.6 Appendix B: Teleportation with losses

We now look more detailed at the loss channel. As described in the main text, loss is described by Kraus operators

$$\hat{K}_\Gamma^{(l)} = \sqrt{\frac{\Gamma}{1-\Gamma}} \frac{\hat{a}^l}{\sqrt{l!}} \sqrt{1-\Gamma}^{\hat{n}}, \quad (4.18)$$

where the l 'th Kraus operator $K_\Gamma^{(l)}$ corresponds to the case of losing l photons. The effect of this operator on the encoded state is:

$$\begin{aligned} \hat{K}_\Gamma^{(l)} (\mu|0_L\rangle + \nu|1_L\rangle) &= \sqrt{\frac{\Gamma}{1-\Gamma}} \frac{\hat{a}^l}{\sqrt{l!}} \left[\mu \left(|\alpha\sqrt{1-\Gamma}\rangle + |-\alpha\sqrt{1-\Gamma}\rangle \right) + \nu \left(|i\alpha\sqrt{1-\Gamma}\rangle + |-i\alpha\sqrt{1-\Gamma}\rangle \right) \right] \\ &\propto \hat{a}^l (\mu|\bar{0}_L\rangle + \nu|\bar{1}_L\rangle), \end{aligned} \quad (4.19)$$

where $|\bar{0}_L\rangle$ and $|\bar{1}_L\rangle$ denote logical states with the reduced amplitude $\alpha_\Gamma \equiv \alpha\sqrt{1-\Gamma}$. The $l=0$ term is corrected by the circuit as described in Appendix A, by scaling the amplitude of the first mode of the Bell state accordingly to α_Γ .

For $l=1$ we get the state:

$$\hat{K}_\Gamma^{(1)} (\mu|0_L\rangle + \nu|1_L\rangle) \propto \mu (|\alpha_\Gamma\rangle - |-\alpha_\Gamma\rangle) + i\nu (|i\alpha_\Gamma\rangle - |-i\alpha_\Gamma\rangle). \quad (4.20)$$

Repeating the calculations of Appendix A, keeping track of the new (-1) signs, we find the output state for the different photon-number measurement results. When $n_1 \neq 0$ and $n_2 \neq 0$ we get:

$$\begin{aligned} &\langle n_1|_1 \langle n_2|_2 \hat{U}_{BS} \hat{a} (\mu|\bar{0}_L\rangle_1 + \nu|\bar{1}_L\rangle_1) (|\bar{0}_L\rangle_2|0_L\rangle_3 + |\bar{1}_L\rangle_2|1_L\rangle_3) \\ &= \frac{\alpha_\Gamma e^{-|\alpha_\Gamma|^2}}{\sqrt{n_1!n_2!}} \tilde{\alpha}_\Gamma^{n_1+n_2} (i^{n_2} - i^{n_1}) (1 - (-1)^{n_1+n_2}) \\ &\quad \times \left[\mu|1_L\rangle_3 + \frac{i}{2} ((-1)^{n_1} + (-1)^{n_2} + 2i^{n_1+n_2}) \nu|0_L\rangle_3 \right]. \end{aligned} \quad (4.21)$$

This time we find a contribution only when $n_1 + n_2$ is odd, as expected. Again, a corrective X gate should be applied when $n_1 \neq 0$ and $n_2 \neq 0$. Additionally, as we only need to consider odd $n_1 + n_2$, the factor on the $|0_L\rangle_3$ term reduces to $(-1)^{(n_1+n_2+1)/2}$, i.e., a corrective Z rotation is required when $n_1 + n_2 \equiv 1 \pmod{4}$.

When $n_1 \neq 0$ and $n_2 = 0$:

$$\begin{aligned} &\langle n_1|_1 \langle 0|_2 \hat{U}_{BS} \hat{a} (\mu|\bar{0}_L\rangle_1 + \nu|\bar{1}_L\rangle_1) (|\bar{0}_L\rangle_2|0_L\rangle_3 + |\bar{1}_L\rangle_2|1_L\rangle_3) \\ &= \frac{\alpha_\Gamma e^{-|\alpha_\Gamma|^2}}{\sqrt{n_1!}} (\sqrt{2}\alpha_\Gamma)^{n_1} (1 - (-1)^{n_1}) (\mu|0_L\rangle_3 + i^{n_1+1}\nu|1_L\rangle_3) \\ &\quad + \frac{\alpha_\Gamma e^{-|\alpha_\Gamma|^2}}{\sqrt{n_1!}} \tilde{\alpha}_\Gamma^{n_1} (1 - i^{n_1}) (1 - (-1)^{n_1}) \left(\mu|1_L\rangle_3 + (-1)^{(n_1+1)/2} \nu|0_L\rangle_3 \right) \\ &= \frac{\alpha_\Gamma e^{-|\alpha_\Gamma|^2}}{\sqrt{n_1!}} (\sqrt{2}\alpha_\Gamma)^{n_1} (1 - (-1)^{n_1}) \\ &\quad \times \left[\left(\mu + \frac{e^{in_1\pi/4}}{\sqrt{2}^{n_1}} (1 - i^{n_1}) (-1)^{(n_1+1)/2} \nu \right) |0_L\rangle_3 + \left(i^{n_1+1} \nu + \frac{e^{in_1\pi/4}}{\sqrt{2}^{n_1}} (1 - i^{n_1}) \mu \right) |1_L\rangle_3 \right]. \end{aligned} \quad (4.22)$$

When $n_1 \equiv 1 \pmod{4}$:

$$\propto \left[\left(\mu - \frac{e^{i\pi/4(n_1-1)}}{\sqrt{2}^{n_1+1}} \nu \right) |0_L\rangle_3 + \left(-\nu + \frac{e^{i\pi/4(n_1-1)}}{\sqrt{2}^{n_1+1}} \mu \right) |1_L\rangle_3 \right]. \quad (4.23)$$

When $n_1 \equiv 3 \pmod{4}$:

$$\propto \left[\left(\mu + \frac{e^{i\pi/4(n_1+1)}}{\sqrt{2^{n_1+1}}} \nu \right) |0_L\rangle_3 + \left(\nu + \frac{e^{i\pi/4(n_1+1)}}{\sqrt{2^{n_1+1}}} \mu \right) |1_L\rangle_3 \right]. \quad (4.24)$$

Thus we get an uncorrectable contribution in both cases. However, for large n_1 this error vanishes due to the factor $\sqrt{2^{n_1+1}}$, and the input state is recovered by applying a logical Z correction when $n_1 \equiv 1 \pmod{4}$. Finally, the case $n_1 = n_2 = 0$ occurs with probability 0, as we expect to measure an odd number of photons if we have lost one photon in the input state.

For $l = 2$ we get

$$\hat{K}_\Gamma^{(2)} (\mu|0_L\rangle + \nu|1_L\rangle) \propto \mu|\bar{0}_L\rangle - \nu|\bar{1}_L\rangle. \quad (4.25)$$

That is, two-photon loss corresponds to an undetectable logical Z rotation.

To summarise, we can distinguish between the cases $l = 0$ and $l = 1$ by the parity of the total number of photons detected, $n_1 + n_2$. In both cases, a logical X correction should be applied whenever both detectors measure more than 0 photons. Additionally, a logical Z correction should be applied whenever the total photon number modulus 4 is 1 or 2.

4.7 Appendix C: generation of logical Bell states with cavity QED

Here we propose a method to generate the required logical Bell states. This is inspired by the experiment by Hacker et al. [64], which used a cavity QED system to generate a two-component cat state, $|\alpha\rangle + |-\alpha\rangle$. The cavity QED system consists of a cavity containing an atom with a three-level energy structure, $|\downarrow\rangle$, $|\uparrow\rangle$ and $|e\rangle$, where the $|\uparrow\rangle \leftrightarrow |e\rangle$ transition is resonant with the cavity. By preparing the atom in the $(|\downarrow\rangle, |\uparrow\rangle)$ -subspace and reflecting a coherent state pulse off the cavity, the reflected state obtains a phase shift depending on the state of the atom. In particular, the reflection coefficients can be written as (see Supplementary Information of Ref. [64])

$$r_\uparrow = 1 - \frac{2\kappa_r(i\Delta + \gamma)}{(i\Delta + \kappa)(i\Delta + \gamma) + g^2}, \quad r_\downarrow = 1 - \frac{2\kappa_r}{i\Delta + \kappa}, \quad (4.26)$$

where κ_r is the coupling rate between the input free-space mode and the cavity, κ is the total decay rate of the cavity, Δ is the detuning between the input field and the cavity, γ is the spontaneous decay rate of the state $|e\rangle$ via modes other than the cavity mode and g is the coupling strength between the atom and the cavity.

When $\Delta = 0$ and in the regime where $\kappa \approx \kappa_r$ and $g^2 \gg \kappa\gamma$ we get $r_\uparrow = 1$ and $r_\downarrow = -1$, so for the atom in the initial state $|+\rangle = (|\uparrow\rangle + |\downarrow\rangle)/\sqrt{2}$ a reflected coherent state becomes $|\alpha\rangle \rightarrow (|\alpha\rangle|\uparrow\rangle + |-\alpha\rangle|\downarrow\rangle)\sqrt{2}$. Subsequently measuring the atom in the state $|+\rangle$ projects the optical field into the cat state $\propto |\alpha\rangle + |-\alpha\rangle$. Additionally, according to Eq. (4.26) and as was experimentally demonstrated in [64], for $\Delta \neq 0$ we can obtain various phases between the coefficients r_\uparrow and r_\downarrow . In particular, for $\Delta \approx \kappa$ (still in the regime $\kappa \approx \kappa_r$ and $g^2 \gg \kappa\gamma$ and further assuming $g \gg \kappa$) we get a $\pi/2$ phase shift between the reflection coefficients. Thus, if a cat state is reflected onto this detuned cavity with the atom prepared in the $|+\rangle$ state, we obtain the state

$$|\alpha\rangle + |-\alpha\rangle \rightarrow \frac{1}{\sqrt{2}}(|\alpha\rangle + |-\alpha\rangle)|\uparrow\rangle + \frac{1}{\sqrt{2}}(i|\alpha\rangle - i|-\alpha\rangle)|\downarrow\rangle, \quad (4.27)$$

where the output state is written in a frame such that α is real. Measuring the atom now projects the optical field onto a 4-component cat state. However, if we instead reflect a second cat state off the cavity we get:

$$\begin{aligned} & \frac{1}{\sqrt{2}} \left[(|\alpha\rangle_1 + |-\alpha\rangle_1) |\uparrow\rangle + (i|\alpha\rangle_1 + |-i\alpha\rangle_1) |\downarrow\rangle \right] \left[|\alpha\rangle_2 + |-\alpha\rangle_2 \right] \\ & \rightarrow \frac{1}{\sqrt{2}} \left[(|\alpha\rangle_1 + |-\alpha\rangle_1) (|\alpha\rangle_2 + |-\alpha\rangle_2) |\uparrow\rangle + (i|\alpha\rangle_1 + |-i\alpha\rangle_1) (i|\alpha\rangle_2 + |-i\alpha\rangle_2) |\downarrow\rangle \right]. \end{aligned} \quad (4.28)$$

Measuring the atom in the $|+\rangle$ state projects the two optical modes into the desired Bell state,

$$\rightarrow \frac{1}{2} \left[(|\alpha\rangle_1 + |-\alpha\rangle_1) (|\alpha\rangle_2 + |-\alpha\rangle_2) + (i|\alpha\rangle_1 + |-i\alpha\rangle_1) (i|\alpha\rangle_2 + |-i\alpha\rangle_2) \right]. \quad (4.29)$$

Chapter 5

Generation of optical Gottesman-Kitaev-Preskill states with cavity QED

In this chapter we present the paper “Generation of optical Gottesman-Kitaev-Preskill states with cavity QED” [31], authored by Jacob Hastrup and Ulrik L. Andersen. This work is submitted for publication and is available at [arxiv.org](https://arxiv.org/abs/2104.07981) (arXiv:2104.07981).

5.1 Abstract

Gottesman-Kitaev-Preskill (GKP) states are a central resource for fault-tolerant optical continuous-variable quantum computing. However, their realization in the optical domain remains to be demonstrated. Here we propose a method for preparing GKP states using a cavity QED system which can be realized in several platforms such as trapped atoms, quantum dots or diamond color centers. We then further combine the protocol with the previously proposed breeding protocol by Vasconcelos et al. to relax the demands on the quality of the QED system, finding that GKP states with more than 10 dB squeezing could be achieved in near-future experiments.

5.2 Introduction

Quantum error correction is an essential step towards building large-scale quantum computers with realistic noisy components. In 2001, Gottesman, Kitaev and Preskill (GKP) proposed an error correction protocol in which each qubit is encoded into the continuous variables of an infinite dimensional bosonic mode [28]. With this encoding, small errors such as displacements and losses of the bosonic mode [53, 55] can be corrected using only Gaussian operations, thus providing an experimentally friendly and efficient framework, especially in the case where the bosonic mode is represented by an optical field. GKP error correction is particularly suitable in combination with optical cluster states [72, 77, 105, 106], a field which have seen tremendous progress in recent years [74–76]. Additionally, GKP error correction can be used in long distance quantum communication schemes [109, 110], implementing quantum repeaters using only beamsplitters,

homodyne detectors and GKP ancilla resource states [68].

However, the encoded states themselves, denoted GKP states or grid states, are non-Gaussian and have proven extremely difficult to produce experimentally. Only in recent years have the states been produced in the motional mode of a trapped ion [43, 111] and in a microwave cavity field coupled to a superconducting circuit [48]. Crucially, they remain to be demonstrated in the optical domain, despite several proposed generation schemes [88–91, 112, 113]. One promising approach is to interfere squeezed states on a multimode interferometer and project one output mode into an approximate GKP state by measuring the remaining modes with photon number resolving detectors [89, 105]. Progress in high quality photon number resolving detectors could make this experiment feasible in the near future. However, the method is fundamentally probabilistic and thus needs multiplexing to be scalable, which imposes a large resource overhead. Furthermore, it is unclear how efficient and noise tolerant the protocol is for generating highly squeezed GKP states (> 10 dB squeezing), which are likely required to achieve fault-tolerance [77, 78, 106].

Another proposal is to build the GKP state using squeezed Schrödinger’s cat states as the non-Gaussian element [90, 91]. The advantage of this approach is that it uses only beamsplitters and homodyne detectors, and that it can be made fully deterministic [91]. However, it requires large amplitude cat states, which are challenging to produce in optics. Still, recently Hacker et al. demonstrated the experimental generation of optical cat states, by reflecting a light pulse off an optical cavity containing an atom [64]. This method can in principle be used to generate cat states of arbitrary amplitude, although the method requires both high cooperativity and large escape efficiency which is experimentally challenging.

In this work, inspired by the experimental progress reported in [64], we propose to use cavity quantum electrodynamics (QED) to generate approximate GKP states by iteratively reflecting squeezed states off a cavity containing a 3-level system. We thus extend the cat generation protocol of [64] by inputting squeezed states, and by applying multiple interactions. We analyse the performance in systems with finite cooperativity and escape efficiency to determine the expected quality of the produced state with realistic devices. Furthermore, we combine the protocol with the cat breeding protocol of ref [90], which turns out to heavily relax the requirements on the quality of the cavity QED system. Finally, we propose a method to generate the input squeezed states also using the cavity QED system, eliminating the need for a squeezed light source at the cavity QED resonance frequency.

5.3 Preliminaries

GKP states

We describe the optical mode as a single bosonic mode with annihilation and creation operators \hat{a} and \hat{a}^\dagger and corresponding quadrature operators $\hat{x} = \frac{1}{\sqrt{2}}(\hat{a} + \hat{a}^\dagger)$ and $\hat{p} = \frac{1}{\sqrt{2}i}(\hat{a} - \hat{a}^\dagger)$ satisfying $[\hat{x}, \hat{p}] = i$.

The aim of our work is to produce good approximate GKP states with a square lattice. In this work the relevant approximation is a finite superposition of squeezed states [114]:

$$\begin{aligned} |0_{\text{GKP}}\rangle &\propto \sum_s \hat{D}(\sqrt{2\pi}s) \hat{S}(r)|\text{vac}\rangle, \\ |1_{\text{GKP}}\rangle &\propto \hat{D}(\sqrt{\pi/2}) |0_{\text{GKP}}\rangle, \end{aligned} \tag{5.1}$$

where $\hat{D}(\alpha) = \exp(\alpha\hat{a}^\dagger - \alpha^*\hat{a})$ is the displacement operator and $\hat{S}(r) = \exp(\frac{1}{2}(r^*\hat{a}^2 - r\hat{a}^{\dagger 2}))$ is the squeezing operator. The summation index, s , is over a finite number of integers around 0. GKP states have a periodic comb structure in both x and p quadratures with high quality GKP states consisting of highly squeezed peaks in both quadratures. Large squeezing in x is achieved with large r as is evident from Eq. (5.1) while large squeezing in p is achieved by including many terms in the sum. For a finite number of terms, the squeezing in p can be further improved by weighing the superposition of Eq. (5.1) such that terms further from the origin have less weight. In this work we quantify the quality of the produced GKP states by their amount of effective squeezing [101] in each quadrature, defined as:

$$\Delta_x = \sqrt{\frac{1}{2\pi} \ln \left(\frac{1}{|\langle \hat{D}(i\sqrt{2\pi}) \rangle|^2} \right)} \quad (5.2)$$

$$\Delta_p = \sqrt{\frac{1}{2\pi} \ln \left(\frac{1}{|\langle \hat{D}(\sqrt{2\pi}) \rangle|^2} \right)}. \quad (5.3)$$

The amount of squeezing is commonly denoted in dB as $\Delta_{\text{dB}} = -10 \log_{10}(\Delta^2)$. For the approximate GKP state of Eq. (5.1) one obtains $\Delta_x = e^{-r}$ while Δ_p depends on the number of terms, e.g. $\Delta_p = (6.6, 10.4, 13.7)\text{dB}$ for (2, 4, 8) terms respectively [33].

Cavity QED system

Since GKP states are non-Gaussian we require a non-Gaussian element to generate them. In this work, we propose to use a cavity QED system as the central and only non-Gaussian element. In particular, we consider the reflection of an incoming optical field onto a single-mode cavity containing a 3-level system, as depicted in Fig. 5.1a. The 3-level system consists of two low energy states, $|0\rangle$ and $|1\rangle$, and one high energy state, $|e\rangle$, which can be optically excited from the state $|1\rangle$ through a Jaynes-Cummings Hamiltonian with coupling strength g . In this paper we denote this 3-level system as an ‘‘atom’’, e.g. as the one used in the experiment of [64]. However, this atom could also be artificial such as a charged quantum dot [115–117] with the states $|0\rangle$ and $|1\rangle$ denoting spin states and $|e\rangle$ denoting a charged exciton state, or it could be a diamond color center [118, 119], such as the nitrogen-vacancy center or silicon-vacancy center, where the states $|0\rangle$ and $|1\rangle$ are represented by spin ground states and $|e\rangle$ is an excited spin state. The cavity resonance frequency and the frequency of the incoming field are equal and tuned to match the $|1\rangle \leftrightarrow |e\rangle$ transition. To couple light into and out of the cavity, one end of the cavity is constructed with a slightly transparent mirror with a coupling rate κ_c to an external free-space field. With the atom prepared in the $(|0\rangle, |1\rangle)$ subspace, an optical field mode reflected on the cavity ideally experiences a controlled phase rotation, \hat{R}_c , depending on the state of the atom [64, 120]:

$$\hat{R}_c \equiv e^{i\pi\hat{n}} \otimes |0\rangle\langle 0| + \hat{\mathbb{I}} \otimes |1\rangle\langle 1| \quad (5.4)$$

If the system is initially in the state $|+\rangle = (|0\rangle + |1\rangle)/\sqrt{2}$, an incoming optical state, $|\psi\rangle$, evolves as:

$$\hat{R}_c|\psi\rangle \otimes |+\rangle = (e^{i\pi\hat{n}}|\psi\rangle \otimes |0\rangle + |\psi\rangle \otimes |1\rangle)/\sqrt{2}. \quad (5.5)$$

Subsequently measuring the system in state $|+\rangle$ yields:

$$\langle + | \hat{R}_c |\psi \rangle \otimes | + \rangle = (e^{i\pi\hat{n}}|\psi\rangle + |\psi\rangle)/\sqrt{2}. \quad (5.6)$$

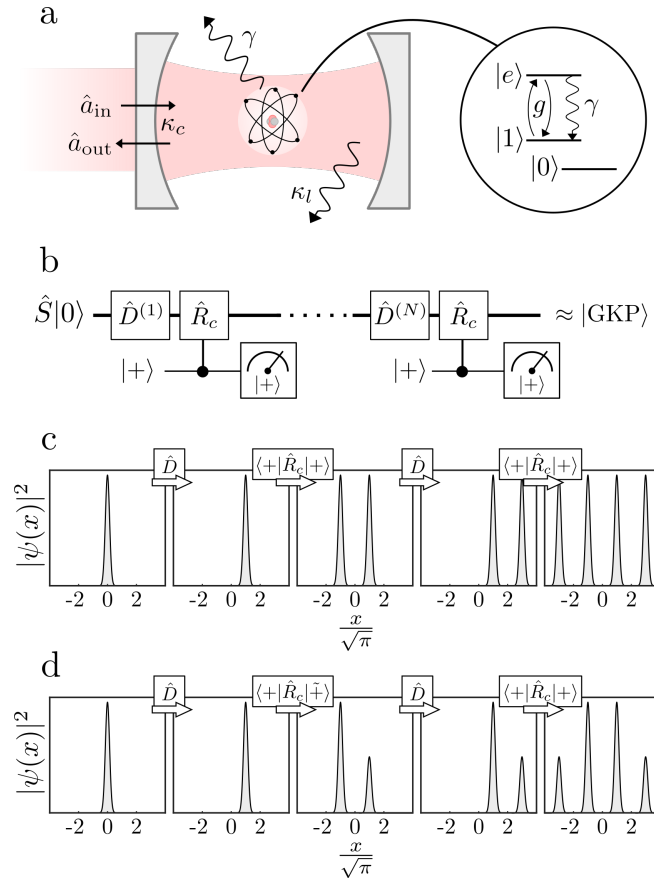


Figure 5.1: (a): Cavity QED system consisting of a cavity containing a 3-level system in which two levels resonantly couple to the cavity field. The cavity couples to a free-space field with rate κ_c and to undesired scattering and loss modes with rate κ_l . Additionally, the excited state of the 3-level system can spontaneously decay through modes different from the cavity mode with rate γ . Ideally, the cavity imprints a controlled rotation, \hat{R}_c (Eq. (5.4)), on the reflection of an incoming mode. (b) Circuit diagram for the GKP state generation protocol. (c) Repeated applications of displacements and controlled rotations evolves an initial squeezed vacuum state into an approximate GKP state. (d) Preparing the atom in an unequal superposition, $|+\tilde{\rangle}$, in the second to last step allows for the final state to have a two-level amplitude weighting of the squeezed peaks.

For example, for a coherent state input we obtain a Schrödinger's cat state, as was recently experimentally demonstrated [64].

Realistic systems, however, are limited by losses and scattering into unwanted modes at rate κ_l , as well as spontaneous decay of the excited state of the atom through modes different than the cavity mode at rate γ . In the Supplementary Material we describe how to model these imperfections. The imperfections are conveniently described by the cooperativity,

$$C = \frac{g^2}{2\gamma\kappa}, \quad (5.7)$$

and escape efficiency

$$\eta = \frac{\kappa_c}{\kappa}, \quad (5.8)$$

where $\kappa = \kappa_l + \kappa_c$ is the total cavity loss. Both C and η should preferably be as large as possible. However, there is a trade-off between the cooperativity and the escape efficiency. This is because the cooperativity can be increased by decreasing κ_c while the escape efficiency is increased by increasing κ_c . Since we would like both high cooperativity and high escape efficiency one has to carefully tune the cavity coupling rate by engineering the cavity design. In the following we therefore quantify the system in terms of the internal cooperativity [121], defined as

$$C_0 = \frac{g^2}{2\kappa_l\gamma} = \frac{C}{1-\eta}. \quad (5.9)$$

Thus, for fixed g , κ_l and γ , the internal cooperativity does not depend on the coupling rate κ_c . Note also that the internal cooperativity is always larger than the actual cooperativity, $C_0 \geq C$. In the following analysis we numerically optimize κ_c for each C_0 in order to optimize the effective squeezing of the output states.

5.4 Results

The idea of our proposed protocol is to repeatedly use the controlled rotation imposed by the cavity to generate an approximate GKP state, as illustrated in Fig. 5.1b and c. That is, inputting a displaced squeezed vacuum state we obtain a squeezed Schrödinger's cat state. Displacing and reflecting the output state on the cavity again further doubles the number of squeezed peaks in the output state and repeating this N times yields a state of the form of Eq. (5.1) with 2^N peaks. The displacement amplitude at the n 'th step is given by

$$\hat{D}_n = \hat{D} \left(2^{n-1} \sqrt{\pi/2} \right). \quad (5.10)$$

For a sufficiently squeezed input state the probability to obtain the measurement result $|+\rangle$ N times is $1/2^N$. However, the first interaction can be made deterministic, by adding a feed-forward displacement operation since

$$\hat{D} \left(i\sqrt{\pi}/(2\sqrt{2}) \right) \left(\hat{D}(\sqrt{2\pi}) - \hat{D}(-\sqrt{2\pi}) \right) \hat{S}(r)|\text{vac}\rangle \approx \left(\hat{D}(\sqrt{2\pi}) + \hat{D}(-\sqrt{2\pi}) \right) \hat{S}(r)|\text{vac}\rangle \quad (5.11)$$

Thus a 4 peak state, which can yield up to 10.4 dB squeezing can be generated with probability 0.5, while an 8 peak state, yielding up to 13.7 dB squeezing, can be generated with probability 0.25.

The solid lines of fig. 5.2a show the obtainable amount of squeezing using the protocol with finite-cooperativity systems. In addition to optimizing κ_c , we also numerically optimize the amount of input squeezing (See Supplementary Material for details on the input squeezing). The optimization is done by optimizing $\min(\Delta_x, \Delta_p)$ such that we ensure effective squeezing in both quadratures. Additionally, we can slightly further improve the performance by slightly tuning the displacement amplitudes and the atomic superposition state (details in the Supplementary Information).

The dashed lines of Fig. 5.2a show the result when implementing these two modifications. Note that for both the solid and dashed lines, there exists an optimal number of interactions, N , for each value of the internal cooperativity. This is because noise from the cavity adds up over

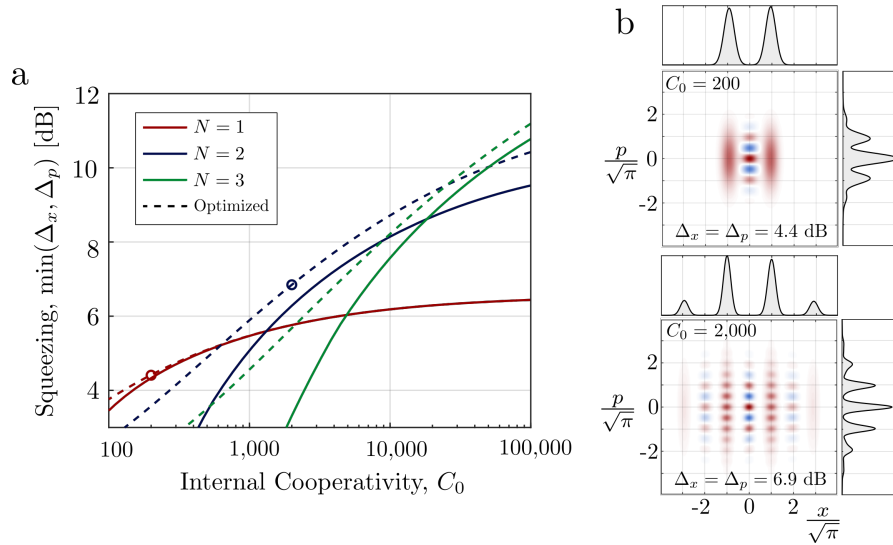


Figure 5.2: (a) Achievable amount of effective squeezing generated by the protocol outlined in Fig. 5.1 with a noisy cavity, as a function of internal cooperativity, C_0 (Eq. (5.9)), optimizing the cavity output coupling rate and the input squeezing parameter. N denotes the number of interactions with the cavity. The dashed lines further optimize over the displacement magnitudes and the initial state of the atom. (b) Wigner functions and quadrature distributions for the states generated with $C_0 = 200$ and $C_0 = 2000$ using $N = 1$ and $N = 2$ respectively, corresponding to open circles in (a).

multiple interactions, and thus at some point the noise added from the cavity outweighs the effect of increasing the number of peaks in the state. Fig. 5.2b shows the Wigner functions and quadrature probability distributions of the achievable states with $C_0 = 200$ and $N = 1$ (left) and $C_0 = 2000$ and $N = 2$ (right). For $C_0 = 200$ the produced state is essentially a squeezed Schrödinger's cat state, but the quadrature distributions reveal the onset of the desired comb-like structure. For $C_0 = 2000$ we see a clear grid structure in the Wigner function and a narrowing of the peaks in the quadrature distribution.

As is evident from Fig. 5.2, the protocol demands very high values of the internal cooperativity to produce high-squeezing grid states. This is due to the multiple interactions required with the noisy cavity, as well as the demanding simultaneous requirements of high cooperativity and high escape efficiency.

To reduce the demands on the cavity QED system we propose to combine the protocol with the Schrödinger's cat state based breeding protocol of Ref. [90]. In that protocol, we begin with a squeezed cat state of the form

$$|\text{sqcat}\rangle = \left[\hat{D} \left(\sqrt{\pi} \sqrt{2}^{M-1} \right) + \hat{D} \left(-\sqrt{\pi} \sqrt{2}^{M-1} \right) \right] \hat{S}(r) |\text{vac}\rangle, \quad (5.12)$$

where M is the number of iterations of the breeding protocol. Two such squeezed cat states are combined on a 50:50 beamsplitter and the p quadrature of one mode is measured with a homodyne detector. Conditioned on the result $p = 0$, the other mode is projected into an approximate GKP-like state. This protocol is then iterated, combining two such output states on another 50:50 beamsplitter and projecting one mode out with homodyne detection, etc. After M iterations,

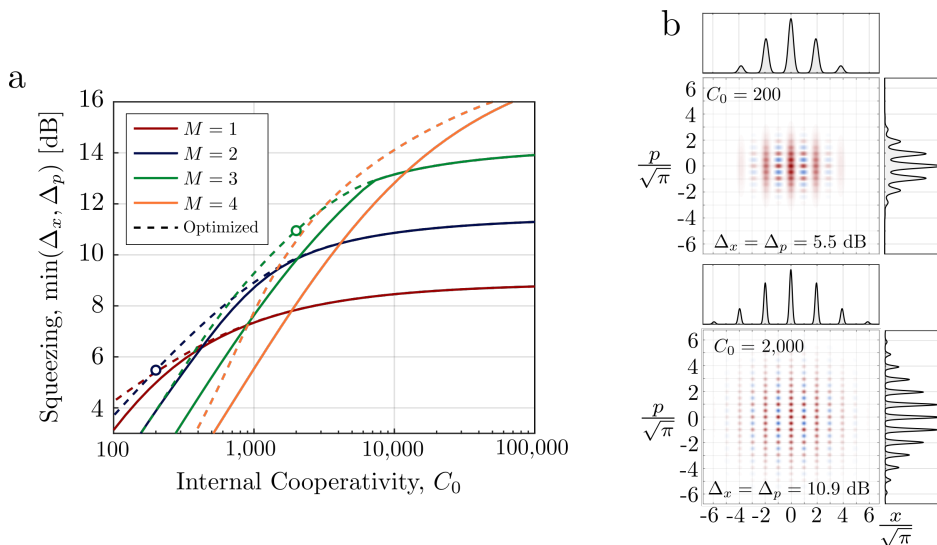


Figure 5.3: Achievable amount of effective squeezing obtained with the cat breeding method [90], using input squeezed cats generated with the cavity QED system. M refers to the number of rounds of the breeding protocol. The dashed lines show the result when fine tuning the displacement amplitude to partly compensate losses in the cavity. (b) Wigner functions and quadrature distributions using $C_0 = 200$ and $C_0 = 2000$ with $M = 2$ and $M = 3$ respectively, corresponding to the points marked with open circles in (a).

the resulting output is an approximate GKP state of which Δ_p increases with the number of iterations and Δ_x equals the squeezing of the initial input cat states. One important feature of this breeding protocol is that homodyne detectors and beamsplitters can be implemented with near unity efficiency. Thus the experimental challenges are focused on producing high quality squeezed cat states. Note from Eq. (5.12) that the amplitude of the initial squeezed cat states depends on the number of iterations, M . Thus to achieve a highly squeezed approximate GKP state we require a large amplitude squeezed cat state, which is more sensitive to noise, such as loss, and thus experimentally more demanding.

A deterministic version of this protocol was proposed in [91], by adding a feed-forward displacement to the final state. Furthermore, it was shown in [91] that this deterministic approach on average generates GKP states with ~ 1 dB more squeezing compared to the probabilistic approach.

Fig. 5.3(a) shows the obtainable amount of effective squeezing generated with the breeding protocol, using squeezed cat states produced by a single reflection on the cavity. As with Fig. 5.2 we also optimize the displacement of the squeezed cat, with the results shown by the dashed lines. We see a substantial increase in the amount of achievable squeezing, reaching more than 10 dB for an internal cooperativity around $C_0 = 1300$, corresponding to a cooperativity of $C = 25$ and escape efficiency $\eta = 0.98$. Note that we have to generate 2^M squeezed cat states to breed each approximate GKP state. Even though each of these squeezed cats are generated under noisy conditions, they still breed into an approximate GKP state with more squeezing than what is possible solely using the cavity. Fig. 5.3b shows Wigner functions and quadrature distributions of two example states generated with $C_0 = 200$ and $C_0 = 2000$ using $M = 2$ and $M = 3$ respectively. Comparing to Fig. 5.2c we observe clear improvement in the quality of the produced

states.

The results presented in Fig. 5.3 are generated using the original probabilistic approach [90], as it allows efficient evaluation of the effective squeezing levels with mixed state inputs, which enables us to numerically optimize the cavity coupling rate and input squeezing levels. However, as mentioned, the protocol can be made fully deterministic following [91], with the added benefit of an expected slight increase in the squeezing levels.

Finally, we address the input squeezed light source. Ideally, one might want to use squeezed light generated from parametric down conversion, as this method can yield very high squeezing values. However, the wavelength and temporal mode profile of the squeezed light from such a source might not be straightforwardly compatible with a high cooperatively cavity QED system. In the Supplementary Material we therefore propose a method to generate squeezed states starting from a coherent state, using the cavity QED system.

5.5 Conclusion

We have presented a method for generating approximate GKP states using a cavity QED system as the central non-Gaussian element. The performance is in practice limited by the internal cooperativity of the system. State of the art systems have demonstrated internal cooperativities of up to 200 [116, 119] which could produce approximate GKP states with 4.4 dB squeezing, which can be improved to 5.5 dB through the breeding method of [90]. However, improved cavity designs are rapidly being developed across multiple platforms, and designs with cooperativities exceeding 1000 have been proposed [122], which could push the achievable amount of effective squeezing above 10 dB in the near future.

5.6 S1: Realistic reflection channel

Here we show how to model the realistic cavity described by finite cooperativity and escape efficiency. We wish to determine reflected field mode by a quantum channel described by Kraus operators as

$$\rho \rightarrow \sum_{(m_l, m_\gamma) \in \mathbb{N}_0^2} \hat{K}_{m_l, m_\gamma} \rho \hat{K}_{m_l, m_\gamma}^\dagger, \quad (5.13)$$

where ρ denotes the density matrix of the incoming optical field. As we shall show in the following, the Kraus operator \hat{K}_{m_l, m_γ} corresponds to the event of losing m_l photons to unwanted cavity losses and m_γ photons via scattering of the atom. We use standard input-output theory to model the system [39, 123]. Thus the input and output fields, \hat{a}_{in} and \hat{a}_{out} , are related to the cavity field, \hat{a}_c in the Heisenberg picture as:

$$\hat{a}_{\text{out}} = \sqrt{2\kappa_c} \hat{a}_c + \hat{a}_{\text{in}}. \quad (5.14)$$

The quantum Langevin equation for the cavity field operator, including excess losses to the mode \hat{a}_l is given by:

$$\dot{\hat{a}}_c = -\frac{i}{\hbar} [\hat{a}_c, \hat{H}] - \sqrt{2\kappa_c} \hat{a}_{\text{out}} - \sqrt{2\kappa_l} \hat{a}_l + \kappa \hat{a}_c, \quad (5.15)$$

where \hat{H} is the cavity Hamiltonian and $\kappa = \kappa_l + \kappa_c$. We consider first the case of the atom in the $|1\rangle, |e\rangle$ -subspace. The cavity Hamiltonian is given by the Jaynes-Cummings Hamiltonian:

$$\hat{H} = \hbar\omega_c \hat{a}_c^\dagger \hat{a}_c + \hbar\omega_a \hat{\sigma}_z / 2 + \hbar g (\hat{a}_c \hat{\sigma}_+ + \hat{a}_c^\dagger \hat{\sigma}_-), \quad (5.16)$$

where $\hat{\sigma}_z = -|1\rangle\langle 1| + |e\rangle\langle e|$, $\hat{\sigma}_- = |1\rangle\langle e|$ and $\hat{\sigma}_+ = |e\rangle\langle 1|$ and g is the coupling rate. Additionally, we consider the quantum Langevin equation for the operator $\hat{\sigma}_-$, including atomic decay into modes different from the cavity mode, denoted \hat{a}_γ :

$$\dot{\hat{\sigma}}_- = -\frac{i}{\hbar}[\hat{\sigma}_-, \hat{H}] + \hat{\sigma}_z(-\gamma\hat{\sigma}_- + \sqrt{2\gamma}\hat{a}_\gamma). \quad (5.17)$$

Inserting \hat{H} we get:

$$\dot{\hat{a}}_c = -i\omega_c\hat{a}_c - ig\hat{\sigma}_- - \sqrt{2\kappa_c}\hat{a}_{\text{out}} - \sqrt{2\kappa_l}\hat{a}_l + \kappa\hat{a}_c \quad (5.18)$$

$$\dot{\hat{\sigma}}_- = -i\omega_a\hat{\sigma}_- + ig\hat{a}_c\hat{\sigma}_z + \hat{\sigma}_z(-\gamma\hat{\sigma}_- + \sqrt{2\gamma}\hat{a}_\gamma). \quad (5.19)$$

These are solved for the cavity field in the frequency domain at resonance, assuming weak excitation of the atom such that $\langle\hat{\sigma}_z\rangle = -1$:

$$\hat{a}_c(\omega) = \frac{\sqrt{2\kappa_c}\hat{a}_{\text{out}}(\omega) + \sqrt{2\kappa_l}\hat{a}_l(\omega) + \frac{ig\sqrt{2\gamma}}{\gamma-i\Delta_a}\hat{a}_\gamma(\omega)}{\kappa - i\Delta_c + \frac{g^2}{\gamma-i\Delta_a}}, \quad (5.20)$$

where $\Delta_c = \omega_c - \omega$ and $\Delta_a = \omega_a - \omega$. Inserting into the input-output relation, (5.14):

$$\begin{aligned} \hat{a}_{\text{in}}(\omega) &= \frac{(\kappa - i\Delta_c + \frac{g^2}{\gamma-i\Delta_a} - 2\kappa_c)\hat{a}_{\text{out}}(\omega) - 2\sqrt{\kappa_l\kappa_c}\hat{a}_l(\omega) - \frac{i2g\sqrt{\gamma\kappa_c}}{\gamma-i\Delta_a}\hat{a}_\gamma(\omega)}{\kappa - i\Delta_c + \frac{g^2}{\gamma-i\Delta_a}} \\ &= r_1\hat{a}_{\text{out}}(\omega) + t_1\hat{a}_l(\omega) + \Gamma\hat{a}_\gamma(\omega) \end{aligned} \quad (5.21)$$

At resonance, $\Delta_c = 0$ and $\Delta_a = 0$, the coefficients can be written in terms of the cooperativity, $C = g^2/(2\gamma\kappa)$, and escape efficiency, $\eta = \kappa_c/\kappa$ as:

$$r_1 = \frac{2C + 1 - 2\eta}{2C + 1} \quad (5.22)$$

$$t_1 = -\frac{2\sqrt{\eta(1-\eta)}}{2C + 1} \quad (5.23)$$

$$\Gamma = -i\frac{2\sqrt{2\eta C}}{2C + 1}. \quad (5.24)$$

In the case of the atom in state $|0\rangle$ the relevant coefficients are obtained by setting $g = 0$ (corresponding to $C = 0$). This gives:

$$r_0 = 1 - 2\eta \quad (5.25)$$

$$t_0 = -2\sqrt{\eta(1-\eta)}, \quad (5.26)$$

and no scattering from the atom. In total, the input field transforms as:

$$\hat{a}_{\text{in}} \rightarrow (r_0\hat{a}_{\text{out}} + t_0\hat{a}_l) \otimes |0\rangle\langle 0| + (r_1\hat{a}_{\text{out}} + t_1\hat{a}_l + \Gamma\hat{a}_\gamma) \otimes |1\rangle\langle 1| \quad (5.27)$$

To find the corresponding Kraus operators we consider the transformation of an arbitrary pure input state,

$$|\psi\rangle = \sum_{n=0}^{\infty} c_n |n\rangle_{\text{in}} = \sum_{n=0}^{\infty} c_n \frac{(\hat{a}_{\text{in}}^\dagger)^n}{\sqrt{n!}} |0\rangle_{\text{in}}. \quad (5.28)$$

Inserting Eq. (5.27):

$$\begin{aligned}
|\psi\rangle &\rightarrow \sum_n \frac{c_n}{\sqrt{n!}} \left[(r_0 \hat{a}_{\text{out}}^\dagger + t_0 \hat{a}_l^\dagger) \otimes |0\rangle\langle 0| + (r_1 \hat{a}_{\text{out}}^\dagger + t_1 \hat{a}_l^\dagger + \Gamma \hat{a}_\gamma^\dagger) \otimes |1\rangle\langle 1| \right]^n |0\rangle_{\text{out}} |0\rangle_l |0\rangle_\gamma \\
&= \left[\sum_n \frac{c_n}{\sqrt{n!}} (r_0 \hat{a}_{\text{out}}^\dagger + t_0 \hat{a}_l^\dagger)^n \right] |0\rangle_{\text{out}} |0\rangle_l |0\rangle_\gamma \otimes |0\rangle\langle 0| \\
&\quad + \left[\sum_n \frac{c_n}{\sqrt{n!}} (r_1 \hat{a}_{\text{out}}^\dagger + t_1 \hat{a}_l^\dagger + \Gamma \hat{a}_\gamma^\dagger)^n \right] |0\rangle_{\text{out}} |0\rangle_l |0\rangle_\gamma \otimes |1\rangle\langle 1|. \tag{5.29}
\end{aligned}$$

For simplicity we consider now the term containing $|1\rangle\langle 1|$. The $|0\rangle\langle 0|$ is expanded in a similar fashion:

$$\begin{aligned}
&\sum_n \frac{c_n}{\sqrt{n!}} (r_1 \hat{a}_{\text{out}}^\dagger + t_1 \hat{a}_l^\dagger + \Gamma \hat{a}_\gamma^\dagger)^n |0\rangle_{\text{out}} |0\rangle_l |0\rangle_\gamma \\
&= \sum_n \frac{c_n}{\sqrt{n!}} \sum_{m=0}^n \binom{n}{m} (r_1 \hat{a}_{\text{out}}^\dagger)^{n-m} (t_1 \hat{a}_l^\dagger + \Gamma \hat{a}_\gamma^\dagger)^m |0\rangle_{\text{out}} |0\rangle_l |0\rangle_\gamma \\
&= \sum_{n=0}^{\infty} \frac{c_n}{\sqrt{n!}} \sum_{m=0}^n \binom{n}{m} (r_1 \hat{a}_{\text{out}}^\dagger)^{n-m} \sum_{m_\gamma=0}^m \binom{m}{m_\gamma} (t_1 \hat{a}_l^\dagger)^{m-m_\gamma} (\Gamma \hat{a}_\gamma^\dagger)^{m_\gamma} |0\rangle_{\text{out}} |0\rangle_l |0\rangle_\gamma. \tag{5.30}
\end{aligned}$$

Reordering the summations as $\sum_{n=0}^{\infty} \sum_{m=0}^n \sum_{m_\gamma=0}^m = \sum_{m=0}^{\infty} \sum_{m_\gamma=0}^m \sum_{n=m}^{\infty}$ and applying the creation operators:

$$\begin{aligned}
&= \sum_{m=0}^{\infty} \sum_{m_\gamma=0}^m \sum_{n=m}^{\infty} \frac{c_n}{\sqrt{n!}} \binom{n}{m} \binom{m}{m_\gamma} r_1^{n-m} t_1^{m-m_\gamma} \Gamma^{m_\gamma} \\
&\quad \times \sqrt{(n-m)!} \sqrt{(m-m_\gamma)!} \sqrt{m_\gamma!} |n-m\rangle_{\text{out}} |m-m_\gamma\rangle_l |m_\gamma\rangle_\gamma. \tag{5.31}
\end{aligned}$$

When tracing out the lossy modes, we obtain an incoherent mixture of the terms in the inner sum. Each of these terms corresponds to losing m_γ photons from scattering of the atom and $m_l = m - m_\gamma$ photons to excess cavity losses. Looking at one of these terms:

$$\begin{aligned}
&\sum_{n=m_l+m_\gamma}^{\infty} \frac{c_n}{\sqrt{n!}} \binom{n}{m_l+m_\gamma} \binom{m_l+m_\gamma}{m_\gamma} \\
&\quad \times r_1^{n-m_l-m_\gamma} t_1^{m_l} \Gamma^{m_\gamma} \sqrt{m_l!} \sqrt{m_\gamma!} \sqrt{(n-m_l-m_\gamma)!} |n-m_l-m_\gamma\rangle \\
&= \sum_{n=m_l+m_\gamma}^{\infty} \frac{c_n}{\sqrt{n!}} \left(\frac{t_1}{r_1} \right)^{m_l} \left(\frac{\Gamma}{r_1} \right)^{m_\gamma} \frac{1}{\sqrt{m_l! m_\gamma!}} \hat{a}_{\text{out}}^{m_l+m_\gamma} r_1^{\hat{n}} |n\rangle \\
&= \left(\frac{t_1}{r_1} \right)^{m_l} \left(\frac{\Gamma}{r_1} \right)^{m_\gamma} \frac{1}{\sqrt{m_l! m_\gamma!}} \hat{a}_{\text{out}}^{m_l+m_\gamma} r_1^{\hat{n}} |\psi\rangle. \tag{5.32}
\end{aligned}$$

Similarly, when including also the $|0\rangle\langle 0|$ term in Eq. (5.29), the term corresponding to losing (m_l, m_γ) photons is:

$$\left[\delta_{m_\gamma,0} \left(\frac{t_0}{r_0} \right)^{m_l} \frac{\hat{a}_{\text{out}}^{m_l}}{\sqrt{m_l!}} r_0^{\hat{n}} \otimes |0\rangle\langle 0| + \left(\frac{t_1}{r_1} \right)^{m_l} \left(\frac{\Gamma}{r_1} \right)^{m_\gamma} \frac{\hat{a}_{\text{out}}^{m_l+m_\gamma}}{\sqrt{m_l! m_\gamma!}} r_1^{\hat{n}} \otimes |1\rangle\langle 1| \right] |\psi\rangle \equiv \hat{K}_{m_l, m_\gamma} |\psi\rangle. \tag{5.33}$$

From this we identify the Kraus operator corresponding to the loss of (m_l, m_γ) photons:

$$\hat{K}_{m_l, m_\gamma} = \delta_{m_\gamma,0} \left(\frac{t_0}{r_0} \right)^{m_l} \frac{\hat{a}_{\text{out}}^{m_l}}{\sqrt{m_l!}} r_0^{\hat{n}} \otimes |0\rangle\langle 0| + \left(\frac{t_1}{r_1} \right)^{m_l} \left(\frac{\Gamma}{r_1} \right)^{m_\gamma} \frac{\hat{a}_{\text{out}}^{m_l+m_\gamma}}{\sqrt{m_l! m_\gamma!}} r_1^{\hat{n}} \otimes |1\rangle\langle 1|. \tag{5.34}$$

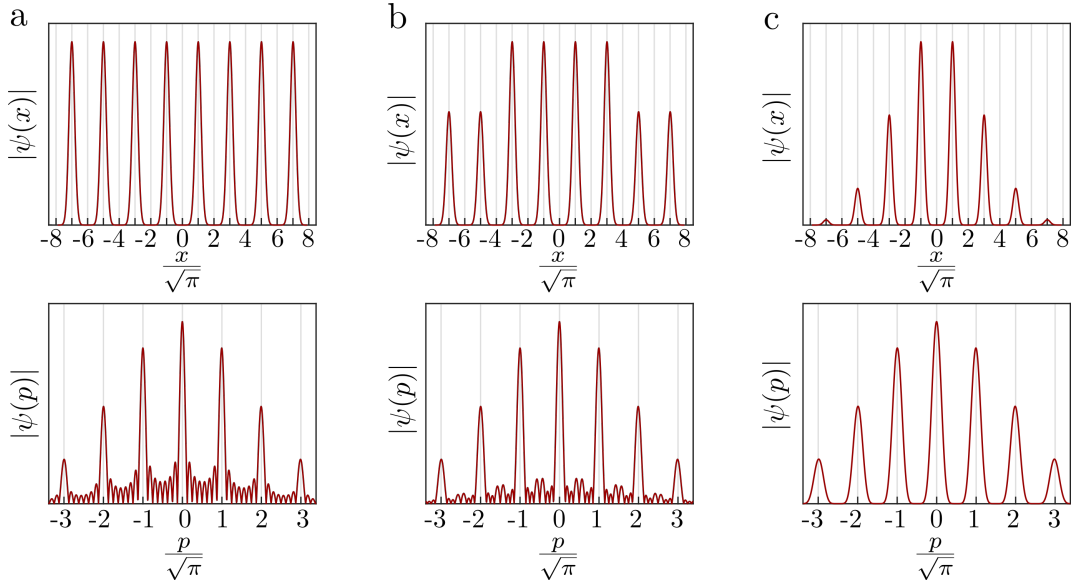


Figure 5.4: x and p quadrature distributions for different approximate GKP states, each composed of $N_{\text{peaks}} = 8$ peaks of 10 dB squeezing with different peaks weightings. (a) Equal weighting. (b) Two-level weighting. (c) Binomial weighting.

5.7 S2: Squeezing in the limit $\eta \rightarrow 1$ and $C \rightarrow \infty$

Here we calculate the effective squeezing levels of ideal states generated by the protocol. These can be written in the form

$$|\psi_{\text{GKP}}\rangle = \sum_s c_s \hat{D}\left(\sqrt{\pi/2}s\right) \hat{S}(r)|\text{vac}\rangle. \quad (5.35)$$

For logical 0 states, c_s is zero for odd s , while for logical 1 states, c_s is zeros for even s . For sufficiently large r such that neighbouring states are non overlapping, normalization is achieved by $\sum_s |c_s|^2 = 1$. The expectations value used to calculate the the effective squeezing level is given by

$$\langle \hat{D}(i\sqrt{2\pi}) \rangle = e^{-\pi e^{-2r}}, \quad (5.36)$$

$$\langle \hat{D}(\sqrt{2\pi}) \rangle = \sum c_s^* c_{s+2}, \quad (5.37)$$

again assuming negligible overlap between neighbouring states. Thus the effective squeezing level in the x quadrature depends only on r , while the effective squeezing in the p quadrature is independent of r and depends instead only on the distribution of the peaks.

Equal weighting

The states generated directly with the cavity, i.e. by the circuit of Fig. 5.1b after N steps have $N_{\text{peaks}} = 2^N$ non-zero coefficients of equal amplitude $1/\sqrt{N_{\text{peaks}}}$. Fig. 5.4a shows the quadrature distributions of this state with 8 peaks. For N_{peaks} peaks Eq. (5.37) yields:

$$\langle \hat{D}(\sqrt{2\pi}) \rangle = \frac{N_{\text{peaks}} - 1}{N_{\text{peaks}}}. \quad (5.38)$$

For $N_{\text{peaks}} = 2, 4$ or 8 we then get $\Delta_p = 6.6\text{dB}, 10.4\text{dB}$ or 13.7 dB respectively. In the limit of many peaks, i.e. large N_{peaks} we get $\Delta_p \approx \sqrt{1/(\pi N_{\text{peaks}})}$ and thus doubling the number of peaks increases the amount of squeezing with 3 dB .

Two-level weighting

As mentioned in the main text, the effective squeezing can be increased by imposing an envelope over the coefficients c_s . In our protocol, we can create a two-level envelope by preparing the atom in an uneven superposition, $a|0\rangle + b|1\rangle$ with $|a|^2 + |b|^2 = 1$, in the second to last interaction. In the resulting normalized output GKP state, the innermost half of the peaks have amplitude $\sqrt{2}a/\sqrt{N_{\text{peaks}}}$ while the outermost half have amplitude $\sqrt{2}b/\sqrt{N_{\text{peaks}}}$, as shown in Fig. 5.4b. In this case we get from Eq. (5.37):

$$\langle \hat{D}(\sqrt{2\pi}) \rangle = \frac{N_{\text{peaks}} - (4|b|^2 + 2|a|^2 - 4\text{Re}[a^*b])}{N_{\text{peaks}}}. \quad (5.39)$$

This expression is optimized for $a = \sqrt{1/2 + 1/\sqrt{20}}$ and $b = \sqrt{1/2 - 1/\sqrt{20}}$, in which case we get

$$\langle \hat{D}(\sqrt{2\pi}) \rangle = \frac{N_{\text{peaks}} - \overbrace{(3 - \sqrt{5})}^{\sim 0.76}}{N_{\text{peaks}}}. \quad (5.40)$$

In the limit of large N_{peaks} we get $\Delta_p \approx \sqrt{3 - \sqrt{5}}\sqrt{1/(\pi N_{\text{peaks}})}$ corresponding to 1.2 dB more squeezing compared to the equal-amplitude distribution. Comparing Fig. 5.4a and b we see that imposing the two-level weighting of the peaks helps to reduce the noise of the p -distribution.

Binomial weighting

The states generated with the cat-breeding protocol also take the form of Eq. (5.35), but with $N_{\text{peaks}} = 2^M + 1$ peaks forming a binomial distribution of the coefficients [90]. Thus the expectation value from Eq. (5.37) is:

$$\begin{aligned} \langle \hat{D}(\sqrt{2\pi}) \rangle &= \frac{\sum_{k=0}^{N_{\text{peaks}}-2} \binom{N_{\text{peaks}}-1}{k} \binom{N_{\text{peaks}}-1}{k+1}}{\sum_{k=0}^{N_{\text{peaks}}-2} \binom{N_{\text{peaks}}-1}{k}^2} \\ &= \frac{\binom{2(N_{\text{peaks}}-2)}{N_{\text{peaks}}-1}}{\binom{2(N_{\text{peaks}}-1)}{N_{\text{peaks}}-1}} \\ &= \frac{N_{\text{peaks}}-1}{N_{\text{peaks}}}, \end{aligned} \quad (5.41)$$

where the 2nd equality follows from Vandermonde's identity in both the numerator and denominator. Coincidentally, this expectation value is the same as for the equal weighting, Eq. (5.38), despite the quadrature distributions being quite different. Fig. 5.4c shows the binomial weighting with 8 peaks. Comparing to the equal weighting, Fig. 5.4a, the binomial distribution greatly reduces the p -quadrature noise floor, but at the cost of broadening the peaks. This trade-off happens to be such that $\langle \hat{D}(\sqrt{2\pi}) \rangle$ remains unchanged. Note that this does not necessarily

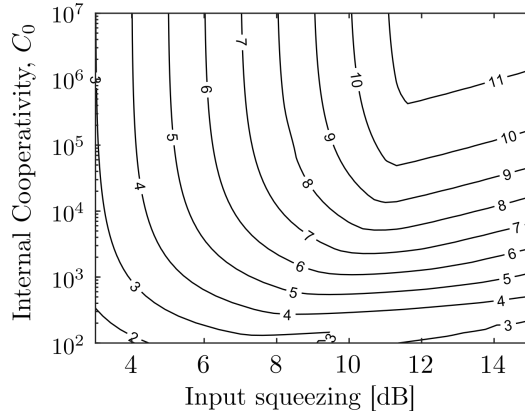


Figure 5.5: Effective squeezing in the least squeezed quadrature, $\min(\Delta_x, \Delta_p)$, in dB of the states generated with $N = 2$ as a function of input squeezing and internal cooperativity.

imply that the two states perform identically in practice, as this will depend on the specifics of the error correction protocol.

5.8 S3: Input squeezing

Fig. 5.5 shows the achievable effective squeezing with $N = 2$ as a function of internal cooperativity and input squeezing, numerically optimizing the coupling rate and displacement amplitudes at each point. For a given internal cooperativity there exists an optimum input squeezing level. This is because a heavily x -squeezed input state has a larger envelope in the p -quadrature. As the state experiences losses during generation, peaks at large $|p|$ experience a shift towards 0, thus shifting relative to the GKP lattice which degrades the effective squeezing level. In general, the achievable output squeezing is a few dB lower than the optimum input squeezing. This is because the effective squeezing in the x -quadrature is completely determined by the input squeezing. As the input state experiences noise from the cavity, the squeezing level in the x -quadrature is thus reduced by a few dB in the produced state, compared to the squeezing of the input state.

5.9 S4: Displacement amplitudes

Fig. 5.6 shows the numerically optimized displacement amplitudes. When the internal cooperativity is large, the optimal amplitudes converge to that of Eq. (5.10) for the cavity-only protocol (a) and $\sqrt{\pi}\sqrt{2}^{M-1}$ for the cat breeding protocol (b), as expected. However, when the internal cooperativity is smaller, we find that the optimal displacement is slightly larger than for the perfect cavity. The slightly larger displacement partly compensates for the loss induced by the cavity. Note that the compensation only works because the noise of cavity reflection channel is not described by pure loss, but by the more complicated channel of Eq. (5.13). The input state thus effectively experience more loss than the coherence between the generated peaks [64], which enable a slight compensation to re-position the peaks on the GKP lattice in the x -quadrature without causing unwanted shrinking of the lattice in the p -quadrature.

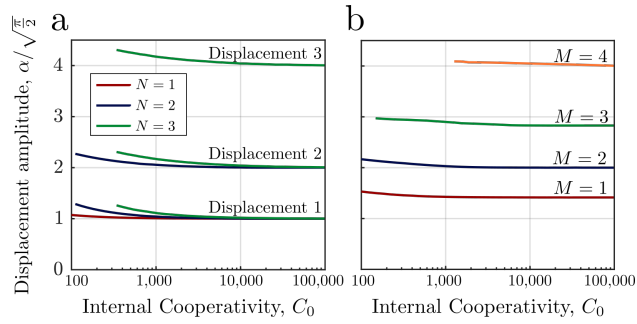


Figure 5.6: Numerically optimized displacement amplitudes as a function of internal cooperativity.

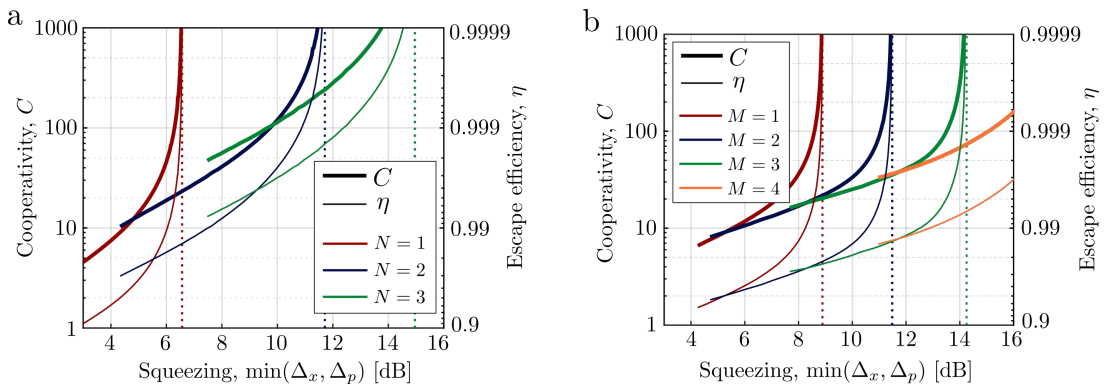


Figure 5.7: Optimal cooperativity (left axis, thick lines) and escape efficiency (right axis, thin lines) as a function of the achievable effective squeezing using only the cavity (a) and with the cat-breeding method (b). The vertical lines shows the achievable amount of effective squeezing in the limit of $\eta \rightarrow 1$ and $C \rightarrow \infty$.

5.10 S5: Required cooperativity and escape efficiency

As discussed in the main text one should optimize the cavity coupling rate to ensure simultaneous high escape efficiency and cooperativity. Fig. 5.7 shows the resulting optimized values of the cooperativity and escape efficiency as a function of the achievable amount of squeezing with a fixed internal cooperativity. For example, 10 dB squeezing can be obtained using $N = 3$ interactions with a system with $C = 110$ and escape efficiency $\eta = 0.997$ using the cavity only or $C = 25$ and $\eta = 0.98$ with $M = 3$ steps of the cat-breeding protocol.

5.11 S6: Calculation of effective squeezing parameters

To perform simulations of the reflection channel, we represent our state numerically in the Fock basis with a max photon number cut-off up to 230. The Fock-state description is convenient, as the Kraus operators describing the channel, Eq. (5.13), is represented in terms of annihilation

operators, which have a simple and sparse Fock state representation,

$$\hat{a} = \sum_k \sqrt{k} |k-1\rangle \langle k|. \quad (5.42)$$

Additionally, the displacement operator can be computed as

$$\hat{D}(\alpha) = \sum_{k,l} \sqrt{\frac{k!}{l!}} \alpha^{l-k} e^{-|\alpha|^2/2} L_k^{l-k}(|\alpha|^2) |l\rangle \langle k|. \quad (5.43)$$

where L are the generalized Laguerre polynomials. Finally, squeezed states are represented by

$$\hat{S}(r)|\text{vac}\rangle = \frac{1}{\sqrt{\cosh(r)}} \sum_k \frac{\sqrt{(2k)!}}{2^k k!} (-\tanh(r))^k |2k\rangle. \quad (5.44)$$

This allow us to simulate the total circuit of Fig. 5.1b and compute the effective squeezing levels of the output state.

For the cat breeding protocol, the Fock representation becomes less efficient, as it involves the combination of two modes, thus squaring the required dimensionality in the Fock basis. Instead, the p -quadrature basis is convenient. The transformation from the Fock basis to the p basis is done via the relation

$$|n\rangle = \int dp \sqrt{\frac{1}{\sqrt{\pi} 2^n n!}} e^{-p^2/2} H_n(p) |p\rangle \quad (5.45)$$

where H_n is the n 'th Hermite polynomial. An arbitrary mixed single-mode state is described in the p basis by a wavefunction $\psi(p, p')$:

$$\rho = \int \int dp dp' \psi(p, p') |p\rangle \langle p'|. \quad (5.46)$$

Two modes with identical wavefunctions mixing on a 50:50 beamsplitter is described by the transformation:

$$\psi(p_1, p'_1) \psi(p_2, p'_2) \rightarrow \psi\left(\frac{p_1 + p_2}{\sqrt{2}}, \frac{p'_1 + p'_2}{\sqrt{2}}\right) \psi\left(\frac{p_1 - p_2}{\sqrt{2}}, \frac{p'_1 - p'_2}{\sqrt{2}}\right). \quad (5.47)$$

Measuring mode 2 at $p_2 = 0$ leaves the other mode in the state

$$\rightarrow \psi\left(\frac{p_1}{\sqrt{2}}, \frac{p'_1}{\sqrt{2}}\right)^2. \quad (5.48)$$

Iterating this procedure M times results in the transformation

$$\psi(p, p') \rightarrow \psi\left(\frac{p}{\sqrt{2^M}}, \frac{p'}{\sqrt{2^M}}\right)^{2^M}. \quad (5.49)$$

The expectation values used to calculate the effective squeezing levels can be evaluated as:

$$\begin{aligned} \langle \hat{D}(\sqrt{2\pi}) \rangle &= \text{Tr} \left(\int dp \int dp' \psi(p, p') \hat{D}(\sqrt{2\pi}) |p\rangle \langle p'| \right) \\ &= \text{Tr} \left(\int dp \int dp' \psi(p, p') e^{-i2\sqrt{\pi}p} |p\rangle \langle p'| \right) \\ &= \int dp \psi(p, p) e^{-i2\sqrt{\pi}p}, \end{aligned} \quad (5.50)$$

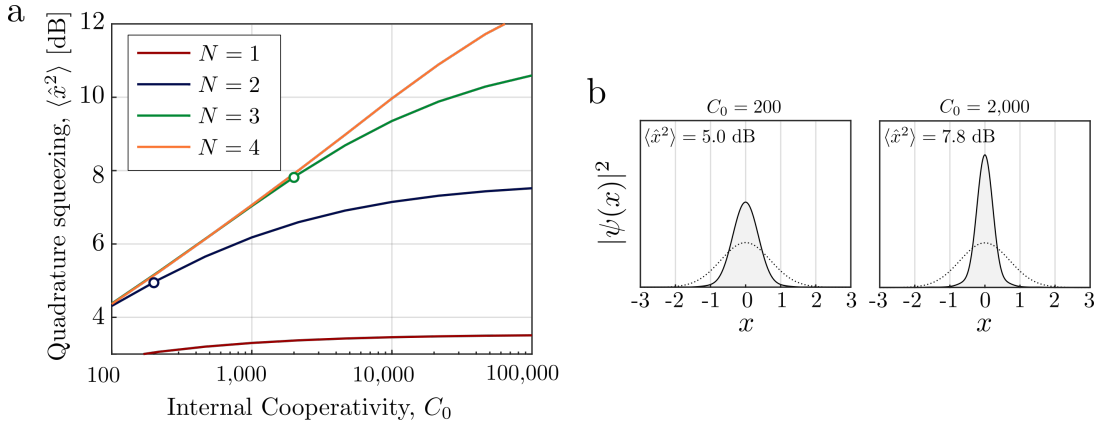


Figure 5.8: (a) Achievable amounts of quadrature squeezing using the protocol of Fig. 5.8 with input vacuum states and small displacement amplitudes. (b) Example quadrature distributions of the obtainable squeezed states generated with $C_0 = 200$ and $C_0 = 2000$ choosing $N = 2$ and $N = 3$ respectively, corresponding to the points marked with open circles in (a). The dotted line shows the quadrature distribution of the vacuum state for comparison.

and

$$\begin{aligned}
 \langle \hat{D}(i\sqrt{2\pi}) \rangle &= \text{Tr} \left(\int dp \int dp' \psi(p, p') \hat{D}(i\sqrt{2\pi}) |p\rangle \langle p'| \right) \\
 &= \text{Tr} \left(\int dp \int dp' \psi(p, p') |p + 2\sqrt{\pi}\rangle \langle p'| \right) \\
 &= \int dp \psi(p - 2\sqrt{\pi}, p).
 \end{aligned} \tag{5.51}$$

We thus compute the input cat state in the Fock-basis, then use Eq. (5.45) to calculate the mixed state wavefunction along the lines $(p\sqrt{2^M}, p\sqrt{2^M})$ and $((p - 2\sqrt{\pi})\sqrt{2^M}, p\sqrt{2^M})$ from which we obtain the expectation values to compute the effective squeezing levels using Eqs. (5.49)-(5.51).

5.12 S7: Generation of squeezed vacuum states

Here we show how to generate the required initial squeezed states, using the cavity QED system and coherent state inputs. The idea is that a squeezed state can be represented as a superposition of coherent states [35]:

$$\hat{S}(r)|\text{vac}\rangle \propto \int \exp\left(-\frac{\alpha^2}{e^{2r}-1}\right) \hat{D}(i\alpha)|\text{vac}\rangle d\alpha, \tag{5.52}$$

which holds for $r > 0$ and the integral is over real α . By creating a discrete superposition of closely spaced coherent states on a line in phase space, we can approximate Eq. (5.52) to achieve an approximate squeezed state. Indeed, quadrature squeezed states were observed in [64] using only two coherent states. We therefore propose to use the method of Fig. 5.1, but with a vacuum input and smaller displacement amplitudes chosen in the p direction. The resulting amount of quadrature squeezing is shown in Fig. 5.8a, where we have numerically tuned the

displacement amplitude to optimize the squeezing. As expected, as the intrinsic cooperativity of the cavity increases, we can achieve larger amounts of quadrature squeezing using a suitable number of interactions. Fig. 5.8b shows the resulting x quadrature distributions at a $C_0 = 200$ and $C_0 = 2000$ for $N = 2$ and $N = 3$ interactions, i.e. states composed of 4 and 8 coherent states on the $x = 0$ axis respectively, showing clear quadrature squeezing relative to the vacuum (dotted line).

While squeezed states can be generated directly from vacuum states using the cavity QED system, comparing the results of Figs. 5.8 and 5.3 the squeezing levels are lower than the approximate squeezing levels achievable using the same intrinsic cooperativity with the cat breeding method of Fig. 5.3. Thus for the cat breeding approach without an external squeezed vacuum source, the approximate squeezing levels will be limited to those presented in Fig. 5.8.

Chapter 6

Unsuitability of cubic phase gates for non-Clifford operations on Gottesman-Kitaev-Preskill states

In this chapter we present the paper “Unsuitability of cubic phase gates for non-Clifford operations on Gottesman-Kitaev-Preskill states” [32], authored by Jacob Hastrup, Mikkel V. Larsen, Jonas S. Neergaard-Nielsen, Nicolas C. Menicucci and Ulrik L. Andersen. This work is published in Physical Review A.

© 2021 American Physical Society.

6.1 Abstract

With the Gottesman-Kitaev-Preskill (GKP) encoding, Clifford gates and error correction can be carried out using simple Gaussian operations. Still, non-Clifford gates, required for universality, require non-Gaussian elements. In their original proposal, GKP suggested a particularly simple method of using a single application of the cubic phase gate to perform the logical non-Clifford T-gate. Here we show that this cubic phase gate approach performs extraordinarily poorly, even for arbitrarily large amounts of squeezing in the GKP state. Thus, contrary to common belief, the cubic phase gate is not suitable for achieving universal fault-tolerant quantum computation with GKP states.

6.2 Introduction

The Gottesman-Kitaev-Preskill (GKP) encoding of a qubit into a quantum harmonic oscillator [28] is a particularly promising approach towards fault-tolerant quantum computation. In particular, all Clifford operations, including error correction, can be implemented using only Gaussian operations along with a supply of ancillary GKP basis states. Furthermore, the GKP encoding scheme has been shown to outperform other bosonic codes against loss [53, 55], which is the dominant noise source in most bosonic systems. For these reasons, the GKP encoding has

gained much interest in recent years, both theoretically and experimentally, across multiple experimental platforms. Most prominently, the states have been generated in trapped-ion [43] and microwave cavity platforms [48]. Furthermore, in the optical regime, large 2-dimensional cluster states have been produced [74, 75], which enable scalable fault-tolerant measurement-based quantum computation when combined with high quality GKP states [72].

A critical step towards universality is the ability to perform non-Clifford operations on the encoded qubits. For GKP qubits, two different approaches for non-Clifford operations were proposed in the original paper [28]. The first approach is to use logical magic states, such as the encoded Hadamard eigenstate, to implement the non-Clifford T-gate via gate teleportation. Such magic states can be distilled using only the computational basis states and Gaussian operations [124], or they can be generated directly using non-Gaussian resources such as photon counting [28, 72, 89] or coupling to a two-level system [33, 48]. The second approach is to apply a single cubic phase gate in combination with Gaussian operations [28]. In principle, the cubic phase gate enables universal control of the oscillator [125], including any desired operations on the GKP state. However, a significant overhead, requiring many applications of the cubic phase gate, is typically required to approximate most non-Gaussian operations well with cubic phase gates. The promise that a single application would suffice to implement a logical non-Clifford operation therefore strongly motivates the development of cubic phase gates for applications with GKP states. GKP also showed that the cubic phase gate could be implemented using a cubic phase state and teleportation with Gaussian operations. Since the ideal cubic phase state is nonphysical, requiring infinite energy, this teleportation-based technique is always approximate. Still, even when using an ideal cubic phase gate the approach is only suitable for GKP states with an asymmetric noise distribution, as was pointed out by GKP in their original paper [28].

In this paper we analyse the details of the cubic phase gate approach and show explicitly that it performs surprisingly poorly, unless the GKP state is prepared with an unrealistic noise distribution. We consider only a perfect implementation of the cubic phase gate in order to discount any imperfections e.g. from finite energy cubic phase states. The results presented here thus represent a best-case scenario for the cubic phase gate approach. The poor performance is therefore solely due to the intrinsic and unavoidable noise present in the GKP states. We also compare the performance to that achieved using a GKP-encoded magic state via gate teleportation, demonstrating that the magic state offers a significantly better approach.

6.3 Preliminaries

We consider a bosonic mode of a quantum harmonic oscillator with position and momentum quadrature operators \hat{x} and \hat{p} satisfying $[\hat{x}, \hat{p}] = i$ with vacuum variance $\text{Var}(\hat{x}) = \text{Var}(\hat{p}) = 1/2$. A detailed review of GKP states and their error-correcting properties can be found elsewhere [28, 105, 126]. We focus on the approximate square GKP states consisting of a sum of equispaced position-squeezed states under a Gaussian envelope:

$$|0_L\rangle \propto \sum_{s \in \mathbb{Z}} e^{-\pi(2s)^2 \Delta_p^2 / 2} \int dx e^{-\frac{(x-2s\sqrt{\pi})^2}{2\Delta_x^2}} |x\rangle \quad (6.1)$$

$$|1_L\rangle \propto \sum_{s \in \mathbb{Z}} e^{-\pi(2s+1)^2 \Delta_p^2 / 2} \int dx e^{-\frac{(x-(2s+1)\sqrt{\pi})^2}{2\Delta_x^2}} |x\rangle, \quad (6.2)$$

where “ L ” denotes logical qubit states, Δ_x and Δ_p quantifies the amount of squeezing, or noise, in the x - and p -quadratures respectively, and $|x\rangle$ are the position eigenstates, i.e. $\hat{x}|x\rangle = x|x\rangle$. Note

that the squeezing is that of each of the peaks of the state, not the overall state, i.e. each peak in the x - and p -quadrature has a measured variance of $\Delta_x/2$ and $\Delta_p/2$ respectively. Hence, Δ_x and Δ_p can be arbitrarily low simultaneously [101]. Numerical values of the squeezing are often expressed in decibels (dB) as $-10 \log_{10}(\Delta^2)$. Importantly, a small amount of noise in p enforces a wide envelope in x and vice versa. In the limit of infinite squeezing, i.e. $(\Delta_x, \Delta_p) \rightarrow (0, 0)$, the position wave functions of the computational basis states approach Dirac combs with spacing $2\sqrt{\pi}$.

We now consider how to implement the non-Clifford T-gate, also known as the $\pi/8$ -gate,

$$\hat{T} = |0_L\rangle\langle 0_L| + e^{i\pi/4}|1_L\rangle\langle 1_L|, \quad (6.3)$$

which, when combined with the Clifford gate set, constitutes a universal gate set. GKP proposed to use a cubic phase gate in combination with shearing and displacement to implement the T-gate:

$$\hat{U}_T = \exp \left[i \frac{\pi}{4} \left\{ \underbrace{2 \left(\frac{\hat{x}}{\sqrt{\pi}} \right)^3}_{\text{cubic phase}} + \underbrace{\left(\frac{\hat{x}}{\sqrt{\pi}} \right)^2}_{\text{shear}} - \underbrace{2 \frac{\hat{x}}{\sqrt{\pi}}}_{\text{displacement}} \right\} \right]. \quad (6.4)$$

One can check that this gate applies a $\pi/4$ phase shift to peaks positioned at odd multiples of $\sqrt{\pi}$ since

$$2x^3 + x^2 - 2x \equiv \begin{cases} 0 \pmod{8} & \text{for even } x, \\ 1 \pmod{8} & \text{for odd } x. \end{cases} \quad (6.5)$$

For ideal GKP states with support only at integer multiples of $\sqrt{\pi}$, \hat{U}_T thus acts as a perfect T-gate. However, approximate GKP states also have support outside these grid points where \hat{U}_T does not exactly apply a 0 or $\pi/4$ phase shift. This is illustrated in Fig. 6.1a, showing the GKP wave function of $|+L\rangle = (|0_L\rangle + |1_L\rangle)/\sqrt{2}$, along with the polynomial in \hat{U}_T modulo 2π . Only for the peaks close to $x = 0$ is the phase shift approximately correct over the width of each peak. For peaks further from the origin, e.g. for $|x|/\sqrt{\pi} > 3$ in the case of Fig. 6.1a, there is a large phase variation across the peaks. The peaks far from the origin thus effectively experience a random phase shift. This results in an increased amount of noise in the p -quadrature, which is seen in Fig. 6.1b. Furthermore, the output state is highly asymmetric with a long tail at positive p . This is because \hat{U}_T can be interpreted as a momentum displacement with an x -dependent displacement magnitude scaling as x^2 . Peaks at large $|x|$ thus get displaced to large p -values.

How does this noise behave as we increase the amount of squeezing in the state? On one hand, as we decrease Δ_x the width of each peak decreases, thus decreasing the total phase variation across each peak. On the other hand, as we decrease Δ_p , peaks further from the origin appear due to the Fourier relation between \hat{x} and \hat{p} . These new peaks now experience a larger phase variation as seen in Fig. 6.1a. It turns out that for $\Delta_x = \Delta_p$, new peaks appear at a rate comparable to the rate at which they narrow, such that the gate fidelity does *not* converge to 1 when increasing the squeezing. This is qualitatively illustrated in Fig. 6.1c, showing the momentum probability density summed over values of p modulo $2\sqrt{\pi}$. Even as the squeezing approaches very large values, the probability density retains a non-zero noise floor with significant support outside integer multiples of $\sqrt{\pi}$.

This poor noise distribution was pointed out in the original paper by GKP [28], stating that one needs to ensure that $\Delta_x \ll \Delta_p$ in order to use \hat{U}_T as a logical T-gate. However, this condition is highly impractical to maintain. For example, the logical Hadamard gate, which is implemented by a $\pi/2$ phase rotation, $\hat{U}_H = \exp(i\pi/4(\hat{x}^2 + \hat{p}^2))$, also swaps the noise of the

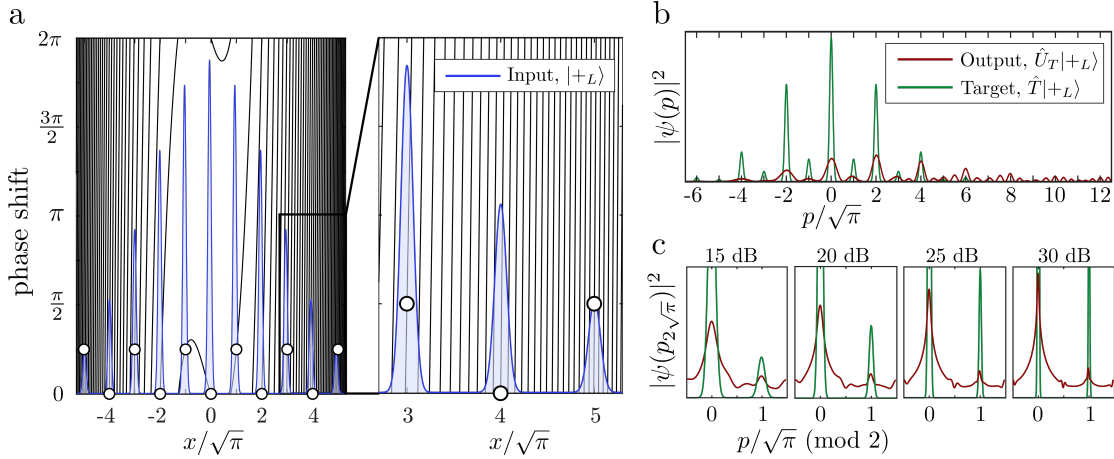


Figure 6.1: (a): Position (x) probability density (blue) of $|+L\rangle = (|0_L\rangle + |1_L\rangle)/\sqrt{2}$ with $\Delta_x = \Delta_p = 15$ dB. Also plotted in black is the phase shift imposed by the operator \hat{U}_T (Eq. (6.4)). The white circles show the value of the phase shift at integer multiples of $\sqrt{\pi}$. The right window is a zoom in on the peaks further from the origin. These peaks experience a large phase variation across their width, greatly limiting the performance of \hat{U}_T as a T-gate. (b): Momentum (p) probability density of $\hat{U}_T|+L\rangle$ compared to the target state $\hat{T}|+L\rangle = (|0_L\rangle + e^{i\pi/4}|1_L\rangle)/\sqrt{2}$. (c): Momentum probability densities summed over values of $p \bmod 2\sqrt{\pi}$, i.e. $|\psi(p_{2\sqrt{\pi}})|^2 = \sum_s |\psi(p + 2s\sqrt{\pi})|^2$ for 15-30 dB squeezing, for $\hat{U}_T|+L\rangle$ and $\hat{T}|+L\rangle$. The ratio of the heights of the $\hat{T}|+L\rangle$ peaks remain constant as the squeezing is increased.

x - and p -quadratures, i.e. swapping $\Delta_x \leftrightarrow \Delta_p$. Additionally, since we want low noise in both quadratures, i.e. both $\Delta_x \ll 1$ and $\Delta_p \ll 1$, the condition $\Delta_x \ll \Delta_p$ requires an extremely low value of Δ_x , which will be difficult, if not impossible, to produce and maintain experimentally. In the following we quantify the above considerations numerically and analytically.

6.4 Error-corrected fidelity

One could try to perform GKP error correction to correct the noise generated by \hat{U}_T . Here we consider the best-case scenario of perfect error correction i.e. using ideal GKP ancillas with infinite squeezing in order to discount any imperfections in the error correction protocol. Such perfect error correction corresponds to a measurement-dependent displacement followed by a projection of the state into the ideal 2-dimensional GKP subspace [124]. The output state is thus described by a qubit which depends on the input state and the syndrome measurement outcome. Averaging the output states over all syndrome outcomes, we generally obtain a mixed state described by a qubit density matrix ρ . Fig. 6.2a shows the position of $\hat{U}_T|+L\rangle$ on the Bloch sphere after error correction for various squeezing levels. For decreasing $\Delta_x = \Delta_p$ the state converges to a point well-inside the Bloch sphere, and not to the target state $|T\rangle = (|0\rangle + e^{i\pi/4}|1\rangle)/\sqrt{2}$. The situation is improved by considering an asymmetric noise distribution, e.g. when $\Delta_p = 5\Delta_x$ (corresponding to 14dB less squeezing in the p -quadrature), as expected. Fig. 6.2b shows the qubit fidelity after error correction, $F = \langle \psi | \hat{T}^\dagger \rho \hat{T} | \psi \rangle$, to the target state $\hat{T}|\psi\rangle$, averaged over four states forming a regular tetrahedron in the Bloch sphere [127]. For $\Delta_x = \Delta_p$ we find that the fidelity is lower for \hat{U}_T compared to doing nothing, i.e. applying the identity gate, \hat{I} , for

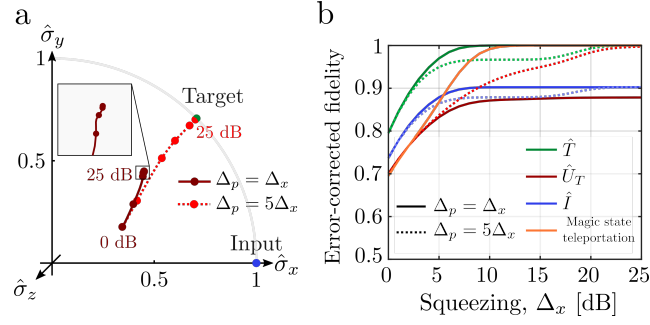
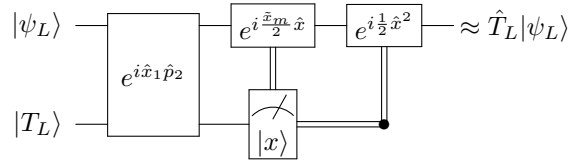


Figure 6.2: (a): x - y plane of the Bloch sphere with the average qubit output of the GKP error correction scheme with $\hat{U}_T|+L\rangle$ as input. Each dot corresponds to a step of 5 dB in the squeezing level of the x -quadrature. (b): Average fidelity [127] with the target qubit state, for the qubit with density matrix, ρ , of the GKP error corrected qubits obtained after application of \hat{U}_T , the identity gate \hat{I} and an ideal logical T-gate, calculated for both $\Delta_p = \Delta_x$ (solid) and $\Delta_p = 5\Delta_x$ (dotted) in the input state, as well as the fidelity obtained by the magic state approach with gate teleportation [28].

all squeezing levels. Thus for symmetric noise, \hat{U}_T is a worse T-gate than the identity gate! Again the situation is improved by asymmetric noise, but the fidelity increases slowly with Δ_x compared to an ideal T-gate.

For comparison we also plot the fidelity obtained when using GKP-encoded magic states to teleport the T-gate, as proposed in [28] using the following circuit:



where $|\psi_L\rangle$ denotes an arbitrary GKP encoded input state. The squeezing level of the magic state ancilla, $|T_L\rangle = (|0_L\rangle + e^{i\pi/4}|1_L\rangle)/\sqrt{2}$, is set equal to that of the input states. The feed-forward displacement, $\exp[i(\tilde{x}_m/2)\hat{x}]$, where $\tilde{x}_m = x_m - \sqrt{\pi}[x_m/\sqrt{\pi}]$ is the remainder of the measurement result modulus $\sqrt{\pi}$, centers the output wavefunction on the GKP lattice. The feed-forward shear, $\exp[i(1/2)\hat{x}^2]$, performs a corrective logical phase gate on the output, conditioned on a logical 1 measurement of the ancilla [28]. The finite squeezing of the ancilla and the phase distortion of the shear gate result in a performance which is worse than the ideal T-gate, but the approach is significantly better than the cubic phase gate approach.

6.5 Modular bosonic subsystem fidelity

An alternative framework for reducing a bosonic state to a 2-dimensional GKP qubit was recently proposed by Pantaleoni et al. [128]. The idea is to decompose an arbitrary bosonic state, $|\Psi\rangle$, into a qubit part and a continuous part, i.e.

$$|\Psi\rangle = |0\rangle \otimes |\psi_0\rangle + |1\rangle \otimes |\psi_1\rangle. \quad (6.6)$$

The decomposition is done by binning the wave function around even and odd multiples of $\sqrt{\pi}$ and stitching the bins together to form two new wave functions $|\psi_0\rangle$ and $|\psi_1\rangle$, as illustrated in

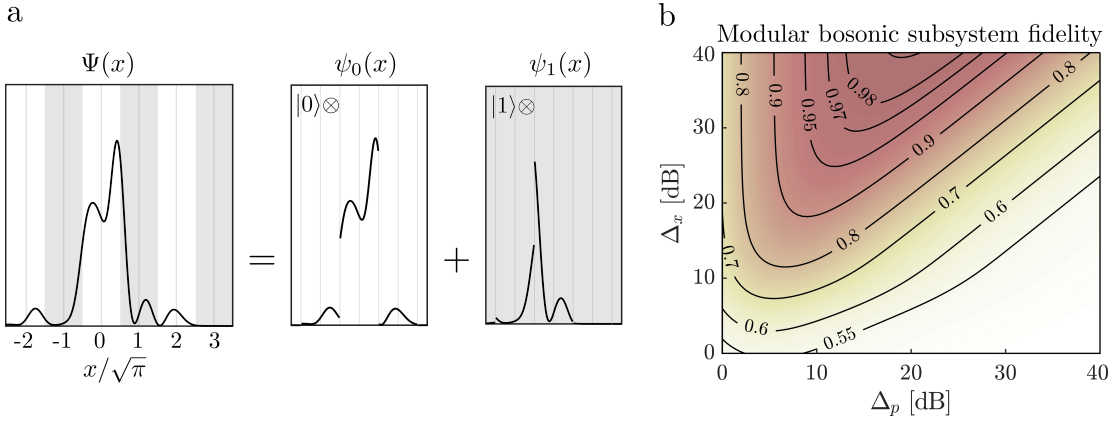


Figure 6.3: (a): Illustration of the modular bosonic subsystem decomposition technique [128] for a random wave function, $\Psi(x)$. The position wave function is decomposed by binning it around even and odd multiples of $\sqrt{\pi}$ and stitching the bins together to form two new wave functions, ψ_0 and ψ_1 . (b): Fidelity with the target qubit state, $(|0\rangle + e^{i\pi/4}|1\rangle)/\sqrt{2}$ of the qubit part of the input state $\hat{U}_T|+_L\rangle$, after tracing out the continuous parts with the modular bosonic subsystem decomposition technique for different values of Δ_x and Δ_p .

Fig. 6.3a. Tracing out the continuous part we are left with a qubit state which contains the logical information of the state. Further details on this technique can be found in the supplementary material and in Ref. [128]. Using this method we can again analyse the fidelity of $\hat{U}_T|+_L\rangle$ with the target state in the qubit subspace, thus providing a complementary figure of merit. The result is shown in Fig. 6.3b. Again we observe that in order to obtain a high fidelity, we need an excess amount of squeezing in the x -quadrature. For example, to achieve a fidelity of 0.95, we require $\Delta_x > 25$ dB, which is significantly more than the squeezing thresholds set for fault-tolerance using magic states to implement a T-gate [72, 129–131]. For $\Delta_x = \Delta_p$ we again observe a convergence in the fidelity below 1. In fact, in the limit of infinite squeezing, $(\Delta_x, \Delta_p) \rightarrow (0, 0)$, one can derive the following analytical result (see supplementary information):

$$F = \frac{1}{2} + \frac{1}{2} \frac{1}{\sqrt{1 + \left(\frac{3\Delta_x}{2\Delta_p}\right)^2}}. \quad (6.7)$$

Thus the fidelity is bounded, confirming the poor performance even in the limit of infinite squeezing. In particular, for the realistic case of $\Delta_x = \Delta_p$ we get $F = 1/2 + 1/\sqrt{13} \approx 0.78 < 1$. To obtain a higher fidelity we require $\Delta_x \ll \Delta_p$ in which case Eq. (6.7) reduces to

$$F \approx 1 - \left(\frac{3}{4} \frac{\Delta_x}{\Delta_p}\right)^2, \quad \text{for } \Delta_x \ll \Delta_p, \quad (6.8)$$

which goes to 1 in the limit $\Delta_x/\Delta_p \rightarrow 0$, as expected. Again, such unbalanced noise ratio is not realistic to maintain during a calculation since the logical Hadamard gate (i.e. a Fourier transformation) swaps the noise between the quadratures.

6.6 Conclusion

We have analysed the performance of the GKP T-gate implemented via the cubic phase gate. All calculations were performed assuming a perfect cubic phase gate, and thus represents a best-case scenario compared to approximate implementations using cubic phase states. In the case of square GKP states with equal squeezing in the position and momentum quadrature we have explicitly shown that the noise generated by the T-gate is detrimental, *for all squeezing levels*. The poor performance is solely due to the noise inherent in all physical GKP states, and cannot be circumvented through error correction. It can in principle be mitigated by using highly asymmetrical GKP states, but this strategy is not compatible with other manipulations of the state, such as the logical Hadamard gate (i.e. a Fourier transform), which swaps the noise of the position and momentum quadratures. Although we have focused our analysis on square GKP states, it is clear that other GKP grids, e.g. hexagonal GKP states, will suffer from the same issues. That is, the rapid variation of the phase applied by the cubic phase gate with respect to x will eventually cause detrimental issues at large $|x|$ for any grid. In fact, one can generalise this to any operator consisting of a finite polynomial in \hat{x} , as the derivative of any finite polynomial is unbounded. Instead, the T-gate should be implemented using GKP-encoded magic states, and efforts towards optical GKP-based quantum computation should be focused on the generation of GKP states and not on the development of cubic phase gates or cubic phase states.

6.7 Supplementary Material

Here we derive Eq. (6.7) from the main text. As explained in the main text, the main idea behind the modular bosonic subsystem decomposition technique [128] is to divide the continuous Hilbert space of the bosonic mode into a 2-dimensional part, describing the logical content of the GKP qubit, and a continuous part. Tracing out the continuous part leaves us with a mixed qubit state, which can be analysed e.g. in terms of fidelity to a target qubit. The decomposition is done by binning the x -quadrature wave function into bins around even and odd multiples of $\sqrt{\pi}$, as illustrated in Fig. 6.3a. An arbitrary pure state can thus be written as:

$$|\Psi\rangle = |0\rangle \otimes |\psi_0\rangle + |1\rangle \otimes |\psi_1\rangle \quad (6.9)$$

where

$$|\psi_0\rangle = \sum_{s \in \mathbb{Z}} \int_{(2s-1/2)\sqrt{\pi}}^{(2s+1/2)\sqrt{\pi}} dx \Psi(x)|x\rangle \quad (6.10a)$$

$$|\psi_1\rangle = \sum_{s \in \mathbb{Z}} \int_{(2s-1/2)\sqrt{\pi}}^{(2s+1/2)\sqrt{\pi}} dx \Psi(x - \sqrt{\pi})|x\rangle \quad (6.10b)$$

with $\Psi(x) = \langle \Psi|x\rangle$ and \mathbb{Z} denoting the integers. Note that the states $|\psi_0\rangle$ and $|\psi_1\rangle$ are not individually normalized but satisfy $\langle \psi_0|\psi_0\rangle + \langle \psi_1|\psi_1\rangle = \langle \Psi|\Psi\rangle = 1$. Tracing out the continuous mode leaves a qubit with density matrix

$$\rho = \begin{pmatrix} \langle \psi_0|\psi_0\rangle & \langle \psi_1|\psi_0\rangle \\ \langle \psi_0|\psi_1\rangle & \langle \psi_1|\psi_1\rangle \end{pmatrix}. \quad (6.11)$$

The fidelity to the target state $\hat{T}|+\rangle = (|0\rangle + e^{i\pi/4}|1\rangle)\sqrt{2}$ is given by

$$F = \langle +|\hat{T}^\dagger \rho \hat{T}|+\rangle = \frac{1}{2} + \text{Re} \left(e^{i\pi/4} \langle \psi_1|\psi_0\rangle \right). \quad (6.12)$$

We now calculate $\langle \psi_1 | \psi_0 \rangle$ for $|\Psi\rangle = \hat{U}_T |_{+L}\rangle$. The normalized wave function of the approximate GKP state $|_{+L}\rangle = (|0_L\rangle + |1_L\rangle)/\sqrt{2}$ for small Δ_x and Δ_p is given by [28]

$$\Psi_{|_{+L}\rangle}(x) = \frac{1}{\pi^{1/4}} \sqrt{\frac{\Delta_p}{\Delta_x}} \sum_s \exp\left(-\frac{(\sqrt{\pi}s)^2}{2} \Delta_p^2\right) \exp\left(-\frac{(x - \sqrt{\pi}s)^2}{2\Delta_x^2}\right). \quad (6.13)$$

Multiplying \hat{U}_T we get:

$$\begin{aligned} \Psi_{\hat{U}_T|_{+L}\rangle}(x) = \\ \frac{1}{\pi^{1/4}} \sqrt{\frac{\Delta_p}{\Delta_x}} \sum_s \exp\left[i\frac{\pi}{4} \left\{ 2\left(\frac{x}{\sqrt{\pi}}\right)^3 + \left(\frac{x}{\sqrt{\pi}}\right)^2 - 2\frac{x}{\sqrt{\pi}} \right\} - \frac{(\sqrt{\pi}s)^2}{2} \Delta_p^2 - \frac{(x - \sqrt{\pi}s)^2}{2\Delta_x^2}\right]. \end{aligned} \quad (6.14)$$

Using Eqs. (6.10) we can now calculate the overlap $\langle \psi_1 | \psi_0 \rangle$, assuming negligible overlap between neighbouring peaks in the GKP wave function, which is valid when $\Delta_x^2 \ll 1$:

$$\begin{aligned} \langle \psi_1 | \psi_0 \rangle = \frac{1}{\sqrt{\pi}} \frac{\Delta_p}{\Delta_x} \sum_s \left(\exp\left[-\frac{(2s\sqrt{\pi})^2}{2} \Delta_p^2\right] \exp\left[-\frac{((2s+1)\sqrt{\pi})^2}{2} \Delta_p^2\right] \right. \\ \left. \times \int_{(2s-\frac{1}{2})\sqrt{\pi}}^{(2s+\frac{1}{2})\sqrt{\pi}} dx \exp\left[-i\frac{\pi}{4} \left(6\frac{x^2}{\pi} + 8\frac{x}{\sqrt{\pi}} + 1\right)\right] \exp\left[-\frac{(x - 2s\sqrt{\pi})^2}{\Delta_x^2}\right] \right). \end{aligned} \quad (6.15)$$

For $\Delta_x^2 \ll 1$ we can expand the limits of the integrals to $\pm\infty$ and evaluate using the formula for Gaussian integrals,

$$\int_{-\infty}^{\infty} dx e^{-ax^2+bx+c} = \sqrt{\frac{\pi}{a}} e^{c+\frac{b^2}{4a}}, \quad (6.16)$$

where from Eq. (6.15) we identify

$$a = \frac{1}{\Delta_x^2} + i\frac{3}{2}, \quad b = \frac{4s\sqrt{\pi}}{\Delta_x^2} - i2\sqrt{\pi}, \quad \text{and} \quad c = -\frac{4s^2\pi}{\Delta_x^2} - i\frac{\pi}{4}. \quad (6.17)$$

Inserting and rewriting:

$$\begin{aligned} \langle \psi_1 | \psi_0 \rangle = \frac{\Delta_p}{\Delta_x \sqrt{\frac{1}{\Delta_x^2} + i\frac{3}{2}}} \sum_s \left\{ \exp\left[-4\pi \left(\frac{1}{\Delta_x^2} - \frac{1}{\Delta_x^2(1 + \frac{9}{4}\Delta_x^4)} + \Delta_p^2\right) s^2 \right. \right. \\ \left. \left. - 2\pi \left(\Delta_p^2 + \frac{3\Delta_x^2}{1 + \frac{9}{4}\Delta_x^4}\right) s - \pi \left(\frac{\Delta_x^2}{1 + \frac{9}{4}\Delta_x^4} + \frac{1}{2}\Delta_p^2\right)\right] \right. \\ \left. \times \exp\left[-i\pi \left(\frac{1}{1 + \frac{9}{4}\Delta_x^4} \left(6s^2 + 4s - \frac{3}{2}\Delta_x^4\right) + \frac{1}{4}\right)\right] \right\}. \end{aligned} \quad (6.18)$$

Now consider the term in the exponential of the last factor. For small $|s|$ we have $(6s^2 + 4s - (3/2)\Delta_x^4)/(1 + (9/4)\Delta_x^4) \equiv 0 \pmod{2}$ and thus the last factor reduces to $\exp[-i\pi/4]$. If $\Delta_x^4 \ll \Delta_p^2$ this holds for all non-vanishing terms in the sum. For $\Delta_x^2, \Delta_p^2 \ll 1$ the terms in the sum then change slowly with s , and we can approximate the sum with an integral:

$$\begin{aligned}
\langle \psi_1 | \psi_0 \rangle = & \\
& \frac{\Delta_p e^{-i\frac{\pi}{4}}}{\Delta_x \sqrt{\frac{1}{\Delta_x^2} + i\frac{3}{2}}} \int ds \exp \left[-4\pi \left(\frac{1}{\Delta_x^2} - \frac{1}{\Delta_x^2 (1 + \frac{9}{4}\Delta_x^4)} + \Delta_p^2 \right) s^2 \right. \\
& \left. - 2\pi \left(\Delta_p^2 + \frac{3\Delta_x^2}{1 + \frac{9}{4}\Delta_x^4} \right) s - \pi \left(\frac{\Delta_x^2}{1 + \frac{9}{4}\Delta_x^4} + \frac{1}{2}\Delta_p^2 \right) \right]. \tag{6.19}
\end{aligned}$$

The integral can again be evaluated using Eq. (6.16) with

$$\begin{aligned}
a &= 4\pi \left(\frac{1}{\Delta_x^2} - \frac{1}{\Delta_x^2 (1 + \frac{9}{4}\Delta_x^4)} + \Delta_p^2 \right), & b &= -2\pi \left(\Delta_p^2 + \frac{3\Delta_x^2}{1 + \frac{9}{4}\Delta_x^4} \right) \\
\text{and } c &= -\pi \left(\frac{\Delta_x^2}{1 + \frac{9}{4}\Delta_x^4} + \frac{1}{2}\Delta_p^2 \right). \tag{6.20}
\end{aligned}$$

Before inserting, we consider the limit of small Δ_x and Δ_p in which we get

$$a \rightarrow \pi(9\Delta_x^2 + 4\Delta_p^2), \tag{6.21}$$

$$b \rightarrow \pi(6\Delta_x^2 + 2\Delta_p^2), \tag{6.22}$$

$$c \rightarrow \pi(\Delta_x^2 + \frac{1}{2}\Delta_p^2), \tag{6.23}$$

$$e^{\frac{b^2}{4a}} \rightarrow 1, \tag{6.24}$$

$$e^c \rightarrow 1. \tag{6.25}$$

Evaluating the integral we thus get:

$$\langle \psi_1 | \psi_0 \rangle = e^{-i\frac{\pi}{4}} \frac{\Delta_p}{\sqrt{9\Delta_x^2 + 4\Delta_p^2} \sqrt{1 + i\frac{3}{2}\Delta_x^2}} \xrightarrow{\Delta_x \rightarrow 0} e^{-i\frac{\pi}{4}} \frac{\Delta_p}{\sqrt{9\Delta_x^2 + 4\Delta_p^2}}. \tag{6.26}$$

Inserting in Eq. (6.12):

$$F = \frac{1}{2} + \frac{\Delta_p}{\sqrt{9\Delta_x^2 + 4\Delta_p^2}} = \frac{1}{2} + \frac{1}{2} \frac{1}{\sqrt{1 + \left(\frac{3\Delta_x}{2\Delta_p}\right)^2}}. \tag{6.27}$$

Chapter 7

Measurement-free preparation of grid states

In this chapter we present the paper “Measurement-free preparation of grid states” [33], authored by Jacob Hastrup, Kimin Park, Jonatan B. Brask, Radim Filip and Ulrik L. Andersen. This work is published in npj Quantum Information.

7.1 Abstract

Quantum computing potentially offers exponential speed-ups over classical computing for certain tasks. A central, outstanding challenge to making quantum computing practical is to achieve fault tolerance, meaning that computations of any length or size can be realised in the presence of noise. The Gottesman-Kitaev-Preskill code is a promising approach towards fault-tolerant quantum computing, encoding logical qubits into grid states of harmonic oscillators. However, for the code to be fault tolerant, the quality of the grid states has to be extremely high. Approximate grid states have recently been realized experimentally, but their quality is still insufficient for fault tolerance. Current implementable protocols for generating grid states rely on measurements of ancillary qubits combined with either postselection or feed forward. Implementing such measurements take up significant time during which the states decohere, thus limiting their quality. Here we propose a measurement-free preparation protocol which deterministically prepares arbitrary logical grid states with a rectangular or hexagonal lattice. The protocol can be readily implemented in trapped-ion or superconducting-circuit platforms to generate high-quality grid states using only a few interactions, even with the noise levels found in current systems.

7.2 Introduction

Quantum computing offers exponential speeds-ups in solving certain computational problems, with wide-ranging consequences for information processing, information security, fundamental physics and chemistry and more. Impressive progress has been achieved towards realising quantum computing, including recent experimental demonstration of a quantum advantage over classical computation [14]. However, real devices are subject to noise and imperfections. As computations grow in size and complexity, errors accumulate and eventually destroy any quantum

advantage unless mitigated. Achieving fault tolerance, where errors are corrected sufficiently fast to allow scalable computation, is a central challenge to making universal quantum computing practical.

Quantum error correction (QEC) enables large-scale quantum computing in the presence of noise by redundantly encoding logical qubits into a larger Hilbert space. In traditional, discrete-variable QEC many physical qubits make up a single logical qubit. However, in 2001 Gottesman, Kitaev and Preskill (GKP) proposed encoding a logical qubit into the infinite-dimensional Hilbert space spanned by the continuous variables of a single bosonic mode [28]. With this encoding, small displacement errors of the bosonic mode can be detected and corrected using only simple Gaussian operations. Furthermore, recent results have shown that the GKP code also performs very well against boson loss [55], in many cases outperforming other bosonic codes designed specifically against loss such as cat codes [26, 65] and binomial codes [62, 82]. In fact, numerical optimization suggests that the hexagonal GKP code might be the optimal loss-resistant code among all bosonic codes [53]. Additionally, GKP codes have recently been shown to have applications within continuous-variable QEC [132] and quantum metrology [101].

An ideal GKP code is embedded in an idealized grid state which forms a lattice structure, consisting of an infinite superposition of position eigenstates. Such states require infinite energy and are hence unphysical. Importantly, however, it is possible to use approximate grid states with finite energy, composed of finitely squeezed states to achieve fault tolerance by concatenating the GKP code with discrete-variable error-correcting codes, provided that the grid states are sufficiently quadrature squeezed. In 2014, a conservative threshold for fault tolerance of 20.5 dB squeezing was derived for a measurement-based quantum computing approach [72]. Later this threshold was significantly reduced to less than 10 dB squeezing by exploiting the analog information contained in the syndrome measurements [129, 133]. Other approaches such as concatenating the GKP code with the surface code [131], the toric code [134, 135] and Knill's C_4/C_6 code [136] have recently been proposed. For any of these proposals the squeezing threshold will depend not only on the involved codes, but also on the type and magnitude of the noise and experimental errors of the given system. It is therefore crucial to test the feasibility of these approaches with high-quality grid states experimentally. Additionally, as with any quantum error-correcting code, one would ideally use grid states with squeezing levels well above the threshold to avoid impractical resource overheads associated with the repeated concatenation of the codes.

The preparation of grid states have, however, proven to be highly challenging. Recently, such states were prepared for the first time in ground-breaking experiments in the motional state of a trapped ion [43] and in a microwave cavity field coupled to a superconducting circuit [48]. The states realised in these experiments clearly exhibit the required grid structure in phase space. However, the quality of the states needs to be improved for implementation with fault tolerant schemes. The main experimental limitation is that during the preparation protocol, the states accumulate noise e.g. from boson dephasing and losses, rendering the produced grid states noisy. To minimize this noise one has to increase the speed of the preparation protocol. The state-preparation protocols currently implemented in experiment use oscillator-qubit couplings and rely on repeated measurements of the ancilla qubit. These measurements and their associated processing times constitute about half of the total preparation time. Therefore, to improve the quality of the GKP codes, it is crucial to replace the slow measurement-based approach with a faster approach.

It has previously been theoretically and experimentally established that arbitrary bosonic states can be deterministically prepared using a qubit coupling via the Jaynes Cummings Hamiltonian

[137–140]. These methods build up the state in the Fock basis and require a number of steps proportional to the number of Fock states supporting the target state. However, since noise such as qubit dephasing and boson loss is built up during each step [140], such methods are ineffective for preparing large useful grid states, which require support on at least 25-100 photons to achieve 10-16 dB of effective squeezing.

In this work, we present a measurement-free grid-state preparation protocol, which is significantly faster than known methods, without introducing additional resources. The key interaction of our protocol is the Rabi interaction Hamiltonian between an oscillator and a two-level system [141, 142], which can be effectively simulated in trapped-ion and microwave systems. This interaction is also used in the experiments of Refs. [43, 48]. Such interactions were recently shown to enable deterministic, non-Gaussian operations by using many weak interactions [143, 144]. Here, we instead use only a few, but stronger interactions, to generate the highly non-Gaussian grid states. Our work thus provides further demonstration of Rabi interactions as a powerful and versatile non-Gaussian resource in trapped ion and superconducting circuit platforms.

The speed-up obtained with our approach is large enough to prepare grid states with more than 10 dB of effective squeezing in practical systems that are readily available in both trapped-ion and microwave cavity platforms. Compared to current experiments this is an improvement of 3 to 6 dB under the same amounts of physical noise. With a further reduction of noise levels in future experiments, our protocol enables the generation of grid states with squeezing levels well above the fault-tolerance threshold levels, thus facilitating scalable quantum computing.

7.3 Results

Preliminaries

In this section we review the basic structure of grid states and the figures of merit used in this article. For a more extensive review, see e.g. Ref. [105].

Bosonic modes of harmonic oscillators are associated with the creation and annihilation operators \hat{a} and \hat{a}^\dagger and the corresponding dimensionless quadrature operators $\hat{X} = \frac{1}{\sqrt{2}}(\hat{a} + \hat{a}^\dagger)$ and $\hat{P} = \frac{1}{\sqrt{2}i}(\hat{a} - \hat{a}^\dagger)$ satisfying $[\hat{X}, \hat{P}] = i$. The 2-dimensional code space of the GKP-code is defined in the common +1 eigenspace of the stabilizer operators

$$\hat{S}_z = \hat{D}(\alpha) \quad \text{and} \quad \hat{S}_x = \hat{D}(\beta). \quad (7.1)$$

Here $\hat{D}(x) = e^{x\hat{a}^\dagger - x^*\hat{a}} = e^{i\sqrt{2}(-\text{Re}(x)\hat{P} + \text{Im}(x)\hat{X})}$ is the displacement operator with displacement amplitude x , satisfying the commutation relation

$$[\hat{D}(\alpha), \hat{D}(\beta)] = 2i \sin(\text{Im}(\alpha\beta^*))\hat{D}(\alpha + \beta). \quad (7.2)$$

By choosing $\text{Im}(\alpha\beta^*) = 2\pi$ we ensure that the stabilizers commute, which enables the existence of simultaneous eigenstates. Furthermore we can define logical operators

$$\hat{Z}_L = \hat{D}\left(\frac{\alpha}{2}\right), \quad \hat{X}_L = \hat{D}\left(\frac{\beta}{2}\right), \quad \text{and} \quad \hat{Y}_L = \hat{D}\left(\frac{\alpha + \beta}{2}\right), \quad (7.3)$$

which commute with the stabilizers and anti-commute with each other. The logical GKP qubit states, $|0\rangle_{\text{GKP}}$ and $|1\rangle_{\text{GKP}}$, are then defined as the ± 1 eigenstates of \hat{Z}_L . These satisfy the expected logic $\hat{X}_L|0\rangle_{\text{GKP}} = |1\rangle_{\text{GKP}}$ and $\hat{X}_L|1\rangle_{\text{GKP}} = |0\rangle_{\text{GKP}}$.

The relative directions and magnitude of α and β determine the lattice of the corresponding grid states. For example, rectangular grid states are generated by $\alpha = i2\pi/\beta^*$. Further choosing $\beta = \sqrt{2\pi}$ yields the square grid states for which the code space is symmetric with respect to X and P . Alternatively, choosing $\alpha = i\sqrt{\frac{4}{\sqrt{3}}}\pi$ and $\beta = e^{-i\frac{\pi}{3}}\alpha$ yields the hexagonal grid states. In the following we will consider only the square grid, returning to the case of rectangular and hexagonal grids in Section 7.3. The (unnormalizable) ideal square grid states can be written as:

$$\begin{aligned} |0\rangle_{\text{GKP}} &= \sum_{s \in \mathbb{Z}} \hat{D}(s\sqrt{2\pi}) |X=0\rangle \\ |1\rangle_{\text{GKP}} &= \sum_{s \in \mathbb{Z}} \hat{D}\left(\left(s + \frac{1}{2}\right)\sqrt{2\pi}\right) |X=0\rangle \end{aligned} \quad (7.4)$$

where $|X=0\rangle$ denotes the eigenstate of \hat{X} with eigenvalue 0 and \mathbb{Z} denotes the set of integers. The ideal grid states are thus infinite superpositions of equidistant position eigenstates and their Wigner functions are an infinite grid of 2-dimensional delta-functions (see Fig. 7.2(b)). Ideal grid states can be approximated by finite-energy states in several ways. The most commonly used representation for deriving fault tolerance thresholds is a superposition of finitely squeezed states of width e^{-r} under a Gaussian envelope of width κ^{-1} :

$$\begin{aligned} |\tilde{0}\rangle_{\text{GKP}} &\propto \sum_{s \in \mathbb{Z}} e^{-\frac{(2\sqrt{\pi}s)^2}{2\kappa^{-2}}} \hat{D}(s\sqrt{2\pi}) \hat{S}_r |\text{vac}\rangle \\ |\tilde{1}\rangle_{\text{GKP}} &\propto \sum_{s \in \mathbb{Z}} e^{-\frac{(2\sqrt{\pi}(s+\frac{1}{2}))^2}{2\kappa^{-2}}} \hat{D}\left(\left(s + \frac{1}{2}\right)\sqrt{2\pi}\right) \hat{S}_r |\text{vac}\rangle, \end{aligned} \quad (7.5)$$

where $\hat{S}_r = e^{-\frac{1}{2}r(\hat{a}^2 - \hat{a}^{\dagger 2})}$ is the squeezing operator (not to be confused with the stabilizers \hat{S}_x and \hat{S}_z). The squeezing parameter r and envelope κ characterises the quality of the states in the X - and P -quadratures respectively and in the limit $(e^{-r}, \kappa) \rightarrow (0, 0)$ the approximate states converge to the exact states of equation (7.4). For $\kappa = e^{-r}$ the states can correct noise equally well in X and P .

However, physical grid states will never exactly be of the form given in equation (7.5). First, physical states are not pure and are generally described by a density matrix $\hat{\rho}$. Secondly, the exact Gaussian envelope can be difficult to obtain and most preparation protocols yield a finite sum of squeezed states. Therefore, the parameters r and κ are not well-defined for practically realizable states. Instead, more generic figures of merit, the *effective squeezing parameters*, have been suggested in Ref. [101]. They quantify the effective degree of squeezing in each quadrature of the peaks constituting the grid state and are defined as:

$$\Delta_X = \sqrt{\frac{1}{2\pi} \ln \left(\frac{1}{|\langle \hat{D}(i\sqrt{2\pi}) \rangle|^2} \right)} \quad (7.6)$$

$$\Delta_P = \sqrt{\frac{1}{2\pi} \ln \left(\frac{1}{|\langle \hat{D}(\sqrt{2\pi}) \rangle|^2} \right)}, \quad (7.7)$$

where the effective squeezing levels in units of dB are given by $\Delta_{\text{dB}} = -10 \log_{10}(\Delta^2)$. The expectation values in these definitions are exactly the expectation values of the stabilizers \hat{S}_z and \hat{S}_x for square GKP states. High quality grid states should therefore have $|\langle \hat{S}_{z/x} \rangle| \approx 1$,

in which case $\Delta_{X/P} \rightarrow \infty$ dB. These definitions also have the nice property that for squeezed states they reproduce the squeezing parameter, i.e. $\Delta_X(\hat{S}_r|\text{vac}) = e^{-r}$ and $\Delta_P(\hat{S}_r|\text{vac}) = e^r$. Furthermore, for approximate square lattice grid states of Eq. (7.5) we extract the parameters $\Delta_X(|\tilde{0}\rangle_{\text{GKP}}) = e^{-r}$ and $\Delta_P(|\tilde{0}\rangle_{\text{GKP}}) \approx \kappa$. The last approximation is very accurate for $e^{-r}, \kappa > 10$ dB. Thus, if the state resembles a grid state consisting of a grid of squeezed peaks in phase-space, the effective squeezing parameters approximately quantify the squeezing of these peaks in each quadrature direction.

However, it is important to note that the effective squeezing is not directly related to the fault-tolerance thresholds. Most GKP-based fault-tolerance thresholds are derived based on the specific, approximate states given in Eq. (7.5) and refer to r and κ . Any other state can therefore in general not be guaranteed to enable fault tolerant computations, even when the effective squeezing parameters are both above these thresholds. Moreover, the effective squeezing parameters say nothing about the logic state of the GKP qubit, e.g. a mixed code state might be strongly squeezed, but might not necessarily be useful for quantum computing.

Nevertheless, it is reasonable to assume that states with a high degree of effective squeezing can be used for fault tolerance if they otherwise closely resemble the approximate pure grid states of Eq. (7.5), e.g. in terms of their fidelity with the approximate states. In the further analysis we therefore compliment the effective squeezing parameters with the fidelity to verify the appropriateness of using the effective squeezing parameters as quantifiers of the protocol performance. Moreover, we also verify that the produced states have the expected grid structure in terms of their Wigner function. Another alternative figure of merit is the *effective shift error* [67] which is discussed and calculated in Supplementary Note S1.

Preparation protocol

Several proposals exist for the preparation of approximate grid states [28, 48, 79, 88–91, 112, 113, 145, 146]. The original GKP paper [28] includes a proposal based on an radiation-pressure-like interaction between two bosonic modes under the Hamiltonian $\hat{X}_1 \hat{a}_2^\dagger \hat{a}_2$ in the quantum non-linear regime. However, experimental realization of the required strongly nonlinear coupling has proven highly challenging and has not yet been achieved.

In [145], a preparation protocol based on the Rabi interaction Hamiltonian $\hat{P} \hat{\sigma}_x$ (where $\hat{\sigma}_x$ is the Pauli- x matrix), between the bosonic mode and a two-level system was proposed. Such an interaction can be realized in trapped ions [45] and microwave cavities [48]. This protocol, however, has three main drawbacks: First it is probabilistic, with a success probability inversely proportional to the mean photon number of the generated state. Secondly, the output states have a box-shaped envelope rather than the Gaussian envelope of equation (7.5). This means that the effective squeezing parameters are suboptimal given the number steps required to prepare the states. Hence, excessively large states need to be generated to obtain useful effective squeezing. Finally, the protocol requires qubit measurements, which in realistic systems will constitute a significant contribution to the total preparation time during which the state decoheres.

The two first issues were solved by Terhal and Weigand in Ref. [79]: By adding a single measurement-based feed-forward displacement operation as well as suitable qubit rotations, the protocol is made deterministic. Furthermore, by using a different strength of the Rabi interactions, the envelope of the output state is made nearly Gaussian, making the protocol much more efficient. However, their protocol still relies on qubit measurements, which limits the quality of the states that can be realistically generated in the laboratory today.

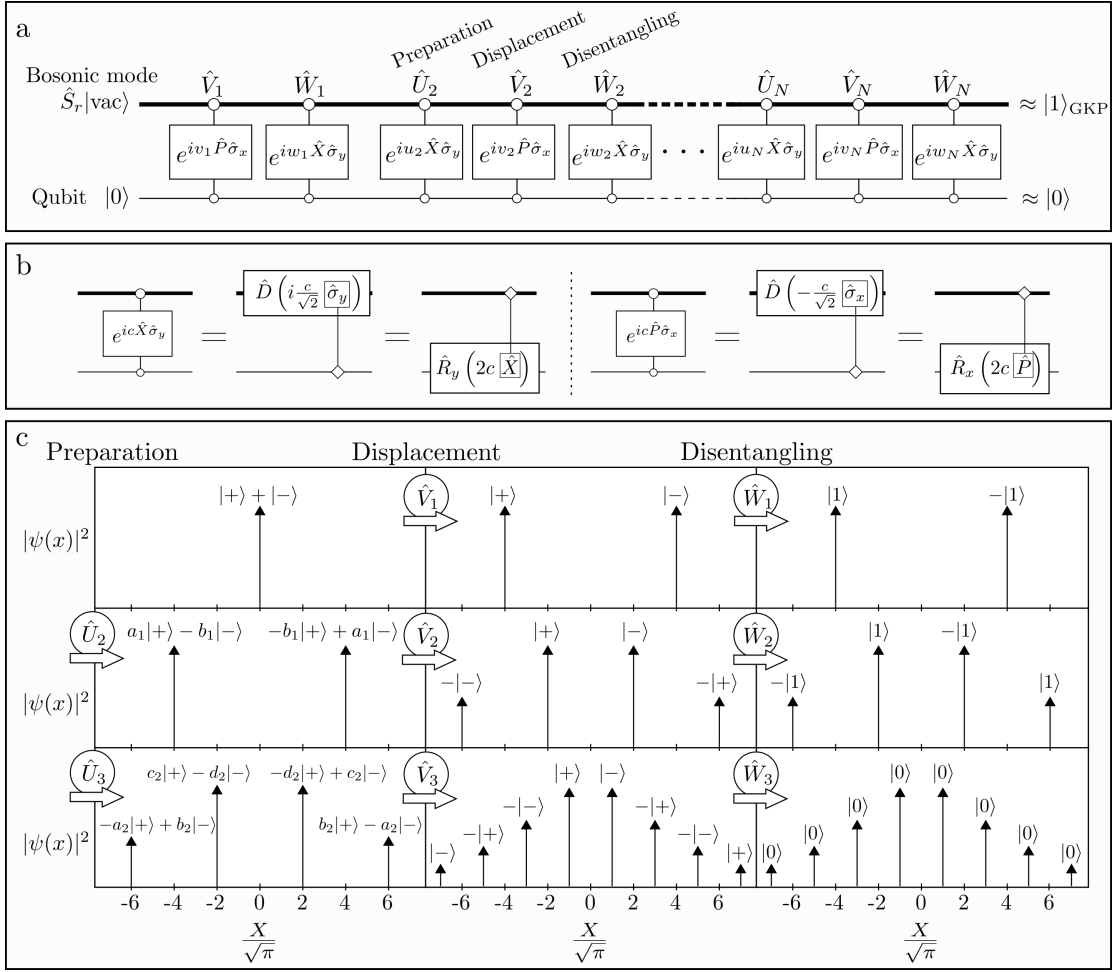


Figure 7.1: Overview of the grid state preparation protocol. **a** Circuit diagram of the measurement-free grid state generation protocol. The bosonic mode interacts with the qubit through a sequence of Rabi gates with interaction Hamiltonians of the form $\hat{P} \hat{\sigma}_x$ and $\hat{X} \hat{\sigma}_y$ to produce an approximate GKP 1 logic state without measurements. **b** The Rabi gates can be viewed either as conditional displacements on the bosonic mode depending on the qubit state or conditional rotations of the qubit depending on the bosonic state. **c** Illustration of the protocol for $N = 3$ for an infinitely squeezed input state. The ket above each peak in the wave function represents the state of the qubit entangled with the given peak. The displacement gates \hat{V} split each peak in two, creating an entangled state. The disentangling gates \hat{W} then rotate the qubit depending on the boson state to remove the entanglement. The preparation gates \hat{U} rotate the qubit before the displacement gates to control the envelope of the resulting state.

Our protocol addresses all the above mentioned problems by adding additional short Rabi interactions of the form $\hat{X}\hat{\sigma}_y$, which effectively act as “deterministic measurements” by disentangling the bosonic mode and the qubit and further enables us to shape the envelope of the state. This interaction can be obtained from the $\hat{P}\hat{\sigma}_x$ Hamiltonian by simple rotations of the qubit and the bosonic mode, i.e. $\hat{\sigma}_y = e^{-i\pi/4\hat{\sigma}_z}\hat{\sigma}_x e^{i\pi/4\hat{\sigma}_z}$ and $\hat{X} = e^{-i\pi/2\hat{n}}\hat{P}e^{i\pi/2\hat{n}}$. Similarly, both interaction types can be obtained from the more commonly considered Rabi Hamiltonian $\hat{X}\hat{\sigma}_x$. Fig. 7.1(a) shows a circuit diagram of the protocol. It consist of N groups of interactions, each consisting of 3 gates:

- a *preparation gate*, $\hat{U}_k = e^{iu_k\hat{X}\hat{\sigma}_y}$.
- a *displacement gate*, $\hat{V}_k = e^{iv_k\hat{P}\hat{\sigma}_x}$.
- a *disentangling gate*, $\hat{W}_k = e^{iw_k\hat{X}\hat{\sigma}_y}$.

These interactions can be interpreted as either conditional displacements of the bosonic mode or conditional rotations of the qubit, as illustrated in Fig. 7.1(b). Since the preparation and disentangling gates are of the same type, i.e. $\hat{X}\hat{\sigma}_y$, the preparation gate of round k can be combined with the disentangling gate of round $k-1$ into a single gate. The interaction strengths of the displacement and disentangling gates are given by

$$v_k = \begin{cases} -\sqrt{\pi}2^{N-1}, & \text{if } k = 1, \\ \sqrt{\pi}2^{N-k} & \text{if } k > 1. \end{cases} \quad (7.8)$$

$$w_k = \begin{cases} -\frac{\sqrt{\pi}}{4}2^{-(N-k)}, & \text{if } k < N, \\ \frac{\sqrt{\pi}}{4} & \text{if } k = N. \end{cases} \quad (7.9)$$

while the interaction strengths of the preparation gates, u_k , are found numerically (see Supplementary Note S2). In the first round the optimal preparation gate strength is $u_1 = 0$ i.e. $\hat{U}_1 = \hat{I}$ so \hat{U}_1 is thus ignored in Fig. 7.1(a). The input state is a squeezed vacuum state $\hat{S}_r|\text{vac}\rangle$ and the output state is an approximation to the state $|1\rangle_{\text{GKP}}$, which can subsequently be transformed into an arbitrary grid state, as will be discussed later. Note that all gates commute with $\hat{D}(i\sqrt{2\pi}) = e^{i2\sqrt{\pi}\hat{X}}$. Therefore, Δ_X is left invariant under the protocol, i.e. the effective squeezing of the output state in the X -quadrature is $\Delta_X = e^{-r}$. The effect of the protocol is thus to create a superposition of 2^N squeezed states and thereby improve Δ_P . The effect of each gate is illustrated in Fig. 7.1(c) for the case of $N = 3$, but the procedure can be extended for arbitrary N .

Infinitely squeezed input states

To illustrate the functionality of the gates, we first consider an infinitely squeezed input state, $|X = 0\rangle$. For brevity we will use the notation $|X = x_0\rangle = |x_0\rangle_x$ in the following. The first operation is the displacement gate \hat{V}_1 which creates an entangled boson-qubit state:

$$\hat{V}_1|0\rangle_x|0\rangle = \frac{1}{\sqrt{2}} (|2^{N-1}\sqrt{\pi}\rangle_x|+\rangle + |-2^{N-1}\sqrt{\pi}\rangle_x|-\rangle), \quad (7.10)$$

where $|\pm\rangle = (|0\rangle \pm |1\rangle)/\sqrt{2}$. The disentangling gate then rotates the qubit to erase the entanglement:

$$\hat{W}_1\hat{V}_1|0\rangle_x|0\rangle = \frac{1}{\sqrt{2}} (|2^{N-1}\sqrt{\pi}\rangle_x - |-2^{N-1}\sqrt{\pi}\rangle_x)|1\rangle. \quad (7.11)$$

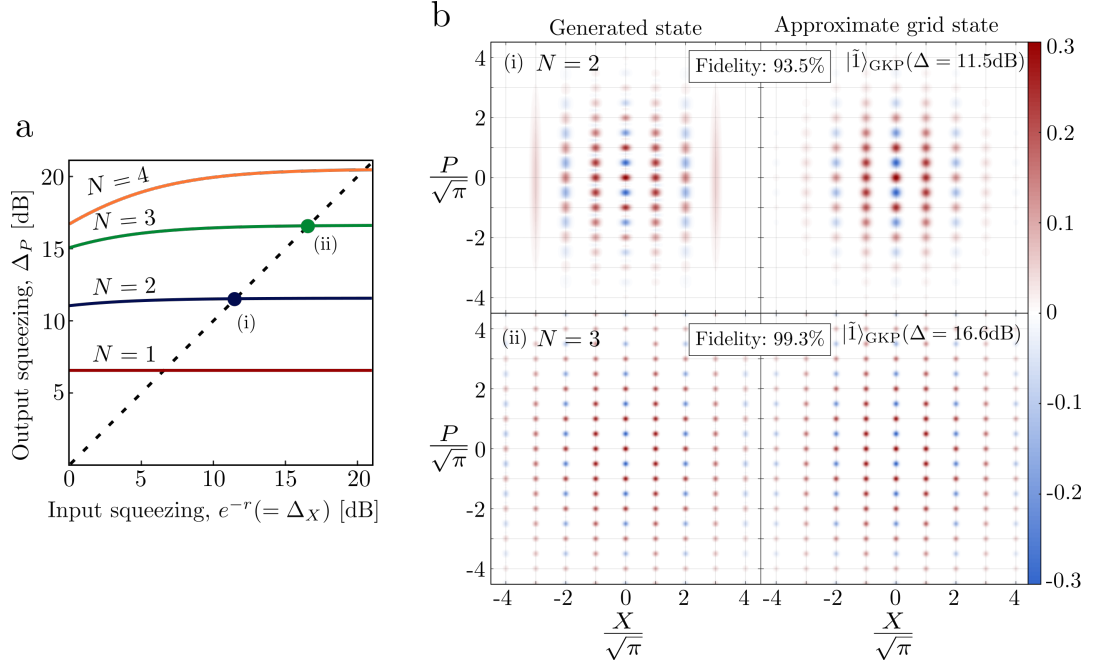


Figure 7.2: Quality of states generated with finite squeezing. **a** Effective squeezing in the P quadrature, Δ_P , as a function of squeezing in the X quadrature of the input state after N rounds. Δ_X is invariant under the protocol. The dashed line is $\Delta_P = \Delta_X = e^{-r}$. **b** Left: Wigner functions of the generated states for $N = 2$ and $N = 3$ with 11.5 dB and 16.6 dB input squeezing respectively. The plotted states are marked with (i) and (ii) in (a). Right: Wigner functions of the target approximate GKP states given by equation (7.5).

We have thus created a superposition between two squeezed states. The second round splits each of these peaks in two, creating a total of four peaks:

$$(\hat{W}_2 \hat{V}_2 \hat{U}_2)(\hat{W}_1 \hat{V}_1)|0\rangle_x|0\rangle = \frac{1}{\sqrt{2}}(-b_1|-3 \cdot 2^{N-2}\sqrt{\pi}\rangle_x + a_1|-2^{N-2}\sqrt{\pi}\rangle_x - a_1|2^{N-2}\sqrt{\pi}\rangle_x + b_1|3 \cdot 2^{N-2}\sqrt{\pi}\rangle_x)|1\rangle. \quad (7.12)$$

The coefficients are controlled by the preparation gate and are given by $a_1 = \sin(\pi/4 + 2^{N-1}\sqrt{\pi}u_2)$ and $b_1 = \cos(\pi/4 + 2^{N-1}\sqrt{\pi}u_2)$. The third round creates 8 peaks and so on for a total of 2^N peaks after N rounds. Thus, the resulting state is

$$\left(\frac{1}{\sqrt{2}} \sum_{k=1}^{2^N} c_k |(2k - 2^N - 1)\sqrt{\pi}\rangle_x \right) |0\rangle, \quad (7.13)$$

where the coefficients c_k can be optimized by tuning the strengths of the preparation gates (see Supplementary Note S2). For these infinitely squeezed input states we can obtain $\Delta_P = \{6.6, 11.6, 16.6, 20.6\}$ dB, for $N = \{1, 2, 3, 4\}$, and $\Delta_X = \infty$ dB as Δ_X is determined solely by the initial squeezing of the input state.

Finitely squeezed input states

For a finitely squeezed input state the protocol outlined above is not exact, and in particular the disentangling operation is not exact. Thus, after tracing out the qubit the resulting state is mixed, but the effect on Δ_P of the output state is very small. This can be seen in Fig. 7.2(a) which shows Δ_P as a function of the input squeezing. Since $\Delta_X = e^{-r}$ is preserved during the protocol, high effective squeezing can be obtained simultaneously in both quadratures even with finitely squeezed input states.

Note that, as seen from Fig. 7.2, even with vacuum input a significant amount of effective squeezing can be obtained. By applying the protocol twice, once in each quadrature direction, we can therefore generate grid-like states with high degrees of effective squeezing in both quadratures. However, a careful analysis (presented in Supplementary Note S3) shows that these states are not well-defined pure states in the GKP basis, and therefore, seemingly, unsuitable for GKP-based computations.

In Fig. 7.2(b) (left) we present the Wigner functions of the generated states for $N = 2$ and $N = 3$ with input squeezing of 11.5 dB and 16.6 dB respectively, in which case equal effective squeezing in X and P is obtained. For comparison, we also plot the Wigner functions of the corresponding target approximate grid states given by equation (7.5) with the same amount of squeezing (right plots in Fig. 7.2(b)). For $N = 2$ we observe very small differences in the edges of the states which are caused by the cut-off in the number of squeezed states in the superposition of the generated state. Despite these differences, the resulting fidelity is already 93.5%. For $N = 3$ the differences becomes much less pronounced and the fidelity increases to 99.3%. Thus, very few rounds of operations are required to make grid states with high effective squeezing and near unity fidelity to the commonly considered approximate grid states of equation (7.5).

Preparation of arbitrary logical states

The state generated so far is the logical $|1\rangle$ state of the square GKP code. It is, however, important to be able to generate an arbitrary logical grid state, i.e. of the form $c_0|0\rangle_{\text{GKP}} + c_1|1\rangle_{\text{GKP}}$. In particular, magic states, such as $|H\rangle = \cos(\pi/8)|0\rangle_{\text{GKP}} + \sin(\pi/8)|1\rangle_{\text{GKP}}$ are highly important as they serve as resources for performing non-Clifford operations via gate teleportation [147].

Furthermore, non-square rectangular grid states—which are equivalent to squeezed square grid states—are also a useful resource, as they remove the need for in-line squeezing using a newly developed modified Glancy and Knill error recovery scheme [69]. In the following we thus discuss how to generate the arbitrary logical grid state with both rectangular and hexagonal lattices.

We first note that rectangular lattices map onto square lattices simply by scaling the quadratures, i.e. $\hat{X} \rightarrow C\hat{X}$ and $\hat{P} \rightarrow C^{-1}\hat{P}$ where C is the scale factor. These scalings can consequently be straightforwardly implemented by appropriate scaling of the interaction parameters, i.e. $u \rightarrow Cu$, $v \rightarrow C^{-1}v$ and $w \rightarrow Cw$. To generate hexagonal states we utilize the fact that the hexagonal logical $|1\rangle$ state is identical to the logical $|1\rangle$ state of the rectangular lattice with $\alpha = i\sqrt{\frac{4}{\sqrt{3}}}\pi$ and $\beta = \sqrt{\sqrt{3}\pi}$. We can thus also initialize the logical $|1\rangle$ state of the hexagonal lattice.

The circuit diagram shown in Fig. 7.3(a) shows how to map the logical $|1\rangle$ state into arbitrary logic states using three Rabi-interactions \hat{u} , \hat{v} and \hat{w} . The idea is to proceed with the scheme for generating the logical $|1\rangle$ state, but exploiting the linearity of the protocol and the fact that the effect of the displacement gate depends on the state of the qubit. Therefore, by initializing

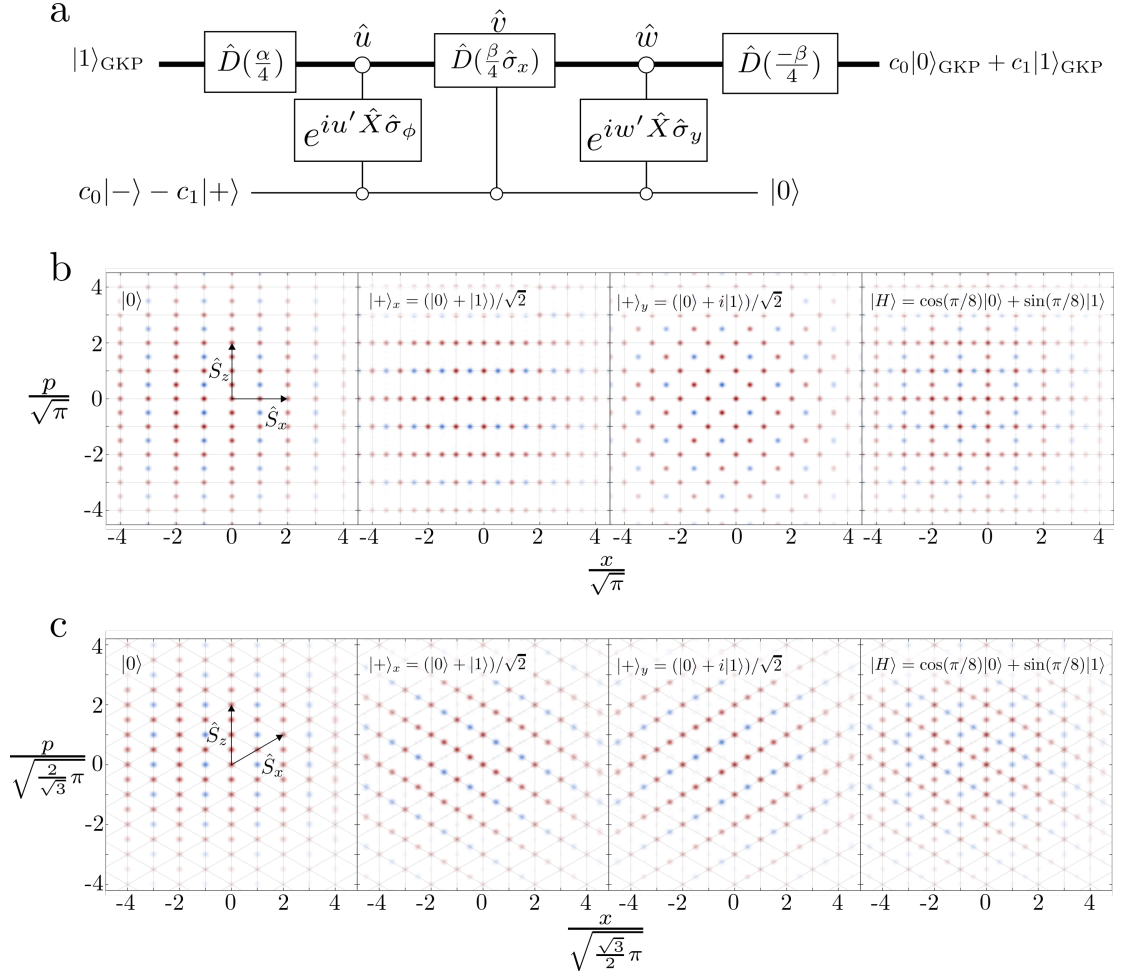


Figure 7.3: Preparation of arbitrary logical GKP states. **a** Circuit diagram for preparing arbitrary logical GKP states. **b** Wigner functions for various logical square grid states numerically generated using our scheme with $N = 3$ and 16.6 dB input squeezing. **c** Wigner functions for various logical hexagonal grid states generated using $N = 3$ and 15 dB input squeezing. The arrows in the top plot of (b) and (c) show the directions and magnitude of the stabilizer displacements \hat{S}_z and \hat{S}_x .

the qubit in the state $c_0|-\rangle - c_1|+\rangle$, we effectively transfer the coefficients of the qubit onto the grid state, leaving the qubit in the $|0\rangle$ state. The additional two, unconditional, displacement operations ensure that the resulting state is on the lattice. The first operation $\hat{D}(\alpha/4)$ can be effectively implemented during the preparation protocol by inverting the sign of w_N , while the second unconditional operation $\hat{D}(\beta/4)$ simply shifts the lattice for all states and can therefore be virtually implemented by a shift of reference frame. The strength of the first conditional operation u' , and the qubit-dependence ϕ of the preparation gate \hat{u} depends on the target logical state and are found by numerical optimization ($\hat{\sigma}_\phi = \cos(\phi)\hat{\sigma}_x + \sin(\phi)\hat{\sigma}_y$ represents a generalized Pauli operator in the x - z plane). The gate \hat{u} is not crucial for the scheme, but only improves the quality of the output states by allowing a degree of control over the envelope of the output

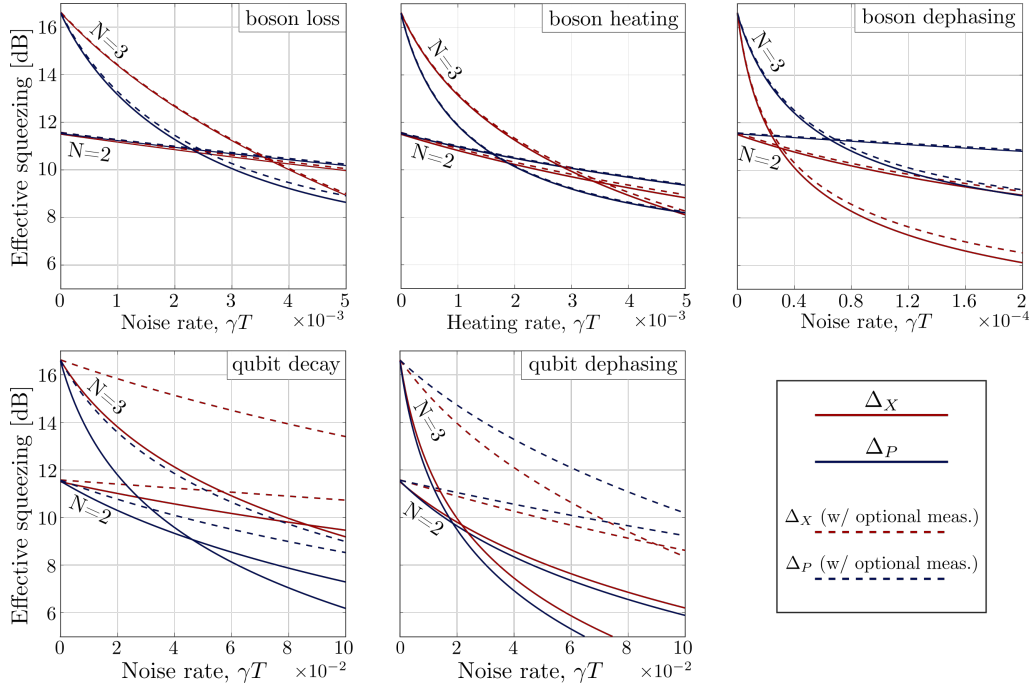


Figure 7.4: Effects of physical noise sources. Effective squeezing in X and P for a square grid state as a function of noise rate for different noise sources during the preparation protocol. γ is the noise rate and T is the time required to implement $e^{i\hat{X}\hat{\sigma}_y}$ and $e^{i\hat{P}\hat{\sigma}_x}$.

state. The strength of the disentangling gate \hat{w} is $w' = -\pi/(\sqrt{2}\text{Re}(\beta))$.

Fig. 7.3(b) and (c) show the Wigner functions of various logical states with square and hexagonal lattices respectively, numerically generated using this protocol, showing clear, well-defined grid structures.

Effects of noise

We now consider the effect of relevant noise sources on our protocol. To include noise effects in our model, we consider each gate as being implemented with a specific Hamiltonian for a set duration, e.g. the gate $e^{ic\hat{X}\hat{\sigma}_y}$ is implemented via the Hamiltonian $\hat{H} = \frac{1}{T}\hat{X}\hat{\sigma}_y$ within the time $t = cT$. To simulate the added noise, we use a master equation approach in which noise is included in the Lindblad terms \hat{L} :

$$\frac{d\rho}{dt} = -\frac{i}{\hbar}[\hat{H}, \rho] + \hat{L}\rho\hat{L}^\dagger - \frac{1}{2}(\hat{L}^\dagger\hat{L}\rho + \rho\hat{L}^\dagger\hat{L}), \quad (7.14)$$

where ρ is the density matrix of the composite boson-qubit system. We consider four common noise channels:

- Boson loss: $\hat{L} = \sqrt{\gamma}\hat{a}$
- Boson dephasing: $\hat{L} = \sqrt{\gamma}(\hat{a}\hat{a}^\dagger + \hat{a}^\dagger\hat{a})$
- Boson heating: $\hat{L}_1 = \sqrt{\gamma_c(\bar{n} + 1)}\hat{a}$, $\hat{L}_2 = \sqrt{\gamma_c\bar{n}}\hat{a}^\dagger$

- Qubit dephasing: $\hat{L} = \sqrt{\gamma}\hat{\sigma}_z$
- Qubit decay: $\hat{L} = \sqrt{\gamma}(\hat{\sigma}_x + i\hat{\sigma}_y)/2$

For the boson heating Lindbladian \bar{n} is the mean occupation of the environment which couples to the system with rate γ_c . Here we consider the case of large \bar{n} such that $\sqrt{\gamma_c(\bar{n} + 1)} \approx \sqrt{\gamma_c\bar{n}} \equiv \gamma$, such that the heating rate of the system is constant. The effect of these noise sources on the effective squeezing of the output states is shown by the solid lines in Fig. 7.4. For each noise source we consider $N = 2$ and $N = 3$ rounds with 11.5 dB and 16.6 dB squeezed input states respectively. It is clear that our protocol is sensitive to all types of noise. By increasing N we also increase the implementation time of the protocol, thus increasing the effect of noise. Therefore, there exists an optimal number of rounds that depends on the magnitude and type of noise. E.g. for large noise contributions, two rounds ($N = 2$) of the scheme produces states with higher effective squeezing degrees than three rounds ($N = 3$), and this is simply a result of the extended time over which noise can accumulate. This clearly illustrates the importance of a fast preparation protocol.

Even though the quality of the generated states is limited by qubit and bosonic errors, the effect of qubit errors can be significantly suppressed by adding a few qubit measurements, after each of the disentangling gates \hat{W} . In the noiseless case, the qubit should be in a known state, disentangled from the bosonic mode at these points, as illustrated in the rightmost windows of Fig. 7.1(c). Therefore, if we measure the qubit in a different state, we know that an error has occurred, and the realization should be discarded and the protocol restarted. The result of such a postselection strategy is shown by the dashed lines in Fig. 7.4, demonstrating that we can improve the effective squeezing of the output state by several dB. Bosonic errors, on the other hand, are largely unaffected by the postselection strategy. Thus, when these errors are dominating the only way to improve the output states is to increase the interaction speed or reduce the rate of the noise. For the calculation of Fig. 7.4 we assumed instantaneous measurements to isolate the effect of qubit projections. In real systems the measurements will take time, during which noise accumulates thus resulting in lower effective squeezing parameters. However, compared to the measurement-based schemes, e.g. phase-estimation [79], we require exponentially fewer measurements and therefore still attain a significant speed-up.

Using realistic noise parameters and operation speeds from recent experiments with trapped ions [43] and microwave cavities [48], we find that grid states with effective squeezing parameters above 10 dB in both quadratures can be realistically generated in both platforms using input states squeezed by 11 dB (see Supplementary Note S4). Squeezing levels of 12.6 dB in trapped ions [46] and 10 dB in microwave cavities [148] have been experimentally generated. The method used for generating squeezed states in trapped ions has been experimentally demonstrated to be compatible with further manipulation using Rabi gates [43], while the method used in the microwave regime requires specialized structures which could compromise the quality of subsequent gates. However, it has recently been shown that Rabi gates can be used to deterministically generate the required squeezed vacuum states starting from vacuum [35]. Thus the protocol presented in this work can readily be implemented in any qubit-oscillator system where Rabi interactions can be efficiently implemented.

7.4 Discussion

In conclusion, we have presented a measurement-free protocol to deterministically prepare GKP states using only few interactions of the type $\hat{X}\hat{\sigma}_y$ and $\hat{P}\hat{\sigma}_x$, which are readily available in trapped-ion and microwave-cavity platforms. Our protocol requires no measurements, resulting in a speed-up over previous methods, which enables the generation of grid states with high effective squeezing levels. Furthermore, by adding a few measurements we can partly detect qubit errors, thus making the protocol robust against qubit noise. Although the exact requirements for general CV states (i.e. states not exactly on the form of Eq. (7.5)) to enable fault-tolerance with the GKP encoding are yet unknown, it seems reasonable that states generated using this protocol suffices, due to their high fidelity with the commonly considered approximate grid states of Eq. (7.5).

Finally, our protocol exemplifies the versatility of sequential applications of non-commuting Rabi Hamiltonians, e.g. $\hat{P}\hat{\sigma}_x$ and $\hat{X}\hat{\sigma}_y$, demonstrating that highly non-Gaussian states can be deterministically engineered with only a few of these interactions. The full power of such repeated combination of Rabi interactions remains still relatively unexplored, but we expect that many other interesting applications are possible using this technique.

During the publication of this manuscript the protocol was experimentally implemented in a trapped ion system [111].

7.5 S1: Effective shift error

In [67] it was show that small displacement errors on ideal grid states can be perfectly corrected, if the magnitude of the displacements are less than $\sqrt{\pi}/6$. Furthermore, any bosonic state ρ can be expanded in a basis of shifted ideal grid states:

$$\rho = \int_{-\sqrt{\pi}}^{\sqrt{\pi}} du \int_{-\sqrt{\pi}}^{\sqrt{\pi}} du' \int_{-\sqrt{\pi}/2}^{\sqrt{\pi}/2} dv \int_{-\sqrt{\pi}/2}^{\sqrt{\pi}/2} dv' \rho_{uv,u'v'} |u, v\rangle \langle u', v'|, \quad (7.15)$$

where

$$|u, v\rangle = \pi^{-\frac{1}{4}} \hat{D}(u/\sqrt{2}) \hat{D}(-iv/\sqrt{2}) |0\rangle_{\text{GKP}}. \quad (7.16)$$

The *effective shift error*, defined as the probability that an approximate logical 0 GKP state has an intrinsic displacement error larger than $\sqrt{\pi}/6$ is then given by:

$$P_{\text{error}}^{\sqrt{\pi}/6} = 1 - \int_{-\sqrt{\pi}/6}^{\sqrt{\pi}/6} du \int_{-\sqrt{\pi}/6}^{\sqrt{\pi}/6} dv \rho_{uv,uv}. \quad (7.17)$$

As pointed out in [105], a low $P_{\text{error}}^{\sqrt{\pi}/6}$ is both sufficient and necessary for useful GKP states. Fig. 7.5 shows $P_{\text{error}}^{\sqrt{\pi}/6}$ of the states generated using our protocol. The tendency for smaller $P_{\text{error}}^{\sqrt{\pi}/6}$ for large N and large input squeezing confirms that the generated states are indeed suitable for the GKP error correction protocol. For comparison, the dotted line shows $P_{\text{error}}^{\sqrt{\pi}/6}$ of the approximate grid states given by Eq. (7.5) of the main text. For low input squeezing and high N our states perform slightly better than the approximate states. This is because high N states have low errors in the P quadrature, independent of the input squeezing. However, since $P_{\text{error}}^{\sqrt{\pi}/6}$ depends on the quality of the state in both X and P , we cannot keep improving it by solely increasing N , without also increasing the input squeezing, and vice versa, as seen from Fig. 7.5.

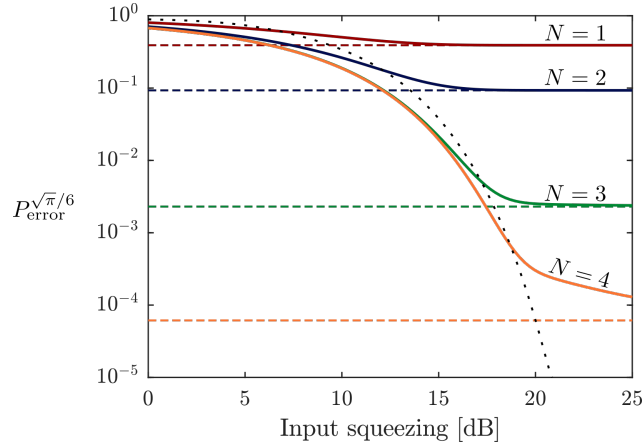


Figure 7.5: Effective shift error as a function of input squeezing. Dashed lines show the limits for infinite squeezing. The black dotted line shows the effective shift error for the approximate GKP states given by Eq. (7.5) of the main text.

7.6 S2: Preparation gate interaction strengths

The preparation gates are used to shape the envelope of the prepared grid state in order to optimize the quality of the states. For infinite input squeezing, the coefficients of Eq. (7.13) from the main text for $N \in 2, 3, 4$ are:

- $N = 2$:

$$\begin{aligned} c_1 &= \cos(\pi/4 + 2\sqrt{\pi}u_2) \\ c_2 &= \sin(\pi/4 + 2\sqrt{\pi}u_2) \end{aligned} \quad (7.18)$$

- $N = 3$:

$$\begin{aligned} c_1 &= \cos(\pi/4 + 4\sqrt{\pi}u_2) \cos(\pi/4 + 6\sqrt{\pi}u_3) \\ c_2 &= \cos(\pi/4 + 4\sqrt{\pi}u_2) \sin(\pi/4 + 6\sqrt{\pi}u_3) \\ c_3 &= \sin(\pi/4 + 4\sqrt{\pi}u_2) \cos(\pi/4 + 2\sqrt{\pi}u_3) \\ c_4 &= \sin(\pi/4 + 4\sqrt{\pi}u_2) \sin(\pi/4 + 2\sqrt{\pi}u_3) \end{aligned} \quad (7.19)$$

- $N = 4$:

$$\begin{aligned} c_1 &= \cos(\pi/4 + 8\sqrt{\pi}u_2) \cos(\pi/4 + 12\sqrt{\pi}u_3) \cos(\pi/4 + 14\sqrt{\pi}u_4) \\ c_2 &= \cos(\pi/4 + 8\sqrt{\pi}u_2) \cos(\pi/4 + 12\sqrt{\pi}u_3) \sin(\pi/4 + 14\sqrt{\pi}u_4) \\ c_3 &= \cos(\pi/4 + 8\sqrt{\pi}u_2) \sin(\pi/4 + 12\sqrt{\pi}u_3) \cos(\pi/4 + 10\sqrt{\pi}u_4) \\ c_4 &= \cos(\pi/4 + 8\sqrt{\pi}u_2) \sin(\pi/4 + 12\sqrt{\pi}u_3) \sin(\pi/4 + 10\sqrt{\pi}u_4) \\ c_5 &= \sin(\pi/4 + 8\sqrt{\pi}u_2) \cos(\pi/4 + 4\sqrt{\pi}u_3) \cos(\pi/4 + 6\sqrt{\pi}u_4) \\ c_6 &= \sin(\pi/4 + 8\sqrt{\pi}u_2) \cos(\pi/4 + 4\sqrt{\pi}u_3) \sin(\pi/4 + 6\sqrt{\pi}u_4) \\ c_7 &= \sin(\pi/4 + 8\sqrt{\pi}u_2) \sin(\pi/4 + 4\sqrt{\pi}u_3) \cos(\pi/4 + 2\sqrt{\pi}u_4) \\ c_8 &= \sin(\pi/4 + 8\sqrt{\pi}u_2) \sin(\pi/4 + 4\sqrt{\pi}u_3) \sin(\pi/4 + 2\sqrt{\pi}u_4) \end{aligned} \quad (7.20)$$

Table 7.1: Optimal interaction strengths u_k , and resulting effective shift errors and effective squeezing for $N = 1, 2, 3, 4$. The optimal distribution is calculated by optimizing over all c_k in Eq. (7.13) and the flat distribution is given by equal c_k 's, which is obtained by removing the "preparation gate" in our protocol.

N	FOM	Optimize $P_{\text{error}}^{\sqrt{\pi}/6}$			Optimize Δ_P			
		$[u_1, \dots, u_N]$	This work	Optimal distribution	$[u_1, \dots, u_N]$	This work	Optimal distribution	Flat distribution
1	$\frac{P_{\text{error}}^{\sqrt{\pi}/6}}{\Delta_P}$	[0]	3.9×10^{-1} 6.6 dB	3.9×10^{-1} 6.6 dB	[0]	3.9×10^{-1} 6.6 dB	3.9×10^{-1} 6.6 dB	3.9×10^{-1} 6.6 dB
2	$\frac{P_{\text{error}}^{\sqrt{\pi}/6}}{\Delta_P}$	[0, 0.045]	9.3×10^{-2} 11.6 dB	9.3×10^{-2} 11.6 dB	[0, 0.093]	9.7×10^{-2} 11.7 dB	9.7×10^{-2} 11.7 dB	1.2×10^{-1} 10.4 dB
3	$\frac{P_{\text{error}}^{\sqrt{\pi}/6}}{\Delta_P}$	[0, 0.053, 0.033]	2.3×10^{-3} 16.6 dB	2.1×10^{-3} 16.6 dB	[0, 0.04, 0.026]	6.7×10^{-3} 17.0 dB	7.6×10^{-3} 17.0 dB	7.8×10^{-2} 13.7 dB
4	$\frac{P_{\text{error}}^{\sqrt{\pi}/6}}{\Delta_P}$	[0, 0.038, 0.027, 0.015]	6.1×10^{-5} 20.6 dB	5.1×10^{-7} 19.9 dB	[0, 0.024, 0.015, 0.008]	1.8×10^{-3} 22.3 dB	1.3×10^{-3} 22.6 dB	3.3×10^{-2} 16.9 dB

and $c_m = c_{2^N - m + 1}$ for $m > 2^{N-1}$. Using these expressions one can tune the interaction strengths, u_k , to optimize the quality of the prepared grid state with respect to any desired figure of merit (FOM). In general, for the finite sum of 2^N infinitely squeezed states as given by Eq. (7.13), the expectation value of $\hat{D}(\sqrt{2\pi})$ used to calculate Δ_P (Eq. (7.3)) is given by

$$\langle \hat{D}(\sqrt{2\pi}) \rangle = \frac{1}{2} \sum_{s=1}^{2^N-1} c_s^* c_{s+1}, \quad (7.21)$$

and the grid-state-basis wavefunction $\rho_{uv,uv}$ used to calculate $P_{\text{error}}^{\sqrt{\pi}/6}$ (Eq. (7.17)) is given by

$$\rho_{uv,uv} = 2\pi^{-1/2} \left| \sum_{s=1}^{2^N-1} c_{s+2^N-1} \cos(2\sqrt{\pi}sv - \sqrt{\pi}) \right|^2 \delta(u), \quad (7.22)$$

assuming symmetry around $X = 0$, i.e. $c_m = c_{2^N - m + 1}$.

Table 7.1 shows the calculated optimal interaction strengths and obtained FOMs when optimizing $P_{\text{error}}^{\sqrt{\pi}/6}$ and Δ_P respectively. For comparison, we also compute the FOMs for the unconstrained optimal distribution, i.e. when freely optimizing over all possible coefficients c_k . We see, that even though we have only N degrees of freedom to tune $2^N - 1$ independent variables, we can obtain practically optimal FOMs. The only notable difference is for $N = 4$ when optimizing $P_{\text{error}}^{\sqrt{\pi}/6}$, for which the optimal distribution is two orders of magnitude better than what can be obtained in our scheme. However, for practical purposes, the quality of the generated states will be limited by external noise sources, and therefore the optimal number of rounds will likely be limited to $N = 3$ (see Supplementary Note S4 7.8).

We also list the values of the FOMs corresponding to a flat distribution, i.e. where all c_k 's are equal. Such a distribution is obtained in our scheme by removing the preparation gates. For $N \geq 3$ we see a significant improvement by tuning the peaks compared to the flat distribution.

For comparison, the technique of adaptive phase estimation [79] also prepares a finite superposition of squeezed states. For $M = 7$ rounds of phase estimation, 8 peaks are obtained corresponding to $N = 3$ in our scheme. The quality of the states obtained depends on measurement results, but the best-case scenario for $M = 7$ has $P_{\text{error}}^{\sqrt{\pi}/6} = 4.1 \times 10^{-3}$ and $\Delta_P = 16.1$ compared to $P_{\text{error}}^{\sqrt{\pi}/6} = 2.3 \times 10^{-3}$ and $\Delta_P = 16.6$ for $N = 3$ of our protocol. Our protocol thus

outperforms adaptive phase estimation for any measurement outcome. However, the phase estimation protocol has the advantage of generating one peak at a time, and therefore the number of rounds can be better tuned to optimize the output state given the noise of the particular system. Yet, we believe that the main advantage of our protocol is the lack of measurements, which ultimately significantly speeds up the protocol, resulting in less accumulated noise. Additionally, for trapped-ion systems, qubit measurements can disturb the bosonic mode depending on the outcome, thus requiring postselection even with the phase estimation protocol. Therefore phase estimation does not scale well in this system, as the success probability decreases exponentially with the number of rounds.

We generally note that $P_{\text{error}}^{\sqrt{\pi}/6}$ is a much more sensitive FOM compared to Δ_P . For example, for $N = 4$ the effective shift error can be improved by several orders of magnitude by tuning the coefficients, whereas the effective squeezing is “only” improved by less than 5 dB, i.e. less than an order of magnitude. Note also, that for $N = 3$ the difference in Δ_P when optimizing Δ_P compared to $P_{\text{error}}^{\sqrt{\pi}/6}$ is only 0.4 dB, where the difference in $P_{\text{error}}^{\sqrt{\pi}/6}$ is approximately a factor 3. This shows that states with similar effective squeezing can have significantly different effective shift errors. Since the effective shift error is more directly related to the error-correcting properties of the GKP states, care should therefore be taken when comparing only effective squeezing parameters.

For the results presented in the main text of this paper we have chosen u_k 's to optimize $P_{\text{error}}^{\sqrt{\pi}/6}$. For finite squeezing we have found no noticeable improvement in the FOMs by further tuning the u_k 's to take into account the finite squeezing, and we have therefore used the values of u_k listed in Table 7.1 for all simulations.

7.7 S3: No initial squeezing

In Fig. 7.2(a) we showed that high effective squeezing can be generated without any initial squeezing in the bosonic mode. This raises the question whether the protocol can be used to generate grid states directly from vacuum. In particular, one can start from vacuum and apply the protocol twice, once in each quadrature direction, to generate high effective squeezing in both quadratures simultaneously. The Wigner functions of the states generated with this approach are shown for $N = 2$ and $N = 3$ in the insets of Fig. 7.6. The states have a clear grid-like structure, but it is not immediately clear if they represent useful GKP logic states, i.e. if they approach the form $c_0|0\rangle_{\text{GKP}} + c_1|1\rangle_{\text{GKP}}$ for some coefficients c_0 and c_1 . To examine this, we calculate the expectation value of the rotated Pauli operators

$$\hat{U}_L = (|c_0|^2 - |c_1|^2)\hat{Z}_L + 2\text{Re}(c'_0c_1)\hat{X}_L + 2\text{Im}(c'_0c_1)\hat{Y}_L. \quad (7.23)$$

If the generated state approaches a logical GKP state we should have $|\langle\hat{U}_L\rangle| \rightarrow 1$ for some (c_0, c_1) . Fig. 7.6 shows the maximum value of $|\langle\hat{U}_L\rangle|$ as a function of N . We observe that $|\langle\hat{U}_L\rangle|$ does not appear to converge to 1, showing that the states do not represent useful GKP logic states. Still, The generated states do have high effective squeezing in both quadratures, so they would be a useful resource for detecting displacements [101].

7.8 S4: Realistic noise parameters

Grid states were generated for the first time very recently in the motional state of a trapped ion [43] and in a microwave cavity field coupled to a superconducting circuit [48]. These experiments obtained effective squeezing parameters of $\Delta_X, \Delta_P \in [5.5; 7.3]$ and $\Delta_X, \Delta_P \in [7.4; 9.5]$

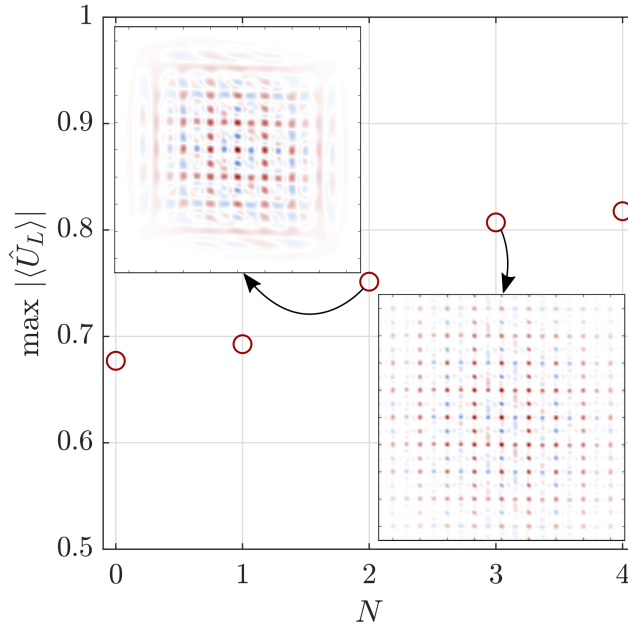


Figure 7.6: Maximum expectation value over all rotated Pauli-operators in the GKP-logical subspace for states generated without initial squeezing. The states are generated by applying the protocol of Fig. 7.1(a) (main text) twice with a $\pi/2$ rotation of the bosonic mode in between. As N increases the expectation value does not converge to 1, showing that these states do not represent pure GKP logical states. The insets show the Wigner functions of the generated state for $N = 2$ and $N = 3$.

respectively. Note that grid states require high effective squeezing in both directions simultaneously, so for a fair comparison one might consider the effective squeezing in the direction with the least amount of squeezing, i.e. $\min(\Delta_X, \Delta_P)$, which in this case 5.5dB and 7.4dB for the two experiments respectively. To benchmark our protocol, we simulate it with the Lindblad master equation, Eq. (7.14), using the parameters given in the experiments, as listed in Table 7.2. The calculated FOMs as a function of input squeezing are shown in Fig. 7.7. In both platforms we can obtain more than 10 dB effective squeezing in both quadratures simultaneously with > 11 dB input squeezing. For the trapped ion platform the optimal number of rounds is with $N = 2$. For the microwave cavity platform both $N = 2$ and $N = 3$ allows for more than 10 dB output effective squeezing for sufficient input squeezing, with $N = 3$ reaching 12 dB using the measurement strategy measurement as explained in the main text (dashed lines of Fig. 7.7).

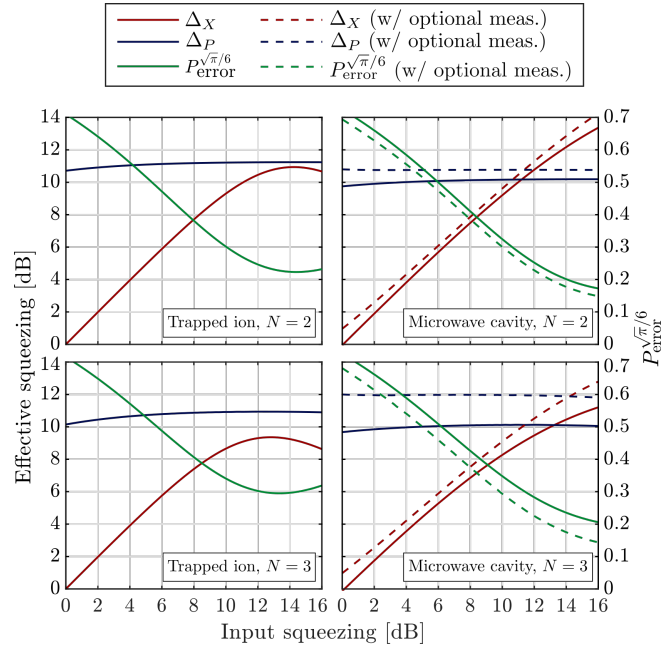


Figure 7.7: Effective squeezing and effective shift error as function of input squeezing as simulated using the master equation Eq. (7.14), using the noise types and strengths associated with recent experiments using trapped ions [43] and microwave cavities [48], as listed in Table 7.2.

Table 7.2: Interaction timescale and relevant noise types and rates in recent experiments with microwave cavities [48] and trapped ions [43]. The interaction timescale, T , is the time required to perform the operations $e^{i\hat{X}\hat{\sigma}_y}$ or $e^{i\hat{P}\hat{\sigma}_x}$.

Trapped ion [43]	
Interaction timescale	$T = 11 \mu\text{s}$
Phonon dephasing	$\gamma^{-1} = 140 \text{ ms}$ $\gamma T = 7.7 \times 10^{-5}$
Microwave cavity [48]	
Interaction timescale	$T = 0.34 \mu\text{s}$
Qubit decay	$\gamma^{-1} = 50 \mu\text{s}$ $\gamma T = 6.8 \times 10^{-3}$
Qubit dephasing	$\gamma^{-1} = 60 \mu\text{s}$ $\gamma T = 5.7 \times 10^{-3}$
Photon decay	$\gamma^{-1} = 245 \mu\text{s}$ $\gamma T = 1.4 \times 10^{-3}$

Chapter 8

Improved readout of qubit-coupled Gottesman-Kitaev-Preskill states

In this chapter we present the paper “Improved readout of qubit-coupled Gottesman-Kitaev-Preskill states” [34], authored by Jacob Hastrup and Ulrik L. Andersen. This work is published at Quantum Science and Technology.

© 2021 IOP Publishing Ltd

8.1 Abstract

The Gottesman-Kitaev-Preskill encoding of a qubit in a harmonic oscillator is a promising building block towards fault-tolerant quantum computation. Recently, this encoding was experimentally demonstrated for the first time in trapped-ion and superconducting circuit systems. However, these systems lack some of the Gaussian operations which are critical to efficiently manipulate the encoded qubits. In particular, homodyne detection, which is the go-to method for efficient readout of the encoded qubit in the vast majority of theoretical work, is not readily available, heavily limiting the readout fidelity. Here, we present an alternative read-out strategy designed for qubit-coupled systems. Our method can improve the readout fidelity with several orders of magnitude for such systems and, surprisingly, even surpass the fidelity of homodyne detection in the low squeezing regime.

8.2 Introduction

Scalable fault-tolerant quantum computation requires physical qubits which can be stored, manipulated and read-out with very high fidelity. One promising approach for realising such high quality qubits, which has received an increasing attention in recent years, is to encode each qubit into the bosonic mode of a quantum harmonic oscillator, such as the motion of a trapped particle, or a microwave or an optical field mode. There are several proposals for such encodings [26, 28, 43, 48, 61, 62, 65, 82, 105, 126], including the Gottesman-Kitaev-Preskill (GKP)

code [28, 43, 48, 105, 126] which has many advantageous properties. In particular, with GKP states, a universal set of operations can be performed using solely Gaussian resources [124, 149], which are generally considered easy and efficient to implement, particularly in optics. Additionally GKP states can be combined with continuous variable cluster states [72, 129] or the surface code [131, 135] to achieve fault-tolerance. Furthermore, the GKP code has been shown to outperform other encoding schemes in terms of its efficiency in correcting against loss [53, 55], which is the main noise factor in many bosonic systems.

These favourable features have sparked numerous new studies on applying GKP states for optical quantum computing [74, 75, 105]. Still, the generation of GKP states in the optical regime has proven extremely challenging and has so far not been demonstrated experimentally, despite several theoretical proposals [88–91, 150]. However, recently GKP states were generated for the first time in the motional state of a trapped ion [43] and in a microwave cavity field coupled to a superconducting circuit [48]. These experiments were made possible by the strong coupling between a bosonic mode and an ancillary qubit, enabling non-Gaussian transformations of the bosonic mode, which is required to produce GKP states. Yet, these experimental platforms lack some of the crucial Gaussian operations that are required for complete manipulation, stabilization and read-out of the encoded GKP qubit [28]. Therefore, new methods specifically designed to qubit-coupled systems are required to take full advantage of the GKP encoding in these systems. For example, stabilization has already been demonstrated using the qubit-coupling [48], but the lack of homodyne detection, i.e. direct measurement of the bosonic quadrature operators, severely limits the read-out fidelity [126].

Here we propose an improved readout scheme for qubit-coupled GKP states. Our method relies on mapping the logical information of the GKP qubit onto the ancilla qubit state. This is similar to the known method based on phase-estimation [79], but by adding an additional interaction between the qubit and the oscillator, we achieve much higher read-out fidelity. In particular, for a GKP state composed of peaks of width Δ , the read-out error of our scheme scales as Δ^6 whereas the previously used method based on qubit-coupling scales as Δ^2 . Thus, as an example, for a 10 dB squeezed GKP state our method improves the read-out fidelity from 96.22% with known techniques to 99.98%.

8.3 Preliminaries

We consider GKP states which are encoded into a bosonic mode with quadrature operators \hat{q} and \hat{p} satisfying $[\hat{q}, \hat{p}] = i$. The code states of the square GKP encoding are defined in the common +1 eigenspace of the commuting displacement operators $\hat{D}(\sqrt{2\pi})$ and $\hat{D}(i\sqrt{2\pi})$, where $\hat{D}(\alpha) = e^{\sqrt{2}i(-\text{Re}[\alpha]\hat{p} + \text{Im}[\alpha]\hat{q})}$. The computational basis states are then defined as the ± 1 eigenstates of $\hat{D}(i\sqrt{\pi/2})$, which acts as a logical Pauli Z operator. However, ideal GKP states are unphysical, as they require infinite energy. Instead, the physically relevant basis states are thus only approximate eigenstates of the logical Pauli Z operator, i.e. $\langle \hat{D}(i\sqrt{\pi/2}) \rangle \approx \pm 1$. There are multiple ways of expressing such approximate states. In this work we consider the commonly used expression for which the basis states consist of a superposition of multiple squeezed states

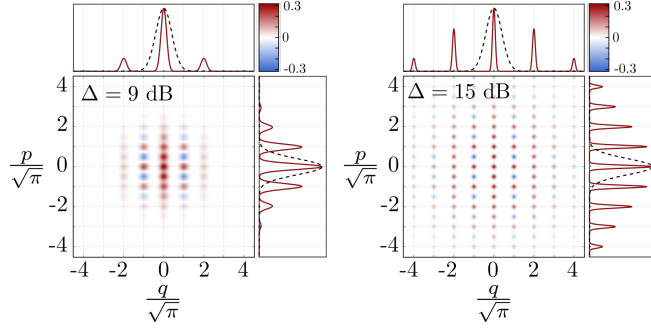


Figure 8.1: Wigner functions and quadrature distributions of the approximate GKP states given by Eq. (8.1a) for symmetric $\Delta = \kappa^{-1}$ with 9 and 15 dB squeezing respectively. The dashed lines in the quadrature distributions show the vacuum quadrature distribution (not normalized) for comparison.

of width Δ , under a Gaussian envelope of width κ :

$$|\tilde{0}\rangle \propto \sum_{s \in \mathbb{Z}} e^{-(\sqrt{\pi/2}2s)^2/\kappa^2} \hat{D}\left(\sqrt{\frac{\pi}{2}}2s\right) \hat{S}_\Delta |\text{vac}\rangle \quad (8.1a)$$

$$|\tilde{1}\rangle \propto \sum_{s \in \mathbb{Z}} e^{-(\sqrt{\pi/2}(2s+1))^2/\kappa^2} \hat{D}\left(\sqrt{\frac{\pi}{2}}(2s+1)\right) \hat{S}_\Delta |\text{vac}\rangle, \quad (8.1b)$$

where $|\text{vac}\rangle$ is the vacuum state and $\hat{S}_\Delta = e^{-\frac{i}{2} \ln(\Delta)(\hat{q}\hat{p} + \hat{p}\hat{q})}$ is the squeezing operator. These approximate code states approach the ideal states for $(\Delta, \kappa^{-1}) \rightarrow 0$. The amount of squeezing is often expressed in dB as $\Delta_{\text{dB}} = -10 \log_{10}(\Delta^2)$. Fig. 8.1 shows example Wigner functions and quadrature distributions of the GKP $|\tilde{0}\rangle$ states with 9 and 15 dB squeezing respectively. For comparison, experimentally produced states have so far demonstrated measured stabilizer expectation values of $\langle \hat{D}(\sqrt{2\pi}) \rangle = 0.56$ and $\langle \hat{D}(i\sqrt{2\pi}) \rangle = 0.41$ corresponding to effective squeezing levels [101] of 5.5-7.3 dB in a trapped ion [43] and $\langle \hat{D}(\sqrt{2\pi}) \rangle = 0.62$ and $\langle \hat{D}(i\sqrt{2\pi}) \rangle = 0.5$ corresponding to 6.6-8.2 dB effective squeezing in a microwave cavity [48]. Note that since the measurement of the stabilizers in these experiments are prone to imperfections during the measurement process, the actual squeezing levels could be slightly higher and care should be taken when directly comparing the different platforms. In principle, the protocols used in those experiments can produce arbitrarily large amounts of squeezing, but in practice the performance is limited by noise, such as bosonic dephasing and losses as well as errors introduced via qubit couplings [43, 48].

It is common to consider the symmetric case where $\Delta = \kappa^{-1}$, but in this paper only Δ is relevant, as we consider only read-out in the computational, i.e., Pauli Z basis. If instead one wishes to read out the GKP qubit in the Pauli X basis, this is done by changing $\hat{q} \rightarrow \hat{p}$ and $\hat{p} \rightarrow -\hat{q}$ in the following operations in which case κ^{-1} becomes the relevant quantity. While we initially consider the pure states of (8.1) we will later turn to more realistic mixed states.

We now consider the problem of how to reliably distinguish between the states $|\tilde{0}\rangle$ and $|\tilde{1}\rangle$ in a physically relevant setting. In particular, we wish to minimize the measurement error probability

$$p_{\text{err}} = \frac{1}{2}(p(1|0) + p(0|1)), \quad (8.2)$$

where $p(x|y)$ is the probability of obtaining measurement outcome x given the input state y .

Since the approximate states $|\tilde{0}\rangle$ and $|\tilde{1}\rangle$ are not orthogonal, this problem is ultimately bounded by the Helstrom bound [56]:

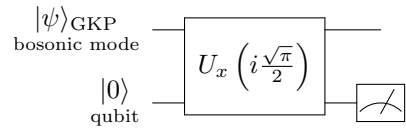
$$p_{\text{err}} \geq p_{\text{err,Helstrom}} = \frac{1}{2} \left(1 - \sqrt{1 - |\langle \tilde{0} | \tilde{1} \rangle|^2} \right). \quad (8.3)$$

The Helstrom bound drops very rapidly with decreasing Δ , but is generally not achievable in a realistic setting. Instead, homodyne detection is often considered as a practical and efficient read-out method. With this method, the state is measured in the bosonic \hat{q} -basis, and the results closer to even multiples of $\sqrt{\pi}$ are considered a 0 while results closer to an odd multiple of $\sqrt{\pi}$ are considered a 1. The measurement error probability for homodyne detection, assuming a negligible overlap between neighbouring squeezed states of the basis states, i.e. $|\langle \text{vac} | \hat{S}_\Delta^\dagger \hat{D}(\sqrt{2\pi}) \hat{S}_\Delta | \text{vac} \rangle| \approx 0$, is given by:

$$p_{\text{err,homodyne}} = \text{erfc} \left(\frac{\sqrt{\pi}}{2\Delta} \right) \approx \frac{2}{\pi} \Delta e^{-\frac{\pi}{4\Delta^2}}, \quad (8.4)$$

where the second approximation follows from a series expansion of the complementary error function. The exponential term in Eq. (8.4) causes the measurement error probability to drop rapidly with decreasing Δ , i.e. homodyne detection is very efficient for highly squeezed states.

However, while homodyne detection can be efficiently implemented in free-space optics, it is less practical for microwave cavities or trapped ions. Instead, these systems can couple to an ancilla qubit, e.g. a superconducting transmon qubit for the microwave platform or an internal spin state for the trapped ions, and the state of the ancilla qubit can subsequently be measured. In particular, it is possible to realise a Rabi-type interaction Hamiltonian, $\hat{q}\hat{\sigma}_x$, where $\hat{\sigma}_x$ is the Pauli X operator of the qubit [48, 83]. The action of this Hamiltonian is sometimes referred to as a conditional displacement, as the bosonic mode gets displaced in a direction depending on the state of the qubit, entangling the qubit and the oscillator. Such interaction can be used to read-out a GKP-qubit using the following simple circuit [43, 48, 126]:



$$\begin{array}{c} |\psi\rangle_{\text{GKP}} \\ \text{bosonic mode} \end{array} \quad \begin{array}{c} |0\rangle \\ \text{qubit} \end{array} \quad \begin{array}{c} \boxed{U_x \left(i\frac{\sqrt{\pi}}{2} \right)} \\ \text{---} \end{array} \quad \begin{array}{c} \boxed{\text{Measurement}} \end{array} \quad (8.5)$$

where

$$U_k(\beta) = \exp [i (-\text{Re}[\beta]\hat{p} + \text{Im}[\beta]\hat{q}) \hat{\sigma}_k] \quad (8.6)$$

for $k \in \{x, y, z\}$. The expected measurement outcome of the qubit is $\text{Prob}(|1\rangle) = \frac{1}{2} \left(1 - \text{Re} \langle \hat{D} \left(i\sqrt{\frac{\pi}{2}} \right) \rangle \right)$.

For ideal GKP basis states for which $\langle \hat{D} \left(i\sqrt{\frac{\pi}{2}} \right) \rangle = \pm 1$ we achieve a perfect read-out. For the approximate states $|\tilde{0}\rangle$ and $|\tilde{1}\rangle$, with negligible overlap between neighbouring squeezed states, we have $\langle \hat{D} \left(i\sqrt{\frac{\pi}{2}} \right) \rangle = \pm e^{-\frac{\pi}{4}\Delta^2}$, so the measurement error probability is:

$$p_{\text{err,simple}} = \frac{1}{2} \left(1 - e^{-\frac{\pi}{4}\Delta^2} \right) \approx \frac{\pi}{8} \Delta^2. \quad (8.7)$$

This scaling is significantly worse than the homodyne strategy of Eq. (8.4). The scaling can be improved by running the circuit multiple times and considering a majority vote, but because of the measurement back-action this strategy has diminishing returns. Additionally, multiple runs of the circuit results in an increased total measurement time during which the state accumulates noise.

8.4 Protocol

In this work we propose to modify the circuit in (8.5), adding an additional Rabi-type interaction of the type $\hat{p}\hat{\sigma}_y$ with interaction strength λ :

$$\begin{array}{c}
 |\psi\rangle_{\text{GKP}} \\
 |0\rangle
 \end{array}
 \begin{array}{c}
 \boxed{U_y(-\lambda)} \\
 \boxed{U_x\left(i\frac{\sqrt{\pi}}{2}\right)}
 \end{array}
 \begin{array}{c}
 \text{---} \\
 \text{---}
 \end{array}
 \begin{array}{c}
 \boxed{\text{---}} \\
 \boxed{\text{---}}
 \end{array}
 \quad (8.8)$$

For $|\lambda| \ll 1$, the measurement error probability of this circuit is given by (derivation given in Appendix A):

$$p_{\text{err,improved}} = \frac{1}{2} \left(1 - e^{-\frac{\pi}{4}\Delta^2} \left(e^{-\frac{\lambda^2}{\Delta^2}} + \sin(\sqrt{\pi}\lambda) \right) \right), \quad (8.9)$$

which reduces to that of Eq. (8.7) for $\lambda = 0$ as expected. However, for $\lambda \neq 0$ it is possible to achieve a better scaling. The minimum is achieved for λ satisfying $\frac{2\lambda}{\Delta^2} e^{-\lambda^2/\Delta^2} = \sqrt{\pi} \cos(\sqrt{\pi}\lambda)$, which for small Δ is approximately at $\lambda = \sqrt{\pi}\Delta^2/2$. Inserting this into Eq. (8.9) and expanding to lowest order in Δ we get:

$$p_{\text{err,improved}} \approx \underbrace{\frac{5\pi^3}{384}}_{\sim 0.4} \Delta^6, \quad (8.10)$$

i.e. a significantly better scaling than (8.7). The measurement error probabilities of the different methods are compared in Fig. 8.2a. The blue curve shows the result of circuit (8.8), with the optimum λ chosen for each point. We see a clear improvement over the simple circuit in (8.5), i.e. for $\lambda = 0$, even when using multiple runs of the simple circuit. For a squeezing of less than 9 dB the modified circuit even outperforms homodyne detection. We found that using circuit (8.8) we could not further improve the performance using multiple rounds and majority voting. This is because the measurement back-action upon getting the wrong measurement heavily modifies the input state, making subsequent measurement rounds useless (see Appendix B for details). One important thing to note is, that the optimum interaction parameter, λ , depends on the quality, or Δ , of the input GKP state. This is different from the homodyne measurement strategy or the simple circuit, both of which are constructed independently on the quality of the input state. Therefore, it is important to calibrate the modified measurement circuit, i.e. tuning λ , according to the squeezing of the input state. Fig. 8.2b shows the performance when fixing λ at different values. For large amounts of squeezing we see that the circuit performs optimally only for input states in a narrow region. In a practical setting it might be difficult to consistently fix the squeezing level of the state to be measured, as it could depend on previous operations of the state. Therefore, the average measurement error probability will likely be higher than what is predicted by Eq. (8.9). However, from Fig. 8.2b we see that the results are generally improved compared to the simple circuit for a wide range of Δ .

So far we have considered only the states of Eq. (8.1). However, these states might not necessarily be physically realistic as, for example, they are pure. Instead, we can construct more general mixed GKP states by applying a Gaussian displacement channel of strength σ to the pure states of Eq. (8.1):

$$\rho_\mu = \frac{1}{\pi\sigma^2} \int d^2\alpha e^{-\frac{|\alpha|^2}{\sigma^2}} \hat{D}(\alpha) |\tilde{\mu}\rangle \langle \tilde{\mu}| \hat{D}^\dagger(\alpha), \quad (8.11)$$

where ρ_μ is the density matrix of the output state and $\mu \in \{0, 1\}$. The performance of the simple circuit (8.5) does not depend on the exact form of the input state but only on the expectation

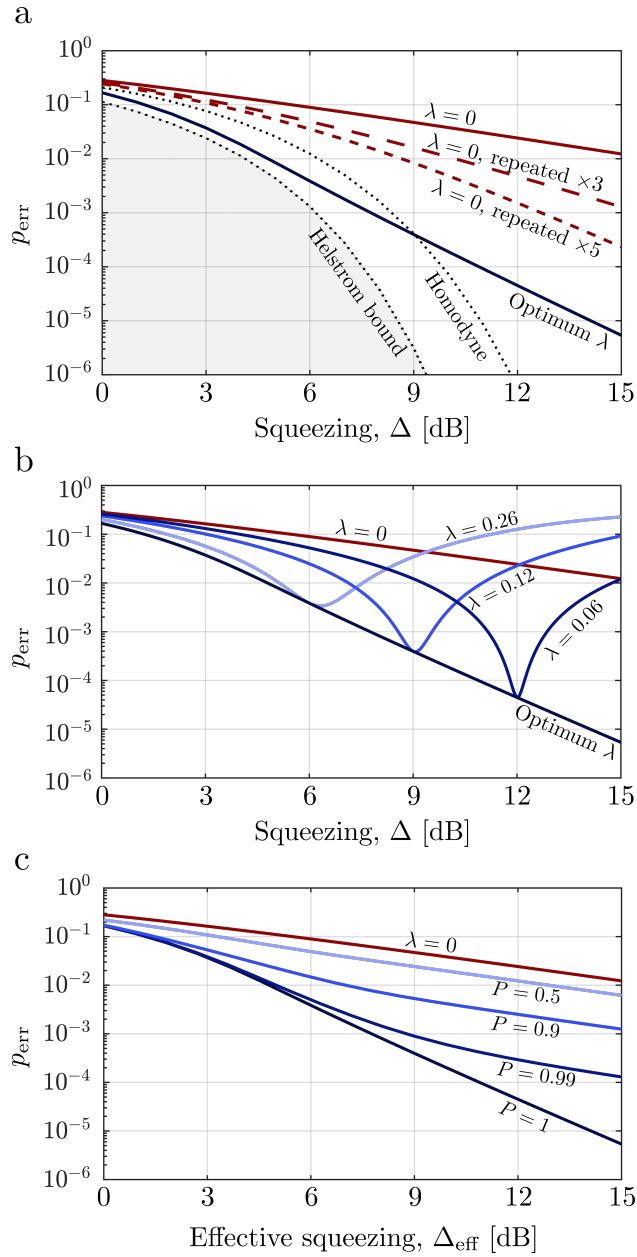


Figure 8.2: (a): Measurement error probability, p_{err} , for various measurement strategies. The red $\lambda = 0$ lines correspond to circuit (8.5), while the blue line corresponds to circuit (8.8) with the interaction parameter λ chosen to minimize p_{err} . (b): Performance for fixed λ as a function of the input squeezing. For large amounts of squeezing the optimal performance is only achieved in a narrow range, requiring good knowledge of the input state. (c): Performance for mixed states generated by applying the Gaussian displacement channel, Eq. (8.11), to the pure input states of Eq. (8.1). For such states, the purity, P , heavily impacts the performance of the protocol, although the performance is always improved compared to the simple circuit.

value $\langle \hat{D}(i\sqrt{\frac{\pi}{2}}) \rangle$. In fact, one can use a similar expectation value to define an effective squeezing parameter Δ_{eff} as [101]:

$$\Delta_{\text{eff}} = \sqrt{\frac{1}{2\pi} \ln \left(\frac{1}{|\langle \hat{D}(i\sqrt{2\pi}) \rangle|^2} \right)}, \quad (8.12)$$

allowing us to describe the amount of squeezing in an arbitrary state. For the states of Eq. (8.1) we simply have $\Delta_{\text{eff}} = \Delta$. For the mixed state of Eq. (8.11) we have $\Delta_{\text{eff}} = \sqrt{\Delta^2 + 2\sigma^2}$. By tuning Δ and σ we can thus now construct GKP states of arbitrary purity, $P = \text{Tr}(\rho^2)$, and effective squeezing. Fig. 8.2c shows the performance of the circuit for states of different purity. We see that the performance degrades for mixed states, although we still obtain superior behavior compared to the simple circuit. This performance degradation can be understood by the fact that the circuit (8.8) is not robust against shifts of the GKP state by an integer multiples of the GKP lattice spacing along the p -axis, i.e. shifts of the type $\hat{D}(i\sqrt{2\pi}n)$ for integer n . Usually, such shifts leaves the logical information of the GKP state intact, and indeed they do not affect the measurement result using homodyne detection or the simple circuit in (8.5). However, for the circuit in (8.8) we have $U_y(-\lambda)\hat{D}(i\sqrt{2\pi}n) = e^{i2n\lambda\sqrt{\pi}\hat{\sigma}_y}\hat{D}(i\sqrt{2\pi}n)U_y(-\lambda)$. Thus a displacement of one or more lattice spacings along the p -axis before the measurement circuit induces an unwanted qubit rotation around the y -axis. The mixed state can to some degree be interpreted as a pure approximate GKP state which has experienced an unknown integer lattice displacement. This therefore results in an unknown rotation of the qubit which ultimately increases the error rate of our circuit. In the literature, GKP states are commonly only quantified in terms of their squeezing level, with the purity being less relevant as it plays no role for e.g. homodyne detection. It is therefore unclear what levels can be expected in experimental setting, which will also likely vary between platforms. Note that the mixed states were constructed in one particular way in this paper, i.e. by combining Eqs. (8.1) and (8.11). The purity alone might therefore not accurately describe performance of the protocol for other states. Still, the result of Fig. 8.2c indicates that high quality states with features beyond just the squeezing are required to take full advantage of the improved measurement scheme.

8.5 Conclusion

We have presented a protocol for efficient read-out of a GKP state in a qubit-coupled oscillator. Our protocol reduces the measurement error rate from a Δ^2 -scaling with previously known methods to a Δ^6 -scaling, enabling low error rates in the absence of homodyne detection. Our protocol is sensitive to the exact form of the input state, with a reduced performance for mixed states. However, our results demonstrate that homodyne detection might not be crucial to efficiently utilize the GKP encoding, e.g. in microwave cavities or trapped ions.

Note added: After preparing this paper, we became aware of a parallel work by de Neeve et. al [111] which experimentally implements the measurement protocol presented here on a trapped-ion platform. Furthermore, they provide a physical interpretation of the improvement obtained by the added interaction. Additionally, we became aware of work by Royer et. al [151], which considers similar alternating Rabi-type interactions to autonomously generate and stabilize approximate GKP states. Those works thus complement the analysis presented in this paper.

8.6 Appendix A: Improved measurement error probability

Here we derive Eq. (8.9) of the main text. To do so we calculate the probability of measuring the qubit in state 0 after the application of circuit (8.8) with input GKP state $|\tilde{0}\rangle$ or $|\tilde{1}\rangle$. This probability is given by the norm of the (not normalized) post-measurement state, $|\langle\psi_0|\psi_0\rangle|$, where $|\psi_0\rangle = \langle 0|U_x\left(i\frac{\sqrt{\pi}}{2}\right)U_y(-\lambda)|\psi\rangle \otimes |0\rangle$ with input GKP state $|\psi\rangle$ given by Eq. (8.1). First we compute the operation $\langle 0|U_x\left(i\frac{\sqrt{\pi}}{2}\right)U_y(-\lambda)|0\rangle$. For this it is convenient to write the U gates as:

$$U_y(-\lambda) = \hat{D}_1 \otimes |+\rangle\langle +| + \hat{D}_1^\dagger \otimes |-i\rangle\langle -i| \quad (8.13)$$

$$U_x\left(i\frac{\sqrt{\pi}}{2}\right) = \hat{D}_2 \otimes |+\rangle\langle +| + \hat{D}_2^\dagger \otimes |-\rangle\langle -|, \quad (8.14)$$

where $\hat{D}_1 = \hat{D}(-\lambda/\sqrt{2})$, $\hat{D}_2 = \hat{D}(i\sqrt{\pi}/(2\sqrt{2}))$, and $|\pm i\rangle = (|0\rangle \pm i|1\rangle)/\sqrt{2}$ and $|\pm\rangle = (|0\rangle \pm |1\rangle)/\sqrt{2}$ are the Pauli- y and Pauli- x eigenstates respectively. Thus $|0\rangle = (|i\rangle + |-i\rangle)/\sqrt{2}$. From the first gate we get:

$$U_y(-\lambda)|0\rangle = \frac{1}{\sqrt{2}} \left(\hat{D}_1|i\rangle + \hat{D}_1^\dagger|-i\rangle \right) \quad (8.15)$$

Transforming the qubit states into the x -basis through $|i\rangle = e^{i\pi/4}(|+\rangle - i|-\rangle)/\sqrt{2}$ and $|-i\rangle = e^{i\pi/4}(-i|+\rangle + |-\rangle)/\sqrt{2}$, we get:

$$U_y(-\lambda)|0\rangle = \frac{e^{i\pi/4}}{2} \left[\left(\hat{D}_1 - i\hat{D}_1^\dagger \right) |+\rangle + \left(-i\hat{D}_1 + \hat{D}_1^\dagger \right) |-\rangle \right]. \quad (8.16)$$

Applying the second gate:

$$U_x\left(i\frac{\sqrt{\pi}}{2}\right)U_y(-\lambda)|0\rangle = \frac{e^{i\pi/4}}{2} \left[\hat{D}_2 \left(\hat{D}_1 - i\hat{D}_1^\dagger \right) |+\rangle + \hat{D}_2^\dagger \left(-i\hat{D}_1 + \hat{D}_1^\dagger \right) |-\rangle \right]. \quad (8.17)$$

After measuring the qubit in state $|0\rangle$:

$$\langle 0|U_x\left(i\frac{\sqrt{\pi}}{2}\right)U_y(-\lambda)|0\rangle = \frac{e^{i\pi/4}}{2\sqrt{2}} \left[\hat{D}_2\hat{D}_1 - i\hat{D}_2\hat{D}_1^\dagger - i\hat{D}_2^\dagger\hat{D}_1 + \hat{D}_2^\dagger\hat{D}_1^\dagger \right], \quad (8.18)$$

thus

$$|\psi_0\rangle = \frac{e^{i\pi/4}}{2\sqrt{2}} \left[\hat{D}_2\hat{D}_1 - i\hat{D}_2\hat{D}_1^\dagger - i\hat{D}_2^\dagger\hat{D}_1 + \hat{D}_2^\dagger\hat{D}_1^\dagger \right] |\psi\rangle. \quad (8.19)$$

We now calculate $p(0|0)$ by inserting the expression for the approximate GKP 0 state, $|\tilde{0}\rangle$ (Eq. (8.1)) and calculating the norm. Here we assume that the circuit do not cause an overlap between distinct peaks of the GKP state, which is valid for small λ . Fixing s in Eq. (8.1), the post-measurement norm of a single peak is then:

$$\begin{aligned} \frac{1}{8} |\langle \text{vac} | \hat{S}_\Delta^\dagger \hat{D} \left(\sqrt{\frac{\pi}{2}} 2s \right)^\dagger \left[\hat{D}_2\hat{D}_1 - i\hat{D}_2\hat{D}_1^\dagger - i\hat{D}_2^\dagger\hat{D}_1 + \hat{D}_2^\dagger\hat{D}_1^\dagger \right]^\dagger \\ \times \left[\hat{D}_2\hat{D}_1 - i\hat{D}_2\hat{D}_1^\dagger - i\hat{D}_2^\dagger\hat{D}_1 + \hat{D}_2^\dagger\hat{D}_1^\dagger \right] \hat{D} \left(\sqrt{\frac{\pi}{2}} 2s \right) \hat{S}_\Delta | \text{vac} \rangle|. \end{aligned} \quad (8.20)$$

This expression consists of 16 terms, which can be evaluated using the relations $\langle \text{vac} | \hat{D}(\alpha) | \text{vac} \rangle = e^{-|\alpha|^2/2}$, $\hat{D}(\beta)\hat{D}(\alpha) = e^{i\text{Im}(\beta\alpha^*)}\hat{D}(\alpha + \beta)$ and $\hat{S}_\Delta^\dagger \hat{D}(\alpha) \hat{S}_\Delta = \hat{D}(\text{Re}(\alpha)/\Delta + i\text{Im}(\alpha)\Delta)$. The 16 terms are:

$$\begin{aligned}
& \langle \text{vac} | \hat{S}_\Delta^\dagger \hat{D} \left(\sqrt{\frac{\pi}{2}} 2s \right)^\dagger \hat{D}_1 \hat{D}_2^\dagger \hat{D}_2 \hat{D}_1^\dagger \hat{D} \left(\sqrt{\frac{\pi}{2}} 2s \right) \hat{S}_\Delta | \text{vac} \rangle \\
&= \langle \text{vac} | \hat{S}_\Delta^\dagger \hat{D} \left(\sqrt{\frac{\pi}{2}} 2s \right)^\dagger \hat{D}_1^\dagger \hat{D}_2^\dagger \hat{D}_2 \hat{D}_1 \hat{D} \left(\sqrt{\frac{\pi}{2}} 2s \right) \hat{S}_\Delta | \text{vac} \rangle \\
&= \langle \text{vac} | \hat{S}_\Delta^\dagger \hat{D} \left(\sqrt{\frac{\pi}{2}} 2s \right)^\dagger \hat{D}_1 \hat{D}_2 \hat{D}_2^\dagger \hat{D}_1^\dagger \hat{D} \left(\sqrt{\frac{\pi}{2}} 2s \right) \hat{S}_\Delta | \text{vac} \rangle \\
&= \langle \text{vac} | \hat{S}_\Delta^\dagger \hat{D} \left(\sqrt{\frac{\pi}{2}} 2s \right)^\dagger \hat{D}_1^\dagger \hat{D}_2 \hat{D}_2^\dagger \hat{D}_1 \hat{D} \left(\sqrt{\frac{\pi}{2}} 2s \right) \hat{S}_\Delta | \text{vac} \rangle = 1 \tag{8.21}
\end{aligned}$$

$$\begin{aligned}
& \langle \text{vac} | \hat{S}_\Delta^\dagger \hat{D} \left(\sqrt{\frac{\pi}{2}} 2s \right)^\dagger \hat{D}_1 \hat{D}_2^\dagger \hat{D}_2 \hat{D}_1 \hat{D} \left(\sqrt{\frac{\pi}{2}} 2s \right) \hat{S}_\Delta | \text{vac} \rangle \\
&= \langle \text{vac} | \hat{S}_\Delta^\dagger \hat{D} \left(\sqrt{\frac{\pi}{2}} 2s \right)^\dagger \hat{D}_1^\dagger \hat{D}_2^\dagger \hat{D}_2 \hat{D}_1^\dagger \hat{D} \left(\sqrt{\frac{\pi}{2}} 2s \right) \hat{S}_\Delta | \text{vac} \rangle \\
&= \langle \text{vac} | \hat{S}_\Delta^\dagger \hat{D} \left(\sqrt{\frac{\pi}{2}} 2s \right)^\dagger \hat{D}_1 \hat{D}_2 \hat{D}_2^\dagger \hat{D}_1 \hat{D} \left(\sqrt{\frac{\pi}{2}} 2s \right) \hat{S}_\Delta | \text{vac} \rangle \\
&= \langle \text{vac} | \hat{S}_\Delta^\dagger \hat{D} \left(\sqrt{\frac{\pi}{2}} 2s \right)^\dagger \hat{D}_1^\dagger \hat{D}_2 \hat{D}_2^\dagger \hat{D}_1^\dagger \hat{D} \left(\sqrt{\frac{\pi}{2}} 2s \right) \hat{S}_\Delta | \text{vac} \rangle = e^{-\frac{\lambda^2}{\Delta^2}} \tag{8.22}
\end{aligned}$$

$$\begin{aligned}
& \langle \text{vac} | \hat{S}_\Delta^\dagger \hat{D} \left(\sqrt{\frac{\pi}{2}} 2s \right)^\dagger \hat{D}_1 \hat{D}_2^\dagger \hat{D}_2^\dagger \hat{D}_1^\dagger \hat{D} \left(\sqrt{\frac{\pi}{2}} 2s \right) \hat{S}_\Delta | \text{vac} \rangle \\
&= \langle \text{vac} | \hat{S}_\Delta^\dagger \hat{D} \left(\sqrt{\frac{\pi}{2}} 2s \right)^\dagger \hat{D}_1 \hat{D}_2 \hat{D}_2 \hat{D}_1^\dagger \hat{D} \left(\sqrt{\frac{\pi}{2}} 2s \right) \hat{S}_\Delta | \text{vac} \rangle^* = e^{-i2\pi s} e^{-i\sqrt{\pi}\lambda} e^{-\frac{\pi}{4}\Delta^2} \tag{8.23}
\end{aligned}$$

$$\begin{aligned}
&= \langle \text{vac} | \hat{S}_\Delta^\dagger \hat{D} \left(\sqrt{\frac{\pi}{2}} 2s \right)^\dagger \hat{D}_1^\dagger \hat{D}_2^\dagger \hat{D}_2^\dagger \hat{D}_1 \hat{D} \left(\sqrt{\frac{\pi}{2}} 2s \right) \hat{S}_\Delta | \text{vac} \rangle \\
&= \langle \text{vac} | \hat{S}_\Delta^\dagger \hat{D} \left(\sqrt{\frac{\pi}{2}} 2s \right)^\dagger \hat{D}_1^\dagger \hat{D}_2 \hat{D}_2 \hat{D}_1 \hat{D} \left(\sqrt{\frac{\pi}{2}} 2s \right) \hat{S}_\Delta | \text{vac} \rangle^* = e^{-i2\pi s} e^{i\sqrt{\pi}\lambda} e^{-\frac{\pi}{4}\Delta^2} \tag{8.24}
\end{aligned}$$

$$\begin{aligned}
& \langle \text{vac} | \hat{S}_\Delta^\dagger \hat{D} \left(\sqrt{\frac{\pi}{2}} 2s \right)^\dagger \hat{D}_1 \hat{D}_2^\dagger \hat{D}_2^\dagger \hat{D}_1 \hat{D} \left(\sqrt{\frac{\pi}{2}} 2s \right) \hat{S}_\Delta | \text{vac} \rangle \\
&= \langle \text{vac} | \hat{S}_\Delta^\dagger \hat{D} \left(\sqrt{\frac{\pi}{2}} 2s \right)^\dagger \hat{D}_1^\dagger \hat{D}_2^\dagger \hat{D}_2^\dagger \hat{D}_1^\dagger \hat{D} \left(\sqrt{\frac{\pi}{2}} 2s \right) \hat{S}_\Delta | \text{vac} \rangle \\
&= \langle \text{vac} | \hat{S}_\Delta^\dagger \hat{D} \left(\sqrt{\frac{\pi}{2}} 2s \right)^\dagger \hat{D}_1 \hat{D}_2 \hat{D}_2 \hat{D}_1 \hat{D} \left(\sqrt{\frac{\pi}{2}} 2s \right) \hat{S}_\Delta | \text{vac} \rangle^* \\
&= \langle \text{vac} | \hat{S}_\Delta^\dagger \hat{D} \left(\sqrt{\frac{\pi}{2}} 2s \right)^\dagger \hat{D}_1^\dagger \hat{D}_2 \hat{D}_2 \hat{D}_1^\dagger \hat{D} \left(\sqrt{\frac{\pi}{2}} 2s \right) \hat{S}_\Delta | \text{vac} \rangle^* = e^{-i2\pi s} e^{-\frac{\lambda^2}{\Delta^2}} e^{-\frac{\pi}{4}\Delta^2}. \tag{8.25}
\end{aligned}$$

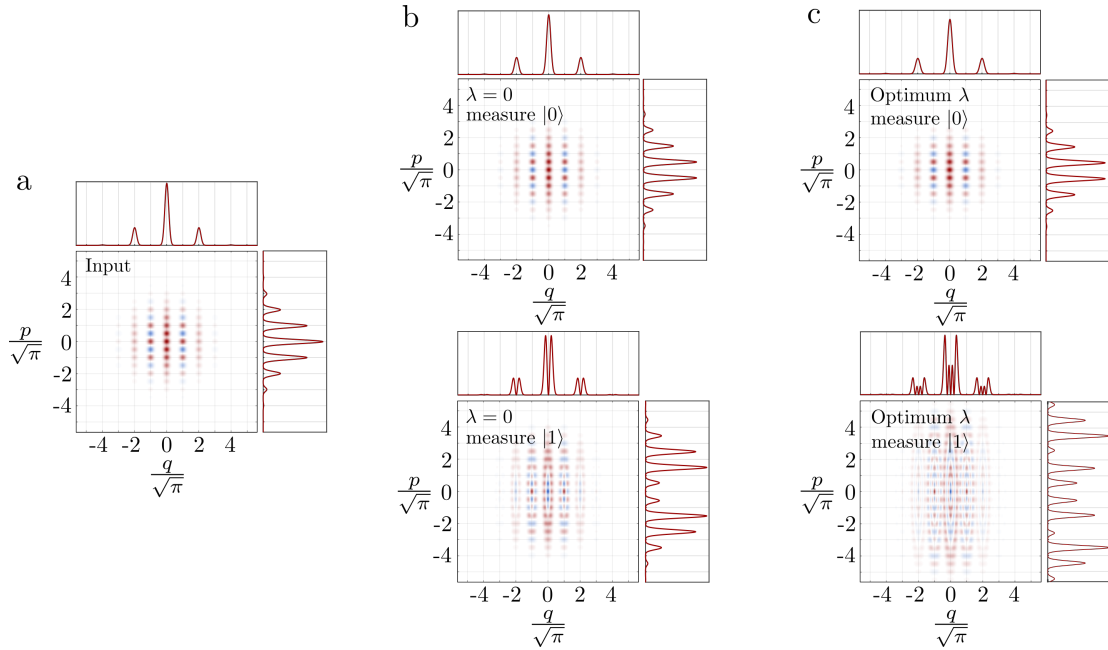


Figure 8.3: (a): Approximate GKP state $|\tilde{0}\rangle$ with 10 dB squeezing. (b): Wigner functions and quadrature distributions of the post-measurement states of the simple circuit (8.5) upon measuring the qubit in states $|0\rangle$ and $|1\rangle$ respectively, given the input state shown in (a). (c): Post-measurement states for the improved circuit (8.8).

Inserting these into Eq. (8.20) we find that each peak contributes with:

$$\frac{1}{2} \left[1 + e^{-\frac{\pi}{4}\Delta^2} \cos(2\pi s) \left(e^{-\frac{\lambda^2}{\Delta^2}} + \sin(\sqrt{\pi}\lambda) \right) \right]. \quad (8.26)$$

Since s is an integer, i.e. $\cos(2\pi s) = 1$, all peaks contribute equally (apart from their initial weighting from the broad Gaussian envelope), and the measurement error probability for the GKP 0 state is thus

$$p(1|0) = 1 - p(0|0) = \frac{1}{2} \left[1 - e^{-\frac{\pi}{4}\Delta^2} \left(e^{-\frac{\lambda^2}{\Delta^2}} + \sin(\sqrt{\pi}\lambda) \right) \right]. \quad (8.27)$$

Similarly, we can calculate the probability $p(0|1)$ by considering the input state $|\tilde{1}\rangle$ for which the result can be obtained directly from Eq. (8.26) by changing $s \rightarrow s + \frac{1}{2}$. In this case $\cos(2\pi s) = -1$ and we get

$$p(0|1) = p(1|0). \quad (8.28)$$

Thus in total the measurement error probability is

$$p_{\text{err}} = \frac{1}{2}(p(0|1) + p(1|0)) = p(0|1) = \frac{1}{2} \left[1 - e^{-\frac{\pi}{4}\Delta^2} \left(e^{-\frac{\lambda^2}{\Delta^2}} + \sin(\sqrt{\pi}\lambda) \right) \right]. \quad (8.29)$$

8.7 Appendix B: Post-measurement state

Since we don't directly measure the bosonic mode, one could try to repeat the measurement circuit to gain more accurate information on the input state. However, the qubit measurement

also projects the bosonic mode into a post-measurement state, which is not necessarily suitable for following operations or measurements. In Fig. 8.3 we show the Wigner functions and quadrature distributions of the post-measurement states for a 10 dB input GKP $|\tilde{0}\rangle$ state. Fig. 8.3b shows the post-measurement states for the qubit results $|0\rangle$ and $|1\rangle$ using the simple circuit in (8.5), while Fig. 8.3c shows the post-measurement states when using the improved circuit in (8.8). In both cases, observation of the wrong qubit measurement outcome, i.e. observing $|1\rangle$ with input state $|\tilde{0}\rangle$ heavily distorts the input GKP state. For this reason, subsequent measurements yield less reliable results, which limits the effect of multiple measurements on the same state. For the improved circuit the post-measurement state is even more distorted compared to the simple circuit. Thus we found that multiple runs of the improved circuit does not further reduce the measurement error.

The repeated measurement of the simple circuit can also be considered as an instance of the non-adaptive phase estimation protocol to prepare approximate GKP states presented in [79]. In that work it is shown that some unlikely measurement outcomes can lead to erroneous states, just like the distorted state in Fig. 8.3b. Furthermore, it was shown that the probability of obtaining such poor states could be lowered by applying an adaptive measurement sequence. It might therefore be possible to further lower the error rate by applying an adaptive measurement strategy through repeated use of the improved circuit, but with settings based on previous qubit measurements. We leave this an interesting open direction for further research.

Chapter 9

Unconditional preparation of squeezed vacuum from Rabi interactions

In this chapter we present the paper “Unconditional preparation of squeezed vacuum from Rabi interactions” [35], authored by Jacob Hastrup, Kimin Park, Radim Filip and Ulrik L. Andersen. This work is published in Physical Review Letters.

© 2021 American Physical Society

9.1 Abstract

Squeezed states of harmonic oscillators are a central resource for continuous-variable quantum sensing, computation and communication. Here we propose a method for the generation of very good approximations to highly squeezed vacuum states with low excess anti-squeezing using only a few oscillator-qubit coupling gates through a Rabi-type interaction Hamiltonian. This interaction can be implemented with several different methods, which has previously been demonstrated in superconducting circuit and trapped-ion platforms. The protocol is compatible with other protocols manipulating quantum harmonic oscillators, thus facilitating scalable continuous-variable fault-tolerant quantum computation.

9.2 Introduction

Quantum continuous variables have become an increasingly promising platform for quantum information processing [152]. In particular, extraordinary experimental progress has been made over the last few years in trapped-ion and superconducting circuit platforms towards fault-tolerant quantum computation [48, 65, 82]. One of the most promising routes towards fault-tolerant continuous-variable quantum computation is the Gottesman-Kitaev-Preskill encoding [28], which has gained substantial interest over the past few years due to experimental and theoretical developments [43, 48, 126]. For this encoding, highly squeezed states are an important resource for constructing high-quality states [33, 43, 79]. The current record for squeezed vacuum

is 15 dB [44] in an optical field using a parametric amplifier. However, non-Gaussian operations are difficult to realise efficiently in the optical regime, and thus it is challenging with current technology to further utilize this highly squeezed state for quantum computation.

On the other hand, qubit-coupled oscillators, such as a motional state of a trapped ion or a microwave cavity field coupled to a superconducting qubit can be manipulated with non-Gaussian operations via the qubit ancilla. In fact, universal control of the harmonic oscillator is in principle possible in such systems [137, 139], although many protocols, such as squeezed state preparation, require specialized methods to be efficient. 12.6 dB squeezing has been reported in the motional state of a trapped ion [46] using a reservoir engineering technique [153]. This technique has the advantage of achieving squeezing in a steady-state configuration, thus facilitating the experimental implementation. However, the process utilizes spontaneous relaxation processes, the rates of which limits the speed at which the state is created and thus ultimately the achievable squeezing due to dephasing during the protocol. In the microwave regime 10 dB squeezing has been experimentally demonstrated [148]. This was achieved using a parametric amplifier realised by a metamaterial consisting of multiple Josephson junctions.

Here we propose a method for the preparation of an approximate squeezed vacuum state in an oscillator strongly coupled to a qubit using only a few unitary interactions through the Rabi Hamiltonian [141, 142]. This Hamiltonian has been experimentally demonstrated in trapped ions and superconducting circuits [48, 83, 154, 155], and plays a key role in the Gottesman-Kitaev-Preskill encoding scheme of these platforms [43, 48, 126]. Thus the protocol facilitates the generation of highly squeezed states using a method that is compatible with further manipulation of the oscillator. Our protocol for the generation of squeezed vacuum is radically different from the common approach based on parametric amplification, and represents a fundamentally new view on squeezed vacuum generation. The obtainable amount of squeezing depends on the types and magnitude of noise in the particular system, but can generally be improved through faster interactions, e.g. through an increased power of the driving fields which control the interaction. Furthermore, the achievable amount of Fisher information is particularly robust against qubit errors during the protocol, making the generated states useful for sensing applications [156–162]. In particular, squeezed states can be used to detect displacements in the considered platforms using either the qubit-coupling [101] or homodyne detection [163]. Finally, squeezed states serve as a fundamental resource for continuous variable communication [152] which could find applications facilitating short-range connections in microwave circuits [164].

9.3 Protocol

We consider a quantum harmonic oscillator described by the quadrature operators \hat{X} and \hat{P} satisfying $[\hat{X}, \hat{P}] = i$. In the vacuum state the oscillator exhibits equal fluctuations in each quadrature of magnitude $\langle \hat{X}^2 \rangle = \langle \hat{P}^2 \rangle = \frac{1}{2}$. The aim of the protocol is to generate a state squeezed in the P -quadrature by a relative amount $\Delta^2 < 1$ such that $\langle \hat{P}^2 \rangle = \frac{\Delta^2}{2}$. The protocol can straightforwardly be generalized to generate squeezing along an arbitrary quadrature direction, either by a rotation from the natural evolution of an the squeezed state under a harmonic potential, or by a suitable change of quadrature operators during the protocol. It is common to quantify the squeezing in dB relative to the vacuum as $\Delta_{\text{dB}} = -10 \log_{10}(\Delta^2)$. A pure squeezed

vacuum state, $|\text{sqvac}\rangle_\Delta$, can be written in the P -, X - and coherent state bases as:

$$|\text{sqvac}\rangle_\Delta \propto \int dp \exp\left(-\frac{p^2}{2\Delta^2}\right) |p\rangle \quad (9.1a)$$

$$\propto \int dx \exp\left(-\frac{x^2}{2\Delta^{-2}}\right) |x\rangle \quad (9.1b)$$

$$\propto \int d\alpha \exp\left(-\frac{\alpha^2}{\Delta^{-2}-1}\right) |\alpha\rangle, \quad (9.1c)$$

where the last line is only valid for $\Delta < 1$ and the integral is over real α . The coherent states with real α are defined as $|\alpha\rangle = e^{-i\sqrt{2}\alpha\hat{P}}|\text{vac}\rangle \propto \int dx \exp\left(-\frac{(x - \sqrt{2}\alpha)^2}{2}\right) |x\rangle$. For our approach, it is useful to view the squeezed state in the coherent state basis, as our strategy will be to directly construct a superposition of coherent states which resembles (9.1c). Since the coherent states form an overcomplete basis with large overlap between close-lying states, we can expect that equation (9.1c) holds to a good approximation even if we discretize the integral:

$$|\text{sqvac}\rangle_\Delta \approx \sum_{\alpha_s \in \mathcal{L}} \exp\left(-\frac{\alpha_s^2}{\Delta^{-2}-1}\right) |\alpha_s\rangle, \quad (9.2)$$

where \mathcal{L} is a lattice on the real line. While the right hand side of Eq. (9.2) is technically a non-Gaussian state, we find that Eq. (9.2) is a good approximation for a lattice spacing of up to ~ 1.5 , which is on the order of the width of a coherent state (details are presented in the Supplementary Material S1, 9.5). It is therefore possible to construct a highly squeezed state, practically indistinguishable from a Gaussian squeezed state, from a relatively sparse superposition of coherent states. A probabilistic method based on this approach was proposed in [165].

We now present a deterministic method to efficiently construct such a superposition of coherent states using a qubit ancilla. The circuit diagram of the protocol is shown in Fig. 9.1a. We use two Rabi-type interaction Hamiltonians $\hat{P}\hat{\sigma}_x$ and $\hat{X}\hat{\sigma}_y$ [141, 142], where $\hat{\sigma}_x$ and $\hat{\sigma}_y$ are the Pauli x and y operators of the qubit. Such Hamiltonians can be efficiently implemented [45, 48, 166, 167], e.g. using a two-tone drive which has been experimentally demonstrated in trapped-ions [83, 154] or from a dispersive Jaynes-Cumming Hamiltonian which has been demonstrated in superconducting circuits [48, 155]. The protocol consists of N pairs of different interactions. The first type of interaction, $\hat{U}_k = \exp(iu_k\hat{P}\hat{\sigma}_x)$, displaces the oscillator in a direction depending on the state of the qubit, while the following interaction, $\hat{V}_k = \exp(iv_k\hat{X}\hat{\sigma}_y)$, approximately disentangles the qubit and the oscillator. The repeated application of these interactions creates a superposition of 2^N coherent states, and leaves the qubit back in the ground state. Note that the interactions used are conceptually similar to the protocol in Ref. [33] which aims to generate a grid state starting from squeezed vacuum. However, unlike this previous work, our target state consists of overlapping coherent states, for which the approximations used in Ref. [33] do not hold. In this work, we show that this limitation can be overcome surprisingly well by numerically optimizing the interaction parameters, u_k and v_k , for each step, which enables the generation of squeezed states using Rabi interactions. Still, to understand why the protocol works and to have a good initial guess from which to optimize the interaction parameters, it is instructive to

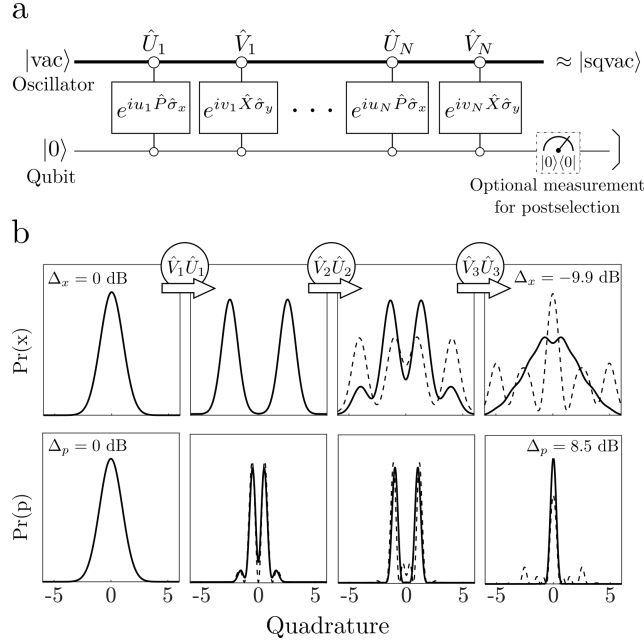


Figure 9.1: (a) Circuit diagram for the generation of a P -squeezed vacuum state. The protocol consists of N steps of interactions through the Hamiltonians $\hat{P}\hat{\sigma}_x$ and $\hat{X}\hat{\sigma}_y$. The interaction parameters u_k and v_k varies from step to step and are found numerically to optimize the protocol. The protocol is deterministic, but the performance can be slightly improved by measuring the qubit and postselecting on the outcome 0. (b) Evolution of the quadrature distributions during each step of the protocol. Dashed lines correspond to interaction parameters given by Eq. (9.3) with $L = 0.45$ and solid lines correspond to numerically optimized interaction parameters. Note that the negative squeezing value in dB here denotes anti-squeezing.

consider a specific set of interaction parameters given by

$$u_k = \begin{cases} 2^{N-1}\sqrt{2}L, & \text{if } k = 1, \\ -2^{N-k}\sqrt{2}L & \text{if } k > 1, \end{cases} \quad (9.3a)$$

$$v_k = \begin{cases} 2^{-(N-k)}\frac{\pi}{4\sqrt{2}L}, & \text{if } k < N, \\ -\frac{\pi}{4\sqrt{2}L} & \text{if } k = N, \end{cases} \quad (9.3b)$$

where L is a free parameter, which determines the spacing of the resulting grid of coherent states. Each step aims to double the number of coherent states in the superposition. The first interaction, \hat{U}_1 , displaces the oscillator and entangles it with the qubit:

$$\hat{U}_1|\text{vac}\rangle|0\rangle = \frac{1}{\sqrt{2}} (|-2^{N-1}L\rangle|+\rangle + |2^{N-1}L\rangle|-\rangle). \quad (9.4)$$

Measuring the qubit in the in the $|0\rangle = (|+\rangle + |-\rangle)/\sqrt{2}$ or $|1\rangle = (|+\rangle - |-\rangle)/\sqrt{2}$ state leaves the oscillator in a superposition of two coherent states, known as a Schrödinger's cat state, which has been experimentally demonstrated using exactly this type of interaction [155]. In our protocol, however, we do not require qubit measurements to disentangle the qubit and the oscillator.

Instead, we apply a second interaction, \hat{V}_1 , which approximately disentangles the qubit and the oscillator,

$$\begin{aligned}
\hat{V}_1 \hat{U}_1 |\text{vac}\rangle |0\rangle &= \frac{1}{\sqrt{2}} \hat{V}_1 (|-2^{N-1}L\rangle |+\rangle + |2^{N-1}L\rangle |-\rangle) \\
&= \frac{e^{-i\pi/4}}{2} \left(\left[e^{-i\pi/8} |-2^{N-1}L + i\frac{v_1}{\sqrt{2}}\rangle + ie^{i\pi/8} |2^{N-1}L + i\frac{v_1}{\sqrt{2}}\rangle \right] |+\rangle \right. \\
&\quad \left. + \left[ie^{i\pi/8} |-2^{N-1}L - i\frac{v_1}{\sqrt{2}}\rangle + e^{-i\pi/8} |2^{N-1}L - i\frac{v_1}{\sqrt{2}}\rangle \right] |-\rangle \right) \\
&= \frac{1}{\sqrt{2}} (|2^{N-1}L\rangle - |-2^{N-1}L\rangle) |1\rangle + \mathcal{O}(v_1), \tag{9.5}
\end{aligned}$$

where $|\pm i\rangle = (|0\rangle \pm i|1\rangle)$ are the $\hat{\sigma}_y$ eigenstates, which are related to the $\hat{\sigma}_x$ eigenstates as $|+\rangle = e^{-i\pi/4}(|i\rangle + i| -i\rangle)/\sqrt{2}$ and $|-\rangle = e^{-i\pi/4}(|i\rangle - i| -i\rangle)/\sqrt{2}$. In the last line we have used the relation $\langle \beta|\alpha\rangle = e^{i\text{Im}(\beta^*\alpha)} e^{-|\beta-\alpha|^2/2}$ to write $|-2^{N-1}L \pm iv_1/\sqrt{2}\rangle = e^{\pm i\pi/8} |-2^{N-1}L\rangle + \mathcal{O}(v_1)$, where $\mathcal{O}(v_1)$ denotes terms on the order v_1 , which can be neglected when the coherent states are well separated, i.e. when $2^N L \gg 1$. Note that due to the complete absence of a measurement, the method does not rely on neither postselection or active feed-forward. Moreover, we circumvent accumulated measurement-induced noise such as measurement errors and bosonic noise. Each subsequent pair of interactions splits each coherent state into two, doubling the total number of peaks. Thus after all N steps we produce the state:

$$\prod_k^N \hat{V}_k \hat{U}_k |\text{vac}\rangle |0\rangle \approx \left(\sum_{s=0}^{2^N-1} |(2s+1-2^N)L\rangle \right) |0\rangle, \tag{9.6}$$

i.e. the oscillator ends in a superposition of multiple coherent states, similar to the target state of Eq. (9.2). However, there are two main issues with Eq. (9.6): First, the result yields an equal superposition of the coherent states, whereas our target state is convolved with a Gaussian envelope. Secondly, the approximation of Eq. (9.6) is only valid when the coherent states are sufficiently well separated, but to obtain a good approximation to a squeezed state, the coherent states need to be overlapping. It turns out that one can overcome these issues surprisingly well by tuning the interaction strengths of the protocol. This is illustrated in Fig. 9.1b, showing the quadrature distributions of the oscillator for each step of the protocol. The solid lines represent the distributions using numerically optimized parameters while the dashed lines show the result for the parameters given by Eq. (9.3). Using the parameters of Eq. (9.3), the final P-quadrature distribution has side-lobes which effectively reduces $\langle \hat{P}^2 \rangle$ to that of vacuum. For the numerically optimized parameters, however, these lobes vanish, thus yielding a highly squeezed state. There are multiple reasons why the protocol is improved by tuning the interaction parameters. Firstly, by tuning the strengths of the second interaction, v_k , the qubit and the oscillator do not completely disentangle, so the subsequent controlled displacement, \hat{U}_{k+1} , does not split each peak equally, but with a preferred direction, resulting in an unequal final distribution. This enables us to obtain an approximately Gaussian envelope over the resulting superposition as in Eq. (9.2). Additionally, as the states start to overlap, the disentangling interactions, \hat{V}_k , have to be adjusted to optimize the disentanglement between the oscillator and qubit in the final step. Furthermore, when the coherent states of unequal amplitude are overlapping their peaks are effectively slightly shifted, which can be corrected by tuning the displacement interactions, \hat{U}_k .

In Fig. 9.1b we have chosen the interaction parameters to optimize only the squeezing in the P quadrature, yielding $\Delta_p = 8.5$ dB for $N = 3$. The anti-squeezing in the X quadrature is slightly

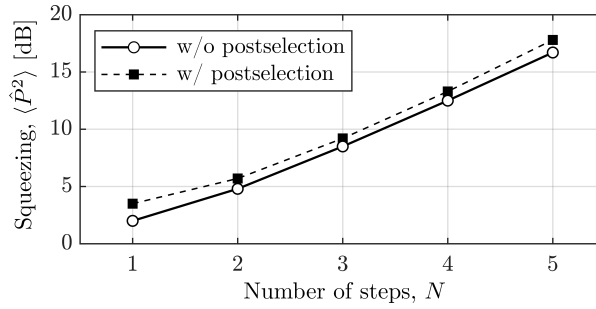


Figure 9.2: Resulting squeezing as a function of the number of steps of the protocol. For each step, the squeezing increases with ~ 3 -4 dB. The dashed curve corresponds to adding the optional measurement in Fig. 9.1a and post-selecting on the outcome $|0\rangle$, which occurs with high probability.

in excess, $\Delta_x = -9.9$ dB, due to the underlying non-Gaussianity of the state, but still quite close to the transform-limit, showing that the output is a good approximation to a pure squeezed vacuum state. Still, even lower anti-squeezing is possible without significantly compromising the squeezing by choosing the interaction parameters differently, e.g. one can obtain $\Delta_p = 8.0$ dB with $\Delta_x = -8.3$ dB (see Supplementary Material S2).

The resulting squeezing for the numerically optimized parameters is shown by the circles in Fig. 9.2. Only a few number of steps is required to generate a highly squeezed state, which is expected as the number of coherent states in the superposition increases exponentially with N . It is possible to further improve this result by roughly 1 dB by post-selecting states for which the qubit is measured in the $|0\rangle$ state after all interactions. The protocol should leave the qubit in state $|0\rangle$ according to Eq. (9.6), but since this is an approximate result, a projection onto $|0\rangle$ helps improving this approximation. A post-selectable result therefore also occurs with high probability. Note that while the produced states are fundamentally non-Gaussian, due to the finite and discrete number of underlying coherent states, the output is practically indistinguishable from a Gaussian squeezed state. We confirm this in the Supplementary Material S1, showing that the generated states have fidelities of > 0.99 with respect to pure Gaussian squeezed vacuum states.

From Fig. 9.2 we see that increasing the number of interactions monotonically increases the resulting squeezing. Thus the protocol can fundamentally be scaled to achieve large amounts of squeezing. However, real physical systems are affected by noise, such as dephasing and loss, which will accumulate during the protocol. Assuming the time for each interaction is proportional to the absolute interaction parameter, the total protocol duration roughly doubles each time N is augmented, as the interaction parameters approximately scale as 2^N according to Eqs. (9.3). The increased squeezing therefore eventually gets counteracted by the accumulated noise. To study the effects of noise, we simulate the protocol using the Master equation,

$$\frac{d\rho}{dt} = -\frac{i}{\hbar}[\hat{H}, \rho] + \hat{L}\rho\hat{L}^\dagger - \frac{1}{2}(\hat{L}^\dagger\hat{L}\rho + \rho\hat{L}^\dagger\hat{L}), \quad (9.7)$$

where ρ is the density matrix of the composite boson-qubit system. The Hamiltonian, \hat{H} , is $\pm\frac{\hbar}{T}\hat{P}\hat{\sigma}_x$ or $\pm\frac{\hbar}{T}\hat{X}\hat{\sigma}_y$ during the two types of interactions, where the sign depends on the sign of the interaction parameter and T is a timescale denoting the time required to implement $\exp(i\hat{P}\hat{\sigma}_x)$ or $\exp(i\hat{X}\hat{\sigma}_y)$. Thus the first interaction takes place in a time Tu_1 after which the interaction Hamiltonian abruptly changes to the next one. \hat{L} is the Lindblad noise operator,

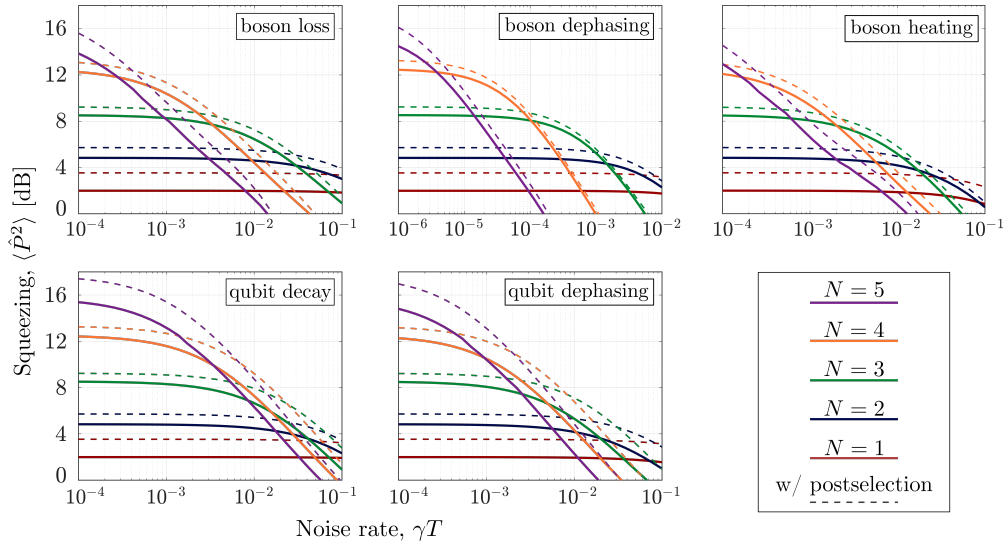


Figure 9.3: Obtainable squeezing as a function of noise rate for different noise sources. For each noise source and noise rate, there exists an optimal number of steps. Post-selecting on the outcome $|0\rangle$ can in some case improve the performance by more than 2 dB.

which determines the type of noise. We consider five types:

- Boson loss: $\hat{L} = \sqrt{\gamma}\hat{a}$
- Boson dephasing: $\hat{L} = \sqrt{\gamma}(\hat{a}\hat{a}^\dagger + \hat{a}^\dagger\hat{a})$
- Boson heating¹: $\hat{L}_1 = \sqrt{\gamma}\hat{a}, \hat{L}_2 = \sqrt{\gamma}\hat{a}^\dagger$
- Qubit decay: $\hat{L} = \sqrt{\gamma}(\hat{\sigma}_x + i\hat{\sigma}_y)/2$
- Qubit dephasing: $\hat{L} = \sqrt{\gamma}\hat{\sigma}_z$

where γ is the noise rate and $\hat{a} = (\hat{X} + i\hat{P})/\sqrt{2}$ is the bosonic annihilation operator. The results are shown in Fig. 9.3. For each noise source and noise rate we find that there exists an optimum number of interactions. Bosonic noise is seen to have a bigger impact compared to qubit noise. Especially boson dephasing can heavily reduce the obtained squeezing, which is expected as squeezed states are generally sensitive to dephasing. The dashed lines show the outcomes which are post-selected on measuring the qubit in state $|0\rangle$. We observe that the positive effect of post-selection is now slightly larger compared to Fig. 9.2, especially for qubit-associated noise. This is because the noise can result in the qubit ending up in the $|1\rangle$ state, in which case the presence of noise can be detected and the event discarded. The post-selection strategy can therefore effectively reduce the effect of noise.

A key property of squeezed states is their ability to detect displacements [156–158], which is quantified by the Fisher information [168], I_C . While the quadrature squeezing is affected by

¹Boson heating is described by two Lindblad operators with strengths dependent on the temperature of the environment bath, $\hat{L}_1 = \sqrt{\gamma_c(1+\bar{n})}\hat{a}$ and $\hat{L}_2 = \sqrt{\gamma_c\bar{n}}\hat{a}^\dagger$, where γ_c is the coupling rate to the bath with mean occupation number \bar{n} . Here we define the heating rate $\gamma_c\bar{n} \equiv \gamma$ and assume $\bar{n} \gg 1$ such that $\gamma_c(1+\bar{n}) \approx \gamma_c\bar{n}$ to isolate the effect of heating rather than thermalization.

all noise types, the Fisher information turns out to be quite robust against qubit errors, as we show in the Supplementary Material S3. For example, for $N = 4$ with a qubit decay rate of $\gamma T = 7 \times 10^{-1}$ we calculate $I_C = 56$, which is equivalent to that of an 11.5 dB squeezed vacuum state. Thus the generated states can still be useful for sensing applications, even though they are generated under noisy conditions.

Finally, we benchmark our approach using noise figures from two recent experiments which implement exactly the types of interactions needed for our protocol in trapped ions [43] and microwave cavities [48]. For the parameters in [43] we calculate 9.3 dB squeezing and a Fisher information of $I_C = 63$ (equivalent to a 11.9 dB squeezed state) using $N = 4$. While this is slightly lower than the 12.6 dB reported in the trapped ion experiment in Ref. [46], we point out that in their experiment the quadrature squeezing was not measured directly, but estimated using only the phonon population distribution. Since the quadrature squeezing is sensitive to small fluctuations and the coherence of the state, the 12.6 dB is likely overestimating the actual squeezing of the generated state. For the parameters in [48] we obtain an optimum squeezing of 7.0 dB at $N = 3$, and an optimum Fisher information at of $I_C = 86$ (equivalent to a 13.3 dB squeezed state) at $N = 5$. The high Fisher information relative to the quadrature squeezing is due to the effect of qubit errors. In particular, these errors translate into non-Gaussian features of the output state which primarily degrade the quadrature squeezing (see Supplementary Material S3 for elaborate discussion).

9.4 Conclusion

In conclusion, we have presented a deterministic protocol to produce a squeezed vacuum state via sequential application of two non-commuting Rabi Hamiltonians of the form $\hat{P}\hat{\sigma}_x$ and $\hat{X}\hat{\sigma}_y$. This interaction can currently be implemented via various methods in trapped-ion and circuit QED systems, but the protocol is not fundamentally limited to those systems and could be relevant for other qubit-oscillator platforms. Unlike previous methods, the protocol deterministically builds the squeezed state through a discrete superposition of coherent states. The protocol does not inherently require qubit measurements, but the performance can be slightly improved by post-selecting on the state of the qubit. The possible amount of quadrature squeezing is ultimately limited by decoherence mechanisms of either the bosonic or qubit modes, while the achievable Fisher information is mainly limited by bosonic noise, and both can be improved by increasing the interaction strength and thus the speed of the protocol.

9.5 S1: Discrete coherent state representation of squeezed vacuum

Here we numerically examine the approximation of Eq. (9.2) of the main text. Specifically, we consider a superposition of equally spaced coherent states with spacing $d\alpha$:

$$|\psi\rangle = \sum_{s=-\infty}^{\infty} \exp\left(-\frac{(d\alpha(s+1/2))^2}{\Delta^{-2}-1}\right) |d\alpha(s+1/2)\rangle \quad (9.8)$$

Fig. 9.4a shows the squeezing of the state, and the fidelity, $|\langle\psi|\text{sqvac}\rangle_{\Delta}|^2$, to the target squeezed vacuum state as a function of $d\alpha$ and Δ . For sufficiently small spacing, $d\alpha \lesssim 1.5$, we observe an excellent agreement between the expected and target squeezing level as well as a high fidelity to the target state. Note that for high squeezing, the squeezing levels can be significantly smaller

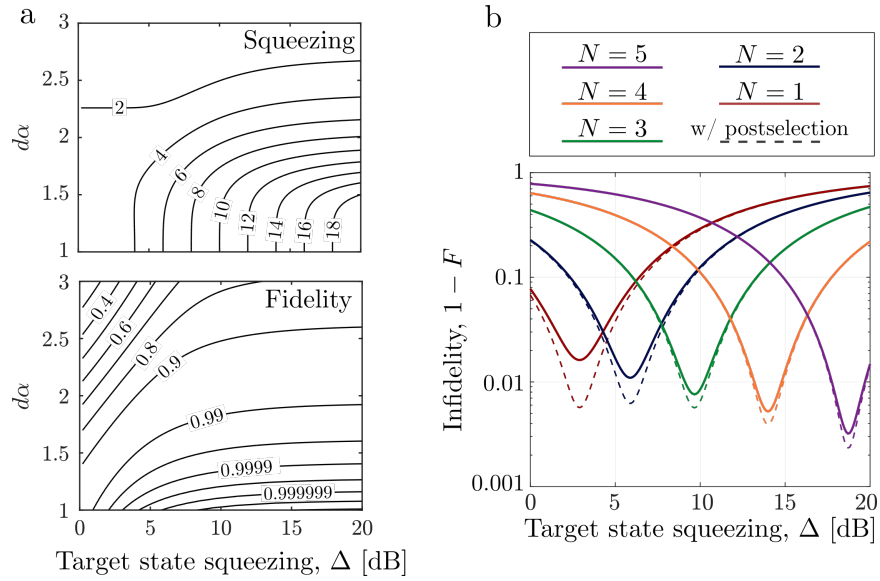


Figure 9.4: (a) Squeezing in dB and fidelity of the coherent state superposition of Eq. (9.8). For $d\alpha \lesssim 1.5$ the squeezing level matches that of the target squeezed vacuum state, and the fidelity is very high, confirming the approximation of Eq. (9.2). (b) Infidelity between the state generated by our protocol and a pure squeezed vacuum state with squeezing parameter Δ .

than the target, even if the fidelity is very high, e.g. for $\Delta = 20$ dB at $d\alpha = 2$. This is because the squeezing level is very sensitive to the small non-Gaussian features which arise from the discretization of Eq. (9.8), which is not captured by the fidelity. For this reason we have chosen the squeezing level as the relevant figure of merit throughout this paper.

In Fig. 9.4b we show the fidelity of the states generated in our protocol with respect to pure Gaussian squeezed vacuum states. For each N the interaction parameters were chosen to optimize the quadrature squeezing and not the fidelity. Yet, the produced states have fidelities of $F > 0.99$, confirming that the generated states are indeed very close to Gaussian squeezed states.

9.6 S2: Optimizing excess anti-squeezing

In the main text we chose the interaction parameters to optimize the quadrature squeezing, i.e. by minimizing $\langle \hat{P}^2 \rangle$. This results in an anti-squeezing a few dB above the transform limit, such that $\langle \hat{P}^2 \rangle \langle \hat{X}^2 \rangle > \frac{1}{4}$. However, it is possible to reduce the amount of excess anti-squeezing by choosing the interaction parameters slightly differently. For example, one can optimize the function $\langle \hat{P}^2 \rangle^{1-w} \left(\langle \hat{P}^2 \rangle \langle \hat{X}^2 \rangle \right)^w$, where w is a weight parameter determining the relative weight between squeezing and excess anti-squeezing. For $w = 0$ we recover the result from the main text. Fig. 9.5 shows the obtainable amount of squeezing and anti-squeezing as a function of w . In conclusion, one can reduce the anti-squeezing to a level close to the transform limit, while only slightly decreasing the squeezing.

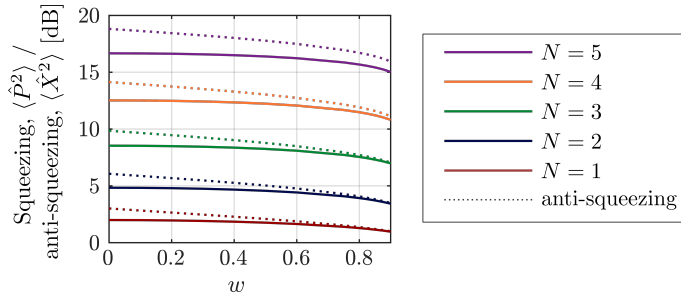


Figure 9.5: Obtainable amount of squeezing and anti-squeezing as a function of the weight parameter w described in the supplementary text 9.6. By appropriately choosing w one can reduce the excess anti-squeezing without significantly compromising the squeezing.

9.7 S3: Fisher information

Squeezed states are useful for detecting small quadrature displacements with a precision beyond the standard quantum limit set by the vacuum state. In a practical setting, the capability of the state to measure a small momentum displacement, d , caused by the displacement operator $\hat{D}(id) = e^{i\sqrt{2}d\hat{X}}$ is given by the classical Fisher information, I_C , with respect to homodyne detection [168]:

$$I_C = 2 \int dp \left(\frac{\partial}{\partial p} \log |\psi(p)|^2 \right)^2 |\psi(p)|^2, \quad (9.9)$$

where $|\psi(p)|^2 = \text{Tr}(\rho|p\rangle\langle p|)$ is the p -quadrature probability density. For a Gaussian state the Fisher information is directly related to the quadrature variance as

$$I_C = 2/(\langle \hat{P}^2 \rangle - \langle \hat{P} \rangle^2), \quad (\text{Gaussian states}) \quad (9.10)$$

On the other hand, for non-Gaussian states the quadrature variance does not necessarily capture the sensing properties of non-Gaussian states. The underlying steps of our protocol are non-Gaussian, and thus the noise accumulated during the protocol can enhance the non-Gaussian properties of the final state. This non-Gaussianity can heavily reduce the quadrature squeezing, without impacting the Fisher information much, and thus the quadrature squeezing does not necessarily capture the quality of the produced states. Fig. 9.6a shows the calculated Fisher information of the state prepared by a noisy protocol, similar to Fig. 9.3 of the main text. We observe that qubit errors have a significantly smaller impact on the Fisher information compared to the squeezing of Fig. 9.3. Bosonic noise, on the other hand, also impacts the Fisher information, although the Fisher information of the obtained state is generally higher than what would be expected from a Gaussian state with squeezing given by Fig. 9.3. The difference between the bosonic and qubit noise can be understood by looking at the resulting quadrature distribution. Fig. 9.6b shows the resulting distributions from a protocol affected by bosonic loss (i) and qubit decay (ii) respectively. While both states have a low amount of squeezing in terms of the variance, the state affected by qubit decay has a much narrower peak, resulting in a higher Fisher information. Thus for sensing applications, the quality of the prepared states is primarily limited by bosonic noise and less by qubit noise.

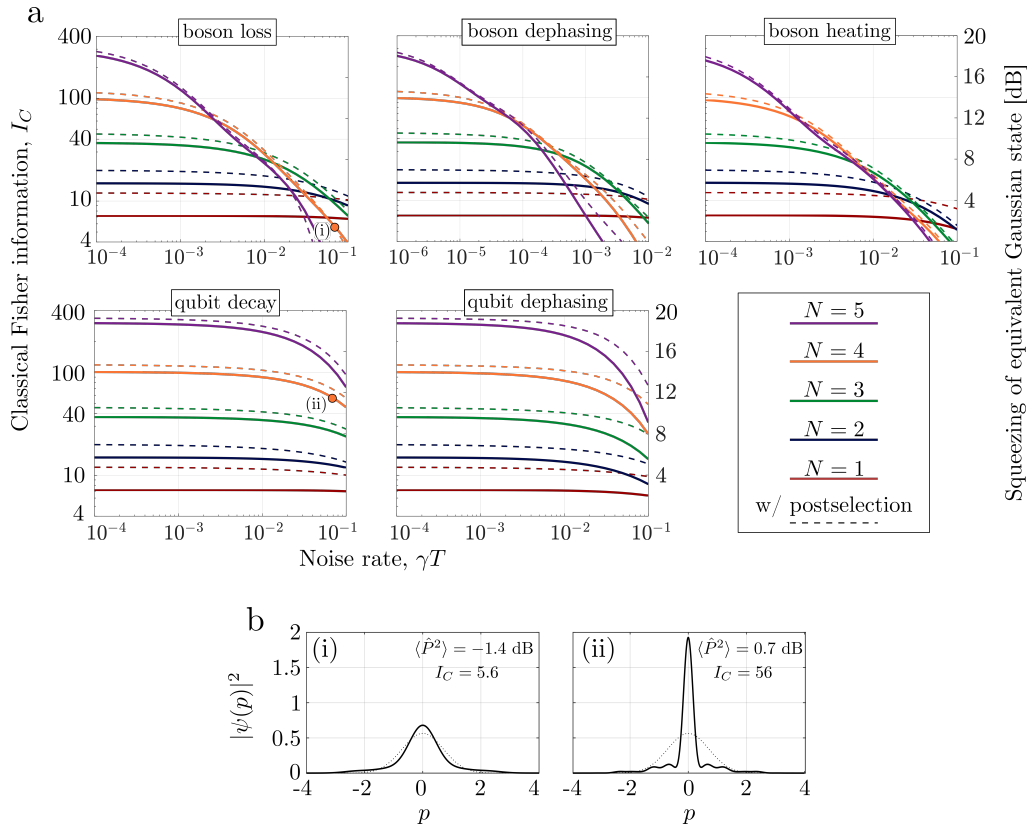


Figure 9.6: (a) Classical Fisher information, I_C , as a function of noise rate for various noise sources applied during the protocol. The Fisher information can also be expressed in terms of the amount of squeezing required in a Gaussian state to achieve the same I_C , through Eq. (9.10), which is shown on the right axis. (b) Example momentum quadrature distributions of the generated states suffering from (i) boson loss and (ii) qubit decay during the preparation protocol, with $\gamma T = 7 \times 10^{-2}$, as marked in (a). The dotted lines show the quadrature distribution of vacuum for comparison.

Chapter 10

Universal unitary transfer of continuous-variable quantum states into a few qubits

In this chapter we present the paper “Universal unitary transfer of [36] continuous-variable quantum states into a few qubits”, authored by Jacob Hastrup, Kimin Park, Jonatan B. Brask, Radim Filip and Ulrik L. Andersen. This work is submitted for publication and is available at arxiv.org (arXiv:2106.12272).

10.1 Abstract

We present a protocol for transferring arbitrary continuous-variable quantum states into a few discrete-variable qubits and back. The protocol is deterministic and utilizes only two-mode Rabi-type interactions which are readily available in trapped-ion and superconducting circuit platforms. The inevitable errors caused by transferring an infinite-dimensional state into a finite-dimensional register are suppressed exponentially with the number of qubits. Furthermore, the encoded states exhibit robustness against noise, such as dephasing and amplitude damping, acting on the qubits. Our protocol thus provides a powerful and flexible tool for discrete-continuous hybrid quantum systems.

10.2 Introduction

Quantum information processing (QIP) can be realized using both discrete variables (DV), such as the energy levels of atoms or superconducting qubits, or continuous variables (CV) [84], such as the quadratures of an electromagnetic field, spin ensemble or mechanical oscillator. Both types of systems have various advantages and disadvantages, depending on the particular task, application and implementation. For example, universal control of noisy many-qubit systems has become available [14], but truly scalable systems and break-even error correction remains to be demonstrated. On the other hand, CV QIP is highly scalable, allowing long range interactions which has been used to demonstrate entanglement of millions of modes [73] and generation of 2D

cluster-states [74,75] with current technology. Furthermore, the infinite dimensionality of a single CV mode can be utilized for hardware-efficient single-mode error correction [48,65,82,111] and high-dimensional operations, such as the quantum Fourier transform, can be implemented with simple, single-mode operations [84]. However, non-Gaussian operations required for universal quantum processing and fault tolerance have proven difficult to realize in pure CV systems.

Two of the leading platforms for quantum computing are trapped ions and superconducting circuits. These systems support both DV QIP through spin or charge qubits, as well as CV QIP through motional modes or microwave cavity modes. Furthermore, the CV and DV modes can couple, enabling CV-DV hybrid interactions. In fact, it is common to utilize this hybrid interaction to enable various operations. For example, for DV QIP, the CV modes can be used to facilitate multi-mode operations and qubit read-out [47,169]. Meanwhile, for CV QIP, the DV modes are used to enable non-Gaussian operations [48,65,82,111] which are required for universality. Thus CV-DV hybrid interactions have proven valuable in overcoming the challenges associated with either CV or DV QIP.

Here, we add a new element to the toolbox of CV-DV hybrid operations by showing that arbitrary quantum states can be coherently and deterministically mapped between a CV mode and a collection of qubits using accessible two-mode interactions. This mapping has several potential applications for QIP. For example, our scheme enables qubit-based memories for CV states. Many types of CV QIP relies on heralded, non-deterministic operations and are therefore dependent on quantum memories. A qubit-based memory could enable DV error correction protocols to be carried out on arbitrary CV states. Additionally, if the qubits are coupled to two different CV modes, e.g. transmon qubits coupled to both a mechanical acoustic mode and a microwave cavity mode, one CV mode can be encoded to the qubits and then decoded onto the other CV mode, enabling qubit-mediated transfer of CV information from one CV mode to another. Furthermore, our scheme can also be used for efficient deterministic generation of arbitrary CV states, such as non-Gaussian states, by preparing the qubits in an equivalent encoded state and then applying the inverse mapping to transfer the state to the CV mode. In general, applications of this protocol will strongly depend on the physical system but promise to aid in solving a wide range of issues in hybrid QIP platforms.

Unlike previous proposal for transferring CV states onto qubits [170,171], our protocol makes efficient use of the available qubit dimensionality, such that only a few qubits are required, while also using experimentally available interactions.

10.3 Protocol

The system we are considering consists of a single CV mode and $N > 1$ qubits, as illustrated in Fig. 10.1a. The protocol is designed to transfer an arbitrary CV state $|\psi\rangle_{\text{CV}}$ into an entangled state of the qubits, leaving the CV mode in an input-independent state, which we denote $|\tilde{0}\rangle_{\text{CV}}$. Since the CV mode has an infinite dimensionality while the qubits have a finite dimension, such a protocol is in principle impossible for arbitrary states. However, in practice we can expect relevant input CV states to have majority of their support in a finite-dimensional subspace, thereby allowing a CV-DV mapping to a good approximation. Furthermore, since the dimension of the qubit subspace scales exponentially, i.e. 2^N , with the number of qubits, N , we can expect the approximation to become very good with only a few qubits. In general, the protocol can be described by the following unitary operation:

$$\hat{U}\left[|\psi\rangle_{\text{CV}}|\mathbf{0}\rangle_{\text{DV}}\right] = \sqrt{(1-\varepsilon)}|\tilde{0}\rangle_{\text{CV}}|\Psi\rangle_{\text{DV}} + \sqrt{\varepsilon}|\Phi_\varepsilon\rangle_{\text{CV/DV}}, \quad (10.1)$$

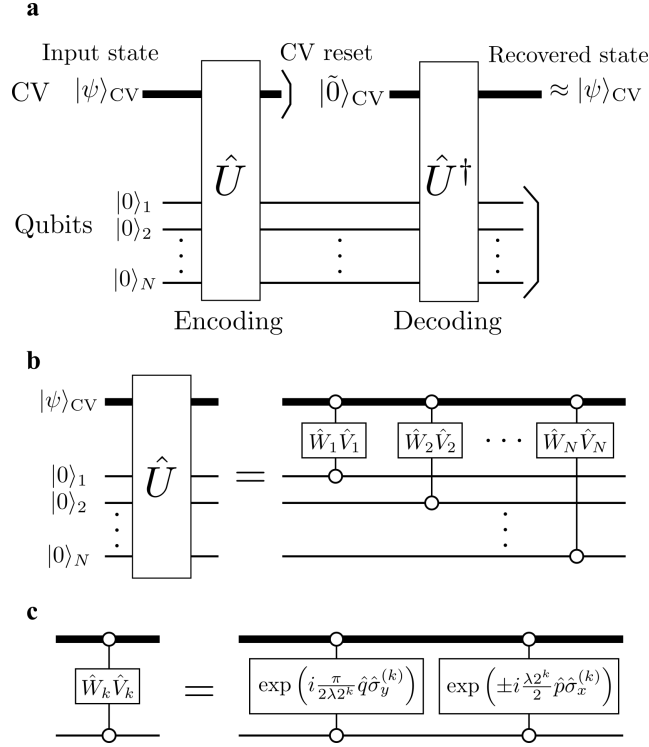


Figure 10.1: (a): Circuit of encoding and decoding to transfer a CV state to a collection of qubits and back. (b): The encoding is achieved by interacting the CV mode sequentially with each of the qubits. (c): Each interaction unitary is composed of two Rabi interactions as given by equation (10.3).

where $|\mathbf{0}\rangle_{\text{DV}} = \bigotimes_{k=1}^N |0\rangle_k$ is the product of the ground states of the qubits, $|\Psi\rangle_{\text{DV}}$ is the encoded DV state and $|\Phi_\varepsilon\rangle_{\text{CV/DV}}$ is a residual entangled CV-DV state defined to make \hat{U} unitary and such that $\langle \Phi_\varepsilon | \tilde{0} \rangle = 0$. ε is a real parameter, $0 \leq \varepsilon \leq 1$, quantifying the error of the protocol, e.g. due to the CV-DV dimensionally mismatch. ε thus depends on the input state, and a successful protocol should aim to minimize ε for a large class of input states.

The input state can be recovered by applying \hat{U}^\dagger . If the CV mode is completely reset to the state $|\tilde{0}\rangle_{\text{CV}}$ after the application of \hat{U} , the fidelity, F , between the input and recovered state is related to ε by:

$$(1 - \varepsilon)^2 \leq F \leq 1 - \varepsilon, \quad (10.2)$$

with the exact value of F depending on the input state (details are given in the Supplementary Material).

We now show how to decompose \hat{U} into experimentally accessible two-mode interactions. A circuit diagram of the encoding unitary is shown in Fig. 10.1b. It consists of N interaction terms, each of which are composed of two interactions, \hat{V}_k and \hat{W}_k , between the CV mode and one of the qubits. These interactions are conditional displacements [45,48,83] which are generated by a Rabi-type Hamiltonian, i.e. a coupling between a quadrature operator of the CV mode and

a Pauli operator of the qubit:

$$\begin{aligned} \hat{V}_k &= \exp\left(i\frac{\pi}{2\lambda 2^k}\hat{q}\hat{\sigma}_y^{(k)}\right) \\ \hat{W}_k &= \begin{cases} \exp\left(i\frac{\lambda 2^k}{2}\hat{p}\hat{\sigma}_x^{(k)}\right), & \text{if } k < N \\ \exp\left(-i\frac{\lambda 2^k}{2}\hat{p}\hat{\sigma}_x^{(k)}\right), & \text{if } k = N \end{cases} \end{aligned} \quad (10.3)$$

where \hat{q} and \hat{p} are the quadrature operators of the CV mode satisfying the commutation relation $[\hat{q}, \hat{p}] = i$ and $\sigma_x^{(k)}$ and $\sigma_y^{(k)}$ are the Pauli- x and y operators of the k 'th qubit. The interaction parameter λ is the only free parameter of the protocol. As we show below, it should be optimized according to the number of qubits and the size of the input state, i.e. the wideness of the support of the input state in phase space. Importantly, a single value of λ can be used to encode a wide range of different CV states, meaning that little knowledge of the input CV state is required for the protocol to work.

In the Supplementary Material we show that the interactions defined in Eqs. (10.3) achieves the desired unitary operation of equation (10.1) for arbitrary states, with ε decreasing with N . The qubit state after the interaction is:

$$|\Psi\rangle_{\text{DV}} \propto \sum_{\mathbf{s}} \psi(q_{\mathbf{s}})|\phi_{\mathbf{s}}\rangle, \quad (10.4)$$

where the sum is over 2^N terms, $|\phi_{\mathbf{s}}\rangle$ form a specific orthonormal basis of the qubit space, ψ is the q -quadrature wavefunction of the input CV state and $q_{\mathbf{s}}$ form an equidistant array of 2^N numbers from $-\lambda(2^N - 1)$ to $\lambda(2^N - 1)$ with spacing 2λ (see Supplementary Material for details). Thus the qubit state samples the wave function at 2^N discrete points. From this feature we can intuitively understand how we should tune λ : First, to accurately capture variations in the CV wavefunction, the distance between the samples should be smaller than any large variation of ψ , i.e. 2λ should be sufficiently small. Second, to capture the entire wavefunction the sampling axis should be sufficiently wide, i.e. $\lambda(2^N - 1)$ should be large. Satisfying both of these constraints becomes easier for larger N , and for fixed N we can expect an optimum λ to exist.

The state $|\tilde{0}\rangle_{\text{CV}}$ is given by:

$$|\tilde{0}\rangle_{\text{CV}} = \frac{1}{\sqrt{2\lambda}} \int dq \operatorname{sinc}\left(\pi\frac{q}{2\lambda}\right) |q\rangle \quad (10.5)$$

where $\operatorname{sinc}(x) = \sin(x)/x$ and $|q\rangle$ denotes a \hat{q} eigenstate, e.g. $\hat{q}|q\rangle = q|q\rangle$. To decode the CV state with the inverse unitary, \hat{U}^\dagger , the CV mode should first be prepared in the state $|\tilde{0}\rangle_{\text{CV}}$. Since the encoding protocol approximately leaves the CV mode in state $|\tilde{0}\rangle_{\text{CV}}$, this can be done by applying \hat{U} to an arbitrary CV state, e.g. vacuum or a thermal state, along with ancillary qubits. In fact, to prepare $|\tilde{0}\rangle_{\text{CV}}$ it suffices to use the same qubit for all N interactions, by resetting the qubit to its ground state after each $\hat{W}\hat{V}$ interaction. Alternatively, $|\tilde{0}\rangle_{\text{CV}}$ can be approximated with fidelity 0.89 by a squeezed vacuum state with squeezing parameter $\log(1.12/\lambda)$ (details in the Supplementary Material). We note that the exact state $|\tilde{0}\rangle_{\text{CV}}$ is in fact unphysical, as it has infinite energy since $\langle\tilde{0}|\hat{q}^2|\tilde{0}\rangle = \infty$ for all λ . However, finite energy states, e.g. the state prepared by applying \hat{U} to vacuum, can approximate $|\tilde{0}\rangle_{\text{CV}}$ with high fidelity.

An example of the encoding and recovery of a CV Schrödinger's cat state is shown in Fig. 10.2. Fig. 10.2e shows how the input CV wavefunction is directly mapped onto the qubits (with a suitable qubit basis choice). Meanwhile, Fig. 10.2b shows how the CV mode approximately

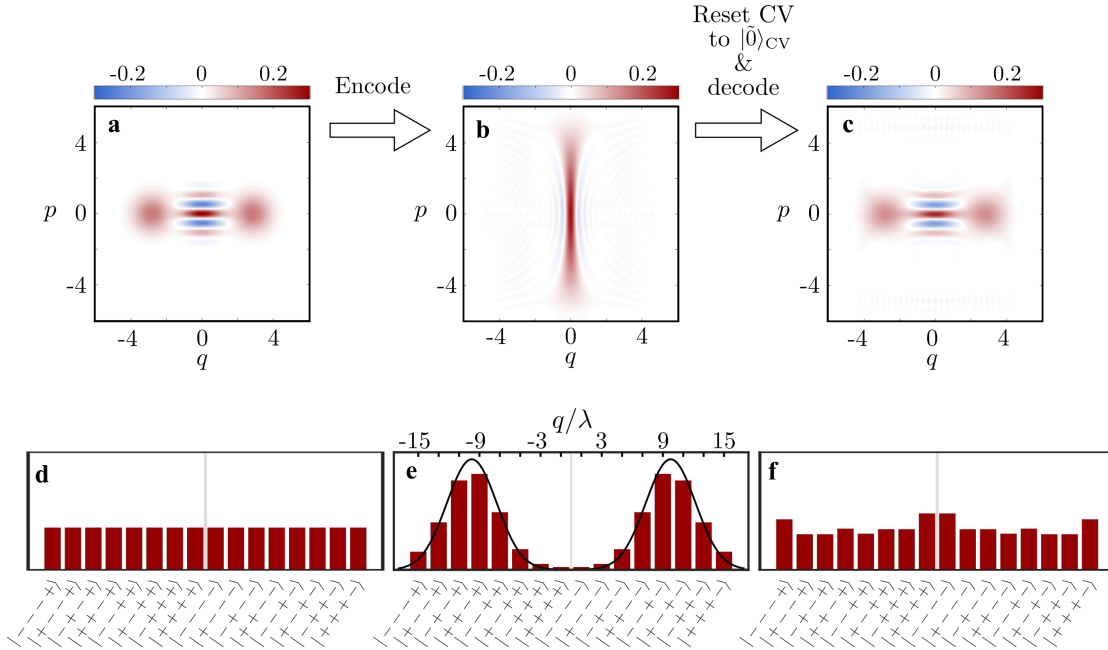


Figure 10.2: Example of encoding and recovery of a CV Schrödinger's cat state, $(e^{-i\sqrt{2}\alpha\hat{p}} + e^{i\sqrt{2}\alpha\hat{p}})|\text{vac}\rangle$ with $\alpha = 2$, using $N = 4$ qubits and $\lambda = 0.29$. Wigner functions (a,b,c) of the CV mode and probability distributions (d,e,f) of the qubits before encoding (a,d), after encoding (b,e), and after decoding (c,f) with the CV mode completely reset to the state $|\tilde{0}\rangle_{\text{CV}}$ after the encoding. The black curve in (e) shows the q quadrature distribution of the input CV state with the x-axis shown at the top of the figure.

transforms to the state $|\tilde{0}\rangle_{\text{CV}}$. The state shown in Fig. 10.2c is the recovered state after the CV mode is completely set to $|\tilde{0}\rangle_{\text{CV}}$ and the qubits are decoded onto the CV mode, i.e. as shown in the circuit of Fig. 10.1a. The small differences between Fig. 10.2a and c are due to the non-zero ε arising from the mapping. However, the key features of the CV state, such as the position of the coherent peaks and the central interference pattern with negative values are preserved.

We now numerically demonstrate this result for specific input states. We first consider Fock states, as these represent fundamental quantum basis states, spanning the entire CV mode, with experimentally relevant quantum states typically having main support on low-photon-number Fock states. Fig. 10.3a shows how ε depends on λ for $N = 4$ and $N = 10$ qubits respectively, using Fock states as inputs. For each input we find that there exists an optimum λ as expected, and that as we add more qubits, this optimum shifts to smaller values. We also find that, for any fixed λ , smaller number Fock states are better encoded than larger number Fock states. Thus one setting optimized to encode large states can simultaneously be used to encode smaller states with as good or better performance.

Fig. 10.3b shows how ε depends on the number of qubits for Fock state inputs, choosing the optimum λ for each point. We observe a clear exponential decrease in ε with increasing number of qubits. Additionally, fixing ε we find that adding a single qubit allows the storage of approximately twice as large input states, e.g. 4 qubits enable the encoding of $|1\rangle$ with $\varepsilon = 0.1$ while 5 qubits allow the encoding of $|3\rangle$ with the same error, 6 qubits can encode $|7\rangle$ and so on. This

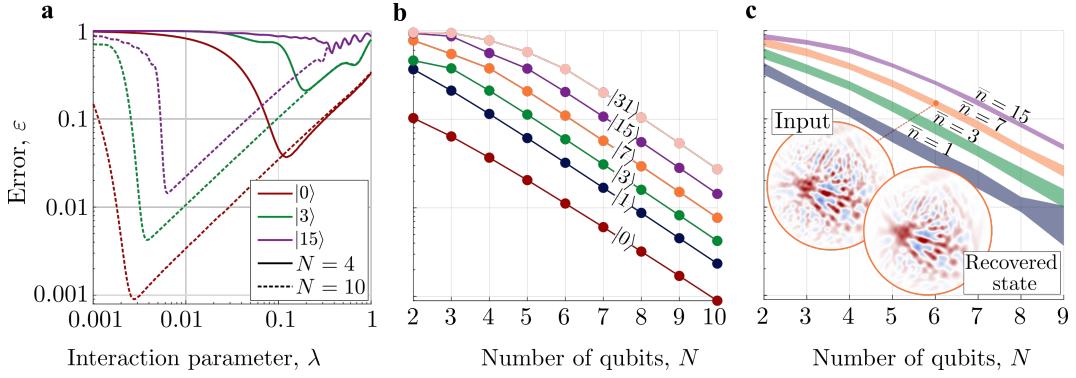


Figure 10.3: (a): Error, ε , as a function of the interaction parameter λ for $N = 4$ and 10 qubits with Fock state inputs. (b): Error as a function of qubit number for Fock state inputs using the optimal λ for each state. (c): Error as a function of qubit number randomly sampled input states with different fixed mean photon number \bar{n} . The shaded areas contains states with ε within one standard deviation from the mean ε of the sample. The inserts show the Wigner function of an example input state with $\bar{n} = 7$ and the corresponding recovered state using $N = 6$ qubits.

exponential scaling implies that very large CV states can be encoded using relatively few qubits.

To demonstrate the versatility of the protocol, Fig. 10.3c shows the performance for randomly sampled input states (see Supplementary Material for details on these states). A typical example of the Wigner function of a random state with $\bar{n} = 7$ photons is shown in the inset of Fig. 10.3c. For each N and \bar{n} in Fig. 10.3c we calculate ε for 100 of such random states using a single λ chosen to approximately optimize the average ε . The shaded area denotes the states within one standard deviation from the mean ε of the samples. As with the Fock states, we observe an exponential decrease in ε with N . In addition, we again note that adding a single qubit allows the encoding of states with approximately twice the mean photon number, keeping ε fixed.

Next, we check the stability of our scheme against errors occurring in the qubit system while the state is encoded. In particular, we consider the qubit dephasing channel,

$$\Lambda_z(\rho) = \hat{K}_z^{(1)}\rho(\hat{K}_z^{(1)})^\dagger + \hat{K}_z^{(2)}\rho(\hat{K}_z^{(2)})^\dagger, \quad (10.6)$$

and qubit amplitude damping channel

$$\Lambda_\gamma(\rho) = \hat{K}_\gamma^{(1)}\rho(\hat{K}_\gamma^{(1)})^\dagger + \hat{K}_\gamma^{(2)}\rho(\hat{K}_\gamma^{(2)})^\dagger, \quad (10.7)$$

with Kraus operators:

$$\begin{aligned} \hat{K}_z^{(1)} &= \sqrt{1-p_z}\hat{I}, & \hat{K}_z^{(2)} &= \sqrt{p_z}\hat{\sigma}_z \\ \hat{K}_\gamma^{(1)} &= |0\rangle\langle 0| + \sqrt{1-\gamma}|1\rangle\langle 1|, & \hat{K}_\gamma^{(2)} &= \sqrt{\gamma}|0\rangle\langle 1| \end{aligned} \quad (10.8)$$

where ρ denotes the qubit density matrix, p_z denotes the probability of a single-qubit phase-flip and γ denotes the probability of a single qubit decay event. Fig. 10.4a shows the fidelity of the recovered state after the CV mode is reset and each qubit have experienced either dephasing or amplitude damping for an input 5-photon Fock state, $|5\rangle$, and a random state with $\bar{n} = 3$ average photons, $|\psi_{\text{ran}}\rangle$ using $N = 6$ qubits. As can be expected, the fidelity drops as the qubits experience more noise. However, a single figure of merit, such as the fidelity, is often insufficient to

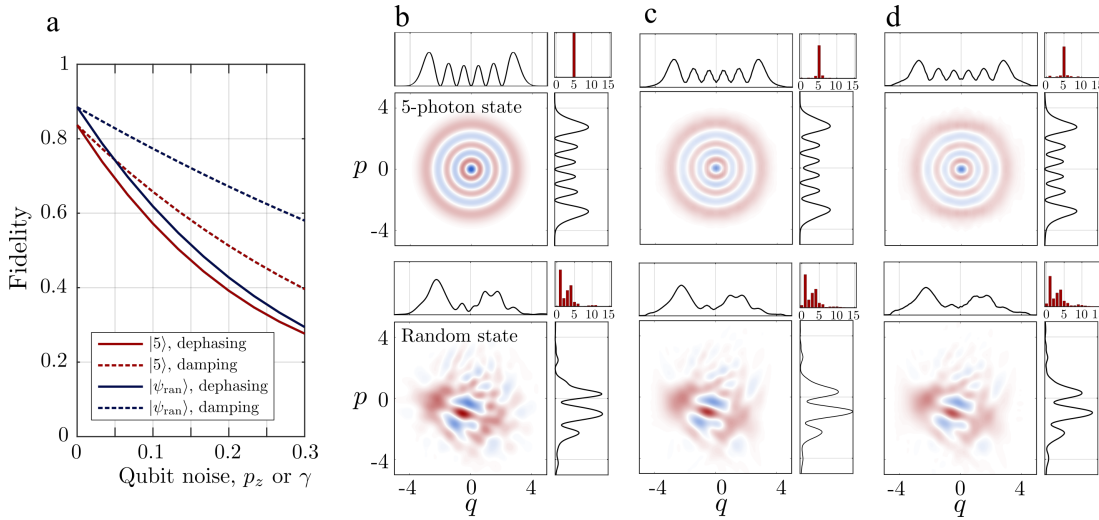


Figure 10.4: (a): Fidelity of recovered states when the qubits undergo dephasing or amplitude damping for an input 5-photon Fock state, and a random state with $\bar{n} = 3$ using $\lambda = 0.07$ and $N = 6$ qubits. (b-d): Wigner functions, quadrature distributions and photon number distributions for the 5-photon Fock state (left) and the $\bar{n} = 3$ photon random state (right). (b): Input states. (c): Output when each qubit undergoes dephasing with $p_z = 0.05$ (d): Output when each qubit undergoes amplitude damping with $\gamma = 0.05$.

capture the full non-classical aspects of non-Gaussian CV states. Therefore, we also qualitatively analyze the Wigner functions, quadrature distributions and photon distributions of the two selected non-Gaussian trial states. Other input states have shown similar behavior. Fig. 10.4c and d shows the recovered states after each qubit has undergone dephasing or amplitude damping with an error probability of $p_z = 0.05$ or $\gamma = 0.05$. For both channels we observe a smearing of the q -quadrature distributions while, the p -quadrature distributions remains almost intact compared to the input for both trial states. More importantly, we find that the negative regions of the Wigner functions (highlighted in blue), which are strong indicators of non-classicality, remain non-negligible. Thus even moderate error rates do not have a severe effect on the recovered states.

10.4 Conclusion

In conclusion we have presented a feasible unitary protocol to map arbitrary CV states into a few qubits. This can be realized using only conditional displacements generated by Rabi-type coupling Hamiltonians, which currently are available in trapped-ion systems [83] and superconducting circuits [48]. The protocol is fully deterministic and requires no measurements or feed-forward. The error rates caused by the finite dimensionality of the qubit subsystem decrease exponentially with the number of qubits. Furthermore, small dephasing or amplitude-damping errors acting on the qubits do not translate into large errors in the protocol. We have focused on encoding arbitrary CV states into qubits, but similar techniques might be used to map arbitrary multi-qubit states into a single CV mode. Such mapping could facilitate multi-qubit operations and hardware-efficient qubit transfers. We leave this as an interesting open direction for future work.

10.5 S1: Fidelity of recovered states

Here we derive Eq. 10.2 of the main text. We begin with the definition of the mapping (Eq. 10.1 of the main text):

$$\hat{U}|\psi\rangle|\mathbf{0}\rangle = \sqrt{1-\varepsilon}|\tilde{0}\rangle|\Psi\rangle + \sqrt{\varepsilon}|\Phi_\varepsilon\rangle. \quad (10.9)$$

Resetting the CV mode to state $|\tilde{0}\rangle$ transforms the state into:

$$|\tilde{0}\rangle\langle\tilde{0}| \otimes \text{Tr}_{\text{CV}} \left(\hat{U}|\psi\rangle\langle\psi| \otimes |\mathbf{0}\rangle\langle\mathbf{0}| \hat{U}^\dagger \right) = |\tilde{0}\rangle\langle\tilde{0}| \otimes [(1-\varepsilon)|\Psi\rangle\langle\Psi| + \varepsilon\rho_\varepsilon] \quad (10.10)$$

where $\rho_\varepsilon = \text{Tr}_{\text{CV}}(|\Phi_\varepsilon\rangle\langle\Phi_\varepsilon|)$. Applying \hat{U}^\dagger and calculating the overlap with $|\psi\rangle|\mathbf{0}\rangle$ we find:

$$F = \langle\psi|\langle\mathbf{0}|\hat{U}^\dagger (|\tilde{0}\rangle\langle\tilde{0}| \otimes [(1-\varepsilon)|\Psi\rangle\langle\Psi| + \varepsilon\rho_\varepsilon]) \hat{U}|\psi\rangle|\mathbf{0}\rangle \quad (10.11)$$

$$= (\sqrt{1-\varepsilon}\langle\tilde{0}|\langle\Psi| + \sqrt{\varepsilon}\langle\Phi_\varepsilon|) (|\tilde{0}\rangle\langle\tilde{0}| \otimes [(1-\varepsilon)|\Psi\rangle\langle\Psi| + \varepsilon\rho_\varepsilon]) (\sqrt{1-\varepsilon}|\tilde{0}\rangle|\Psi\rangle + \sqrt{\varepsilon}|\Phi_\varepsilon\rangle) \quad (10.12)$$

$$= (1-\varepsilon)\langle\Psi|[(1-\varepsilon)|\Psi\rangle\langle\Psi| + \varepsilon\rho_\varepsilon]|\Psi\rangle \quad (10.13)$$

$$= (1-\varepsilon)^2 + (1-\varepsilon)\varepsilon\langle\Psi|\rho_\varepsilon|\Psi\rangle \quad (10.14)$$

where we used $\langle\tilde{0}|\Phi_\varepsilon\rangle = 0$ and $\langle\tilde{0}|\tilde{0}\rangle = 1$ in the third equality. Since $0 \leq \langle\Psi|\rho_\varepsilon|\Psi\rangle \leq 1$ we have

$$(1-\varepsilon)^2 \leq F \leq (1-\varepsilon)^2 + (1-\varepsilon)\varepsilon = 1-\varepsilon \quad (10.15)$$

10.6 S2: Analytical analysis of the protocol

Here we show that the proposed circuit approximately transfers arbitrary CV states onto the qubits. As stated in the main text, the relevant interaction operators are:

$$\hat{V}_k = \exp\left(iv_k\hat{q}\hat{\sigma}_y^{(k)}\right), \quad (10.16)$$

$$\hat{W}_k = \begin{cases} \exp\left(iw_k\hat{p}\hat{\sigma}_x^{(k)}\right), & \text{for } k < N, \\ \exp\left(-iw_k\hat{p}\hat{\sigma}_y^{(k)}\right), & \text{for } k = N, \end{cases} \quad (10.17)$$

with

$$v_k = \frac{\pi}{2\lambda 2^k}, \quad (10.18)$$

$$w_k = \frac{\lambda 2^k}{2}. \quad (10.19)$$

We begin by considering the action of the operators \hat{V}_k and \hat{W}_k on the \hat{q} eigenstates, $|q\rangle$. Using the relations $\exp(i\alpha\hat{q})|q\rangle = e^{i\alpha q}|q\rangle$ and $\exp(i\alpha\hat{p})|q\rangle = |q-\alpha\rangle$ we get:

$$\hat{V}_k|q\rangle|0\rangle_k = \frac{1}{\sqrt{2}} \left(e^{iv_k q}|q\rangle|i\rangle_k + e^{-iv_k q}|q\rangle|-i\rangle_k \right) \quad (10.20)$$

$$= \frac{e^{i\pi/4}}{2} \left[(e^{iv_k q} - ie^{-iv_k q})|q\rangle|+\rangle_k + (-ie^{iv_k q} + e^{-iv_k q})|q\rangle|-\rangle_k \right] \quad (10.21)$$

$$= \cos\left(\frac{\pi}{4} + v_k q\right)|q\rangle|+\rangle_k + \cos\left(\frac{\pi}{4} - v_k q\right)|q\rangle|-\rangle_k, \quad (10.22)$$

where $|\pm i\rangle_k = (|0\rangle_k \pm i|1\rangle_k)/\sqrt{2}$ are the $\hat{\sigma}_y^{(k)}$ eigenstates and $|\pm\rangle = (|0\rangle_k \pm |1\rangle_k)/\sqrt{2}$ are the $\hat{\sigma}_x^{(k)}$ eigenstates. Applying \hat{W}_k :

$$\hat{W}_k \hat{V}_k |q\rangle |0\rangle_k = \cos\left(\frac{\pi}{4} + v_k q\right) |q - w_k\rangle |+\rangle_k + \cos\left(\frac{\pi}{4} - v_k q\right) |q - (-w_k)\rangle |-\rangle_k \quad (10.23)$$

Iterating Eq. (10.23) we get the output for the sequence of operations. For example, after interaction with the first two qubits (with $N > 2$) we get:

$$\begin{aligned} \hat{W}_2 \hat{V}_2 \hat{W}_1 \hat{V}_1 |q\rangle |0\rangle_1 |0\rangle_2 = & \\ & \cos\left(\frac{\pi}{4} + v_1 q\right) \cos\left(\frac{\pi}{4} + v_2(q - w_1)\right) |q - (w_1 + w_2)\rangle |+\rangle_1 |+\rangle_2 \\ & + \cos\left(\frac{\pi}{4} - v_1 q\right) \cos\left(\frac{\pi}{4} + v_2(q - (-w_1))\right) |q - (-w_1 + w_2)\rangle |-\rangle_1 |+\rangle_2 \\ & + \cos\left(\frac{\pi}{4} + v_1 q\right) \cos\left(\frac{\pi}{4} - v_2(q - w_1)\right) |q - (w_1 - w_2)\rangle |+\rangle_1 |-\rangle_2 \\ & + \cos\left(\frac{\pi}{4} - v_1 q\right) \cos\left(\frac{\pi}{4} - v_2(q - (-w_1))\right) |q - (-w_1 - w_2)\rangle |-\rangle_1 |-\rangle_2 \end{aligned} \quad (10.24)$$

By induction, after interaction with all n qubits we obtain the following expression:

$$\prod_{k=1}^N \hat{W}_k \hat{V}_k |q\rangle |\mathbf{0}\rangle = \sum_{\mathbf{s}} \prod_{k=1}^N \cos\left[\frac{\pi}{4} + s_k v_k \left(q - \sum_{l=1}^{k-1} s_l w_l\right)\right] \left|q - \sum_{l=1}^{N-1} s_l w_l + s_N w_N\right\rangle |\phi_{\mathbf{s}}\rangle \quad (10.25)$$

where $|\mathbf{0}\rangle = |0\rangle_1 |0\rangle_2 \dots |0\rangle_N$ is the joint qubit ground state and the sum with summation index $\mathbf{s} = (s_1, s_2, \dots, s_N)$ with $s_k = \pm 1$ is over all 2^N combinations of the signs, s_k . $|\phi_{\mathbf{s}}\rangle$ is a qubit product state where mode k is in the s_k eigenstate of $\hat{\sigma}_x^{(k)}$, e.g., $|\phi_{(1,1,-1,-1)}\rangle = |+\rangle_1 |+\rangle_2 |-\rangle_3 |-\rangle_4$ and $|\phi_{(1,-1,1,1)}\rangle = |+\rangle_1 |-\rangle_2 |+\rangle_3 |+\rangle_4$. By linearity, we can extend the action of the operators to an arbitrary pure state, $|\psi\rangle = \int dq \psi(q) |q\rangle$:

$$\begin{aligned} & \prod_{k=1}^N \hat{W}_k \hat{V}_k |\psi\rangle |\mathbf{0}\rangle \\ & = \sum_{\mathbf{s}} \int dq \psi(q) \prod_{k=1}^N \cos\left[\frac{\pi}{4} + s_k v_k \left(q - \sum_{l=1}^{k-1} s_l w_l\right)\right] \left|q - \sum_{l=1}^{N-1} s_l w_l + s_N w_N\right\rangle |\phi_{\mathbf{s}}\rangle \end{aligned} \quad (10.26)$$

Translating the integration variable, $q \rightarrow q + (\sum_{l=1}^{N-1} s_l w_l - s_N w_N) \equiv q + q_{\mathbf{s}}$:

$$\begin{aligned} & = \sum_{\mathbf{s}} \int dq \psi(q + q_{\mathbf{s}}) \prod_{k=1}^N \cos\left[\frac{\pi}{4} + s_k v_k \left(q - \sum_{l=1}^{k-1} s_l w_l + \sum_{l=1}^{N-1} s_l w_s - s_N w_N\right)\right] |q\rangle |\phi_{\mathbf{s}}\rangle \\ & = \sum_{\mathbf{s}} \int dq \psi(q + q_{\mathbf{s}}) \prod_{k=1}^N \cos\left[\frac{\pi}{4} + s_k v_k \left(q + \sum_{l=k}^{N-1} s_l w_l - s_N w_N\right)\right] |q\rangle |\phi_{\mathbf{s}}\rangle \\ & = \sum_{\mathbf{s}} \int dq \psi(q + q_{\mathbf{s}}) \prod_{k=1}^N \cos\left[\frac{\pi}{4} s_k + v_k q + \sum_{l=k}^{N-1} s_l v_k w_l - s_N v_k w_N\right] |q\rangle |\phi_{\mathbf{s}}\rangle \end{aligned} \quad (10.27)$$

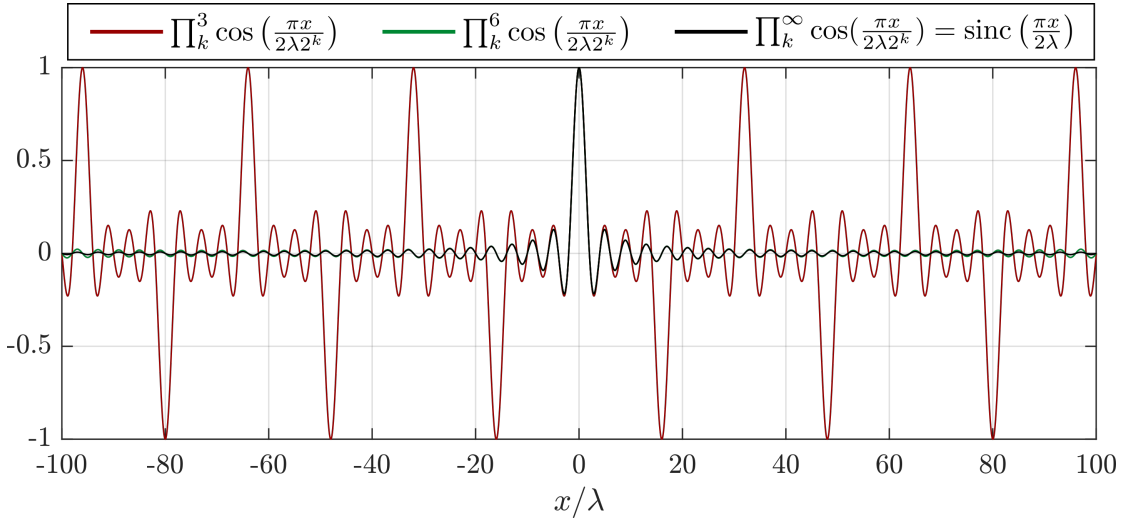


Figure 10.5: Comparison of functions of the type $\prod_{k=1}^N \cos(\pi \frac{x}{2\lambda 2^k})$ for $N = 3$, $N = 6$ and $N = \infty$.

Now consider the sum over l inside the cosine: From our choice of v_k and w_k (Eqs. (10.18) and (10.19)) we get $v_k w_l = 2^{l-k} \pi/4$. Thus when $l \geq k + 3$, $s_l v_k w_l$ is a multiple of 2π , which can be ignored inside the cosine. When $l = k + 2$ we get $s_l v_k w_l = s_{k+2} v_k w_{k+2} = s_{k+2} \pi$, which takes cos to $-\cos$, regardless of the sign s_{k+2} . This term thus contributes an overall -1 phase factor which can be ignored. The remaining relevant terms are thus $l = k$ and $l = k + 1$:

$$\begin{aligned}
&= \sum_{\mathbf{s}} \int dq \psi(q + q_{\mathbf{s}}) \\
&\quad \times \prod_{k=1}^{N-2} \cos \left[\frac{\pi}{2} (s_k + s_{k+1}) + v_k q \right] \cos \left[\frac{\pi}{2} (s_{N-1} - s_N) + v_{N-1} q \right] \cos [v_N q] |q\rangle |\phi_{\mathbf{s}}\rangle
\end{aligned} \tag{10.28}$$

The $\pi/2$ terms either add up to $\pm\pi$ if $s_k = s_{k-1}$ or to 0 if $s_k = -s_{k-1}$. Each $\pm\pi$ inside a cosine contributes a -1 phase factor, so depending on \mathbf{s} the total phase is either $+1$ or -1 :

$$\begin{aligned}
&= \sum_{\mathbf{s}} \int dq (-1)^{\gamma_{\mathbf{s}}} \psi(q + q_{\mathbf{s}}) \prod_{k=1}^N \cos(v_k q) |q\rangle |\phi_{\mathbf{s}}\rangle \\
&= \sum_{\mathbf{s}} \int dq (-1)^{\gamma_{\mathbf{s}}} \psi(q + q_{\mathbf{s}}) \prod_{k=1}^N \cos \left(\pi \frac{q}{2\lambda 2^k} \right) |q\rangle |\phi_{\mathbf{s}}\rangle,
\end{aligned} \tag{10.29}$$

where $\gamma_{\mathbf{s}} = \sum_{k=1}^{N-2} (s_k + s_{k+1})/2 + (s_{N-1} - s_N)/2$. This phase factor due to $\gamma_{\mathbf{s}}$ can be absorbed into $|\phi_{\mathbf{s}}\rangle$ as $(-1)^{\gamma_{\mathbf{s}}} |\phi_{\mathbf{s}}\rangle \equiv |\bar{\phi}_{\mathbf{s}}\rangle$.

For $N \gg 1$ the term $\prod_{k=1}^N \cos(\pi \frac{q}{2\lambda 2^k})$ is peaked at q around integer multiples of $\lambda 2^{N+1}$ with a peak width on the order of λ . In particular, for $N = \infty$ we get $\prod_{k=1}^{\infty} \cos(\pi \frac{q}{2\lambda 2^k}) = \sin(\pi \frac{q}{2\lambda}) / (\pi \frac{q}{2\lambda}) \equiv \text{sinc}(\pi \frac{q}{2\lambda})$, which approaches $\lambda \delta(q/2)$ for $\lambda \rightarrow 0$ where $\delta(x)$ is the Dirac delta function. Fig. 10.5 shows a comparison of $\prod_{k=1}^N \cos(\pi \frac{x}{2\lambda 2^k})$ for $N = 3$, $N = 6$ and $N = \infty$.

With this in mind, we make two approximations: First, we approximate $\prod_{k=1}^N \cos\left(\pi \frac{q}{2\lambda 2^k}\right) \approx \text{sinc}\left(\pi \frac{q}{2\lambda}\right)$. This approximation fails above $|q| = \lambda 2^{N+1}$, so we should ensure that $\psi(q + q_{\mathbf{s}})$ goes to 0 before the approximation fails. Since $q_{\mathbf{s}} \in [-\lambda(2^N - 1); \lambda(2^N - 1)]$, we should ensure that ψ has vanishing support beyond $\psi(|2^{N+1}\lambda - \lambda(2^N - 1)|) = \psi(|\lambda(2^N - 1)|)$, which can be satisfied by choosing sufficiently large N .

For the second approximation we assume $\int dq \psi(q + q_{\mathbf{s}}) \text{sinc}\left(\pi \frac{q}{2\lambda}\right) \approx \int dq \psi(q_{\mathbf{s}}) \text{sinc}\left(\pi \frac{q}{2\lambda}\right)$. We thus approximate $\psi(q + q_{\mathbf{s}})$ with its value at $q = 0$, as this is where the sinc function is mainly supported. This approximation requires the variation of ψ to be slower than the variation of the sinc function, i.e. $|\frac{d\psi}{dq}| \ll 1/\lambda$, which is satisfied by choosing λ sufficiently small.

In total we get:

$$\begin{aligned} \prod_{k=1}^N \hat{W}_k \hat{V}_k |\psi\rangle |\mathbf{0}\rangle &\approx \int dq \sum_{\mathbf{s}} \psi(q_{\mathbf{s}}) \text{sinc}\left(\pi \frac{q}{2\lambda}\right) |q\rangle |\bar{\phi}_{\mathbf{s}}\rangle \\ &= \int dq \frac{\text{sinc}\left(\pi \frac{q}{2\lambda}\right)}{\sqrt{2\lambda}} |q\rangle \otimes \sum_{\mathbf{s}} \sqrt{2\lambda} \psi(q_{\mathbf{s}}) |\bar{\phi}_{\mathbf{s}}\rangle. \end{aligned} \quad (10.30)$$

Thus the wavefunction ψ has been transferred from the bosonic mode to the qubits. The factor $\sqrt{2\lambda}$ normalizes the CV mode. We note that our approximations require both large $\lambda 2^N$ and small λ . For finite N , there thus exists an optimum λ which depends on how broadly ψ is supported in phase-space.

10.7 S3: Overlap between $|\tilde{0}\rangle_{\text{CV}}$ and squeezed vacuum

A squeezed vacuum state with squeezing parameter r is given by:

$$|S(r)\rangle = \frac{e^{r/2}}{\pi^{1/4}} \int dq \exp\left(\frac{(qe^r)^2}{2}\right) |q\rangle. \quad (10.31)$$

The fidelity between $|S(r)\rangle$ and $|\tilde{0}\rangle_{\text{CV}}$ is:

$$|\langle S(r) | \tilde{0} \rangle|^2 = \frac{e^r}{2\lambda\sqrt{\pi}} \left[\int dq \text{sinc}\left(\pi \frac{q}{2\lambda}\right) \exp\left(\frac{(qe^r)^2}{2}\right) \right]^2 \quad (10.32)$$

$$= \frac{2}{\sqrt{\pi}} \lambda e^r \text{erf}\left(\frac{\pi}{2\sqrt{2}} \frac{1}{\lambda e^r}\right)^2, \quad (10.33)$$

where $\text{erf}(x) = (2/\sqrt{\pi}) \int_0^x dz e^{-z^2}$ is the error function. This expression is optimized for $\lambda e^r \approx 1.12 \Leftrightarrow r \approx \log(1.12/\lambda)$ for which the fidelity takes the value 0.89.

10.8 S4: Random states

The random states used in this paper are generated as follows: First, we generate a large number (e.g. 200) of complex numbers, $\{c_0, c_1 \dots c_{200}\}$, with uniformly random amplitudes between 0 and 1 and phases between 0 and 2π . From these we construct an unnormalized CV state in the Fock basis as:

$$|\psi_{\text{random}}\rangle = \sum_m c_m |m\rangle. \quad (10.34)$$

We then apply an exponential filter to dampen high number Fock terms:

$$\rightarrow \sum_m e^{-\kappa m} c_m |m\rangle, \quad (10.35)$$

where κ is tuned such that the resulting state has the desired mean photon number. Lastly, the state is normalized.

Chapter 11

Conclusion and outlook

Throughout this thesis we have presented a series of protocols to generate and manipulate continuous-variable states of various quantum systems. Here, we take a step back to reflect on the potential of these systems as well as their future challenges.

Optics

In optics, there have been many exciting developments for quantum information processing in the past few years. One of these is the field of large-scale cluster states which has seen much progress both theoretically and experimentally [73–78, 106, 172–176]. A key missing component for universal fault-tolerant quantum computation with optical cluster states are GKP states. The first demonstration of optical GKP states is thus a central near-future milestone. In principle, generating optical GKP states of some quality should be possible with current technology [31, 89, 106]. However, truly useful GKP states capable of efficient error correction will likely require at least 10 dB squeezing, if not more. Creating such states is certainly beyond what can be achieved within state-of-the-art technology. On a promising note there has been much progress in the development of high-quality photon detectors [177, 178] which might eventually provide a low-loss source of non-Gaussianity. Another promising note is the development of strong light-atom interactions [64, 116, 119], which, as we have shown in chapter 5, can also provide a suitable non-Gaussianity for GKP states [31].

Yet, even if high quality GKP states could be generated, it is worth questioning if that is the most efficient use of the technology used for their generation. That is, if technology one day becomes good enough to produce highly squeezed GKP states, that same technology can most likely also be used to produce even better states of lower complexity, such as two or four-component cat states, or even just extremely good single-photon states. Thus even though GKP states appear to be superior for loss-correction [53, 55], it is important to explore and develop potential architectures for other codes, which might be easier to generate in practice. Cat codes are a particularly interesting case for optics, as they can be generated with only a few non-Gaussian interactions [29, 64]. In chapters 3 and 4 we have shown that state generation and error correction is possible optically. Important next steps will be to examine whether an all-optical cat-based computational architecture, perhaps inspired by the coherent-state encoding proposed by Ralph et al. in Ref. [59], including both gates and error-correction can be designed and made feasible.

Another important application within optics is quantum communication. Recent theoretical works have analyzed the prospects of using bosonic codes for long-distance quantum communication [57, 109, 110]. However, all of these results indicate that a very high density of low-loss repeaters are necessary. Furthermore, for GKP-based communication [109, 110] the required amount of squeezing is very demanding (> 15 dB). Thus bosonic error correction in its current form does not stand out as a particularly promising approach for long-distance communication. Still, the field is quite unexplored and it would be worth it to explore other types of bosonic codes as well as other types of higher-level multi-mode error-correction schemes. In general, bosonic codes seem to perform best in low-loss regimes. However, for communication we would prefer to perform error-correction as infrequently as possible to minimize the required number of repeaters. This in turn requires protocols which can be robust in the presence of relatively large amounts of loss, a regime which might not be ideal for bosonic codes.

For GKP states there is also room for further analysis of their performance under loss. While initial investigations have shown that they should perform well against losses [55], the optimal physically implementable recovery strategy against loss is unclear. Many theoretical papers circumvent the issue by converting loss into Gaussian displacements by adding an amplification channel. However, for experimental implementations this might not be practical. Furthermore, it seems unlikely that the optimal recovery strategy involves applying an additional noise channel. Recent work by Fukui et al. [109] has shown that in some cases losses can be corrected without an amplification channel. This involves balancing losses between the input state to be corrected and an ancilla used for syndrome detection. For communication, this might be a very sensible strategy as the loss on the ancilla can be part of the communication link such that no excessive noise is required. However, for computation the logical state has likely experienced more loss than the ancillas and, again, it would be unlikely if the optimal recovery strategy involves applying a lossy channel to the ancilla.

Qubit-coupled systems

Non-optical continuous-variable systems have also seen a tremendous progress in recent years. In this thesis we have lumped together microwave cavities and trapped ions due to the similar interactions suitable for GKP state generation available in these systems. In reality, these systems are of course very different, which will greatly impact how GKP-based research will continue to develop.

The development of GKP codes for these qubit-coupled systems is currently at a very interesting place, as some “conventional” Gaussian tools for manipulating GKP states, and in particular homodyne detection and beamsplitters, are not as straight forward as in optics. Thus basic operations for handling GKP states are being reinvented, which leaves some open questions. For example, all currently proposed large-scale architectures for GKP-based quantum computers rely on homodyne detectors for error correction and measurements [70, 131, 135, 179]. It is thus relevant to ask whether qubit-based measurement schemes [34, 48, 79, 111, 151] are efficient in the long run. For microwave modes, homodyne detection might be carried out by releasing the cavity state to a waveguide, but such waveguide coupling would also introduce coupling losses, which further increases the demands on the GKP states.

Another important factor in these systems is to ensure that the logical performance of the GKP states can be made much better than the qubits used to generate and measure them. In chapters 7 and 9 of this thesis, we saw that the effects of qubit errors could be mitigated by using the ancilla itself as a flag for qubit errors, which are detected by a final or intermediate

qubit measurement. Such mitigation strategy might be further improved by considering more qubits or noise-bias ancillas [146, 180]. However, losses during state generation will still limit the quality of the generated states. It is therefore also relevant to consider if loss detection during the generation protocol can be implemented. For example, in the measurement-free protocol presented in chapter 7 the bosonic mode has a well-defined excitation-number parity after each round of interactions. Thus it might make sense to perform intermediate parity measurements, e.g. through a dispersive coupling to an ancilla qubit [65], to probe whether excitations have been lost. The final state can then be post-selected on trials in which the parity measurements correspond to the theoretically expected parity.

Finally, both systems face a challenge of scalability, and demonstrating multi-qubit interactions will be an important milestone. In trapped ions, it is possible to scale to multiple modes either by considering different vibrational modes of a single ion, or—in a more scalable approach—to add multiple ions each with their own motional mode [43, 181–183]. For microwave modes, it is also possible to engineer interactions between multiple cavities [184]. However, the high-quality 3D cavities in state-of-the-art experiments [48, 65, 184] are relatively large and bulky which will quickly limit scalability.

Appendix A

Notes on numerical implementations

In this Appendix we go through the basic building blocks underlying the numerical methods used in many of the papers presented in this thesis. These methods were implemented in MATLAB using custom code written from scratch. Similar tools for Python can be found in the Strawberry Fields library developed by Xanadu [185].

In particular, we will outline a Fock-basis approach. This approach is useful, as it can be used to simulate arbitrary bosonic quantum states, including non-Gaussian states. The downside is, that the required numerical resources can in some case become quite large, especially for multi-mode states. Thus, for Gaussian states one should instead use a co-variance matrix representation which is much more efficient [41, 84, 186]. Furthermore, some classes of non-Gaussian states have certain structures that allows for more efficient approaches compared to the Fock basis approach described here [187, 188], although these methods were not required for the results presented in this thesis.

States

Recall from chapter 2 that any bosonic pure state can be represented as an infinite superposition of energy eigenstates, $|n\rangle$, of the harmonic oscillator:

$$|\psi\rangle = \sum_{n=0}^{\infty} c_n |n\rangle. \quad (\text{A.1})$$

In practice, only a finite number of the coefficients are non-zero, or non-vanishing. Thus we can store this state as a finite vector

$$[c_0, c_1, \dots, c_{n_{max}}], \quad (\text{A.2})$$

where n_{max} is numerical a cutoff, which should be chosen large enough to avoid numerical artifacts in the final simulation results. Typical values of n_{max} range from 10 to 1000, depending on the particular simulation. A convenient feature of this Fock-basis approach is that n_{max} is the only numerical parameter (apart from the precision used to represent real numbers). Thus,

if the simulation produces numerical artifacts, we can usually eliminate them by simply running the simulation again with a larger n_{max} , at the cost of a longer execution time.

Some commonly encountered states are:

Vacuum states. The vacuum state, $|\text{vac}\rangle$ is perhaps the most simple state in the Fock basis, and is represented by

$$c_n = \begin{cases} 1 & \text{if } n = 0, \\ 0 & \text{otherwise.} \end{cases} \quad (\text{A.3})$$

Fock states. The Fock state $|m\rangle$ is similarly represented by

$$c_n = \begin{cases} 1 & \text{if } n = m, \\ 0 & \text{otherwise.} \end{cases} \quad (\text{A.4})$$

Coherent states. Coherent states, $|\alpha\rangle$, are given by

$$c_n = e^{-|\alpha|^2/2} \frac{\alpha^n}{\sqrt{n!}}. \quad (\text{A.5})$$

Note that for coherent states, we can define the coefficients recursively as $c_0 = e^{-|\alpha|^2/2}$ and $c_n = \frac{\alpha}{\sqrt{n}} c_{n-1}$, which is typically faster than using Eq. (A.5) directly, albeit the initialization of coherent states is rarely the bottleneck of simulations.

Squeezed vacuum. Squeezed vacuum, $\hat{S}(\xi)|\text{vac}\rangle$ with $\xi = r e^{i\theta}$, are given by:

$$c_n = \begin{cases} \frac{1}{\sqrt{\cosh(r)}} (-e^{i\phi} \tanh(r))^{n/2} \frac{\sqrt{n!}}{(n/2)!!} & \text{for even } n, \\ 0 & \text{for odd } n. \end{cases} \quad (\text{A.6})$$

Similarly to coherent states, squeezed vacuum can be calculated recursively by $c_0 = \frac{1}{\sqrt{\cosh(r)}}$, $c_1 = 0$ and $c_n = -e^{i\phi} \tanh(r) \sqrt{\frac{n-1}{n}} c_{n-2}$.

Quadrature eigenstates. Quadrature eigenstates are a bit unusual, in that they cannot be normalized. Yet, they can still be meaningfully described using the wavefunction of Fock states, $\psi_n(q) = \langle q|n\rangle$, which should be normalized according to $\int |\psi_n(q)|^2 dq = 1$ and for which $|\psi_n(q)|^2$ gives the probability density of getting measurement results q with a homodyne detection of the Fock state $|n\rangle$. We can then define an unnormalized vector in the Fock basis as:

$$c_n = \sqrt{\frac{1}{\sqrt{\pi}}} 2^n n! e^{q^2/2} H_n(q), \quad (\text{A.7})$$

where $H_n(q)$ is the n 'th Hermite polynomial. To get an eigenstate in a rotated quadrature basis each vector element is simply multiplied by $e^{in\theta}$, where θ describes the rotation angle. Note that a quadrature eigenstate is *not* equal to a squeezed vacuum state in the limit $r \rightarrow \infty$, as the squeezed vacuum state is normalized while the quadrature eigenstate is not.

Mixed states can similarly be represented in the Fock basis as:

$$\rho = \sum_{n=0}^{\infty} \sum_{m=0}^{\infty} \rho_{m,n} |m\rangle \langle n|, \quad (\text{A.8})$$

which are stored numerically as a matrix

$$\begin{pmatrix} \rho_{0,0} & \cdots & \rho_{0,n_{max}} \\ \vdots & \ddots & \vdots \\ \rho_{n_{max},0} & \cdots & \rho_{n_{max},n_{max}} \end{pmatrix}. \quad (\text{A.9})$$

Operators

A quantum operator, \hat{O} , can be represented in the Fock basis by matrices with element $\langle n|\hat{O}|m\rangle$ at index (n, m) . Their effect on pure states are given by matrix-vector multiplication, i.e. $|\psi\rangle \rightarrow \hat{O}|\psi\rangle$, while their effect on mixed states are given by matrix-matrix multiplication, $\rho \rightarrow \hat{O}\rho\hat{O}^\dagger$. Similarly to states, operators require a numerical cutoff which should match that of the state which is transformed by the operator.

Here we list the Fock basis representation of some common operators:

Annihilation/creation operators. The annihilation operator, \hat{a} , and creation operators, \hat{a}^\dagger , are given by

$$\hat{a} = \begin{pmatrix} 0 & 1 & 0 & 0 \\ 0 & 0 & \sqrt{2} & 0 \\ 0 & 0 & 0 & \sqrt{3} \\ 0 & 0 & 0 & 0 \\ & & & \ddots \\ & & & & 0 & \sqrt{n_{max}} \\ 0 & & & & 0 & 0 \end{pmatrix}, \quad \hat{a}^\dagger = \begin{pmatrix} 0 & 0 & 0 & 0 \\ 1 & 0 & 0 & 0 \\ 0 & \sqrt{2} & 0 & 0 \\ 0 & 0 & \sqrt{3} & 0 \\ & & & \ddots \\ & & & & 0 & 0 \\ \sqrt{n_{max}} & & & & 0 & 0 \end{pmatrix}. \quad (\text{A.10})$$

These are sparse matrices and can be stored as such in MATLAB using the built-in sparse() function to greatly reduce memory cost and increase calculation speeds.

Number operators The number operator, \hat{n} , is a diagonal operator in the Fock basis:

$$\hat{n} = \text{diag}(0, 1, \dots, n_{max}) \quad (\text{A.11})$$

Similarly to the annihilation and creation operators, it should be implemented as a sparse matrix.

Quadrature operators. Given the annihilation and creation operators above, the quadrature operators are simply calculated using the relations

$$\hat{q} = \frac{1}{\sqrt{2}}(\hat{a} + \hat{a}^\dagger), \quad \hat{p} = \frac{1}{\sqrt{2}i}(\hat{a} - \hat{a}^\dagger). \quad (\text{A.12})$$

More generally, we can define quadrature operators with arbitrary rotation, θ , as

$$\hat{q}_\theta = \frac{1}{\sqrt{2}}(e^{-i\theta}\hat{a} + e^{i\theta}\hat{a}^\dagger) \quad (\text{A.13})$$

Similarly to the operators above, the quadrature operators are sparse and should be implemented as such.

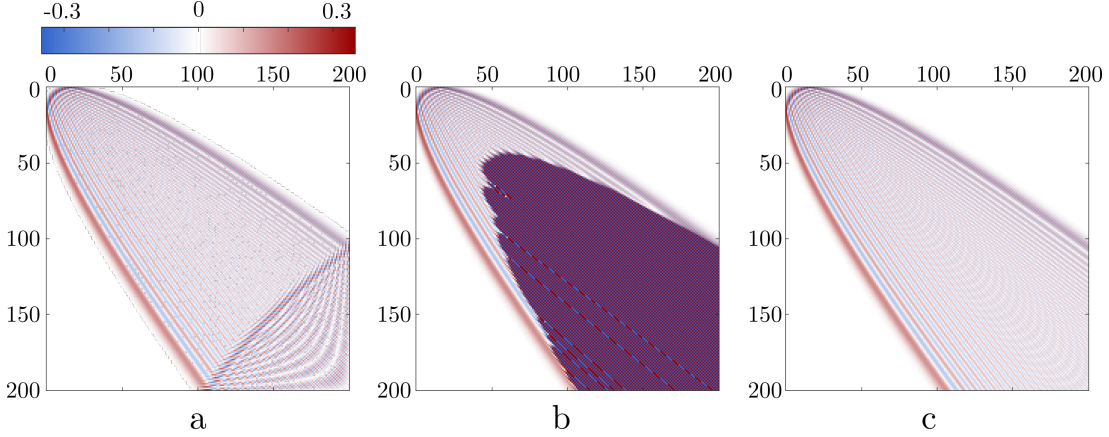


Figure A.1: Matrix elements $\langle n|\hat{D}|m\rangle$ for numerically implemented displacement operators with $\alpha = 4$ and $n_{max} = 200$ using (a): matrix exponential of $\alpha\hat{a}^\dagger - \alpha^*\hat{a}$, (b): the recursion formula of Eq. (A.17), and (c): the recursion formula for the Laguerre polynomials, Eq. (A.16).

Rotation operators. Similarly to the number operator, the phase rotation operator, $\hat{R}(\theta) = \exp(i\theta\hat{n})$, is diagonal in the Fock basis:

$$\hat{R} = \text{diag}(0, e^{i\theta}, e^{i2\theta}, \dots, e^{in_{max}\theta}), \quad (\text{A.14})$$

and can be efficiently stored as a sparse matrix.

Displacement operators. The displacement operator, $\hat{D}(\alpha) = \exp(\alpha\hat{a}^\dagger - \alpha^*\hat{a})$, is a bit more tricky to implement. At first glance, one might be tempted to implement it through a matrix exponential of $\alpha\hat{a}^\dagger - \alpha^*\hat{a}$, using the matrix expression of \hat{a} and \hat{a}^\dagger from Eq. (A.10). However, due to the numerical cutoff, this will not produce the correct matrix elements $\langle n|\hat{D}|m\rangle$, as shown in Fig. A.1a. Instead, we should use the analytical expressions for the matrix elements of the displacement operators [189]:

$$\langle n|\hat{D}|m\rangle = \sqrt{\frac{m!}{n!}} \alpha^{n-m} e^{-|\alpha|^2/2} L_m^{(n-m)}(|\alpha|^2), \quad (\text{A.15})$$

where $L_m^{(k)}(\alpha)$ is the generalized Laguerre polynomials. Unfortunately, the built-in MATLAB function for the generalized Laguerre polynomials is rather slow, but they can be efficiently calculated from scratch using the recursion formula, $L_0^{(k)}(\alpha) = 1$, $L_1^{(k)}(\alpha) = 1 + k - \alpha$ and

$$L_{m+1}^{(k)}(\alpha) = \frac{(2m + 1 + k - \alpha)L_m^{(k)}(\alpha) - (m + k)L_{m-1}^{(k)}(\alpha)}{m + 1}. \quad (\text{A.16})$$

Another, and perhaps slightly simpler method to calculate $\langle n|\hat{D}|m\rangle$ is by using the relation

$\hat{D}\hat{a}^\dagger\hat{D}^\dagger = \hat{a}^\dagger - \alpha^*$ and the fact that $\hat{D}^\dagger\hat{D} = \hat{I}$. With these we can write:

$$\begin{aligned}
\langle n|\hat{D}|m\rangle &= \frac{1}{\sqrt{m}}\langle n|\hat{D}\hat{a}^\dagger|m-1\rangle \\
&= \frac{1}{\sqrt{m}}\langle n|\hat{D}\hat{a}^\dagger\hat{D}^\dagger\hat{D}|m-1\rangle \\
&= \frac{1}{\sqrt{m}}\langle n|(\hat{a}^\dagger - \alpha^*)\hat{D}|m-1\rangle \\
&= \frac{\sqrt{n}\langle n-1|\hat{D}|m-1\rangle - \alpha^*\langle n|\hat{D}|m-1\rangle}{\sqrt{m}}. \tag{A.17}
\end{aligned}$$

Thus we have a recursion relation for the matrix elements, allowing us to calculate all matrix elements starting from the boundary values $\langle n|\hat{D}|0\rangle = \langle n|\alpha\rangle = e^{-|\alpha|^2/2}\frac{\alpha^n}{\sqrt{n!}}$. However, this recursion is prone to numerical instabilities given the default 64-bit precision used for floating-point data in MATLAB, as shown in Fig. A.1b. Such instabilities do not seem to appear when using the Laguerre polynomial approach, Fig. A.1c, and therefore that approach has been used for this thesis.

Note that due to the numerical cutoff, \hat{n}_{max} , the displacement operator is not unitary. As a result, the norm of a state can change when transformed by the numerical displacement operator. This turns out to be a very useful feature, which can be used to check if the chosen value of \hat{n}_{max} is sufficiently large. In particular, if the norm starts to get significantly reduced, we should rerun the calculation with a larger n_{max} . Intuitively what happens is, that the displacement operator tries to displace the state onto energy levels above n_{max} , but since these states are assumed to have zero occupation by the simulation, the norm of the state shrinks. If one were to use the matrix exponential implementation of the displacement operator, this effect would not happen, and it would thus be harder to detect if the numerical cutoff is sufficient.

Squeezing operators. The squeezing operator, $\hat{S}(\xi) = \exp[\frac{1}{2}(\xi^*a^2 - \xi\hat{a}^{\dagger 2})]$. While analytical values for the matrix elements $\langle n|\hat{S}(\xi)|m\rangle$ have been derived [190, 191], these contain large sums which are prone to numerical errors and are thus less suited for numerical implementation compared to the case for the displacement operator. Instead, one can calculate the elements recursively by utilizing the relation $\hat{S}\hat{a}\hat{S}^\dagger = \hat{a}\cosh(r) + \hat{a}^\dagger e^{i\phi}\sinh(r)$. In particular we can write:

$$\begin{aligned}
\langle n-1|\hat{S}|m-1\rangle &= \frac{1}{\sqrt{m}}\langle n-1|\hat{S}\hat{a}|m\rangle \\
&= \frac{1}{\sqrt{m}}\langle n-1|\hat{S}\hat{a}\hat{S}^\dagger\hat{S}|m\rangle \\
&= \frac{1}{\sqrt{m}}\langle n-1|(\hat{a}\cosh(r) + \hat{a}^\dagger e^{i\phi}\sinh(r))\hat{S}|m\rangle \\
&= \frac{1}{\sqrt{m}}\left(\sqrt{n}\cosh(r)\langle n|\hat{S}|m\rangle + \sqrt{n-1}e^{i\phi}\sinh(r)\langle n-2|\hat{S}|m\rangle\right). \tag{A.18}
\end{aligned}$$

Rearranging, we get:

$$\langle n|\hat{S}|m\rangle = \frac{\sqrt{m}\langle n-1|\hat{S}|m-1\rangle - \sqrt{n-1}e^{i\phi}\sinh(r)\langle n-2|\hat{S}|m\rangle}{\sqrt{n}\cosh(r)} \tag{A.19}$$

Together with the expression for $\langle n|\hat{S}|0\rangle$ from Eq. (A.6), one can recursively calculate the Fock-basis matrix elements of \hat{S} . However, this approach sometimes leads to numerical

instabilities using the 64-bit precision of MATLAB, as with the displacement operator, so care should be taken when implementing the squeezing operator with this approach. Alternatively, one can apply the matrix exponential to $\frac{1}{2}(\xi^* \hat{a}^2 - \xi \hat{a}^{\dagger 2})$, although this might lead to errors if n_{max} is too small.

Wigner function

To calculate the Wigner function, $W(\rho; q, p)$, of a given state with density matrix ρ , we can use the fact that the Wigner function is linear with respect to the input state, $W(c_1\rho^{(1)} + c_2\rho^{(2)}; q, p) = c_1W(\rho^{(1)}; q, p) + c_2W(\rho^{(2)}; q, p)$. Thus in the Fock basis we get:

$$W(\rho; q, p) = \sum_{n=0}^{\infty} \sum_{m=0}^{\infty} \rho_{m,n} W(|m\rangle\langle n|; q, p) \quad (\text{A.20})$$

Finally, we just have to calculate the Wigner functions of $|m\rangle\langle n|$ which are given by [192]:

$$\begin{aligned} W(|m\rangle\langle n|, q, p) &= \frac{(-1)^m}{\pi} \langle n | \hat{D} \left(\sqrt{2}(q + ip) \right) | m \rangle \\ &= \frac{(-1)^m}{\pi} \sqrt{\frac{m!}{n!}} \sqrt{2}^{n-m} (q + ip)^{n-m} e^{-q^2 - p^2} L_m^{(n-m)}(2q^2 + 2p^2). \end{aligned} \quad (\text{A.21})$$

Bibliography

- [1] R. P. Feynman. Simulating Physics with Computers. *International Journal of Theoretical Physics*, 21, 467 (1982)
- [2] S. S. Vazhkudai et al.. The Design, Deployment, and Evaluation of the CORAL Pre-Exascale Systems. www.osti.gov/biblio/1489443 (2018)
- [3] J. S. Bell. On the Einstein Podolsky Rosen Paradox. *Physics Physique Fizika*, 1, 195 (1964)
- [4] P. Shor. Algorithms for quantum computation: discrete logarithms and factoring. *Proceedings 35th Annual Symposium on Foundations of Computer Science*, pages 124–134 (1994)
- [5] L. K. Grover. A fast quantum mechanical algorithm for database search. *Proceedings of the Annual ACM Symposium on Theory of Computing*, pages 212–219 (1996)
- [6] S. Jordan. Quantum Algorithm Zoo. www.quantumalgorithmzoo.org (2011)
- [7] J. Biamonte, P. Wittek, N. Pancotti, P. Rebentrost, N. Wiebe and S. Lloyd. Quantum machine learning. *Nature*, 549, 195 (2017)
- [8] V. Dunjko and H. J. Briegel. Machine learning & artificial intelligence in the quantum domain: A review of recent progress. *Reports on Progress in Physics*, 81, 74001 (2018)
- [9] Y. Cao et al.. Quantum Chemistry in the Age of Quantum Computing. *Chemical Reviews*, 119, 10856 (2019)
- [10] S. McArdle, S. Endo, A. Aspuru-Guzik, S. C. Benjamin and X. Yuan. Quantum computational chemistry. *Reviews of Modern Physics*, 92, 015003 (2020)
- [11] C. Berger et al.. Quantum technologies for climate change: Preliminary assessment. *arXiv preprint at <https://arxiv.org/abs/2107.05362>* (2021)
- [12] R. Orús, S. Mugel and E. Lizaso. Quantum computing for finance: Overview and prospects. *Reviews in Physics*, 4, 1000282 (2019)
- [13] A. Ajagekar and F. You. Quantum computing for energy systems optimization: Challenges and opportunities. *Energy*, 179, 76 (2019)
- [14] F. Arute et al.. Quantum supremacy using a programmable superconducting processor. *Nature*, 574, 505 (2019)
- [15] H. S. Zhong et al.. Quantum computational advantage using photons. *Science*, 370, 1460 (2020)

-
- [16] Y. Wu et al.. Strong quantum computational advantage using a superconducting quantum processor. *arXiv preprint at <https://arxiv.org/abs/2106.14734>* (2021)
- [17] F. J. MacWilliams and N. J. A. Sloane. The theory of error-correcting codes. Elsevier (1977)
- [18] W. C. Huffman and V. Pless. Fundamentals of error-correcting codes. Cambridge university press (2010)
- [19] P. W. Shor. Scheme for reducing decoherence in quantum computer memory. *Physical Review A*, 52, R2493(R) (1995)
- [20] A. M. Steane. Error Correcting Codes in Quantum Theory. Technical Report (1996)
- [21] S. B. Bravyi, A. Y. Kitaev and L. D. Landau. Quantum codes on a lattice with boundary. *arXiv preprint at <https://arxiv.org/abs/quant-ph/9811052>* (1998)
- [22] A. G. Fowler, M. Mariantoni, J. M. Martinis and A. N. Cleland. Surface codes: Towards practical large-scale quantum computation. *Physical Review A*, 86, 32324 (2012)
- [23] D. Litinski. A game of surface codes: Large-scale quantum computing with lattice surgery. Technical Report (2019)
- [24] C. Gidney and M. Ekerå. How to factor 2048 bit RSA integers in 8 hours using 20 million noisy qubits. *Quantum*, 5, 1 (2021)
- [25] M. Webber, V. Elfving, S. Weidt and W. K. Hensinger. The Impact of Hardware Specifications on Reaching Quantum Advantage in the Fault Tolerant Regime. *arXiv preprint at <https://arxiv.org/abs/2108.12371>* (2021)
- [26] Z. Leghtas, G. Kirchmair, B. Vlastakis, R. J. Schoelkopf, M. H. Devoret and M. Mirrahimi. Hardware-efficient autonomous quantum memory protection. *Physical Review Letters*, 111, 120501 (2013)
- [27] M. Bergmann and P. Van Loock. Quantum error correction against photon loss using multicomponent cat states. *Physical Review A*, 94, 042332 (2016)
- [28] D. Gottesman, A. Kitaev and J. Preskill. Encoding a qubit in an oscillator. *Physical Review A*, 64, 012310 (2001)
- [29] J. Hastrup, J. S. Neergaard-Nielsen and U. L. Andersen. Deterministic generation of a four-component optical cat state. *Optics Letters*, 45, 640 (2020)
- [30] J. Hastrup and U. L. Andersen. All-optical cat-code quantum error correction. *arXiv preprint at <https://arxiv.org/abs/2108.12225>* (2021)
- [31] J. Hastrup and U. L. Andersen. Generation of optical Gottesman-Kitaev-Preskill states with cavity QED. *arXiv preprint at <https://arxiv.org/abs/2104.07981>* (2021)
- [32] J. Hastrup, M. V. Larsen, J. S. Neergaard-Nielsen, N. C. Menicucci and U. L. Andersen. Unsuitability of cubic phase gates for non-Clifford operations on Gottesman-Kitaev-Preskill states. *Physical Review A*, 103, 032409 (2021)
- [33] J. Hastrup, K. Park, J. B. Brask, R. Filip and U. L. Andersen. Measurement-free preparation of grid states. *npj Quantum Information*, 7, 17 (2021)
- [34] J. Hastrup and U. L. Andersen. Improved readout of qubit-coupled Gottesman-Kitaev-Preskill states. *Quantum Science and Technology*, 6, 035016 (2021)

-
- [35] J. Hastrup, K. Park, R. Filip and U. L. Andersen. Unconditional Preparation of Squeezed Vacuum from Rabi Interactions. *Physical Review Letters*, 126, 153602 (2021)
- [36] J. Hastrup, K. Park, J. B. Brask, R. Filip and U. L. Andersen. Universal unitary transfer of continuous-variable quantum states into a few qubits. *arXiv preprint at <https://arxiv.org/abs/2106.12272>* (2021)
- [37] C. C. Gerry and P. L. Knight. *Introductory Quantum Optics*. Cambridge university press (2005)
- [38] R. Loudon. *The Quantum Theory of Light*. Oxford University Press (2000)
- [39] D. F. Walls and G. J. Milburn. *Quantum Optics*. Springer-Verlag Berlin Heidelberg (2008)
- [40] G. S. Agarwal. *Quantum Optics*. Cambridge university press (2012)
- [41] A. Serafini. *Quantum continuous variables: a primer of theoretical methods*. CRC press (2017)
- [42] E. Wigner. On the quantum correction for thermodynamic equilibrium. *Physical Review*, 40, 749 (1932)
- [43] C. Flühmann, T. L. Nguyen, M. Marinelli, V. Negnevitsky, K. Mehta and J. P. Home. Encoding a qubit in a trapped-ion mechanical oscillator. *Nature*, 566, 513 (2019)
- [44] H. Vahlbruch, M. Mehmet, K. Danzmann and R. Schnabel. Detection of 15 dB Squeezed States of Light and their Application for the Absolute Calibration of Photoelectric Quantum Efficiency. *Physical Review Letters*, 117, 110801 (2016)
- [45] P. C. Haljan, K. A. Brickman, L. Deslauriers, P. J. Lee and C. Monroe. Spin-dependent forces on trapped ions for phase-stable quantum gates and entangled states of spin and motion. *Physical Review Letters*, 94, 153602 (2005)
- [46] D. Kienzler et al.. Quantum harmonic oscillator state synthesis by reservoir engineering. *Science*, 347, 53 (2015)
- [47] C. D. Bruzewicz, J. Chiaverini, R. McConnell and J. M. Sage. Trapped-ion quantum computing: Progress and challenges. *Appl. Phys. Rev*, 6, 21314 (2019)
- [48] P. Campagne-Ibarcq et al.. Quantum error correction of a qubit encoded in grid states of an oscillator. *Nature*, 584, 368 (2020)
- [49] P. van Loock et al.. Hybrid quantum computation in quantum optics. *Physical Review A*, 78, 022303 (2008)
- [50] J. S. Ivan, K. Kumar Sabapathy and R. Simon. Operator-sum representation for bosonic Gaussian channels. *Physical Review A*, 84, 042311 (2011)
- [51] Y. X. Liu, Ş. K. Özdemir, A. Miranowicz and N. Imoto. Kraus representation of a damped harmonic oscillator and its application. *Physical Review A*, 70, 042308 (2004)
- [52] A. Arqand, L. Memarzadeh and S. Mancini. Quantum capacity of a bosonic dephasing channel. *Physical Review A*, 102, 042413 (2020)
- [53] K. Noh, V. V. Albert and L. Jiang. Quantum Capacity Bounds of Gaussian Thermal Loss Channels and Achievable Rates with Gottesman-Kitaev-Preskill Codes. *IEEE Transactions on Information Theory*, 65, 2563 (2019)

-
- [54] E. Knill and R. Laflamme. Theory of quantum error-correcting codes. *Physical Review A*, 55, 900 (1997)
- [55] V. V. Albert et al.. Performance and structure of single-mode bosonic codes. *Physical Review A*, 97, 32346 (2018)
- [56] C. W. Helstrom. Quantum Detection and Estimation Theory. Academic Press (1976)
- [57] L. Li, C. L. Zou, V. V. Albert, S. Muralidharan, S. M. Girvin and L. Jiang. Cat Codes with Optimal Decoherence Suppression for a Lossy Bosonic Channel. *Physical Review Letters*, 119, 030502 (2017)
- [58] H. Jeong and M. S. Kim. Efficient quantum computation using coherent states. *Physical Review A*, 65, 042305 (2002)
- [59] T. C. Ralph, A. Gilchrist, G. J. Milburn, W. J. Munro and S. Glancy. Quantum computation with optical coherent states. *Physical Review A*, 68, 042319 (2003)
- [60] A. P. Lund, T. C. Ralph and H. L. Haselgrove. Fault-tolerant linear optical quantum computing with small-amplitude coherent states. *Physical Review Letters*, 100, 1 (2008)
- [61] A. L. Grimsmo, J. Combes and B. Q. Baragiola. Quantum Computing with Rotation-Symmetric Bosonic Codes. *Physical Review X*, 10, 011058 (2020)
- [62] M. H. Michael et al.. New class of quantum error-correcting codes for a bosonic mode. *Physical Review X*, 6, 031006 (2016)
- [63] Z. Leghtas, G. Kirchmair, B. Vlastakis, M. H. Devoret, R. J. Schoelkopf and M. Mirrahimi. Deterministic protocol for mapping a qubit to coherent state superpositions in a cavity. *Physical Review A*, 87, 042315 (2013)
- [64] B. Hacker et al.. Deterministic creation of entangled atom–light Schrödinger-cat states. *Nature Photonics*, 13, 110 (2019)
- [65] N. Ofek et al.. Extending the lifetime of a quantum bit with error correction in superconducting circuits. *Nature*, 536, 441 (2016)
- [66] T. Matsuura, H. Yamasaki and M. Koashi. Equivalence of approximate Gottesman-Kitaev-Preskill codes. *Physical Review A*, 102, 32408 (2020)
- [67] S. Glancy and E. Knill. Error analysis for encoding a qubit in an oscillator. *Physical Review A*, 73, 012325 (2006)
- [68] B. W. Walshe, B. Q. Baragiola, R. N. Alexander and N. C. Menicucci. Continuous-variable gate teleportation and bosonic-code error correction. *Physical Review A*, 102, 62411 (2020)
- [69] K. H. Wan, A. Neville and S. Kolthammer. Memory-assisted decoder for approximate Gottesman-Kitaev-Preskill codes. *Physical Review Research*, 2, 043280 (2020)
- [70] K. Noh, C. Chamberland and F. G. S. L. Brandão. Low overhead fault-tolerant quantum error correction with the surface-GKP code. Technical Report (2021)
- [71] N. C. Menicucci, P. Van Loock, M. Gu, C. Weedbrook, T. C. Ralph and M. A. Nielsen. Universal quantum computation with continuous-variable cluster states. *Physical Review Letters*, 97, 110501 (2006)
- [72] N. C. Menicucci. Fault-tolerant measurement-based quantum computing with continuous-variable cluster states. *Physical Review Letters*, 112, 120504 (2014)

- [73] J. I. Yoshikawa et al.. Invited Article: Generation of one-million-mode continuous-variable cluster state by unlimited time-domain multiplexing. *APL Photonics*, 1, 060801 (2016)
- [74] M. V. Larsen, X. Guo, C. R. Breum, J. S. Neergaard-Nielsen and U. L. Andersen. Deterministic generation of a two-dimensional cluster state. *Science*, 366, 369 (2019)
- [75] W. Asavanant et al.. Generation of time-domain-multiplexed two-dimensional cluster state. *Science*, 366, 373 (2019)
- [76] M. V. Larsen, X. Guo, C. R. Breum, J. S. Neergaard-Nielsen and U. L. Andersen. Deterministic multi-mode gates on a scalable photonic quantum computing platform. *Nature Physics* (2021)
- [77] M. V. Larsen, C. Chamberland, K. Noh, J. S. Neergaard-Nielsen and U. L. Andersen. Fault-Tolerant Continuous-Variable Measurement-based Quantum Computation Architecture. *PRX Quantum*, 2, 030325 (2021)
- [78] I. Tzitrin et al.. Fault-tolerant quantum computation with static linear optics. *arXiv preprint at <https://arxiv.org/abs/2104.03241>* (2021)
- [79] B. M. Terhal and D. Weigand. Encoding a qubit into a cavity mode in circuit QED using phase estimation. *Physical Review A*, 93, 012315 (2016)
- [80] M. Rymarz, S. Bosco, A. Ciani and D. P. Divincenzo. Hardware-Encoding Grid States in a Nonreciprocal Superconducting Circuit. *Physical Review X*, 11, 011032 (2021)
- [81] P. T. Cochrane, G. J. Milburn and W. J. Munro. Macroscopically distinct quantum-superposition states as a bosonic code for amplitude damping. *Physical Review A*, 59, 2631 (1999)
- [82] L. Hu et al.. Quantum error correction and universal gate set operation on a binomial bosonic logical qubit. *Nature Physics*, 15, 503 (2019)
- [83] C. Flühmann, V. Negnevitsky, M. Marinelli and J. P. Home. Sequential Modular Position and Momentum Measurements of a Trapped Ion Mechanical Oscillator. *Physical Review X*, 8, 021001 (2018)
- [84] C. Weedbrook et al.. Gaussian quantum information. *Reviews of Modern Physics*, 84, 621 (2012)
- [85] S. Muralidharan, L. Li, J. Kim, N. Lütkenhaus, M. D. Lukin and L. Jiang. Optimal architectures for long distance quantum communication. *Scientific Reports*, 6, 20463 (2016)
- [86] M. Pysher, Y. Miwa, R. Shahrokhshahi, R. Bloomer and O. Pfister. Parallel generation of quadripartite cluster entanglement in the optical frequency comb. *Physical Review Letters*, 107, 030505 (2011)
- [87] S. Yokoyama et al.. Ultra-large-scale continuous-variable cluster states multiplexed in the time domain. *Nature Photonics*, 7, 982 (2013)
- [88] M. Eaton, R. Nehra and O. Pfister. Non-Gaussian and Gottesman-Kitaev-Preskill state preparation by photon catalysis. *New Journal of Physics*, 21, 113034 (2019)
- [89] D. Su, C. R. Myers and K. K. Sabapathy. Conversion of Gaussian states to non-Gaussian states using photon-number-resolving detectors. *Physical Review A*, 100, 052301 (2019)

- [90] H. M. Vasconcelos, L. Sanz and S. Glancy. All-optical generation of states for “Encoding a qubit in an oscillator”. *Optics Letters*, 35, 3261 (2010)
- [91] D. J. Weigand and B. M. Terhal. Generating grid states from Schrödinger-cat states without postselection. *Physical Review A*, 97, 022341 (2018)
- [92] M. Dakna, T. Anhut, T. Opatrný, L. Knöll and D.-G. Welsch. Generating Schrödinger-cat-like states by means of conditional measurements on a beam splitter. *Physical Review A*, 55, 3184 (1997)
- [93] A. Ourjoumtsev, R. Tualle-Brouri, J. Laurat and P. Grangier. Generating Optical Schrödinger Kittens for Quantum Information Processing. *Science*, 312, 83 (2006)
- [94] J. S. Neergaard-Nielsen, B. M. Nielsen, C. Hettich, K. Mølmer and E. S. Polzik. Generation of a superposition of odd photon number states for quantum information networks. *Physical Review Letters*, 97, 083604 (2006)
- [95] K. Wakui, H. Takahashi, A. Furusawa, M. Sasaki, H.-a. Bachor and T. C. Ralph. Photon subtracted squeezed states generated with periodically poled KTiOPO4. *Optics Express*, 15, 3568 (2007)
- [96] T. Gerrits et al.. Generation of optical coherent-state superpositions by number-resolved photon subtraction from the squeezed vacuum. *Physical Review A*, 82, 31802(R) (2010)
- [97] G. S. Thekkadath, B. A. Bell, I. A. Walmsley and A. I. Lvovsky. Engineering Schrödinger cat states with a photonic even-parity detector. *Quantum*, 4, 239 (2020)
- [98] A. E. Lita, A. J. Miller and W. N. Nam. Counting near-infrared single-photons with 95% efficiency. *Optics Express*, 16, 3032 (2008)
- [99] P. C. Humphreys et al.. Tomography of photon-number resolving continuous-output detectors. *New Journal of Physics*, 17, 103044 (2015)
- [100] W. H. Zurek. Sub-Planck structure in phase space and its relevance for quantum decoherence. *Nature*, 412, 712 (2001)
- [101] K. Duivenvoorden, B. M. Terhal and D. Weigand. Single-mode displacement sensor. *Physical Review A*, 95, 12305 (2017)
- [102] D. Achilles et al.. Photon-number-resolving detection using time-multiplexing. *Journal of Modern Optics*, 51, 1499 (2004)
- [103] S. Takeda and A. Furusawa. Toward large-scale fault-tolerant universal photonic quantum computing. *APL Photonics*, 4, 060902 (2019)
- [104] P. Reinhold, S. Rosenblum, W. L. Ma, L. Frunzio, L. Jiang and R. J. Schoelkopf. Error-corrected gates on an encoded qubit. *Nature Physics*, 16, 822 (2020)
- [105] I. Tzitrin, J. E. Bourassa, N. C. Menicucci and K. K. Sabapathy. Progress towards practical qubit computation using approximate Gottesman-Kitaev-Preskill codes. *Physical Review A*, 101, 032315 (2020)
- [106] J. E. Bourassa et al.. Blueprint for a scalable photonic fault-tolerant quantum computer. *Quantum*, 5, 392 (2021)

- [107] W. Asavanant, K. Takase, K. Fukui, M. Endo, J.-I. Yoshikawa and A. Furusawa. Wavefunction engineering via conditional quantum teleportation with a non-Gaussian entanglement resource. *Physical Review A*, 103, 043701 (2021)
- [108] E. Knill. Scalable quantum computing in the presence of large detected-error rates. *Physical Review A*, 71, 042322 (2005)
- [109] K. Fukui, R. N. Alexander and P. van Loock. All-Optical Long-Distance Quantum Communication with Gottesman-Kitaev-Preskill qubits. *Physical Review Research*, 3, 033118 (2021)
- [110] F. Rozpedek, K. Noh, Q. Xu, S. Guha and L. Jiang. Quantum repeaters based on concatenated bosonic and discrete-variable quantum codes. *npj Quantum Information*, 7, 102 (2021)
- [111] B. De Neeve, T.-L. Nguyen, T. Behrle and J. P. Home. Error correction of a logical grid state qubit by dissipative pumping. *arXiv preprint at <https://arxiv.org/abs/2010.09681>* (2020)
- [112] S. Pirandola, S. Mancini, D. Vitali and P. Tombesi. Constructing finite-dimensional codes with optical continuous variables. *Europhysics Letters*, 68, 323 (2004)
- [113] S. Pirandola, S. Mancini, D. Vitali and P. Tombesi. Continuous variable encoding by ponderomotive interaction. *European Physical Journal D*, 37, 283 (2006)
- [114] N. Shukla, S. Nimmrichter and B. C. Sanders. Squeezed comb states. *Physical Review A*, 103, 12408 (2021)
- [115] P. Lodahl, S. Mahmoodian and S. Stobbe. Interfacing single photons and single quantum dots with photonic nanostructures. *Reviews of Modern Physics*, 87, 347 (2015)
- [116] D. Najer et al.. A gated quantum dot strongly coupled to an optical microcavity. *Nature*, 575, 622 (2019)
- [117] C. Y. Hu, A. Young, J. L. O'Brien, W. J. Munro and J. G. Rarity. Giant optical Faraday rotation induced by a single-electron spin in a quantum dot: Applications to entangling remote spins via a single photon. *Physical Review B*, 78, 085307 (2008)
- [118] E. Janitz, M. K. Bhaskar and L. Childress. Cavity quantum electrodynamics with color centers in diamond. *Optica*, 7, 1232 (2020)
- [119] M. K. Bhaskar et al.. Experimental demonstration of memory-enhanced quantum communication. *Nature*, 580, 60 (2020)
- [120] L. M. Duan and H. J. Kimble. Scalable photonic quantum computation through cavity-assisted interactions. *Physical Review Letters*, 92, 127902 (2004)
- [121] H. Goto, S. Mizukami, Y. Tokunaga and T. Aoki. Figure of merit for single-photon generation based on cavity quantum electrodynamics. *Physical Review A*, 99, 053843 (2019)
- [122] S. Al-Sumaidae, M. H. Bitarafan, C. A. Potts, J. P. Davis and R. G. DeCorby. Cooperativity enhancement in buckled-dome microcavities with omnidirectional claddings. *Optics Express*, 26, 11201 (2018)
- [123] C. W. Gardiner and M. J. Collett. Input and output in damped quantum systems: Quantum stochastic differential equations and the master equation. *Physical Review A*, 31, 3761 (1985)

- [124] B. Q. Baragiola, G. Pantaleoni, R. N. Alexander, A. Karanjai and N. C. Menicucci. All-Gaussian Universality and Fault Tolerance with the Gottesman-Kitaev-Preskill Code. *Physical Review Letters*, 123, 200502 (2019)
- [125] S. Lloyd and S. L. Braunstein. Quantum computation over continuous variables. *Physical Review Letters*, 82, 1784 (1999)
- [126] B. M. Terhal, J. Conrad and C. Vuillot. Towards scalable bosonic quantum error correction. *Quantum Science and Technology*, 5, 043001 (2020)
- [127] M. D. Bowdrey, D. K. Oi, A. J. Short, K. Banaszek and J. A. Jones. Fidelity of single qubit maps. *Physics Letters A*, 294, 258 (2002)
- [128] G. Pantaleoni, B. Q. Baragiola and N. C. Menicucci. Modular Bosonic Subsystem Codes. *Physical Review Letters*, 125, 040501 (2020)
- [129] K. Fukui, A. Tomita, A. Okamoto and K. Fujii. High-Threshold Fault-Tolerant Quantum Computation with Analog Quantum Error Correction. *Physical Review X*, 8, 021054 (2018)
- [130] H. Yamasaki, K. Fukui, Y. Takeuchi, S. Tani and M. Koashi. Polylog-overhead highly fault-tolerant measurement-based quantum computation: all-Gaussian implementation with Gottesman-Kitaev-Preskill code. *arXiv preprint at <https://arxiv.org/abs/2006.05416>* (2020)
- [131] K. Noh and C. Chamberland. Fault-tolerant bosonic quantum error correction with the surface Gottesman-Kitaev-Preskill code. *Physical Review A*, 101, 12316 (2020)
- [132] K. Noh, S. M. Girvin and L. Jiang. Encoding an Oscillator into Many Oscillators. *Physical Review Letters*, 125, 080503 (2020)
- [133] K. Fukui. High-threshold fault-tolerant quantum computation with the GKP qubit and realistically noisy devices. *arXiv preprint at <https://arxiv.org/abs/1906.09767>* (2019)
- [134] Y. Wang. Quantum Error Correction with the GKP Code and Concatenation with Stabilizer Codes. *Master's thesis* (2019)
- [135] C. Vuillot, H. Asasi, Y. Wang, L. P. Pryadko and B. M. Terhal. Quantum error correction with the toric Gottesman-Kitaev-Preskill code. *Physical Review A*, 99, 32344 (2019)
- [136] K. Fukui, A. Tomita and A. Okamoto. Analog Quantum Error Correction with Encoding a Qubit into an Oscillator. *Physical Review Letters*, 119, 180507 (2017)
- [137] C. K. Law and J. H. Eberly. Arbitrary control of a quantum electromagnetic field. *Physical Review Letters*, 76, 1055 (1996)
- [138] A. Ben-Kish et al.. Experimental Demonstration of a Technique to Generate Arbitrary Quantum Superposition States of a Harmonically Bound Spin-[Formula presented] Particle. *Physical Review Letters*, 90, 4 (2003)
- [139] S. Krastanov et al.. Universal control of an oscillator with dispersive coupling to a qubit. *Physical Review A*, 92, 040303(R) (2015)
- [140] R. W. Heeres et al.. Cavity State Manipulation Using Photon-Number Selective Phase Gates. *Physical Review Letters*, 115 (2015)
- [141] A. F. Kockum, A. Miranowicz, S. De Liberato, S. Savasta and F. Nori. Ultrastrong coupling between light and matter. *Nature Reviews Physics*, 1, 19 (2019)

- [142] P. Forn-Díaz, L. Lamata, E. Rico, J. Kono and E. Solano. Ultrastrong coupling regimes of light-matter interaction. *Reviews of Modern Physics*, 91, 025005 (2019)
- [143] K. Park, P. Marek and R. Filip. Qubit-mediated deterministic nonlinear gates for quantum oscillators. *Scientific Reports*, 7, 1 (2017)
- [144] K. Park, P. Marek and R. Filip. Deterministic nonlinear phase gates induced by a single qubit. *New Journal of Physics*, 20, 053022 (2018)
- [145] B. C. Travaglione and G. J. Milburn. Preparing encoded states in an oscillator. *Physical Review A*, 66, 052322 (2002)
- [146] Y. Shi, C. Chamberland and A. Cross. Fault-Tolerant preparation of approximate GKP states. *New Journal of Physics*, 21, 093007 (2019)
- [147] S. Bravyi and A. Kitaev. Universal quantum computation with ideal Clifford gates and noisy ancillas. *Physical Review A*, 71, 022316 (2005)
- [148] M. A. Castellanos-Beltran, K. D. Irwin, G. C. Hilton, L. R. Vale and K. W. Lehnert. Amplification and squeezing of quantum noise with a tunable Josephson metamaterial. *Nature Physics*, 4, 928 (2008)
- [149] H. Yamasaki, T. Matsuura and M. Koashi. Cost-reduced all-Gaussian universality with the Gottesman-Kitaev-Preskill code: Resource-theoretic approach to cost analysis. *Physical Review Research*, 2, 023270 (2020)
- [150] K. R. Motes, B. Q. Baragiola, A. Gilchrist and N. C. Menicucci. Encoding qubits into oscillators with atomic ensembles and squeezed light. *Physical Review A*, 95, 053819 (2017)
- [151] B. Royer, S. Singh and S. M. Girvin. Stabilization of finite-energy Gottesman-Kitaev-Preskill states. *Physical Review Letters*, 125, 260509 (2020)
- [152] L. S. Braunstein and P. Van Loock. Quantum information with continuous variables. *Reviews of Modern Physics*, 77, 513 (2005)
- [153] J. I. Cirac, A. S. Parkins, R. Blatt and P. Zoller. "Dark" squeezed states of the motion of a trapped ion. *Physical Review Letters*, 70, 556 (1993)
- [154] D. Lv et al.. Quantum Simulation of the Quantum Rabi Model in a Trapped Ion. *Physical Review X*, 8, 021027 (2018)
- [155] N. K. Langford et al.. Experimentally simulating the dynamics of quantum light and matter at deep-strong coupling. *Nature Communications*, 8, 1715 (2017)
- [156] V. Giovannetti, S. Lloyd and L. Maccone. Quantum-enhanced measurements: Beating the standard quantum limit. *Science*, 306, 1330 (2004)
- [157] P. A. Ivanov and N. V. Vitanov. Quantum sensing of the phase-space-displacement parameters using a single trapped ion. *Physical Review A*, 97, 32308 (2018)
- [158] M. Penasa et al.. Measurement of a microwave field amplitude beyond the standard quantum limit. *Physical Review A*, 94, 022313 (2016)
- [159] P. A. Ivanov, N. V. Vitanov and K. Singer. High-precision force sensing using a single trapped ion. *Scientific Reports*, 6, 28078 (2016)

-
- [160] C. Hempel, B. P. Lanyon, P. Jurcevic, R. Gerritsma, R. Blatt and C. F. Roos. Entanglement-enhanced detection of single-photon scattering events. *Nature Photonics*, 7, 630 (2013)
- [161] S. C. Burd et al.. Quantum amplification of mechanical oscillator motion. *Science*, 364, 1163 (2019)
- [162] J. B. Clark, F. Lecocq, R. W. Simmonds, J. Aumentado and J. D. Teufel. Observation of strong radiation pressure forces from squeezed light on a mechanical oscillator. *Nature Physics*, 12, 683 (2016)
- [163] M. Naghiloo et al.. Heat and Work Along Individual Trajectories of a Quantum Bit. *Physical Review Letters*, 124, 110604 (2020)
- [164] W. Pfaff et al.. Controlled release of multiphoton quantum states from a microwave cavity memory. *Nature Physics*, 13, 882 (2017)
- [165] K. Roszak, R. Filip and T. Novotný. Decoherence control by quantum decoherence itself. *Scientific Reports*, 5, 09796 (2015)
- [166] D. Ballester, G. Romero, J. J. García-Ripoll, F. Deppe and E. Solano. Quantum simulation of the ultrastrong-coupling dynamics in circuit quantum electrodynamics. *Physical Review X*, 2, 021007 (2012)
- [167] A. Mezzacapo, U. Las Heras, J. S. Pedernales, L. DiCarlo, E. Solano and L. Lamata. Digital quantum rabi and dicke models in superconducting circuits. *Scientific Reports*, 4, 7482 (2014)
- [168] M. Paris and J. Rehacek. Quantum state estimation. Springer Science & Business Media (2004)
- [169] P. Krantz, M. Kjaergaard, F. Yan, T. P. Orlando, S. Gustavsson and W. D. Oliver. A quantum engineer's guide to superconducting qubits. *Appl. Phys. Rev*, 6, 021318 (2019)
- [170] J. Fiurášek. Encoding the quantum state of cavity mode into an atomic beam. *Physical Review A*, 66, 015801 (2002)
- [171] X.-Y. Chen, L. Han and L.-Z. Jiang. Quantum state conversion between continuous variable and qubits systems. *Physics Letters A*, 359, 587 (2006)
- [172] R. N. Alexander, N. C. Gabay, P. P. Rohde and N. C. Menicucci. Measurement-Based Linear Optics. *Physical Review Letters*, 118 (2017)
- [173] D. Su, K. K. Sabapathy, C. R. Myers, H. Qi, C. Weedbrook and K. Brádler. Implementing quantum algorithms on temporal photonic cluster states. *Physical Review A*, 98, 32316 (2018)
- [174] B.-H. Wu, R. N. Alexander, S. Liu and Z. Zhang. Quantum computing with multidimensional continuous-variable cluster states in a scalable photonic platform. *Physical Review Research*, 2, 023138 (2020)
- [175] M. V. Larsen, J. S. Neergaard-Nielsen and U. L. Andersen. Architecture and noise analysis of continuous-variable quantum gates using two-dimensional cluster states. *Physical Review A*, 102, 042608 (2020)
- [176] G. Pantaleoni, B. Q. Baragiola and N. C. Menicucci. Hidden qubit cluster states. *Physical Review A*, 104, 012431 (2021)

- [177] F. Marsili et al.. Detecting single infrared photons with 93% system efficiency. *Nature Photonics*, 7, 210 (2013)
- [178] J. Chang et al.. Detecting telecom single photons with 99.5 - 2.07 + 0.5 % system detection efficiency and high time resolution. *APL Photonics*, 6, 36114 (2021)
- [179] K. Fukui, A. Tomita and A. Okamoto. Tracking quantum error correction. *Physical Review A*, 98, 022326 (2018)
- [180] S. Puri et al.. Stabilized Cat in a Driven Nonlinear Cavity: A Fault-Tolerant Error Syndrome Detector. *Physical Review X*, 9, 041009 (2019)
- [181] K. R. Brown, C. Ospelkaus, Y. Colombe, A. C. Wilson, D. Leibfried and D. J. Wineland. Coupled quantized mechanical oscillators. *Nature*, 471, 196 (2011)
- [182] M. Harlander, R. Lechner, M. Brownnutt, R. Blatt and W. Hänsel. Trapped-ion antennae for the transmission of quantum information. *Nature*, 471, 200 (2011)
- [183] W. Chen, J. Gan, J. N. Zhang, D. Matuskevich and K. Kim. Quantum computation and simulation with vibrational modes of trapped ions. *Chinese Physics B*, 30, 060311 (2021)
- [184] Y. Y. Gao et al.. Programmable Interference between Two Microwave Quantum Memories. *Physical Review X*, 8, 021073 (2018)
- [185] N. Killoran, J. Izaac, N. Quesada, V. Bergholm, M. Amy and C. Weedbrook. Strawberry Fields: A software platform for photonic quantum computing. *Quantum*, 3, 129 (2019)
- [186] J. B. Brask. Gaussian states and operations – a quick reference. *arXiv preprint at <https://arxiv.org/abs/2102.05748>* (2021)
- [187] J. E. Bourassa et al.. Fast simulation of bosonic qubits via Gaussian functions in phase space. *arXiv preprint at <https://arxiv.org/abs/2103.05530>* (2021)
- [188] C. Chamberland et al.. Building a fault-tolerant quantum computer using concatenated cat codes. *arXiv preprint at <https://arxiv.org/abs/2012.04108>* (2020)
- [189] K. E. Cahill and R. J. Glauber. Ordered expansions in boson amplitude operators. *Physical Review*, 177, 1857 (1969)
- [190] L. Albano, D. F. Mundarain and J. Stephany. On the squeezed number states and their phase space representations. *Journal of Optics B: Quantum and Semiclassical Optics*, 4, 352 (2002)
- [191] M. S. Kim, F. A. De Oliveira and P. L. Knight. Properties of squeezed number states and squeezed thermal states. *Physical Review A*, 40, 2494 (1989)
- [192] U. Leonhardt. *Measuring the Quantum State of Light*. Cambridge university press (1997)